Microsystems Technology
Institute of Sensor and
Actuator Systems
TU Wien (Austria)

Flexoelectricity in PVDF and TiO_x Thin Films

Material Characterization for MEMS Applications

Die approbierte gedruckte Originalversion dieser Dissertation ist an der TU Wien Bibliothek verfügbar.
The approved original version of this doctoral thesis is available in print at TU Wien Bibliothek.
TU Bibliothek Your knowledge hub

DISSERTATION

FRANZ JOSEF MAIER

September 2023

Thesis supervisor:

Univ.-Prof. Dr. Ulrich SCHMID

Table of contents

Table of contents 2

Used Symbols 3

Acknowledgements 5

Abstract 6

1 Introduction 8

2 Theory 16

2.1 Electronic properties of materials ... 16

2.2 Leakage currents ... 26

2.3 Electro-mechanical transduction mechanisms ... 36

2.4 Micromechanical resonators ... 54

3 Methods 59

3.1 Thin film deposition ... 59

3.2 Patterning techniques ... 63

3.3 Cantilever fabrication process ... 68

3.4 Measurement methods ... 74

3.5 Used materials ... 92

4 Results and Discussion 101

4.1 α-phase PVDF MEMS cantilevers ... 101

4.2 Flexoelectric TiO_x cantilever ... 116

4.3 Electric behaviour of $IrO_x/TiO_x/IrO_x$ capacitors ... 135

4.4 Temperature-dependent cantilever characterization ... 167

5 Conclusio 171

6 Outlook 176

7 References 178

Die approbierte gedruckte Originalversion dieser Dissertation ist an der TU Wien Bibliothek verfügbar.
The approved original version of this doctoral thesis is available in print at TU Wien Bibliothek.
TU WIEN Bibliothek Your knowledge hub

Used Symbols

a	…Lattice constant	m	h	…Thickness	m
A	…Area	m^2	i	…Imaginary number	1
b	…Width	m	I	…Area moment of inertia	$kg \cdot m^2$
B	…Magnetic flux density	T	I_E	…Electric field intensity	W/m^2
c_{ijk}	…Stiffness tensor	1	J	…Current	A
C	…Capacitance	F	k	…Wavenumber	1/m
d_{ijk}	…Piezoelectric constant	m/V	k_B	…Boltzmann constant	J/K
D	…Flexural rigidity	$Pa \cdot m^4$	l	…Length	m
e	…Surface piezoelectric constant	m/V	M_{ij}	…Born effective charge tensor	C
E	…Electric field	V/m	P	…Polarization	C/m^2
E_C	…Conduction band energy	eV	q	…Elementary charge	C
E_V	…Valence band energy	eV	Q	…Quality factor	1
E_G	…Bandgap energy	eV	Q_C	…Electric charge	C
E_F	…Fermi energy	eV	Q_e	…Electrostrictive coefficient	m^4/C^2
E_{mod}	…Young's modulus	GPa	r	…Radius	m
f	…Frequency	Hz	t	…Time	s
f_0	…Resonance frequency	Hz	T	…Temperature	K
f_a	…Actuation frequency	Hz	u_{ijk}	…Strain	1
f_m	…Measurement frequency	Hz	v	…Velocity	m/s
F_E	…Electrostatic force	N	V	…Voltage	V
g_{ijk}	…Gradient tensor	1	w	…Deflection	m

Die approbierte gedruckte Originalversion dieser Dissertation ist an der TU Wien Bibliothek verfügbar.
The approved original version of this doctoral thesis is available in print at TU Wien Bibliothek.
TU WIEN Bibliothek Your knowledge hub

G	…Curvature	1/m	x,y,z	…Cartesian coordinates	m
Γ_{ijkl}	…Flexocoupling constant	V	Z	…Impedance	Ω
δ	…Tip deflection	m			
ε_0	…Vacuum permittivity	F/m			
ε_r	…Relative permittivity	1			
κ	…Spring constant	N/m			
λ	…Wavelength	m			
μ_{ijkl}	…Flexoelectric coefficient	C/m			
μ_{mob}	…Electron mobility	$m^2/(V\cdot s)$			
υ	…Poisson constant	1			
ρ	…Mass density	kg/m^3			
σ_{ijk}	…Stress	N/m^2			
$\varphi_{m/i}$	…Metal/insulator work function	eV			
Φ	…Barrier height	eV			
χ	…Electric susceptibility	1			
χ_a	…Electron affinity	J/mol			
ϕ_G	…Thermodynamical potential	eV			
ω	…Angular frequency	rad/s			

Die approbierte gedruckte Originalversion dieser Dissertation ist an der TU Wien Bibliothek verfügbar.
The approved original version of this doctoral thesis is available in print at TU Wien Bibliothek.
TU WIEN Bibliothek Your knowledge hub

Acknowledgements

I would like to express my sincere gratitude to my supervisor, Univ.-Prof. Dr. Ulrich Schmid, for their invaluable guidance, encouragement, and support throughout my research journey. Their extensive knowledge, expertise, and insightful feedback have been crucial to the successful completion of this project.

I would also like to thank Dr. Michael Schneider, for their assistance, collaboration, and mentorship during this research project. Their constructive criticism, helpful discussions, and technical expertise have been instrumental in shaping the direction of my research and in advancing my understanding of the field.

I am grateful to my family and friends for their unwavering love, encouragement, and support throughout my academic journey. Their constant support and motivation have been a source of strength and inspiration to me.

Lastly, I would like to extend my sincere appreciation to all the individuals who have contributed to my research in various ways, whether through their feedback, insights, or participation in my studies. Your contributions have been invaluable and have enriched my research experience.

Thank you all for your support, encouragement, and guidance. Without your help, this achievement would not have been possible.

Die approbierte gedruckte Originalversion dieser Dissertation ist an der TU Wien Bibliothek verfügbar.
The approved original version of this doctoral thesis is available in print at TU Wien Bibliothek.
TU WIEN Bibliothek Your knowledge hub

Abstract

In this work, two cantilevered micro-electro-mechanical systems (MEMS) device architectures were evaluated, whereas the actuation was done with the flexoelectric effect. The first approach is based on a non-polar, α-phase polyvinylidene fluoride (PVDF) structure sandwiched between two gold electrodes. In the second approach, iridium oxide (IrO_x) serves as electrode material, and titanium oxide (TiO_x) as a functional material. For the Au/∝-phase PVDF/Au transducer, ∝-phase PVDF was produced with a spin-on method on a heated chuck, which allows the realization of ultra-thin (< 200 nm) PVDF films with an average roughness below 20 nm. It was found that this soft material exhibits a significant electrostrictive response. Consequently, it was demonstrated that electrostrictive PVDF cantilevers could compete with their piezoelectric counterparts while drastically reducing fabrication complexity. Temperature-dependent cantilever tip deflection measurements were performed, which showed that the impact on the tip deflection from room temperature up to 160°C is linked to the changes in the effective Young's modulus of the cantilever. Even though ∝-phase PVDF was reported in literature to exhibit a giant flexoelectric effect, this finding could not be verified. The latter findings from PVDF films differ, however, entirely from the sputter-deposited rutile TiO_x devices fabricated and analysed in addition in this study. On device level, a linear dependence of curvature as a function of voltage was measured when exciting cantilevered MEMS transducers sinusoidally. The actuation was identified as flexoelectric, with a flexoelectric coefficient of ~2 nC/m. Segmented top electrodes were designed to stimulate additional electric field gradients to improve the performance of these devices even further. In addition, the pure electrical performance of the $IrO_x/TiO_x/IrO_x$ stack is determined in detail on mechanically non-released test structures, focusing on capacitance and leakage current measurements. On average, the devices in this thesis showed a permittivity range between 60 and 95. The leakage current measurements revealed capacitive-memristive leakage current hysteresis effects, which were linked to the electrical charging and discharging of oxygen vacancies. Additionally, a dynamic generation of these vacancies with an applied electric field was shown, which led to a repeatable formation and dissociation of low-resistivity vacancy filaments in the TiO_x layer. A drastic change in the temperature dependence of the leakage current characteristics was found, depending on the atmosphere to which the IrO_x bottom electrode was exposed before sputter-

Die approbierte gedruckte Originalversion dieser Dissertation ist an der TU Wien Bibliothek verfügbar.
The approved original version of this doctoral thesis is available in print at TU Wien Bibliothek.
TU Bibliothek Your knowledge hub WIEN

depositing the TiO_x thin film. When getting in contact with air the formation of OH-bridges on the surface of the IrO_x is a leading factor in the temperature-dependent leakage current behaviour. The temperature dependence of the leakage current is most probably due to the deprotonation of OH-bridges. The herein-released oxygen can passivate electrically active oxygen vacancies, thus decreasing the leakage current at increasing temperatures. With this knowledge, the first temperature-dependent cantilever measurements were performed, demonstrating this passivating behaviour.

Die approbierte gedruckte Originalversion dieser Dissertation ist an der TU Wien Bibliothek verfügbar.
The approved original version of this doctoral thesis is available in print at TU Wien Bibliothek.
TU Bibliothek Your knowledge hub WIEN

1 Introduction

Most processes in life are a series of signal acquisition from the ambient, data processing and actuation for the desired output. A detector is needed to enable the first step in this series which shows the importance of such sensing elements. With the ability of humans to build their own detectors, it is only a logical next step to decrease their size and cost while increasing their efficiency. With the development of silicon-based (Si) technology, these three essential requirements could be addressed. First, only pure optical and electrical detectors could use the benefits of this new technology. The first emergence of a detector microsystem based on silicon technology can be attributed to piezoresistive semiconductor strain gages, while ink jet printing nozzles are an early example for an actuator microsystem.[1,2] Soon after, systems with both mechanical and electrical components were developed. These first micro-electro-mechanical systems (MEMS) included micro switches, pressure sensors, accelerometers, mechanical resonators or torsion mirrors.[3,4] Depending on the size of the functional parts of these systems can also be called nano electro-mechanical systems (NEMS). As the naming suggests, to actuate and sense with these devices, transducer elements are needed to provide an electrical-mechanical coupling. Several transducer mechanisms are exploited in silicon MEMS devices, especially for actuation and sensing purposes. Besides the capacitive approach as standard, one transducer principle strongly emerging in the last decade is based on the piezoelectric effect. The piezoelectric effect describes the linear deformation of a non-centrosymmetric crystal with an externally applied electric field or *vice versa*.[5] However, there is an often-overlooked effect called the flexoelectric effect.[6]

The flexoelectric effect is an electromechanical effect that describes the mechanical deformation due to an electric field gradient or a change in polarization due to a mechanical stress gradient.[7] The flexoelectric effect gained particular interest over the last decades due to its potential to outperform the piezoelectric effect on the nanoscale. This gain in interest is due to an inverse cubic scaling of the mechanical deformation regarding the electric field gradient.[8] Conversely, the strain generated from the piezoelectric effect decreases linearly

Die approbierte gedruckte Originalversion dieser Dissertation ist an der TU Wien Bibliothek verfügbar.
The approved original version of this doctoral thesis is available in print at TU Wien Bibliothek.
TU Wien Bibliothek Your knowledge hub

with decreasing thickness at a constant electric field.[9][1] Additionally, in practical application, the piezoelectric constant for common materials such as barium titanate ($BaTiO_3$), lead-zirconium titanate (PZT), strontium titanate ($SrTiO_3$) or aluminium nitride (AlN) decreases with decreasing film thickness due to a lower degree of crystallinity in thinner films.[10–12] The linear scaling of the flexoelectric coefficient with permittivity of the functional material can also give the flexoelectric effect a further significant role in the realm of actuation principles, as modern electronic materials can provide exceedingly high permittivity values up to 10000.[13,14] The flexoelectric effect was first described by Bursian *et al.* as a non-local piezoelectric effect.[15] Non-locality means that for a flexoelectric analysis, it is not enough to focus only on the unit cell of a given material, but multiple unit cells must be considered. An induced polarization arises when a strain gradient is applied across a material, as the strain distribution of a given unit cell differs from the neighbouring unit cell. *Vice versa*, when an electric field gradient is applied, the electric forces vary from one unit cell to the neighbouring ones, leading to mechanical deformation.

The effect was first shown experimentally in 1968 when a non-piezoelectric α-phase $BaTiO_3$ beam was subjected to a 3-point beam bending characterization. The authors did not expect any generated charges at all, as the α-phase of $BaTiO_3$ is not piezoelectric, but still generated charges were measured. As the bending of a beam introduces a stress gradient across the beam's cross-section, the flexoelectric effect was first considered.[16] For the following decades, fewer research efforts were invested in the flexoelectric effect. This is due to the flexoelectric effect being negligibly small at length scales above several µm due to both the comparably low material coefficients and the increasing complexity of introducing a field gradient.[17]. When writing this manuscript, most of the investigations on the flexoelectric effect were conducted at ferroelectric, oxidic materials like PZT, $SrTiO_3$ or $BaTiO_3$.[18–20] The reason is that the flexoelectric effect scales with the permittivity and ferroelectrics tend to show a high permittivity of up to 10^5 compared to other more common oxides in microelectronics and MEMS like titanium oxide (TiO_2), aluminium oxide (Al_2O_3) or tantalum oxide (Ta_2O_5) with permittivity values typically between 30 and 100.[21] Non-oxide materials, like silicon nitride or aluminium nitride, tend to have an even lower permittivity, with a permittivity below 30.[22,23]

[1] Practically, applying the same voltage V when going to thinner devices with thickness h leads to the same generated strain as the electric field increases as $E = V/h$. However, there is a higher chance to increase the electric field above the breakdown field strength of the dielectric layer and therefore damaging the device.

Die approbierte gedruckte Originalversion dieser Dissertation ist an der TU Wien Bibliothek verfügbar.
The approved original version of this doctoral thesis is available in print at TU Wien Bibliothek.
TU Bibliothek WIEN Your knowledge hub

For these reasons, non-piezoelectric phases of ultra-high permittivity materials like PZT, $SrTiO_3$ or $BaTiO_3$ and variations of these material systems were investigated previously.[24] Determining the flexoelectric activity in such electronic materials can be challenging, as they often possess ferroelectric hysteresis and residual piezoelectric phases.[25] A ferroelectric hysteresis introduces effects such as domain wall polarization and polarization switching effects.[7] Standard methods to investigate the flexoelectric effect often originate in the field of mechanical engineering on mm-sized samples. For example, a force is applied to a truncated pyramid (or cylinder), and the resulting charge is measured.[26] When a force is applied to a truncated-shaped design, such as a pyramid, the cross-sectional area changes in the direction of the applied force, as shown in *Figure 1*.

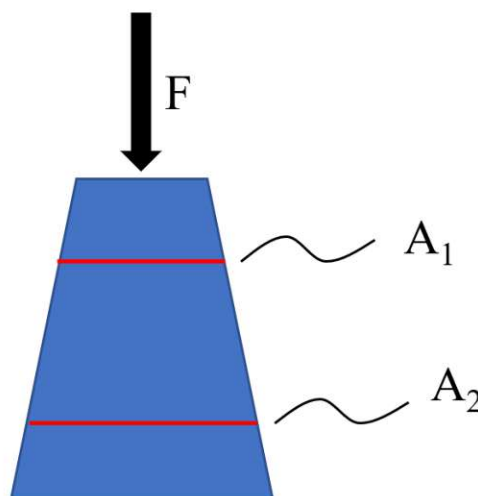

Figure 1 *Schematics for the truncated pyramid experiment. A force F is applied on the truncated pyramid, resulting in different stress values at the two red cross-sections due to the difference in the area of A_1 and A_2.*

This change in the area leads to a local change in stress distribution and, therefore, the desired stress gradient to study the flexoelectric effect results. To exclude parasitic effects due to the residual piezoelectricity, these truncated shapes are compared to flat (non-truncated) shapes (*i.e.* cylinders or cubes), and the resulting charge generation behaviour of both test devices is compared. There are several problems with this approach: first, the stress generated in a pyramid is not constant at a given cross-section, and secondly, it was shown that even small non-zero piezoelectric coefficients (*e.g.,* from residual piezoelectric phases or domain walls) could substantially influence the resulting flexoelectric coefficient.[17]

Additionally, at the start of the thesis in 2017, there were several studies on the giant flexoelectric coefficient present in α-phase polyvinylidene fluoride (PVDF).[27–29] In these studies, α-phase PVDF films with ~10µm thickness were cut into straight and truncated strips.

Die approbierte gedruckte Originalversion dieser Dissertation ist an der TU Wien Bibliothek verfügbar.
The approved original version of this doctoral thesis is available in print at TU Wien Bibliothek.
TU Bibliothek WIEN Your knowledge hub

These strips were then loaded with a sinusoidal force. Again, the resulting charge generation of the straight and truncated strips was compared.

Typical values of the flexoelectric coefficients μ_{eff} obtained from various methods are given in *Table 1*.

Material	μ_{eff} [nC/m]
$SrTiO_3$	4.6 - 7 [20,24]
$PbZrO_3$	$2.5\cdot10^3$ - $14\cdot10^3$ [18]
$BaTiO_3$	$5\cdot10^5$ [24]
β-phase PVDF-TrFE[2]	3.04 [30]
α-phase PVDF	18 - 10^4 [27,31]

Table 1 *Overview of effective flexoelectric coefficient values μ_{eff} of solid hard and soft materials.*

For pure PVDF, there is a considerable discrepancy between the values for the flexoelectric coefficient, reported in literature, demonstrating that the experimental determination of μ is not straightforward.

As advances in micro- and nanotechnology enabled the realization of smaller and smaller devices, the flexoelectric effect gained more attention. This led to a reignition of research in the flexoelectric field in the 2000s. With advances in micro-electromechanical systems, it is now possible to produce sub-µm transducers with complex geometry.[32] In 2015, Bhaskar *et al.* first showed a flexoelectric cantilever made from $SrTiO_3$ built with semiconductor technology at sub-µm scales, which exhibited very promising results characterized by a flexoelectric coefficient of $\mu_{eff} = 4.6$ nC m^{-1}.[20]

Flexoelectric devices show several advantages. Most importantly, centrosymmetric crystal structures exhibit flexoelectric properties. This increases the range of usable, functional materials for NEMS/MEMS applications manifold. [8] Additionally, the flexoelectric effect is present at temperatures above the Curie-temperature of the functional material. This makes the

[2] TrFE stands for trifluoroethylene and is a co-polymer which is often added to PVDF. See section 3.5 for details.

Die approbierte gedruckte Originalversion dieser Dissertation ist an der TU Wien Bibliothek verfügbar.
The approved original version of this doctoral thesis is available in print at TU Wien Bibliothek.
TU Bibliothek WIEN Your knowledge hub

flexoelectric effect particularly useful in high-temperature environments. [33] Also, when looking at MEMS cantilever applications specifically, the cantilever structures do not have to follow a bimorph design. In detail, this means that the typical support layer in piezoelectric cantilevers can be omitted. Every layer that must be added to a MEMS stack can lead to significant problems. In the example of a cantilever MEMS, such issues include delamination or cracking at the interface of two layers due to mismatched crystal structures and introducing static bends of the cantilever due to interface stresses. Also, omitting the device layer means that the cantilevers can be made thinner, leading to lower stiffness and higher tip deflection.

A prime candidate for flexoelectric silicon MEMS applications is titanium dioxide (TiO_2). The high permittivity of the rutile crystallographic phase leads to a pronounced flexoelectric actuation. [34] Rutile is also the most common phase of TiO_2. It has been calculated that rutile possesses a permittivity of 129/170 in the a/c-axis direction.[34,35] For MEMS applications, TiO_2 can also be fabricated with complementary metal–oxide–semiconductor (CMOS) compatible processing, which is a significant advantage to other non-CMOS compatible materials, such as $BaTiO_3$ or PZT. For the analysis of the flexoelectric effect, it is also advantageous that TiO_2 has no piezoelectric phase. This makes it easier to confidently identify flexoelectric contribution regarding the total electromechanical actuation of a MEMS device. The paraelectric nature of TiO_2 also means that linearity of the polarization with respect to the electric field is expected.

Prior to this work, to the best of the author`s knowledge, there was only one study on TiO_2 reporting on the flexoelectric effect.[36] In this work published by 2016 Narvaez *et al.*, bulk single crystal TiO_2 was presented, showing an effective flexoelectric coefficient of ~ 2 nC/m. This work used a 3-point bending method of a macro-sized beam with dimensions in the millimetre range (length/width/thickness: 20 mm/2 mm/0.175–0.53 mm) and measured the generated charges. The authors argue that with this method, the surface piezoelectric effect significantly affects the resulting flexoelectric coefficient. Still, this source is often cited for the flexoelectric coefficient of TiO_2, even though the authors themselves argue that it is not a pure flexoelectric coefficient. In the case where an electric field gradient leads to a mechanical sample deformation, the surface piezoelectric effect can be neglected. For this reason and the reasons above, the direct flexoelectric effect of TiO_2 was chosen to be investigated in this thesis.

For the application of the flexoelectric TiO_2 cantilever, the choice of the electrode material is crucial, as it strongly influences the microstructural properties and, consequently, the electrical behaviour of the capacitor. In this thesis, iridium dioxide was selected as electrode material for

Die approbierte gedruckte Originalversion dieser Dissertation ist an der TU Wien Bibliothek verfügbar.
The approved original version of this doctoral thesis is available in print at TU Wien Bibliothek.
TU Bibliothek WIEN Your knowledge hub

TiO_2 for several reasons. Foremost, iridium dioxide can act as a seed layer for TiO_2, as it has the same crystallographic class, namely rutile, with a lattice difference between the rutile TiO_2 and rutile IrO_2 of 0.086 Å in a/b-axis direction. Due to the improved film quality when using a seed layer, a higher permittivity of the TiO_2 can be achieved, as shown in chapter 3.5. Additionally, the excellent lattice match reduces any stress between the IrO_2 and TiO_2 thin films.[37]

In addition to TiO_2, PVDF was chosen as an interesting functional material for MEMS applications. From a research perspective, the huge discrepancy in the flexoelectric coefficient for α-phase PVDF indicated the need for further research. From a device perspective, PVDF is preferred due to its accessibility, and even with the lowest estimations of the flexoelectric coefficient (~18 nC/m), actuation would still be high enough for a reasonable flexoelectric application in MEMS, especially when operated in resonance.

Interestingly, a flexoelectric actuation of a cantilever is possible. From an electrical perspective, a cantilever is a parallel-plate capacitor, so there should not be any field gradients and hence, any absence of flexoelectricity. However, a bending of non-piezoelectric cantilevers when applying an electric field, has been measured previously.[33] As to this date, the typical explanation is that the polarization does not jump from 0 in the electrode to the bulk polarization of the functional material but rather that there is a continuous change in polarization from the electrode to the functional material, and thus a field gradient is present.

Besides the electro-mechanical performance, understanding the pure electrical processes happening in the TiO_2 thin films is vital for further optimization of the material properties. As the spatial gradient of the electric field is the primary cause for the flexoelectric effect, a spatial measurement of the electric field at the dielectric/electrode interface in nanoscale resolution would be best. However, there are not many readily available techniques to characterize the electric field on a nanoscale, which is why more common measurement methods were chosen, such as capacitance and leakage measurements, to understand better the electrical processes occurring in the functional material. Especially leakage current characterization at different temperatures can give much information about microscopic, material-related effects. Using standard measurement methods to characterise microscopic processes has the disadvantage of recording only an integrated behaviour over all occurring electrical processes. As such, only generalized statements about the material can be made. However, by comparison with the literature and by the characterization of many differently synthesized samples as well as parameter variations, the amount of information enabled new insights.

TU Bibliothek Your knowledge hub WIEN
Die approbierte gedruckte Originalversion dieser Dissertation ist an der TU Wien Bibliothek verfügbar.
The approved original version of this doctoral thesis is available in print at TU Wien Bibliothek.

In the course of this work, a resistive behaviour that is dependent on the electrical history of the material was observed. This phenomenon is either called the memristive (from memory and resistive) effect or the resistive switching effect.[38] While the first describes the effect in general, the latter originates from the phenomenon that, in some cases, the dielectric resistance can be switched instantaneously under specific conditions. There are several mechanisms on which these effects are based. One hypothesis introduces the generation of electrically active particles or pseudo-particles in transition-metal oxides, where the oxygen is removed from the lattice, and the emergent positively charged site acts like a charged particle.[39] These holes increase the conductivity of the dielectric and can form a column connecting the two electrodes. The column formation results in a shorted capacitor with drastically reduced resistance (low resistance state, LRS). When the electric field is reversed, this column breaks down, and the resistance is increased again (high resistance state, HRS). The switch from HRS to LRS and *vice versa* happens on the scale of nanoseconds and has potential use in resistive random-access memory (ReRAM). This technology is most favourable for advanced nanoelectronics devices as it allows faster switching behaviour and longer retention times than existing RAM technologies.[40] TiO_2 was the first material where memristive properties have been reported and has been the focus of intensive research activities for the memristive effect.[41–47]

There are also other types of memristive behaviour, such as interface effects, where an oxygen exchange between electrode and insulator can change leakage current behaviour. In this model, the electric field can move oxygen from the insulator into the metal electrode, therefore removing the oxygen from the insulator, resulting in an increased oxygen vacancy density at the interface. This, in turn, increases the leakage current through decreased resistance of the insulator or a reduced Schottky barrier height, depending on the material selection. When the electric field is reversed, the oxygen re-enters the insulator, passivating the vacancies, and thus recovers the leakage current levels to the unbiased state. [38,48]

Another phenomenon that affects the leakage current behaviour is that the interface composition changes when in contact with different atmospheres. The surfaces of materials such as IrO_2 or Pt can bind oxygen and hydrogen from the atmosphere to form OH bridges or adsorb H_2O molecules.[49,50] When this happens, the surface's electrical properties also change. In addition, these example materials also exhibit catalytic behaviour, specifically an aqueous oxygen evolution, meaning that oxygen can be generated locally by splitting H_2O molecules at these surfaces.[51,52]

Die approbierte gedruckte Originalversion dieser Dissertation ist an der TU Wien Bibliothek verfügbar.
The approved original version of this doctoral thesis is available in print at TU Wien Bibliothek.
TU WIEN Bibliothek Your knowledge hub

As the flexoelectric effect in capacitor-type MEMS is proposed to originate at the interface of the insulator to the electrode, this atmosphere and oxygen vacancy-dependent electrical effects can also impact the electromechanical behaviour. Previous studies have shown a correlation between oxygen vacancy density and the flexoelectric coefficient. [53,54]

This thesis investigates flexoelectricity in $IrO_x/TiO_x/IrO_x$ and Au/PVDF/Au MEMS cantilevers. The design and geometry of the PVDF cantilevers and their correlation to the flexoelectric effect are analysed while also investigating the electrostrictive effect in detail. The TiO_x cantilevers are studied in-depth for their mechanical and electrical performance. A flexoelectric enhancement of the TiO_x cantilevers by artificially introducing electric field gradients by a segmented top electrode was theoretically derived and experimentally tested. The flexoelectric behaviour of the TiO_x cantilevers was analysed regarding the impact of the exposed atmosphere during fabrication, as well as in different ambient temperature and humidity environments during operation. The findings obtained from these investigations enabled a deeper understanding of the origin of the flexoelectric effect, especially in oxide materials.

Die approbierte gedruckte Originalversion dieser Dissertation ist an der TU Wien Bibliothek verfügbar.
The approved original version of this doctoral thesis is available in print at TU Wien Bibliothek.
TU Wien Bibliothek Your knowledge hub

2 Theory

2.1 Electronic properties of materials

Energy band structure

Charged particles in solids can interact with an applied electric field in various ways. In some materials, electrons in the electric field show almost gas-like behaviour, while electrons are nearly stationary in others. There are four main categories for the classification of conductivity in solids. There are conductors, semimetals, semiconductors, and insulators. Their difference is best described by the energy band diagram, where a schematic of the different positions of energy bands for the four standard material classes is illustrated in *Figure 2*. According to Bloch's theorem, for a periodic arrangement of atoms (nuclei), the solution of the electrons' wavefunction ψ is degenerated, meaning that there are n possible solutions of the accompanying Schrödinger equation for a given wavevector k of the electron.

Die approbierte gedruckte Originalversion dieser Dissertation ist an der TU Wien Bibliothek verfügbar.
The approved original version of this doctoral thesis is available in print at TU Wien Bibliothek.
TU WIEN Bibliothek Your knowledge hub

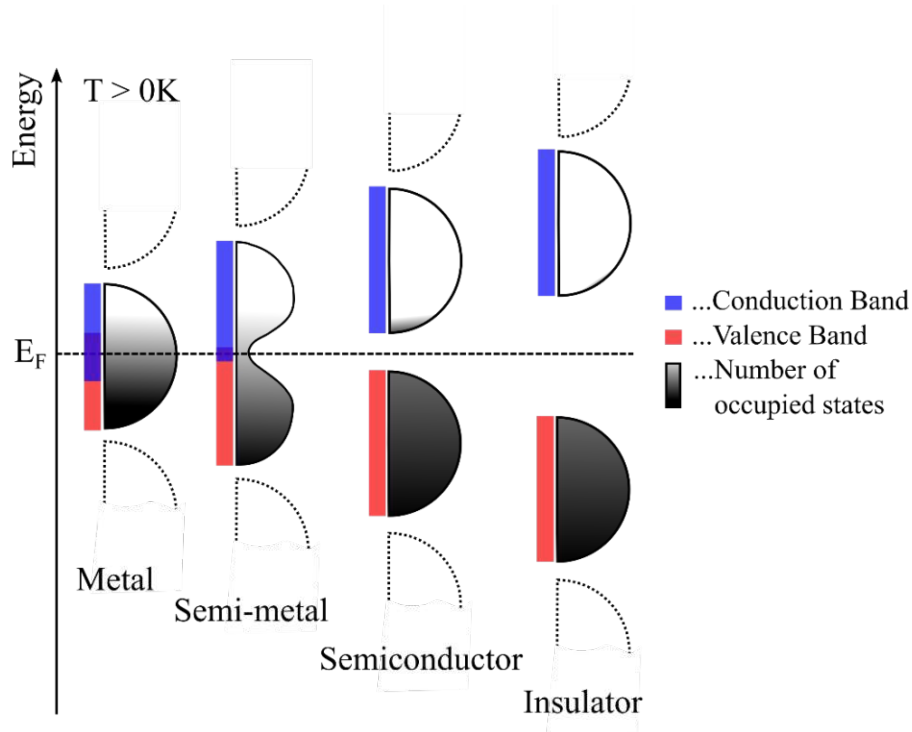

***Figure 2** Schematic band-diagram of different types of electrical conduction. The number of occupied states for different types of materials is depicted as a black-to-white shading, where black means all states are occupied and white means unoccupied states. The width of the band-diagram is respective to the density of states (DOS, i.e., the number of energy states per unit volume). The red and blue bars indicate the range of the valence as well as the conduction band, respectively. For metals and semi-metals, both bands can overlap. The dotted lines indicate other present energy bands that are in a first approximation unimportant.*

$$\hat{H}_{n,k}\psi_{n,k} = E_{n,k}\psi_{n,k} \qquad (1)$$

Where *H* is the Hamiltonian operator and *E* is the electron's energy. Even though there are *n* solutions, only two are most essential. These latter two solutions can be identified as either a solution where the electron is either bound loosely to the nucleus or where the electron acts as a free particle, which allows for electrical conduction. Lower energy states than the loosely bound ones, as seen by the dotted lines in *Figure 2*, correspond to core electrons, which can be regarded as electrically inactive. Energy states higher than the lowest free-electron energy band have too high energy to significantly contribute to electrical conduction.

Die approbierte gedruckte Originalversion dieser Dissertation ist an der TU Wien Bibliothek verfügbar.
The approved original version of this doctoral thesis is available in print at TU Wien Bibliothek.
TU WIEN Bibliothek Your knowledge hub

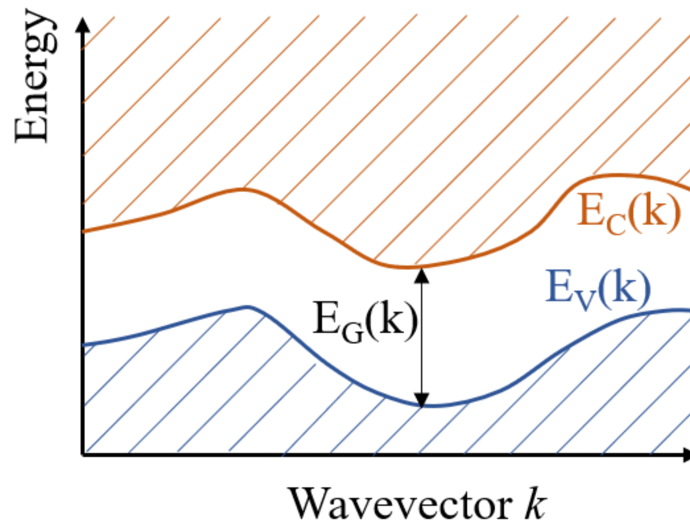

Figure 3 *Schematics of an electronic band structure for a semiconductor material. A typical dependency of the available electron energies concerning the electron's wavevector is shown. The conduction band E_C is shown in orange, and the valence band E_V in blue, respectively. The difference between E_C and E_V is the band gap energy E_G.*

As shown in *Figure 3*, the wavevector dependency of the energy leads to the formation of bands, whereas the most prominent ones are called the valence and conduction band, respectively. Loosely bound electrons have energies above the conduction band energy E_C, and electrons close to the nucleus have energies below the valence band energy E_V.

There are certain energy levels that electrons cannot have for insulators and semiconductors, as there is no solution for the corresponding Schrödinger equation. This range of forbidden energies is called the band gap and has the energy $E_G(k)$. If such a bandgap exists, non-conducting electrons in the valence band must gain E_G to get to the conduction band. This means that a certain amount of energy is needed to generate electrons for electrical conduction. For insulators, the value of E_G is even more significant, making conduction even less likely. The larger the bandgap is, the less conductive the material is, generally speaking. For example, insulating aluminum nitride has a bandgap of about 6 eV at room temperature, whereas semiconducting silicon has a bandgap of 1.14 eV.

Another important energy is the so-called Fermi-energy E_F. The Fermi energy is the upper energy limit where all possible energy states are occupied for a "resting" material, i.e., at 0 K with no external influences. This definition also implies that all electronic energy states are unoccupied above the Fermi energy (at T = 0K). When the temperature is added to the picture, the Fermi energy stays the same, but the distribution of occupied states changes. At 0 K, there

Die approbierte gedruckte Originalversion dieser Dissertation ist an der TU Wien Bibliothek verfügbar.
The approved original version of this doctoral thesis is available in print at TU Wien Bibliothek.
TU Bibliothek WIEN Your knowledge hub

is a sharp transition between fully occupied states to non-occupied ones. At temperatures above 0 K, a state is likely occupied above the Fermi energy, as depicted in *Figure 4*.

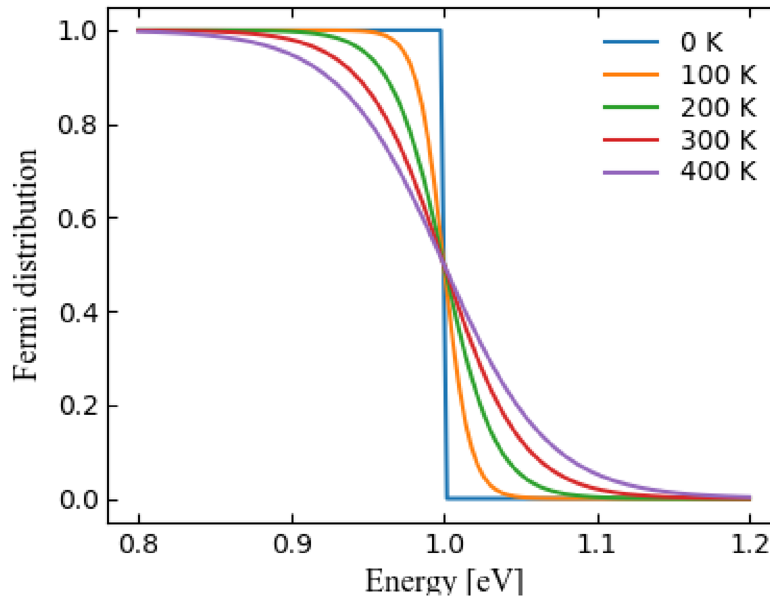

Figure 4 *Fermi-Dirac distribution calculated for a fictitious material with a chemical potential of 1 eV. The distribution at different temperatures is shown.*

The E_F can also lie in the band gap, which is the case for insulators and semiconductors. For metals, the conduction, and the valence band overlap, meaning E_F is above E_C. When the Fermi energy is closer to the conduction band, the conduction is more "electron-like"; when it is closer to the valence band, it is more "hole-like". Semimetals are similar to metals. However, only a limited number of electrons are permitted near the Fermi energy. In an undoped (also called intrinsic) semiconductor, the Fermi energy lies in the band gap and is located in the middle of the forbidden band with an energy value halfway between E_C and E_V. If the semiconductor materials are doped with other elements, the E_F can be brought closer to either the valence or the conduction band, depending on the dopant type. When the E_F is closer to the valence band, it is p-doped and has a dominating hole-like conduction, and when E_F is closer to the conduction band, it is called n-doped, and the conduction is predominantly electron-like.

Another effect that the Fermi energy helps to describe is when two materials with different Fermi energies come into contact. As depicted in *Figure 5*, their Fermi energies equalize when coming into contact, thus modifying locally at the interface of the band structures. In this band diagram, the horizontal axis is a spatial axis (labelled as x-coordinate), whereas in *Figure 3*, the

TU Bibliothek WIEN Your knowledge hub
Die approbierte gedruckte Originalversion dieser Dissertation ist an der TU Wien Bibliothek verfügbar.
The approved original version of this doctoral thesis is available in print at TU Wien Bibliothek.

horizontal axis is the electron wave vector *k*. As the barrier height $E_{Barrier}$ stays fixed, the bands must compensate at the interface, leading to band bending.

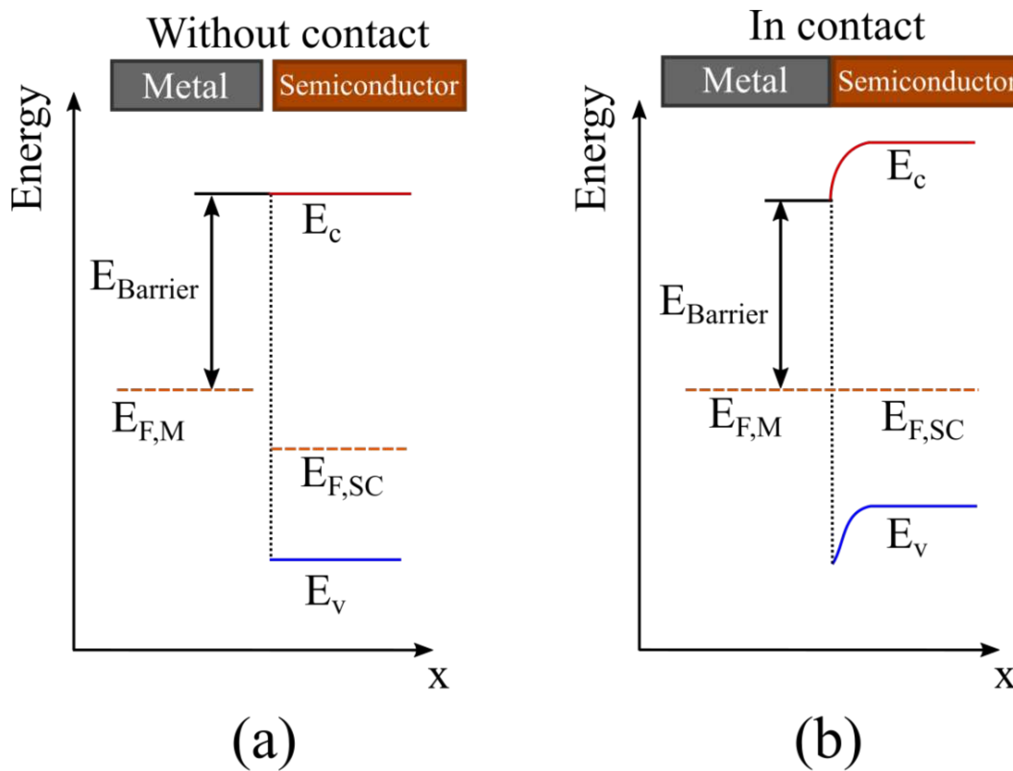

Figure 5 *The band diagram of a metal with Fermi energy (orange, dashed) $E_{F,M}$ and a semiconductor with Fermi energy $E_{F,SC}$ without contact (left) and when brought in contact (right). When the materials come into contact, $E_{F,M}$ and $E_{F,SC}$ equalize and $E_{F,SC} = E_{F,M}$. As a consequence, band bending occurs at the interface, while the barrier height $E_{Barrier}$ stays the same. In the example above, the case is shown where the $E_{F,SC}$ is smaller than $E_{F,M}$, which leads to an ohmic contact, as no rectifying barrier influences the conduction.*

In the shown example, the Fermi energy of the semiconductor is lower than that of the metal, leading to a downward bent edge. This leads to a so-called ohmic contact, where the interface has no depletion region and no rectifying behaviour. An upward bent is observed when the semiconductor's Fermi energy is higher than the metal ones. This can lead to a depletion region with a rectifying behaviour, and such an interface leads electrically to a so-called Schottky contact.

Die approbierte gedruckte Originalversion dieser Dissertation ist an der TU Wien Bibliothek verfügbar.
The approved original version of this doctoral thesis is available in print at TU Wien Bibliothek.
TU WIEN Bibliothek Your knowledge hub

Die approbierte gedruckte Originalversion dieser Dissertation ist an der TU Wien Bibliothek verfügbar.
The approved original version of this doctoral thesis is available in print at TU Wien Bibliothek.
TU Bibliothek WIEN Your knowledge hub

Polarization

Polarization is a property of dielectric materials and has two components: a component from intrinsic mechanisms and externally applied electric fields. One can imagine a positively charged nucleus and a surrounding electron cloud to understand the primary mechanism, as schematically shown in *Figure 6*.

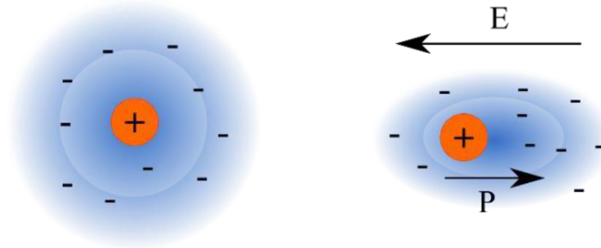

Figure 6 *A schematic of the basic principle of a dielectric polarization response to an electric field. On the left is the positive atomic nucleus surrounded by an electron cloud under no external field. On the right side, the effect of an electric field is shown. A polarization opposite to the applied electric field is induced by a spatial displacement of the electron cloud compared to the nucleus.*

When an electric field E is applied, the electrons are shifted relative to the position of the nucleus. This builds up a polarization P in the atom. This displacement of electrons happens in a first approximation instantaneously, so that alternating electric fields in the range of 10^{14}-10^{16} Hz can be followed. [55]

This polarization component is purely induced externally and is written as:

$$P = \varepsilon_0 \chi E \tag{2}$$

Where ε_0 is the electric permittivity in free space and χ is the electric susceptibility. The susceptibility is related to the permittivity ε_r as $\chi = \varepsilon_r - 1$.

The mechanism shown in *Figure 6* is not the only possible polarization mechanism. Different possibilities exist for a material to react to an external electric field. A compact overview is given on the following pages.

<u>Ionic</u>

Ionic crystals, like salt (NaCl), for example, consist of polar molecules. No matter how you pair up the Na+ and Cl- atoms, there will be an inherent polarization. Even though this molecule is polar, the solid in total is not (given there is no surface), as the molecules are placed such that they cancel out these individual dipole moments. Applying an electric field breaks this charge-

neutral atomic lattice so that the solid in total becomes polar. [56] Ionic polarization responds in the range of 10^{12}-10^{13} Hz. [55]

Dipolar

Dipolar polarization acts only on inherently polar molecules. For the polar molecule water, for example, the O-H-O structure, with a 104.5°angle between the two H-O bonds, has a dipole moment due to two free ion-electron pairs of the oxygen that disrupt the charge-related optimal angle of 109.5° which would make the molecule non-polar. This dipole moment will interact with any external electric field, and the molecules will rotate and stretch to compensate for the external field. This polarization mechanism is present in the ranges from 10^{2}-10^{12} Hz. Water, for example, has a response time of roughly $5 \cdot 10^{-11}$ s. [55]

Interfacial or space charge

This polarization mechanism occurs when a charge builds up at the surface of the dielectric due to an external electric field. This typically happens when the dielectric is connected to electrodes (which is discussed later on in section 2.2). Due to the dependency on the drift velocity of charges, this process has the largest response time range regarding the electric field and is in the order of 10^{-7}-10^{6} Hz. [55]

Ferro- and paraelectricity

The polarization response of most dielectric materials is linear with the electric field up to a material-dependent saturation of the *P-E* curve. In *Figure 7*, typical *P-E* curves are shown. Some materials, like PVDF or $BaTiO_3$, do not experience this linear relationship with the electric field, but show a pronounced hysteresis in the *P-E* characteristics. Such materials are called *ferroelectric*. In ferroelectric materials, comparable to ferromagnetic materials, there are certain domains in the crystal in which the dipoles are aligned in a particular direction.

The crystal consists of several domains, where each domain's polarisation is initially oriented randomly to the other domains. When an electric field is applied and steadily increased, all the dipole directions in the domains start to align with the external field. The *P-E* curve for this initial electrical stressing of the ferroelectrics is marked with 1 in *Figure 7*. The higher the field

Die approbierte gedruckte Originalversion dieser Dissertation ist an der TU Wien Bibliothek verfügbar.
The approved original version of this doctoral thesis is available in print at TU Wien Bibliothek.
TU Bibliothek WIEN Your knowledge hub

strength, the more effective the alignment to the electric field is. At a specific field strength, all domains are aligned, and the *P*-*E* response becomes linear. When decreasing the electric field, marked with 2, the domains still tend to stay in the previously aligned direction. This means there is still a net polarization even when no electric field is applied, which is called remnant polarization P_r. When the electric bias is reversed, the domains align in the opposite direction, leading to a negative polarization, marked with 3. The field strength needed to cancel the remnant polarization is called the coercive field strength E_{coe}.

On the other hand, paraelectric materials have unaligned domains when applying a small external electric field, resulting in a non-linear *P*-*E* relation without hysteresis.

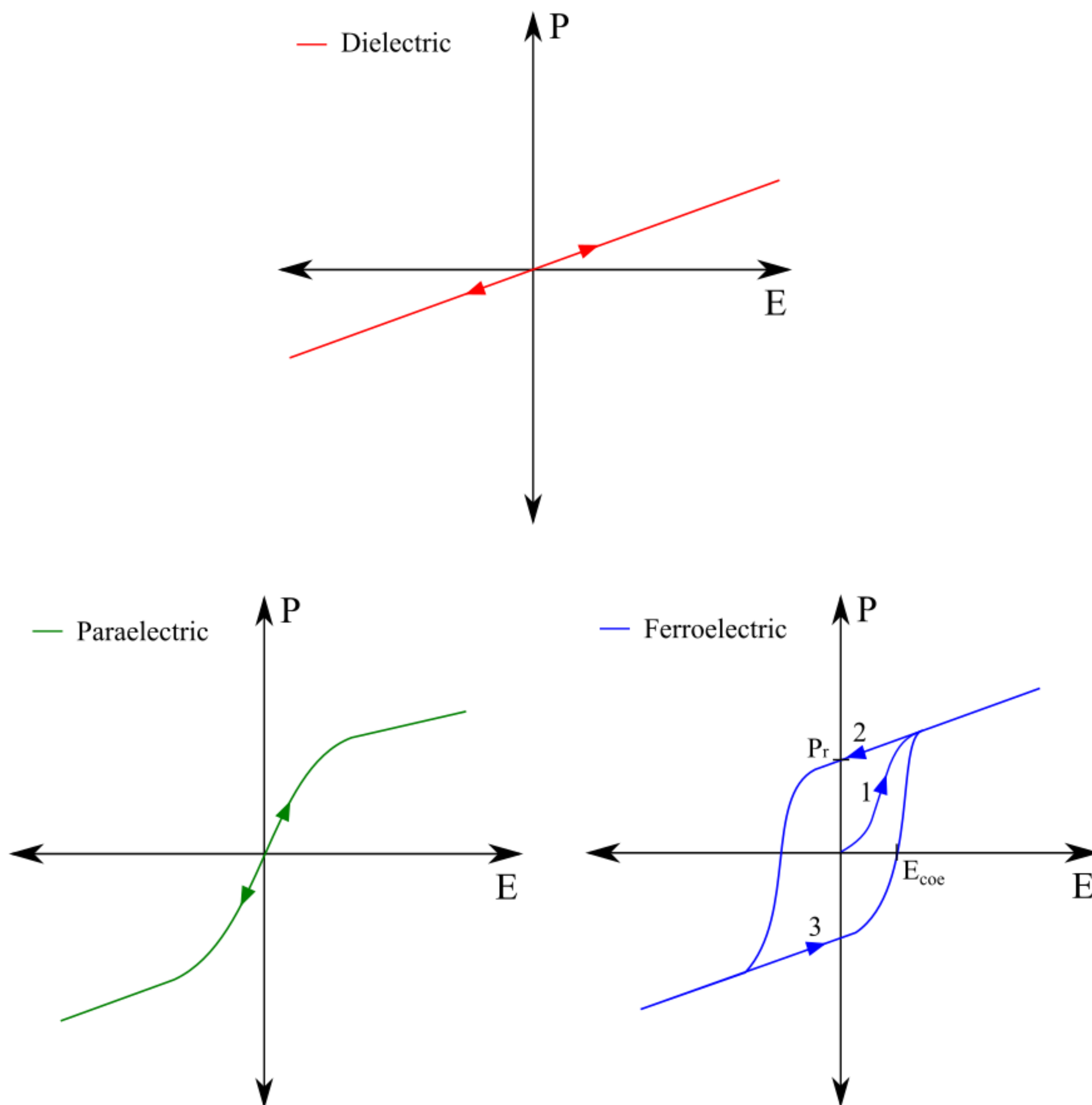

***Figure** 7 The difference in the polarization response of the three different classes, di-, para- and ferroelectrics. When applying an electric field, dielectric materials show linear behaviour. Paraelectric materials show non-linear behaviour, and ferroelectric materials show a hysteretic behaviour in addition to non-linear behaviour.*

Die approbierte gedruckte Originalversion dieser Dissertation ist an der TU Wien Bibliothek verfügbar.
The approved original version of this doctoral thesis is available in print at TU Wien Bibliothek.
TU WIEN Bibliothek Your knowledge hub

Die approbierte gedruckte Originalversion dieser Dissertation ist an der TU Wien Bibliothek verfügbar.
The approved original version of this doctoral thesis is available in print at TU Wien Bibliothek.
TU Bibliothek WIEN Your knowledge hub

The capacitor

A typical use of a dielectric is in a capacitor, where the dielectric has a significant impact on its electrical behaviour. The capacitor is also the primary building block in the cantilevered MEMS devices mainly used to characterise the flexoelectric effect as a transducer. A capacitor is a device to store electric charges by bringing two conductors with a potential difference close to each other while being electrically isolated from each other. The conductors can be isolated via vacuum or by a non-conducting dielectric. Capacitors come in many forms and shapes, but for this work, a plate capacitor type is described, as depicted schematically in *Figure 8*. For the following explanation, it is assumed that the permittivity of the dielectric is independent of the electric field.

When a voltage is applied to two electrodes with a vacuum in-between, a charge difference between the electrodes arises, resulting in an electrostatic force. This electrostatic force (which is directly related to the electric field by the elementary charge q) changes linearly with the applied voltage. Decreasing the distance between the capacitors while keeping the electrodes' charge Q_C constant increases the attractive force.

Considering no losses, one can then open the circuit, and this attraction will keep the charged particles on the corresponding electrodes, thus preserving the potential energy input.

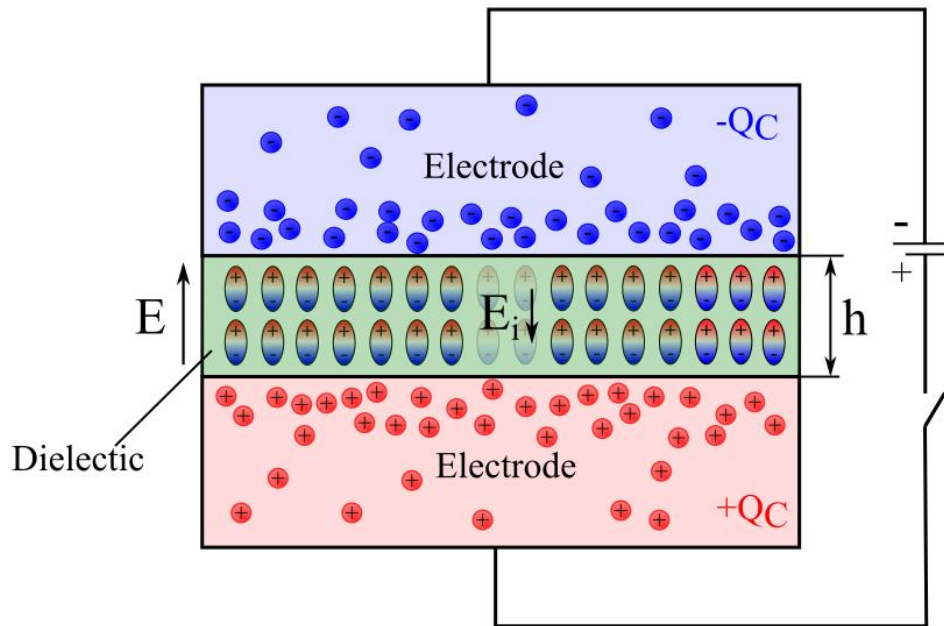

Figure 8 *A schematic planar plate capacitor illustration. Two electrodes (shaded in red and blue depending on the charge) are separated by a dielectric (shaded in green). When a voltage is applied, opposite charges Q_C build up on the two electrodes that attracts each other. The attractive force depends on the applied voltage V and the distance h between the electrodes. When a dielectric is present, a polarization is induced which introduces an internal electric field E_i in opposite direction to the external electric field E. The internal electric field dampens the total electric field between the electrodes. The dampening factor is called permittivity χ.*

The capacitance C is a quantity indicating the magnitude of stored charge per voltage applied in a plate capacitor and can be calculated as follows:

$$C = \varepsilon_0 \varepsilon_r \frac{A}{h} \tag{3}$$

Where A is the area of the capacitor and h is the thickness, ε_0 is the vacuum permittivity and ε_r the relative dielectric constant (which is 1 for vacuum). In an ideal capacitor, the capacitance is constant with the applied voltage, as an increase in voltage leads to an increased charge density according to:

$$C = \frac{Q_C}{V} = const. \tag{4}$$

If a dielectric is sandwiched between the two electrodes, the electric field E decreases by the permittivity of the dielectric. Unlike conductors, dielectrics restrict the movement of charges, leading to an incomplete compensation of the externally applied electric field. Dipoles within

Die approbierte gedruckte Originalversion dieser Dissertation ist an der TU Wien Bibliothek verfügbar.
The approved original version of this doctoral thesis is available in print at TU Wien Bibliothek.
TU WIEN Bibliothek Your knowledge hub

the dielectric are induced and align in the opposite direction to the applied electric field E. This results in a decrease of the total electric field strength between the electrodes by a factor of ε_r.

When the capacitor circuit is closed (i.e., the electrodes are connected via a conductor) and the voltage set to zero, the charges can compensate via the external electrical connection, returning to an uncharged state as a function of time. Real capacitors with an open circuit cannot keep their charge indefinitely, as small currents can flow across the insulator to equalize the potential drop. These currents are called leakage currents and can significantly influence the performance of capacitors. The next chapter will discuss how charges can flow through an insulator.

2.2 Leakage currents

Leakage currents are an essential topic in the semiconductor industry, as the performance of electronic devices is strongly dependent on keeping this quantity at the lowest level possible. In the past, silicon dioxide was the standard material for the realization of *e.g.* capacitors. It is straightforward to realize when exposing a silicon surface to an oxygen-containing atmosphere at elevated temperatures and offers very low leakage current density values in the range of 10^{-9} A/cm^2 at 1 V.[57] Lower leakage currents reduce charging losses during switching and heat build-up due to Joule heating. The most substantial disadvantage of SiO_2 as a capacitor material is the low permittivity of around 3. This lower permittivity also means a lower capacitance, as seen in *equation 3*.

For example, for metal-oxide semoconductor field effect transistor (MOSFET), SiO_2 is primarily used as a gate oxide. To fulfill the computational need of a high MOSFET density in a processor, the MOSFET sizes have to be reduced to a minimum. This includes the gate oxide thickness of such MOSFETs. However, as the thickness of the SiO_2 reached below 2 nanometres, the probability of electrons tunnelling through the insulating gate oxide layer increased above average, thus enhancing the leakage currents to 1 A/cm^2 at 1V, which is too high for practical use.[58] Additionally, a high capacitance is needed to scale the device geometries down in size, due to negative bias temperature instabilites and carrier mobility lowering.[59] The capacitance also has an impact on the on/off switching times.[60] To keep the high capacitance while avoiding excessive tunneling leakage currents, one promising solution is to change the insulating material to a candidate with a higher permittivity. With such

TU Bibliothek, WIEN Your knowledge hub
Die approbierte gedruckte Originalversion dieser Dissertation ist an der TU Wien Bibliothek verfügbar.
The approved original version of this doctoral thesis is available in print at TU Wien Bibliothek.

a material, the dielectric can have enough thickness to avoid excessive tunneling currents, while ensuring optimized device performance. Prime candidates for this application are HfO_2 and Al_2O_3 due to both their moderately high permittivity of 24 and 8 and their excellent insulating properties. [61]

To reduce the leakage current, it is crucial to understand why electrons can overcome the energy barrier represented by the insulator. The most conventional way to describe the processes responsible for the leakage current is with the help of a band diagram. As outlined in section 2.1, the band diagram shows the energy levels an electron can occupy within a particular material. There is a gap between the bound electrons representing the valence band and the free electrons in the conduction band for insulators. Assuming electrons are the dominant charge carriers, only electrons in the conduction band will contribute to the total leakage current.

The band diagram of a capacitor with an applied voltage across the opposing electrodes is shown in *Figure 9*.

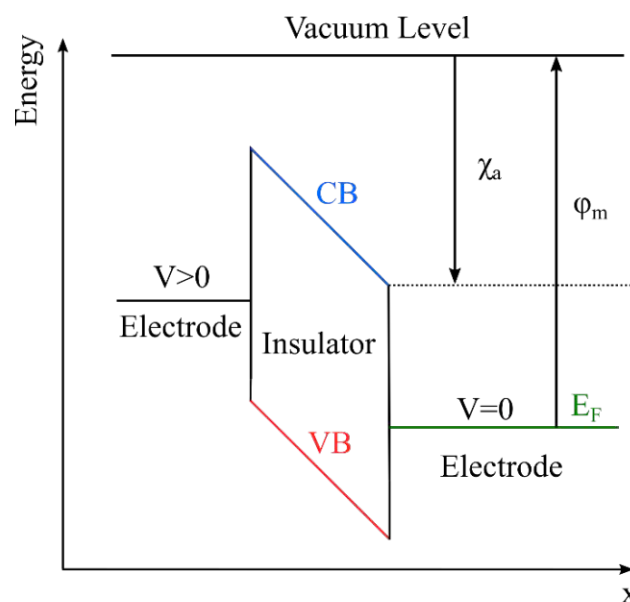

Figure 9 *Schematic energy band diagram of a capacitor structure with an applied external voltage. The effect of band bending when the electrodes come into contact with the insulator, as explained previously, is omitted for the sake of clarity. The conduction band is shown in blue, the valence band in red and the position of the Fermi energy is indicated in green. The electron affinity of the insulator χ_a and the electrode work function φ_m is also shown with respect to the vacuum level.*

Next, an overview of the used terms is given:

Work function φ_m: The energy needed to remove an electron from the material to the vacuum level.

Die approbierte gedruckte Originalversion dieser Dissertation ist an der TU Wien Bibliothek verfügbar.
The approved original version of this doctoral thesis is available in print at TU Wien Bibliothek.
TU WIEN Bibliothek Your knowledge hub

Electron affinity χ_a: Is the energy needed to insert an electron from the vacuum level into the conduction band of the insulator.

With this terminology, a so-called barrier height can be defined, which is, in this most straightforward picture, the difference between the electrode work function and the electron affinity of the insulator. In this idealized picture, this maximum barrier height must be overcome for electrons to get in the conduction band of the insulator. A potential difference also needs to be applied to ensure current flow, which is identified as a tilt of the conduction and valence band, as shown in *Figure 9*.

There are two possibilities for electrons to travel through the capacitor. One way is that there is enough potential energy in the system from an applied voltage to get electrons from the electrode's Fermi level into the insulator's conduction band. Temperature is also a key factor here, as thermal energy increases the electron energy. Another way is that the electrons tunnel through the barrier either into the conduction band or directly to the other electrode. It is often also necessary to consider both thermal activation and tunnelling.

Another physical quantity that significantly impacts the leakage current behaviour is point-like, structural defects that are electronically active and either located in the insulator or at the interfaces to the electrodes. These defects include missing atoms, interstitial atoms, lattice deformations, or unsaturated bonds in predominantly amorphous materials. Such defects can affect the conduction properties of a material by capturing injected electrons and re-emitting them after a particular response time. As the difference between the trap energy to the conduction band can be smaller than the barrier height, they increase the amount of conducting electrons.

Additionally, to the categorization into thermal and tunnelling mechanisms, a separation into interface and bulk mechanisms can be made. All the following mechanisms are schematically depicted in *Figure 10*. Generally, the effects are described with equations for the total current flow (see *equations 5*, *6*, *7*), which are derived from the balance of probability of an electron getting into the conduction band and leaving the CB at the other electrode.

Some assumptions are made for the leakage current models shown in the following. These are:

- Parameters in the models are constant and do not change with the electric field or in time.
- The electric field is uniform and undistorted across the dielectric.

Die approbierte gedruckte Originalversion dieser Dissertation ist an der TU Wien Bibliothek verfügbar.
The approved original version of this doctoral thesis is available in print at TU Wien Bibliothek.
TU WIEN Bibliothek Your knowledge hub

- Carriers are emitted isotropically from the trap states. This is not necessarily the case in all materials, especially when trap states have complex geometries or orientations.
- The density of trap states stays constant during the application of the electric field.
- Carrier-carrier interaction is absent

Common leakage current mechanisms and models

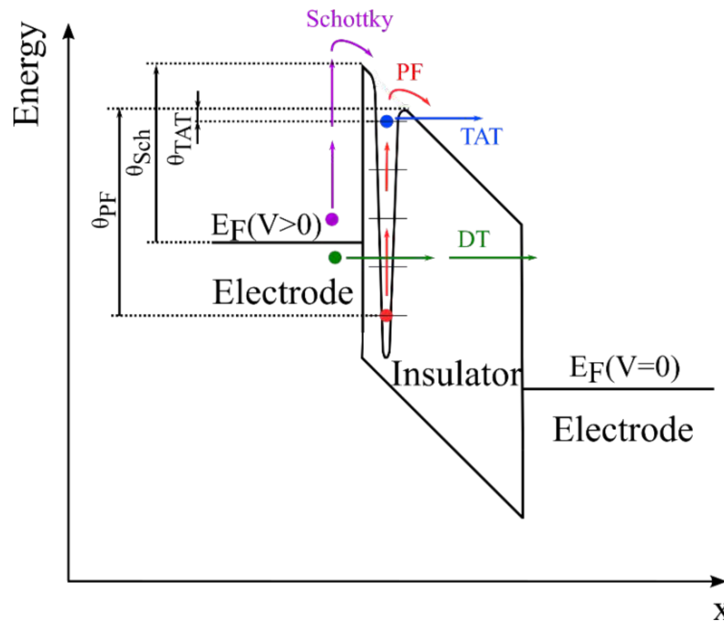

Figure 10 *Schematic energy band diagram of a capacitor with an applied voltage V>0 and ignoring band bending. Four typical leakage current mechanisms are shown. One exemplary interface mechanism is the thermionic Schottky effect (purple). Bulk effects include the direct tunnelling effect (DT, green), the thermionic Poole-Frenkel (PF, red), and the trap-assisted tunnelling effect (TAT, blue).*

Field-enhanced thermionic emission (Schottky effect)

Generally, thermionic emission describes the leakage current caused by the thermal excitation of electrons from the electrode into the conduction band of the insulator, as shown in purple in *Figure 10*. When the temperature is raised, electrons can gain higher energy than the work function. This means the electron can leave the electrode and get injected into the dielectrics' conduction band. The term *field-enhanced* describes the lowering of the potential barrier when an electric field is applied. The model often uses the Maxwell-Boltzmann distribution to describe the thermal distribution of carrier energies. This distribution characterizes the probabilities of carriers having various energies due to thermal excitation. The equation for the leakage current generated by the Schottky effect is the following:[62]

Die approbierte gedruckte Originalversion dieser Dissertation ist an der TU Wien Bibliothek verfügbar.
The approved original version of this doctoral thesis is available in print at TU Wien Bibliothek.
TU Bibliothek WIEN Your knowledge hub

$$J_{Sch} = C_{Sch} T^2 e^{-\frac{e\left(\Phi_{Sch} - \sqrt{\frac{q\,E}{\pi\,\varepsilon_0 \varepsilon_r}}\right)}{k_B T}} \tag{5}$$

Where E is the electric field, Φ_{Sch} the Schottky barrier, T the temperature, C_{Sch} a constant, k the Boltzmann constant, ε_0 the vacuum dielectric constant, ε_r the relative dielectric constant and q is the elementary charge.

When a metal comes into contact with a semiconductor (given the correct electronic properties, as discussed in section 2.1), the Fermi energies are equalized and a transfer of charge carriers occurs, resulting in a space charge in the semiconductor. The space charge is repuslive to the carriers and results in a potential barrier, called Schottky barrier. The currents across this barrier shows field-enhanced thermionic emission behaviour. Therefore, a link between the Schottky effect and the Schottky contact is given.[63]

Poole-Frenkel

The Poole-Frenkel effect describes the thermionic ionization of captured electrons in traps. The leakage current is derived from the rate of the probability of electrons being trapped and electrons being emitted from those traps. Bending the conduction band through an external voltage and having higher temperatures can stimulate electron capture and emission from traps, by lowering the effective barrier the electron is facing and thus increasing the leakage current level. Those traps are usually attributed to localized states which can capture and emit injected electrons. The standard formula for the Poole-Frenkel current is the following: [64]

$$J_{PF} = C_{PF} E e^{-\frac{q\left(\Phi_{PF} - \sqrt{\frac{q\,E}{\pi\,\varepsilon_0 \varepsilon_r}}\right)}{k_B T}} \tag{6}$$

Where C_{PF} is a constant and Φ_{PF} the Poole-Frenkel barrier height, respectively.

The Poole-Frenkel model is based on several assumptions that simplify the complex physical processes involved. Here are the additional key assumptions typically made in the Poole-Frenkel model:[65]

- No quantum mechanical effects, such as tunneling, are considered. Carriers are assumed as classical particles with definite energy levels and trajectories.

Die approbierte gedruckte Originalversion dieser Dissertation ist an der TU Wien Bibliothek verfügbar.
The approved original version of this doctoral thesis is available in print at TU Wien Bibliothek.
TU Bibliothek WIEN Your knowledge hub

- Only a single trap energy level is considered, neglecting the presence of multiple trap levels with varying energies.

Direct tunnelling

As shown in green in *Figure 10*, direct tunnelling represents the process when charge carriers move directly from one electrode through the whole barrier to the other electrode. It is known from quantum physics that a particle has a probability to transverse a barrier, even if it should not be possible from classical theory. Even though the electron's wavefunction vanishes for a potential with infinite height, when the potential has a finite value, the wavefunction only decays exponentially, leaving a non-zero probability of existing on the other side of the barrier. In theory, the particle does not lose any energy when travelling through the barrier. Applying an electric field across the dielectric results in a thinner barrier, enhancing the tunnelling probability. This phenomenon is modeled in the Fowler-Nordheim equation.
When the dielectric has trap states, the electrons can tunnel in and out of such, which is described in the trap assisted tunnelling.

Trap assisted tunnelling

In the trap-assisted tunnelling (TAT) model, electrons can tunnel between traps and therefore, "circumvent" the barrier between individual traps, as in the case of the Pool-Frenkel. Like all the other tunnelling mechanisms, TAT is, from the purely theoretical point of view, only dependent on the applied electric field and not on temperature. There are different equations for TAT, depending on the amount and type of traps an electron passes while travelling to the other side of the insulator. In this thesis, the inter-trap tunnelling equation was used, which assumes Fowler-Nordheim trap emission [66]:

$$J_{TAT} = C_{TAT} e^{-\frac{8\pi\sqrt{2qm_s}}{3h}\frac{\Phi_{TAT}^{\frac{3}{2}}}{E}} \tag{7}$$

Die approbierte gedruckte Originalversion dieser Dissertation ist an der TU Wien Bibliothek verfügbar.
The approved original version of this doctoral thesis is available in print at TU Wien Bibliothek.
TU Bibliothek WIEN Your knowledge hub

Where C_{TAT} is a constant, Φ_{TAT} is the trap-assisted tunnelling barrier, m_s is the effective electron mass, and h the Planck's constant.

In literature, the TAT in oxide-based capacitors is often associated with forming oxygen vacancies. [67,68]

This model makes certain assumptions to simplify the complex quantum mechanical processes involved. Here are the additional key assumptions typically made in the trap-assisted tunneling model:

- The model is semiclassical. Quantum mechanical effects, such as wave-particle duality and complex interference phenomena are ommited.
- The tunneling process is elastic, meaning that the energy of the carrier before and after tunneling remains the same. This might not accurately capture inelastic tunneling processes that involve energy exchanges.

Trap-dependent space-charge limited conduction

Space-charge-limited conduction (SCLC) was first described for vacuum diodes and is very simple in its formalism.[69] It is derived from the time it takes for charge carriers to travel through the dielectric. For a plane capacitor, the amount of charge that can be stored is:

$$Q_C = CV \tag{8}$$

Where Q_C is the charge, C is the capacitance, and V is the applied voltage. Given no time dependency on the movement of the electric charges, the current J_{SCLC} can then be written as:

$$J_{SCLC} = \frac{Q_C}{t} \tag{9}$$

Where J is the current and t the time it takes for the electrons to travel from one side of the capacitor to the other. With the known distance between the electrodes, h, and the drift-velocity of the electrons, which is the product of the electric field and the electron mobility μ_{mob}, the time it takes to cross the dielectric can be written as:

Die approbierte gedruckte Originalversion dieser Dissertation ist an der TU Wien Bibliothek verfügbar.
The approved original version of this doctoral thesis is available in print at TU Wien Bibliothek.
TU Bibliothek WIEN Your knowledge hub

$$t = \frac{h}{E\ \mu_{mob}} = \frac{h^2}{V\ \mu_{mob}} \tag{10}$$

Which, with the formula for the capacitance of a plate capacitor (*equation 2*), results in a quadratic dependency as a function of the applied voltage:

$$J_{SCLC} \propto \frac{\mu_{mob}\ \varepsilon}{h^3} V^2 \tag{11}$$

The SCLC is expected in capacitors with a low barrier ohmic metal/insulator interface. If the latter condition is fulfilled, a large number of carriers can be injected, which travel through the insulator, similar to the case for a vacuum diode.

The square law for the leakage current holds true if following additional assumptions are true:

- Only one type of charge carrier
- Diffusion currents can be neglected, only drift currents are considered
- No traps are present

The situation changes in real dielectrics, where electronic active traps are present in the material and other conduction types are contributing to the total leakage current. In this work, the trap-assisted SCLC is modelled as follows: at low voltages[3], the travel time for electrons through the dielectric is longer than the dielectric relaxation time. Injected charge carriers can therefore distribute evenly across the dielectric so that charge neutrality is maintained and no space charge regions exist.[70] This means that the SCLC behaviour does not determine the current observed, and the thermal activation of charge carriers is the primary driving mechanism for conduction. Also, the traps are not active at these low voltage ranges. When this is the case, the conduction behaviour is ohmic ($J \propto V$). At intermediate voltages, the traps are activated. These active traps contribute to the electrical conduction, most likely due to trap assisted tunnelling and hopping mechanisms.[71] Carrier mobility and lifetime are also affected by traps due to scattering and recombination effects. The traps are activated mainly across low-resistance filament-like structures throughout the dielectric. Also, new traps can be generated, which increases the current further. In this regime, the current increases exponentially with increasing voltage ($J \propto V^{exp}$, where *exp* is material dependent).[72] Finally, at higher voltages, all possible

[3] The exact voltage levels depend on the dielectric material and can be determined from current-voltage measurements. In section 4.3, the voltage levels for $IrO_x/TiO_x/IrO_x$ capacitors are shown.

Die approbierte gedruckte Originalversion dieser Dissertation ist an der TU Wien Bibliothek verfügbar.
The approved original version of this doctoral thesis is available in print at TU Wien Bibliothek.
TU Bibliothek Your knowledge hub WIEN

traps are active and an excessive amount of charges are flowing. [73] Here the current has the above shown pure SCLC behaviour, as rate of carrier injection is so high, that a space charge at the cathode exists, limiting the current.

Capacitive and memristive effects

When oxygen is separated from the lattice through an external electric field or other influences, such as being exposed to a vacuum while being heated, it leaves behind a structural defect (“hole”) called oxygen vacancy.[39] This can be notated in the Kröger-Vink notation as[74]:

$$O_{\ddot{O}} \rightarrow V_{\ddot{O}} + 2e^{-} + \frac{1}{2}\,O_2 \qquad (12)$$

where $O_{\ddot{O}}$ is the lattice oxygen and $V_{\ddot{O}}$ is a positively charged oxygen vacancy. Depending on the oxide, these vacancies can act as either n- or p-doping. In the case of TiO_2, an oxygen vacancy acts as an n-dopant.[44,75] This is because the oxidation state of titanium is 4+ and that of oxygen is 2- and in this case, the TiO_2 is fully oxidized with no net charges in the molecule. When an oxygen atom is missing, there is a net oxidation state of 2+ in the TiO_2 molecule. This charged state of the TiO contributes to electric conduction.

Additionally, the oxygen and the oxygen vacancy can then drift and diffuse through the capacitor. The generation and movement of oxygen vacancies lead to complex leakage current characteristics known as capacitive and memristive effects. [48,75,76]

Capacitive effects can stem from multiple effects.[77] One is the local separation of positive and negative ions under an applied electric field. Another is from a oxygen vacancy redistribution under an electric field.[78,79] The different effects lead to different capacitive behaviour, such as pure capacitive, the double-layer, pseudocapacitive or faradaic capacitance.[80] These capacitive effects impact the total leakage current, as the separation of charge carriers under an external electric field generates an internal electric field. Depending on the relaxation time of the separated charges, this can lead to effects where a leakage current is present for some time after turning the applied electric field off. This behaviour is seen in a hysteresis in the current-voltage curves, as will be demonstrated in section 4.3.

The other type of effect the oxygen vacancies cause is the memristive effect. There are two principal identifiers for memristive effects. These are a continuous, and a sudden change from an LRS to an HRS (or *vice versa*). The continuous change is generally attributed to interface effects. These could be a change in Schottky-barrier height, changes in the resistance of the

Die approbierte gedruckte Originalversion dieser Dissertation ist an der TU Wien Bibliothek verfügbar.
The approved original version of this doctoral thesis is available in print at TU Wien Bibliothek.
TU WIEN Bibliothek Your knowledge hub

interface due to the generation of oxygen vacancies or an oxygen exchange between the insulator and the electrode.[38,48]

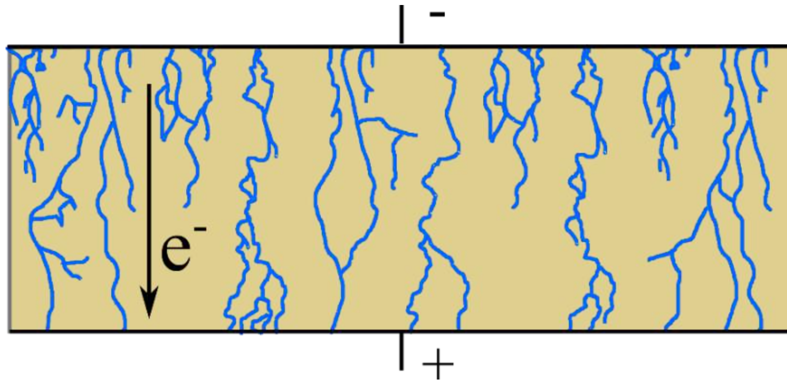

Figure 11 *Schematics of the percolation paths electrons form when travelling through a dielectric via vacancies or oxygen ions.*

The sudden change in resistance originates from conductive pathways, as illustrated schematically in *Figure 11* that are generated by either ionized oxygen atoms, oxygen vacancies, dielectric metal ions or electrode metal ions under an applied electric field.[40] Some research also suggests the formation of sub-stoichiometric conductive phases, *e.g.*, the Magneli phases Ti_nO_{2n-1} for titanium dioxide.[81] These are also often called resistive switching effects, as they are used in devices where a sudden change in resistance from a low-resistance to a high-resistance state (LRS and HRS, respectively) is desired.

Die approbierte gedruckte Originalversion dieser Dissertation ist an der TU Wien Bibliothek verfügbar.
The approved original version of this doctoral thesis is available in print at TU Wien Bibliothek.
TU Bibliothek WIEN Your knowledge hub

2.3 Electro-mechanical transduction mechanisms

Transduction describes the conversion of one form of energy to another. For this thesis, electromechanical transduction is the most important type of conversion. With this type of transduction, electrical quantities are converted to mechanical quantities and *vice versa*. There are a variety of effects that couple electrical and mechanical quantities. The type of electromechanical transduction investigated in this thesis is the generation of electrical dipoles and hence, polarization charges under a mechanical field gradient applied externally or the generation of mechanical stress by applying an external electrical field gradient to dielectric materials.

Piezoelectricity, for example, is caused by dipoles generated under uniform mechanical load due to how the atoms are ordered in the piezoelectric materials. When looking at thin films, it is also not enough to only consider effects linked explicitly to the bulk of the material. In addition, the surface can significantly impact the electromechanical response. Next, the different sub-groups of this transduction mechanism will be presented and discussed.

Bulk flexoelectricity

When the flexoelectric effect was first introduced, it was done due to the need to explain the charges generated when bending a centrosymmetric $BaTiO_3$ α-phase crystal.[16] This phase of $BaTiO_3$ should have no piezoelectric response due to its centrosymmetry. Due to the polarization scaling with the strain gradient, the latter study's authors classified this phenomenon as a non-local piezoelectric effect. Nonlocality in this context means that in addition to the electric fields and phonons from nearest neighbour atoms of a given atom, the electric fields and phonons from atoms throughout the crystal are necessary to describe this effect. This picture becomes more evident when analysing what is happening to a crystal when applying a strain gradient.

Die approbierte gedruckte Originalversion dieser Dissertation ist an der TU Wien Bibliothek verfügbar.
The approved original version of this doctoral thesis is available in print at TU Wien Bibliothek.
TU Bibliothek WIEN Your knowledge hub

Die approbierte gedruckte Originalversion dieser Dissertation ist an der TU Wien Bibliothek verfügbar.
The approved original version of this doctoral thesis is available in print at TU Wien Bibliothek.
TU WIEN Bibliothek Your knowledge hub

Internal strains

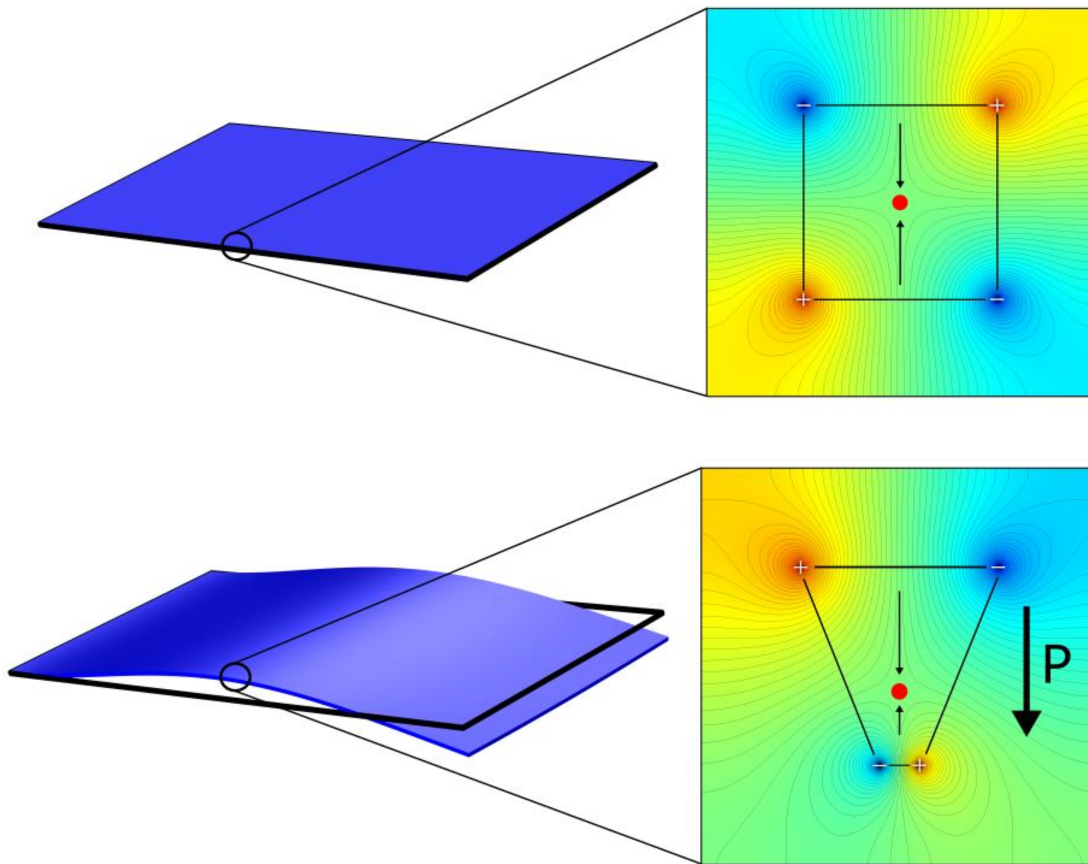

Figure 12 *A schematic drawing illustrating the direct flexoelectric effect. A plate with and without a deformation is depicted on the left-hand side. On the right-hand side, the electric field of an exemplary unit cell of such a plate is shown, where the grey lines indicate contour lines of the electric field strength. On the top is an unbent plate made of a centrosymmetric crystal. The forces acting on the central atom (red dot) are balanced and cancel each other out. When bent, as shown in the lower part, the resulting strain gradient deforms the unit cell as depicted, and the forces are not balanced anymore, and the resulting internal strain causes a net polarization in the cell.*

When analysing the physics of mechanical deformation on the atomic level, a derivation by Born can be followed.[82] First, an important distinction has to be made. Namely, there is a different result when a continuous medium is strained in contrast when the medium consists of discrete atoms that are displaced. In a discrete arrangement of atoms, there is a complex interactivity between the individual forces, resulting in a different deformation than from the model with a continuous uncharged medium. This difference in strain from the discrete to the continuous model is called internal strain. In *Figure 12,* the internal deformation of a unit cell in a bent plate is shown. In a lattice where every atom is a symmetry centre, the internal strain is zero; by definition, all the forces have an equal opposing force. On the other hand, a strain gradient causes even such symmetric crystals to have an internal strain. This internal strain is

essential when describing the flexoelectric effect, as seen in the following derivation. The internal strain is microscopic with length scales in the sub-Å range and does not affect the dimensions of the strained volume.

Now that there is a basic understanding of the flexoelectric effect, one can turn to the current models to describe this effect. The original formulation for the relationship of the polarization *P* to the total strain for a flexo- and piezoelectric medium, which Kogan gave, was the following:[83]

$$P_i = \chi_{ij} E_j + d_{ijk} u_{jk} + \mu_{klij} \frac{\partial u_{kl}}{\partial x_j} \tag{13}$$

Here *ijk* are indices for cartesian coordinates. The first term, where the susceptibility χ is multiplied by the electric field *E,* describes the amplification of the electric field in a material through polarization. The second term describes the piezoelectric effect with a linear relationship between *P* and the strain *u* by the piezoelectric constant *d*. The last term describes the flexoelectric effect with the characteristic strain gradient behaviour. Here, μ is the flexoelectric coefficient, and *x* is the position. For the converse effect, the same behaviour can be observed:

$$\sigma_i = c_{ijkl} u_{kl} + d_{ijk} E_j + \mu_{klij} \frac{\partial E_k}{\partial x_j} \tag{14}$$

Here the total stress σ consists of a term with Hook's law where *c* is the stiffness tensor, a piezoelectric $d{\cdot}E$ term and the flexoelectric term at the end.

A description based on the thermodynamic potential ϕ_G of a piezoelectric and flexoelectric system gives a more descriptive picture. The thermodynamic potential includes polarization and strain terms and their derivatives. The detailed derivation of the energy function is given in [84] so that the following term results.

Die approbierte gedruckte Originalversion dieser Dissertation ist an der TU Wien Bibliothek verfügbar.
The approved original version of this doctoral thesis is available in print at TU Wien Bibliothek.
TU WIEN Bibliothek Your knowledge hub

$$\phi_i = \frac{\chi_{ij}^{-1}}{2} P_i P_j + \frac{c_{ijkl}}{2} u_{ij} u_{kl} - \frac{g_{ijkl}}{2} \frac{\partial P_i}{\partial x_j} \frac{\partial P_j}{\partial x_l} - d_{ijk} P_i u_{jk} - \Gamma_{klij} \left(P_k \frac{\partial u_{ij}}{\partial x_l} - u \frac{\partial P_k}{\partial x_l} \right) - P_i E_i - u_{ij} \sigma_{ij} \quad (15)$$

The constant Γ is called the flexocoupling constant, that couples the polarization with the strain gradient. Minimizing the potential energy by applying the Lagrange-Equations $\partial\phi_G/\partial A - \frac{d}{dx}(\partial\phi_G/\partial(\partial A/\partial x)) = 0$, where the substitute A can be P or u, yields the constitutive equations. Here, the direct and converse representatives for a purely flexoelectric case are shown:

$$E_i = \chi_{ij}^{-1} P_j - \Gamma_{klij} \frac{\partial u_{kl}}{\partial x_j} - g_{ijkl} \frac{\partial^2 P_i}{\partial x_j \partial x_l} \quad (16)$$

$$\sigma_{ij} = c_{ijkl} u_{kl} + \Gamma_{ijkl} \frac{\partial P_k}{\partial x_l} \quad (17)$$

When comparing these *equations 16* and *17* with the definitions set in *equations 13* and *14*, a scaling of the flexoelectric coefficient becomes apparent:

$$\mu_{klij} = \chi_{is} \Gamma_{klsj} \quad (18)$$

This is a significant result, as this means that the flexoelectric effect scales with the permittivity of the material. This result made the flexoelectric effect much more interesting for technical applications when applying high-permittivity materials. Another feature of interest is that strain gradients scale with the inverse of the thickness cubed (h^{-3}), and thus for smaller geometrical dimensions, the effect generates a significantly larger amount of polarization charges. Consequently, this makes nanomechanical devices preferred candidates to exploit the flexoelectric effect.

Kogan first estimated the magnitude of the flexoelectric coupling constant [83]. They arrived at this estimation by considering a lattice of point charges with charge q and lattice spacing a, respectively. When a strain gradient is then applied to this lattice, the energy density changes in a first approximation in the order of $\frac{q}{4\,\pi\,\varepsilon_0\,a}\frac{1}{a^3}$. This change can then be compared to the

Die approbierte gedruckte Originalversion dieser Dissertation ist an der TU Wien Bibliothek verfügbar.
The approved original version of this doctoral thesis is available in print at TU Wien Bibliothek.
TU Bibliothek WIEN Your knowledge hub

flexoelectric term in the energy density function (*equation 15*) and the estimation for the flexocoupling constant is achieved:

$$\Gamma \sim \frac{q}{4\,\pi\,\varepsilon_0\,a} \tag{19}$$

This estimate results in a flexocoupling voltage range of 1…10 V and works well for materials with a permittivity of moderate value. However, this estimate does not hold for some extremely high permittivity materials like the second order phase transition ferroelectrics like PZT. [18,85] This could either be because there is some hidden flexoelectric mechanism at such an incredibly high permittivity, or there are residual piezoelectric phases or nano-sized polar regions, which was shown to have a substantial impact on the flexoelectric coefficient of the material.[17]

It should also be mentioned that the direct and converse flexoelectric coefficients should have the same value; otherwise, basic thermodynamic principles would be hurt. Assuming that the coefficients have a different value, it would be possible to build a Perpetuum mobile. For example, when $\mu_{direct} > \mu_{converse}$, the harvested energy would be larger than the amount of energy needed to drive the machine, and thus the feedback loop creates endless ever-increasing motion.

Bulk piezoelectric effect

In the previous chapter, it was shown that the internal strain in a crystal causes the flexoelectric effect. This is also the case for the piezoelectric effect, but with the difference that the internal strain, when applying a constant strain throughout the material, arises from the asymmetry of the crystal's unit cell, as schematically illustrated in *Figure 13*.

Die approbierte gedruckte Originalversion dieser Dissertation ist an der TU Wien Bibliothek verfügbar.
The approved original version of this doctoral thesis is available in print at TU Wien Bibliothek.
TU WIEN Bibliothek Your knowledge hub

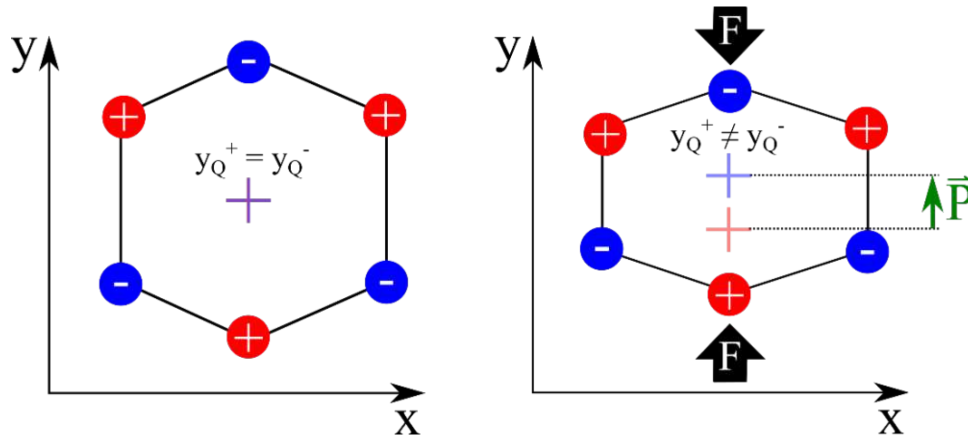

Figure 13 *A schematic unit cell of a piezoelectric material. On the left, no external force is applied to the unit cell, and the y-position of the centre of positive charges* y_Q^+ *equals the one of negative charge* y_Q^-*. On the right side is the same unit cell with an external force applied. The applied force changes the positions of the charges, and the charge centres don't align anymore, leading to a net polarization in the unit cell.*

The piezoelectric effect is substantially more pronounced than the flexoelectric effect due to the significantly higher coefficient, which is generally about three magnitudes higher when comparing μ and d.[17] However, going to lower dimensions, the flexoelectric response increases while the piezoelectric coefficient stays constant, meaning that at some point, the flexoelectric contribution dominates the piezoelectric one. The exact point where the flexoelectric effect dominates piezoelectricity depends on the materials, which are compared, but a general rule of thumb predicts a value below one µm. [86]

As was shown earlier, the piezoelectric effect is characterized by a linear relation of P and u:

$$P_i = \chi_{ij} E_j + d_{ijk} u_{jk} \tag{20}$$

As can be seen, the piezoelectric effect is independent of the permittivity. Reducing the thickness of a piezoelectric plate capacitor reduces the amount of strain/polarization gained when the electric field is kept constant. This is because the total strain within the material is equal to the sum of the individual unit cells. There are fewer unit cells when the material is thinner, and the corresponding sum of the individual strain contributions is smaller than in thicker materials. This makes the piezoelectric effect less pronounced, especially in NEMS. Practically, this dimensional effect is less severe, as unit-wise, a voltage (V) is applied (and not an electric field kV/cm), and the resulting electric field has an inverse proportional thickness scaling.

Die approbierte gedruckte Originalversion dieser Dissertation ist an der TU Wien Bibliothek verfügbar.
The approved original version of this doctoral thesis is available in print at TU Wien Bibliothek.
TU Bibliothek WIEN Your knowledge hub

Die approbierte gedruckte Originalversion dieser Dissertation ist an der TU Wien Bibliothek verfügbar.
The approved original version of this doctoral thesis is available in print at TU Wien Bibliothek.
TU Bibliothek WIEN Your knowledge hub

Dynamic flexoelectric effect

In contrast to the piezoelectric effect, the flexoelectric effect also involves a time-dependent contribution to the polarization of the material. This effect is called the dynamic flexoelectric effect. When looking at an acoustic wave passing through the bulk of a material (for example, TiO_2), the force that the acoustic wave exhibits on the heavier ions (Ti^{2+}) is different to that on the lighter ions (O^-). This difference in forces leads to a desynchronization of the heavy ions to the lighter ones and, in turn, causes a polarization wave in the material.

It has been shown that the dynamic flexoelectric constant follows this relation:[6]

$$\mu_{klij}^{d} = -\frac{1}{\rho}\chi_{in}M_{ns}c_{sjkl} \tag{21}$$

Where M denotes the so-called Born effective charge tensor, a characteristic for the response of a set of charges to perturbations, and ρ the density. For acoustic waves, the magnitude of the dynamic coefficient is in order of the bulk flexoelectric coefficient. If the wavelength of the acoustic wave is substantially larger than the thickness of the sample in which the wave is travelling, then this excitation is negligible with respect to the dynamic flexoelectric effect, and the dynamic contribution tends to zero. For micro- and nanoscaled devices, excitation frequencies must be 10^{10}-10^{12} Hz to have a measurable impact.

Surface piezoelectric effect

When considering samples with finite sizes, surface effects will be introduced. Typically, in macroscopic devices, these surface effects can be ignored as the volume of the bulk is much higher than the area of the surface. However, reducing the dimensions of the sample increases the surface/volume ratio, and the surface effects gain increasing importance and can even dominate bulk effects.[87] When looking at the unit cell of a crystal at the surface, a so-called relaxation of the outermost atomic layers will happen. This reconstruction, a rearranging of the atoms in the uppermost surface layer, happens because the missing neighbours at the interface change the attraction potentials in the unit cell. These reconstructed surface layers can have polarization due to a disturbed balance of electrostatic forces. In *Figure 14,* the surface

reconstruction of rutile TiO_2 is schematically shown. It is seen that the electronic structure of the interface layer is strongly perturbed.

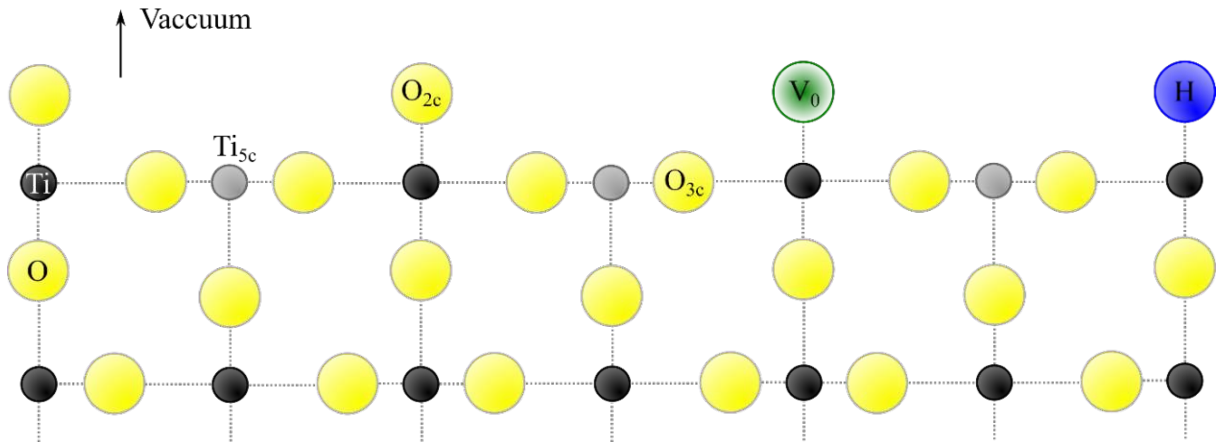

Figure 14 *(1x1) surface reconstruction of a (110) oriented TiO_2 surface. The atomic layer facing the vacuum differs from the bulk. The atoms denoted as Ti_{5c}, O_{2c} and O_{3c} are missing their neighbours, thus changing their electronic structure. Even more, oxygen vacancies (green) and adsorbed hydrogen (blue) also change the electronic surface properties.*

Like in the piezoelectric effect, this polarization can deform the surface layer by applying an electric field and *vice versa*.

A thermodynamic potential is introduced to model the surface piezoelectric effect and to derive the constitutive equations.[88] The sample is modelled as a three-layered slab, where in the middle is the bulk of the dielectric material and the top and bottom layers are piezoelectric layers with h_λ thickness. Here, h_λ represents the size of a unit cell. The derivation originates from the following relationship for the converse effect in a bending case:

$$G = \frac{2h}{D} e \frac{\varepsilon_r}{\varepsilon_\lambda} h_\lambda E = \frac{2h}{D} \tilde{e} h_\lambda E \tag{22}$$

Where G is the curvature of the bent plate, h is the thickness, D is the flexural rigidity, e is the surface piezoelectric constant, E is the applied electric field to the stack and ε_r as well as ε_λ are the bulk and surface dielectric constants, respectively.

This result has several surprising consequences:

- The contribution is independent of the surface-to-volume ratio.

Die approbierte gedruckte Originalversion dieser Dissertation ist an der TU Wien Bibliothek verfügbar.
The approved original version of this doctoral thesis is available in print at TU Wien Bibliothek.
TU WIEN Bibliothek Your knowledge hub

- The contribution scales linearly with the bulk permittivity.

- The surface piezoelectric coefficient is in the same order of magnitude as the flexoelectric coefficient.

These results make it very difficult to discern the surface piezoelectric effect from the flexoelectric effect, as the latter quantity also scales with the bulk permittivity, and the coefficient has the same order of magnitude. Additionally, the surface piezoelectric effect for a bent slab has a very similar linear curvature as a function of the applied electric field as the flexoelectric response of a bent slab, which is also described in this section.

Surface flexoelectric effect

The surface flexoelectric effect is the electric response of the surface to an external mechanical strain. [89] To get an overview, a schematic of a simple surface, depicted as a layer of atoms as seen from the top, is shown in *Figure 15*. When calculating the magnitude of this effect, one comes to a fundamental problem, namely which unit cell to define. As seen in the figure, there are two possible unit cells. When calculating the dipole moment of these cells, the result is that both have a polarization opposite to one another. This means that the result depends on which unit cell is chosen, which should not be the case.

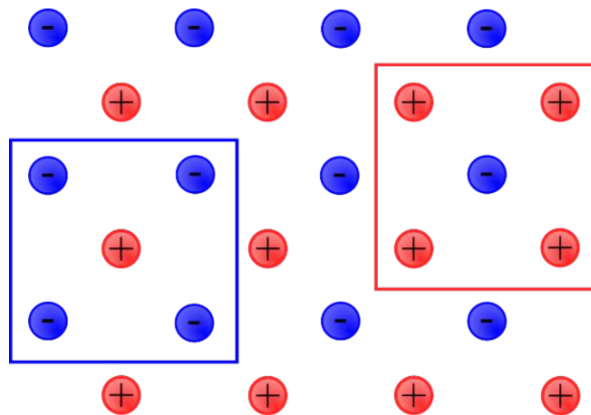

Figure 15 *A simple lattice made of positively (+) and negatively (-) charged particles. This surface can define two types of unit cells marked with the blue and red rectangle.*

Die approbierte gedruckte Originalversion dieser Dissertation ist an der TU Wien Bibliothek verfügbar.
The approved original version of this doctoral thesis is available in print at TU Wien Bibliothek.
TU Bibliothek WIEN Your knowledge hub

Compared to the surface piezoelectric effect, this effect does not scale with the permittivity of the material. This makes the surface flexoelectric effect in materials with a high permittivity negligible. In low permittivity materials, the coefficient of the surface flexoelectric effect can be as large as the bulk flexoelectric effect.

As to this date, it is unclear if this effect exists, as there are multiple arguments against it. The author *Resta* argues that the surface flexoelectric effect is negligible in the thermodynamic limit, as the macroscopic electric field inside a bulk slab is not depending on what happens at the slab surfaces, meaning that surface-charge induced fields do not extend far enough into the bulk. The author also proves that the macroscopic field is constant in the bulk of the slab, and a well-defined linear response function of the material can be expected. [90]

Flexoelectric bending

The converse flexoelectric effect was initially measured by determining the deflection of a $BaTiO_3$ cantilever when an external electric field was applied. [16] By definition, the converse bulk flexoelectric effect only exists if there is a polarization gradient in the material. However, there is some apparent contradiction. As shown in *Figure 16*, the basic electronic structure is a capacitor when considering a MEMS cantilever. In theory, a capacitor has no field gradient inside the dielectric material as the electric field perpendicular to the dielectric/electrode interface is constant inside the materials and makes an instant jump from one material to the other. So, the question is, as an electromechanical response is measured in non-piezoelectric materials, which correlate linearly with the strain gradient, where do the gradients come from?

Die approbierte gedruckte Originalversion dieser Dissertation ist an der TU Wien Bibliothek verfügbar.
The approved original version of this doctoral thesis is available in print at TU Wien Bibliothek.
TU Bibliothek WIEN Your knowledge hub

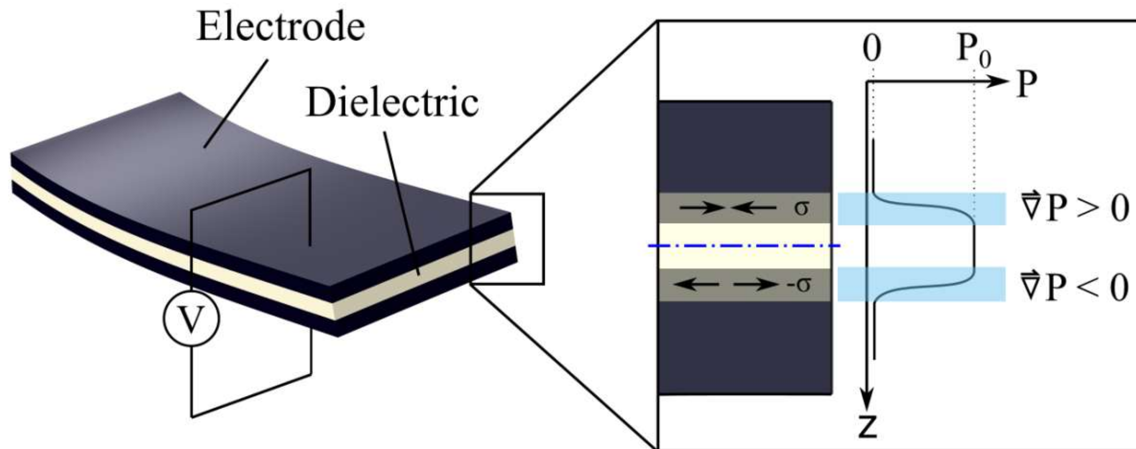

Figure 16 *A 3D model of a 3-layered cantilever structure with an applied voltage V is depicted. The two black layers symbolize the electrode, and the white layer is the dielectric. On the right, the cantilever stack is seen with a symbolic polarization curve along the thickness of the cantilever. A polarisation gradient exists as the polarization does not jump from 0 to P_0, but has a smooth transition between the two values according to an unknown function. As the gradients have opposite signs at the two interfaces, the stresses also have opposite signs. As the cantilever's neutral axis (blue line) is between the two interfaces, their torsion moments add up, and bending occurs.*

It is reasonable to assume that the most significant gradient will be at the interface, as the polarization changes from a constant value to 0. Theoretically, there should be a polarisation jump at the interface, but pure step functions are considered unphysical for most systems. This is why a linear decrease in polarisation is assumed for the following derivation. [88]

A simple plate with height h and free mechanical boundary conditions (no clamping etc.) is considered as model. For the electrical properties of the electrodes, they are regarded as 2-dimensional objects due to simplicity, and blocking boundary conditions are assumed, *i.e.* the electric field inside the electrodes is 0.

To get an equation of balance for bending moments, *equation 17* is multiplied with a cartesian coordinate along the thickness of the slab, x_3, and is then integrated over the cross-section:

$$b\int_{-h/2}^{h/2}\sigma_{11}x_3dx_3 \;=\; b\,f_{13}\int_{-h/2}^{h/2}\frac{\partial P_3}{\partial x_3}x_3dx_3 + b\,c_{11}\int_{-h/2}^{h/2}u_{11}\,x_3dx_3 \tag{23}$$

Here b is the width of the plate. On the left-hand side of the equation is the total bending moment. The first term on the right-hand side is the bending moment caused by polarization gradients (flexoelectric bending), and the last term originates from an optional external bending

Die approbierte gedruckte Originalversion dieser Dissertation ist an der TU Wien Bibliothek verfügbar.
The approved original version of this doctoral thesis is available in print at TU Wien Bibliothek.
TU Bibliothek WIEN Your knowledge hub

moment. Looking at the flexoelectric bending term, in the first step, the polarization gradient times position x_3 will be integrated by parts, where one part is 0 for the case that both interfaces show the same polarization function. The second step is the integration of the polarization, which can be written as the height times the average polarization based on the mean value theorem.[4]

$$\int_{-h/2}^{h/2} \frac{\partial P_3}{\partial x_3} x_3 dx_3 = -\int_{-h/2}^{h/2} P_3 dx_3 = -h\langle P_3 \rangle \tag{24}$$

For a slab where the dimensions are larger than the interface layer (which has a thickness in the nm scale), the average polarization will equal the bulk polarization ($\langle P_3 \rangle \approx P$). This is because the polarization drop at the interface gets less significant when the thickness increases. This is an interesting result, as the flexoelectric bending moment scales with the bulk polarization as opposed to the polarization gradient at the interface. Of course, these are still forces applied to the surface where the gradients are present.

Next, some results for strain calculation from plate theory are used. It is assumed that for a thin plate, only small forces are necessary to bend it. Therefore, at both cantilever surfaces, the stresses along the x_3-axis are zero:[91]

$$\sigma_{13} = \sigma_{23} = \sigma_{33} = 0 \tag{25}$$

As the plate is assumed to be thin and these stress components at the surface are zero, the latter are also negligible in the bulk of the cantilever and are considered zero. When this result is used in the fundamental equations for homogeneous deformations of a rod, we obtain the following relations:[92]

$$\begin{aligned} u_{11} &= u_{22} = x_3 G \\ u_{33} &= -x_3 \frac{c_{12}}{c_{11}} G \\ u_{12} &= u_{23} = u_{13} = 0 \end{aligned} \tag{26}$$

and apply them to *equation 15* to obtain:

[4] In this case we refer to the mean of a function which is defined as:

$$\langle f \rangle = \frac{1}{b-a} \int_a^b f(x) dx$$

Die approbierte gedruckte Originalversion dieser Dissertation ist an der TU Wien Bibliothek verfügbar.
The approved original version of this doctoral thesis is available in print at TU Wien Bibliothek.
TU Bibliothek WIEN Your knowledge hub

$$\phi_G = \frac{\chi_{33}^{-1}}{2} h P^2 + \frac{D}{2} G^2 - 2hPG\left(f_{1133} - \frac{c_{12}}{c_{11}} f_{1111}\right) \tag{27}$$

When the plate can mechanically move free, and σ_{33} is 0, then this potential can be minimized with respect to G ($d\phi_G/dG=0$). This leads to the equation with which one can calculate the flexoelectric bending:

$$G = \frac{h}{D} \mu E \tag{28}$$

Consequently, the curvature scales linearly with the electric field, and the flexural rigidity takes the following form:

$$D = \frac{E_{mod}\, h^3}{12(1-\nu^2)} \tag{29}$$

As expected, due to the scaling of D with h^3, the thinner the plate is, the higher the curvature gets. It is essential to point out that this result is derived for a single slab of dielectrics with infinitesimally thin electrodes. Therefore, when applying this equation to real cantilevers, the thickness is more ambiguous, as the electric field only exists in the dielectrics, while the mechanical strain drops across the whole cantilever (dielectrics + electrodes). In this thesis, the bending case is derived with an original approach to see how *equations 23* and *28* change when physical electrodes exist.

This is achieved by setting up the balance of the moment equation like *equation 23*, with the difference being that the integral now spans over the electrodes.

$$\int_{-h_c/2}^{h_c/2} \sigma_{11}\, x_3\, dx_3 \;=\; \mu \int_{-h_c/2}^{h_c/2} \frac{\partial E_3}{\partial x_3} x_3\, dx_3 \;=\; \mu \int_{-h_d/2}^{h_d/2} \frac{\partial E_3}{\partial x_3} x_3\, dx_3 \tag{30}$$

For this equation, the external forces are set to 0. Instead of covering the whole cantilever thickness h_c, the integral over the bending moment originating from the flexoelectric effect (right-hand side) can be reduced to the thickness of the dielectric h_d, as there is no electric field in the electrodes. The right-hand side can be evaluated similarly to *equation 24*, which equals $-\mu\, h_d\, E = -\mu\, V$. The relation between stress and strain is assumed to follow Hooke's law and that there is no strain in the x_2 direction:

Die approbierte gedruckte Originalversion dieser Dissertation ist an der TU Wien Bibliothek verfügbar.
The approved original version of this doctoral thesis is available in print at TU Wien Bibliothek.
TU Bibliothek WIEN Your knowledge hub

$$u_{11} = \frac{\sigma_{11}}{E_{mod}} - \frac{\nu\sigma_{22}}{E_{mod}}$$

$$u_{22} = \frac{\sigma_{22}}{E_{mod}} - \frac{\nu\sigma_{11}}{E_{mod}} = 0 \tag{31}$$

The strain that occurs for cylindrical bending can be calculated by analysing how the mechanical strain changes in the radial direction of the plate, as can be derived from the schematic illustration in *Figure 17*.

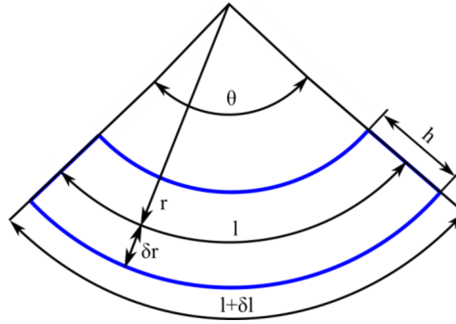

Figure 17 *Schematics to derive the strain in a bending case.*

The distance l can be expressed by the radial position r times the angular span of the beam θ. Similarly, the length of $l+\delta l$ at any different radial position $r+\delta r$ is then $\theta\cdot(r+\delta r)$. Both relations can be rewritten as:

$$\theta = \frac{l}{r} = \frac{l + \delta l}{r + \delta r} \tag{32}$$

From this, a relation can be made, and the strain can be set in relation to the radius:

$$\frac{\delta r}{r} = \frac{\delta l}{l} = u \tag{33}$$

Here, δr can be identified as the x_3 direction for the moment integral. The $1/r$ factor is defined as the curvature and, for small deflections, can be approximated as the second derivative of the deflection with regards to the x_1 direction:

$$u_{11} = x_3 \frac{\partial^2 w}{\partial {x_1}^2} \tag{34}$$

Now, with *equations 31* and *34* combined, the moment integral can be evaluated further:

Die approbierte gedruckte Originalversion dieser Dissertation ist an der TU Wien Bibliothek verfügbar.
The approved original version of this doctoral thesis is available in print at TU Wien Bibliothek.
TU WIEN Bibliothek Your knowledge hub

$$M = \int_{-h_c/2}^{h_c/2} \sigma_{11}\, x_3\, dx_3 = \int_{-h_c/2}^{h_c/2} \frac{E_{mod}\, x_3^2}{1 - \nu^2} \frac{\partial^2 w}{\partial {x_1}^2}\, dx_3 = \frac{E_{mod}\, h_c^3}{12(1-\nu^2)} \frac{\partial^2 w}{\partial {x_1}^2} \tag{35}$$

In this result, $\partial^2 w/\partial x_1^2$ can be identified as the curvature G for small deflections, and the remaining coefficients can be identified as the flexural rigidity D. For reasons of simplicity, the cantilever is assumed to have the same Young's modulus for the electrodes and the dielectrics. Compared to the separate integration across the electrodes plus the dielectrics, this results in a 14.5% error when using values for a 200/200/200 nm $IrO_2/TiO_2/IrO_2$ plate stack when compared to D with an averaged Young's modulus. Combining the result from *equation 31* with *equation 35* yields the result

$$G = \mu \frac{V}{D} \tag{36}$$

Which is the equation commonly used to evaluate the flexoelectric effect in cantilevers. By this, it is shown in a straightforward derivation that the flexural rigidity depends on the cantilever thickness, while the flexoelectric moment is linearly dependent on the applied voltage.

TU Bibliothek Your knowledge hub WIEN
Die approbierte gedruckte Originalversion dieser Dissertation ist an der TU Wien Bibliothek verfügbar.
The approved original version of this doctoral thesis is available in print at TU Wien Bibliothek.

Die approbierte gedruckte Originalversion dieser Dissertation ist an der TU Wien Bibliothek verfügbar.
The approved original version of this doctoral thesis is available in print at TU Wien Bibliothek.
TU Bibliothek WIEN Your knowledge hub

Electrostriction

Electrostriction is an effect that exists in every dielectric, which involves the contribution of more than one chemical element. It describes the displacement of atoms in the dielectrics with the square of the electric field.

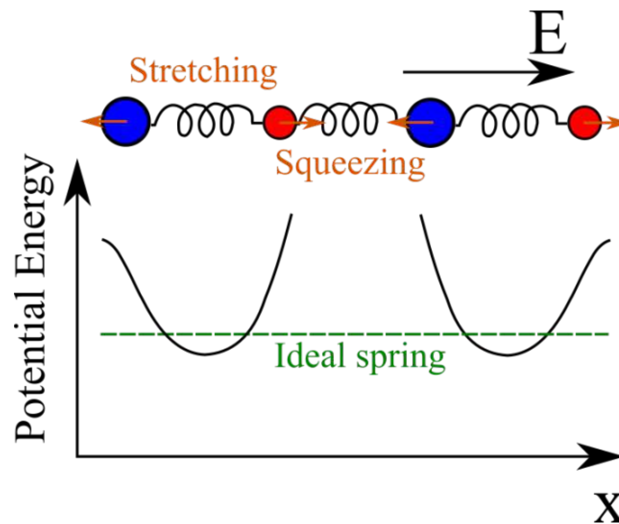

Figure 18 *Schematic model to explain the electrostrictive effect. Blue and red rigid polarizable atoms of different species are connected via non-linear springs. An external electric field E is applied, and the reactive motion of the ions is shown in orange. Depending on the ion pair, stretching or squeezing can be observed. The potential energy of this spring system is also shown, where the limit for an ideal spring is marked in green.*

The cause of the electrostrictive effect can be explained as follows.[93] As seen in *Figure 18*, a model consisting of a one-dimensional chain of rigid ions of equal distance is assumed. As an external electric field is applied, positive ions are displaced towards the negative and negative ions are displaced towards the positive potential. However, in real crystals, the repulsive and attractive forces are uneven (it is easier to stretch than to contract). Two situations arise: in one, the ion pair distance is enlarged, and in the other, the ion pair distance is reduced. For an idealized spring system, this would lead to a net strain of zero. However, in real systems, the forces between an ion pair are not symmetric regarding stretching or squeezing, and this slight difference leads to a net displacement in the crystal lattice.

Electrostriction is distinctive in that the actuation is favoured in one compared to the opposite direction. Experimentally this displacement, or stress, is proportional to the square of the electric field, which has interesting consequences when a sine wave electric field is applied to the dielectrics:

$$\sigma \sim E^2 = {E_0}^2 sin(\omega t)^2 = {E_0}^2 \frac{1 - cos(2\omega t)}{2} \tag{37}$$

Where E_0 is the amplitude of the applied electric field, ω is the angular frequency, and t is the time. For pure electrostriction, a sine wave actuation with frequency ω causes a stress oscillation with $2\,\omega$. For mechanical resonators, this means that to excite the resonator in its natural resonance frequency, the applied field must be half the frequency of the mechanical resonance. This can be exploited to determine the electrostrictive effect in resonators separate from the linear electromechanical mechanisms like piezoelectricity or flexoelectricity.

Maxwell Stress

Maxwell stress describes the interaction of electromagnetic forces with a mechanical impulse. In the case of a charged particle, this interaction is commonly known as the Lorentz force. The Maxwell stress tensor is a generalization of the Lorentz force for charge distributions in 3-dimensional space. In an electric field and without a magnetic field and in vacuum, the equation for the Maxwell stress σ is:

$$\sigma_{ij} = \varepsilon_0 E_i E_j - \frac{1}{2}\varepsilon_0 E^2 \delta_{ij} \tag{38}$$

Where δ_{ij} is the Kronecker delta.

When a voltage is applied to a capacitor, a Maxwell stress is applied to the sandwiched dielectric. This force squeezes the dielectric from the bottom and top sides and also causes the dielectric to expand laterally, as depicted in *Figure 19*. This deformation due to the applied voltage means, that this effect can be used for actuation of MEMS devices.

Die approbierte gedruckte Originalversion dieser Dissertation ist an der TU Wien Bibliothek verfügbar.
The approved original version of this doctoral thesis is available in print at TU Wien Bibliothek.
TU WIEN Bibliothek Your knowledge hub

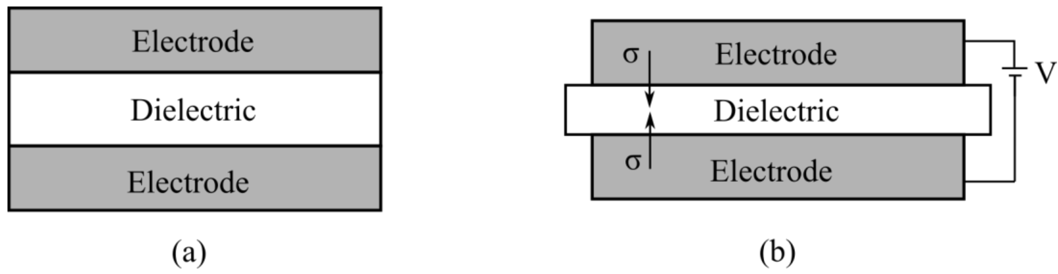

Figure 19 *(a) A plate capacitor without any voltage applied. (b) When a voltage is applied, the two electrodes attract and cause the Maxwell stress σ. This stress causes the dielectric to deform and hence this effect can be used for actuation.*

However, this effect is negligibly small for harder materials and only plays a role in very soft materials with a low Young`s modulus (<1 GPa, $TiO_2$ has 157 GPa for comparison). Since this effect is negligible even for polymers like PVDF due to a Young`s modulus of roughly 2 GPa, this actuation effect is not considered for this work.[94]

Die approbierte gedruckte Originalversion dieser Dissertation ist an der TU Wien Bibliothek verfügbar.
The approved original version of this doctoral thesis is available in print at TU Wien Bibliothek.
TU WIEN Bibliothek Your knowledge hub

2.4 Micromechanical resonators

There is a wide variety of micromechanical resonators, from simple structures, like cantilevers or membranes, to complex systems, like motors.[1,95] For material characterization, it is advisable to select simple structures, as the determination of material parameters in comparison with theoretical predictions is much straightforward. Three essential building blocks for MEMS were considered: cantilevers, bridges, and membranes. Cantilevers are one-sided clamped beam structures. Bridges, in contrast, are beam structures clamped on two sides. Membranes are plates which are fixed on the outer rim of the plate and can move freely in directions perpendicular to the top and bottom surfaces. Cantilever structures were chosen to assess material properties, as they offer one significant advantage: compared to the other two basic mechanical structures, they are less sensitive to film stresses. As will be explained in section 3.2, film stress is a significant concern, as it can lead to a wrong interpretation for, e.g. material parameter analysis when not appropriately considered or may even lead to a complete failure of the MEMS structure. For beams, the film stress is compensated by static bending. This static bending, however, can make measurements more complicated, such as investigations with laser Doppler vibrometry, by reflecting the laser beam out of the optical measurement head. The problem with static bending can be substantially minimized by carefully engineering the film stresses in the cantilever to compensate across the whole structure or to have every thin film at a stress level close to 0. Thin film stress-compensating cantilever structures can be seen in *Figure 20 a* and *c* with the problematic static bends in *b* and *d*.

Die approbierte gedruckte Originalversion dieser Dissertation ist an der TU Wien Bibliothek verfügbar.
The approved original version of this doctoral thesis is available in print at TU Wien Bibliothek.
TU Bibliothek WIEN Your knowledge hub

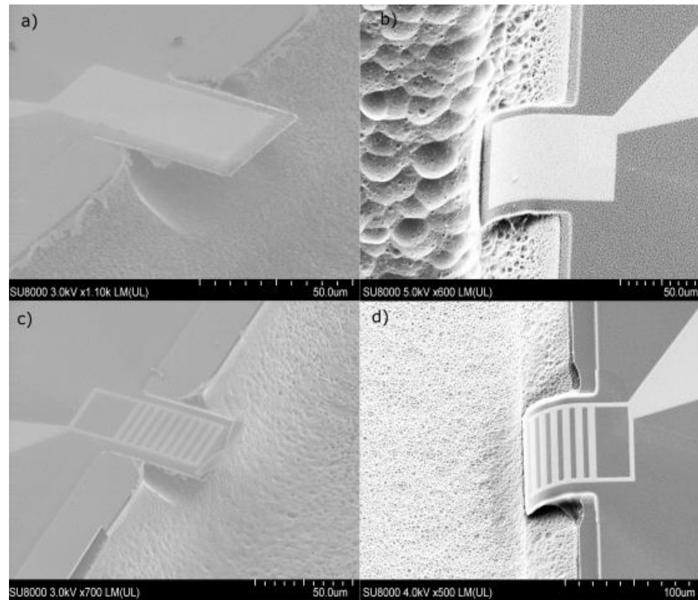

Figure 20 *A SEM image of typical cantilever structures investigated in this study. In a and c, stress-compensated cantilevers are illustrated, while in b and d, strong static, parasitic bending occurs.*

A basic mathematical description of a beam is given by the Euler-Bernoulli equation:[96]

$$\rho \cdot A \cdot \frac{\partial^2 w(x,t)}{\partial t^2} + E_{mod} \cdot I \cdot \frac{\partial^4 w(x,t)}{\partial x^4} = 0 \tag{39}$$

Where ρ is the beam density, A the cross-section of the beam, w the deflection, t the time, E_{mod} the Young's modulus and I the area moment of inertia. This equation is an idealized version with the following two main assumptions:

- Beam cross-sections remain the same during bending. This results from the approximation that bending the beam does not introduce shear forces.
- Deformation angles remain small so that the curvature is equal to the second derivative of the deflection (*e.g.*, 10° bending results in a 1.5% error).

The second assumption is also essential, as the second derivative is used for calculating the curvature of the cantilever and hence, for determining the flexoelectric coefficient.

To estimate the dynamic behaviour of the beams, the following analysis is based on the definitions and explanations given in [97]. The solution of the Euler-Bernoulli beam equation for the boundary conditions of a cantilevered beam is:

Die approbierte gedruckte Originalversion dieser Dissertation ist an der TU Wien Bibliothek verfügbar.
The approved original version of this doctoral thesis is available in print at TU Wien Bibliothek.
TU Bibliothek WIEN Your knowledge hub

$$w_n(x) = \ b_0 \cdot \left[\cosh(\beta_n x - \cos(\beta_n x) + \frac{\cos(\beta_n L) + \cosh(\beta_n L)}{\sin(\beta_n L) + \sinh(\beta_n L)} (\sin(\beta_n x) - \sinh(\beta_n x)) \right] \quad (40)$$

Where w_n is the mode-dependent deflection, b_0 is a coefficient, and β_n is a coefficient that is frequency dependent. The index n is important, as this means that several solutions exist for this equation. Each solution is at a specific resonance frequency and has a different deflection profile, a so-called mode. The deflection solution for the first four modes is shown in *Figure 21*.

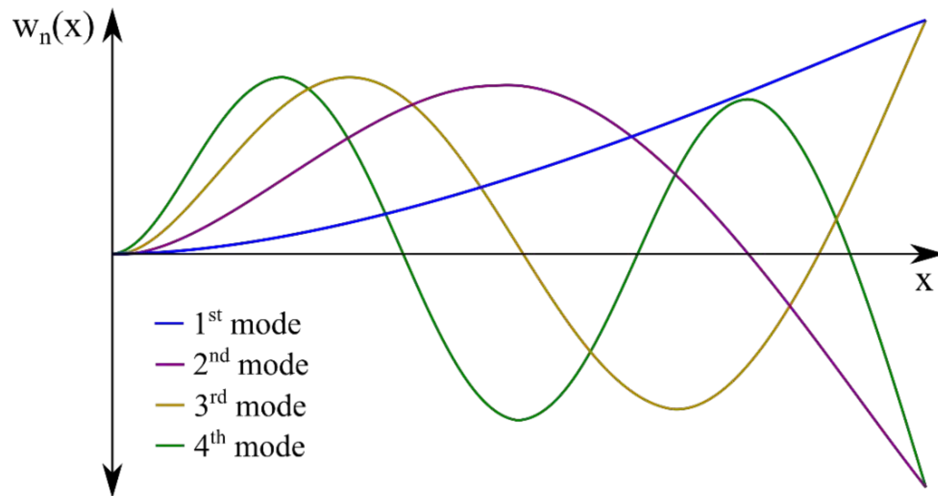

Figure 21 *The analytical solutions for the mode-dependent deflections w_n for the first four modes of a cantilevered beam.*

The solution is more complex in two dimensions, but the shapes are comparable to the 1D case. In *Figure 22,* a frequency-dependent mode shape measurement of a cantilever is shown. The different mode shapes at their respective resonance frequency can be identified.

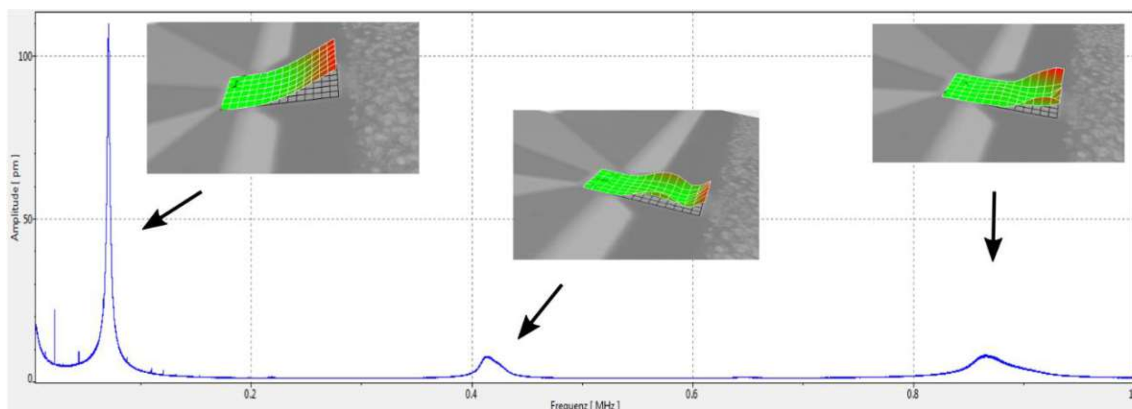

Figure 22 *Deflection spectrum of a typical MEMS cantilever excited with a chirp signal (amplitude of 1 V) from 10 kHz to 1 MHz.*

Die approbierte gedruckte Originalversion dieser Dissertation ist an der TU Wien Bibliothek verfügbar.
The approved original version of this doctoral thesis is available in print at TU Wien Bibliothek.
TU Wien Bibliothek Your knowledge hub

For this cantilever, three different shapes at three frequencies can be observed. In the Euler-Bernoulli theory, damping of the cantilever motion is not included, and therefore the deflection spectrum has infinitely thin peaks, approaching a line spectrum. In non-ideal systems, however, the line spectrum widens to Lorentzian peaks. This is due to the so-called quality factor (Q), a value of all energy losses in a resonator within one oscillation cycle. For mechanical resonators, the primary individual loss components sum up to the global Q-factor as follows:[98]

$$\frac{1}{Q} = \frac{1}{Q_{medium}} + \frac{1}{Q_{clamping}} + \frac{1}{Q_{intrinsic}} + \frac{1}{Q_{other}} \tag{41}$$

These losses represent the following damping sources:

- Q_{medium} -> Accounts for losses due to the deflection being damped when the resonator oscillates in a medium.
- $Q_{clamping}$ -> These are losses due to energy losses to the substrate where the cantilever is clamped.
- $Q_{intrinsic}$ -> This term is for the losses inside the resonator material, such as due to material impurities or thermo-mechanical losses.
- Q_{other} -> This term accounts for any losses that are not listed here.

These losses result in the peak widening, *i.e.* the lower the Q, the wider and lower the peak height.

The phase-frequency relationship for a resonator describes how the phase angle between the applied force and the displacement of the resonator changes as the frequency of the applied force varies. In the following, the phase-frequency relationship for a simple harmonic oscillator (which is a reasonable approximation for the fundamental mode of a cantilever structure) is given:

At resonance frequency

At the resonance frequency corresponding to the fundamental flexural mode, the cantilever responds with maximum amplitude, and its displacement lags the applied force by 90 degrees due to inertia and stiffness effects. When the displacement is at its zero point (nodal location) the force has its maximum value, and as the force crosses its zero point, the displacement is at

TU Bibliothek, WIEN Your knowledge hub
Die approbierte gedruckte Originalversion dieser Dissertation ist an der TU Wien Bibliothek verfügbar.
The approved original version of this doctoral thesis is available in print at TU Wien Bibliothek.

its maximum (antinodal location). This way, the force is always acting in the direction of the cantilever motion and no energy is wasted, resulting in the maximum amplitude of the system.

Below resonance frequency

At frequencies significantly below resonance, the mechanical resonator's phase response is typically close to 0 degrees. Here the resonator can follow the actuation without lags, as the frequency is low enough to ignore inertia effects and the amplitude is low enough to ignore sitffness effects. The amplitude is lower, as a quarter of the force in a period is counteracting the resonator motion and hence the amplitude is much smaller than at 90° phase shift.

Above resonance frequency

When the actuation frequency is far above the resonance frequency of a mechanical resonator, the phase relation between the applied force and the displacement of the resonator is typically close to 180 degrees. Here the frequency is high enough that inertia effects are significant as the cantilever motion cannot follow the actuation signal and the resonator exhibits the highest force when the actuation signal is opposite to the cantilever deflection. Again, a quarter of the force in a period is counteracting the resonator motion

It's important to note that the phase shifts are not exactly 0, 90 or 180° due to the presence of small damping effects, slight phase shifts introduced by the mechanical system, and possible resonant behavior associated with other modes of vibration (higher-order modes).

TU Bibliothek Your knowledge hub WIEN
Die approbierte gedruckte Originalversion dieser Dissertation ist an der TU Wien Bibliothek verfügbar.
The approved original version of this doctoral thesis is available in print at TU Wien Bibliothek.

3 Methods

3.1 Thin film deposition

There are multiple ways to deposit films with thickness in the nanometre range. Sputtering is the primary technique used to deposit metals and dielectrics in this work. For the PVDF cantilevers, gold was deposited by evaporation, and the PVDF thin films were realized by spin coating.

Sputtering

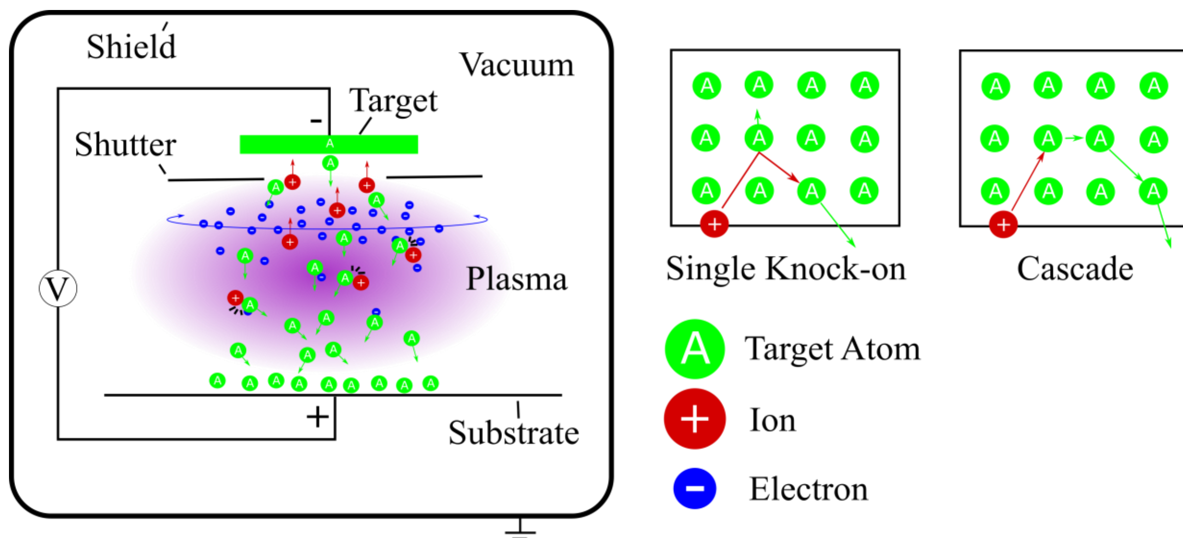

Figure 23 *On the left side is a schematic of a sputtering machine. On the right side are two possible mechanisms for incoming ions to knock out target atoms.*

With the sputtering technique, a substrate can be coated with a target material by accelerating ionized background gas atoms towards a block of the target material (target, in short). The kinetic energy of the impacting ions results in the ejection of target atoms, which drift towards and sublimate on the substrate.[99] Partial ionization of the background gas is achieved by plasma ignition due to large static (DC) electric fields. A schematic of a DC-magnetron sputtering process is illustrated in *Figure 23*.

Die approbierte gedruckte Originalversion dieser Dissertation ist an der TU Wien Bibliothek verfügbar.
The approved original version of this doctoral thesis is available in print at TU Wien Bibliothek.
TU Bibliothek WIEN Your knowledge hub

The sputtering chamber is initially evacuated to a base pressure of 10^{-7} mbar to remove any remaining gaseous contaminations. The process gas is introduced with a constant gas flow rate. The used gas can vary, depending on if no chemical reaction is wanted (then inert argon is commonly used) or if a chemical reaction between the gas and the target atoms is stimulated. A plasma is ignited by applying a static electric field (with power values in the 200 to 2000 W region after ignition). The plasma comprises free electrons, ions or ionic molecules and neutral gas constituents.

The positively charged ionic particles are accelerated towards the target. Once the accelerated ion reaches the target, it can knock out target atoms. These knock-out events can either happen in a single step or as a cascade, as shown in *Figure 23* on the right. Once the target atom is ejected from the material's surface, the kinetic energy and drift direction is kept initially. On their way to the substrate, the target atoms will collide with the gaseous constituents, resulting in energy and momentum transfer and, thus, a wider angular distribution. After passing the plasma, the target atom will be adsorbed on the surface of the substrate. A standard method to increase plasma density, and hence, the ionization rate, is placing a magnetron above the target to force the electrons on circular paths in the plasma region close to the target.

Essential parameters for sputtering are the plasma power, the background gas pressure, the gas type and the distance between the substrate and target, respectively. The plasma power determines the kinetic energy the gas ions, and therefore the target atoms, have. The increased kinetic energy leads to higher ionization and sputter rates. Within certain limits, higher energy favours a more ordered, *i.e.* crystalline growth.[100] The gas pressure and substrate-target distance affect the target atom's mean free path (and, consequently, the angle range under which the target atoms hit the substrate). With a higher gas pressure, more ions are present per unit length, making it more likely to collide with a target atom and transfer kinetic energy and momentum. With a higher electrode distance, the interaction probability of target atoms with gas ions is enhanced.

For reactive sputtering, a reactive gas is used either exclusively or in combination with an inert carrier gas. The reactive gas is activated in the plasma region and chemically reacts with the target atom. This work mainly uses oxygen plasma to deposit iridium oxide and titanium oxide, with pure iridium or titanium targets, respectively.

A LS730S sputter equipment from VonArdenne (Germany) was used in this work.

Die approbierte gedruckte Originalversion dieser Dissertation ist an der TU Wien Bibliothek verfügbar.
The approved original version of this doctoral thesis is available in print at TU Wien Bibliothek.
TU WIEN Bibliothek Your knowledge hub

Evaporation

Another coating technique that was used was thermal evaporation. Here the substrate and the coating material are placed in a vacuum chamber. The coating material, for example, gold, is loaded into a metallic container and is heated up to the evaporation point of the material. The pressure in the chamber is significantly lower ($< 10^{-8}$ mbar) compared to sputtering (10^{-3} mbar range) during deposition, as no plasma is needed. The evaporated atoms (or clusters), therefore, have a very narrow angular distribution, as the mean free path in such a low vacuum is in the range of meters, whereas for typical pressures in sputtering, it is in the centimetre range. Due to the narrow angular distribution, only surfaces directly facing the container are coated, which leads to an uneven coating if the substrate is very rough or has a distinct 3D topography. This can also be beneficial, for example, in the lift-off process, as explained in the lift-off chapter in section 3.2.

Spin-coating

Spin coating is a favourable technique for depositing materials in the liquid state. For this simple method, depicted in *Figure 24*, a substrate is rotated at speeds of 500-5000 rpm while the solution is cast in the centre of the substrate.[101] Due to the centrifugal force, the solution spreads evenly with high uniformity over the entire substrate. The solvent of the solution is usually volatile and evaporates, leaving the solute material as a thin film. The solvent evaporation strongly depends on the volatility, the vapour pressure and the ambient condition. The resulting film thickness can range from tenths of nanometers to several micrometres.

Die approbierte gedruckte Originalversion dieser Dissertation ist an der TU Wien Bibliothek verfügbar.
The approved original version of this doctoral thesis is available in print at TU Wien Bibliothek.
TU Wien Bibliothek Your knowledge hub

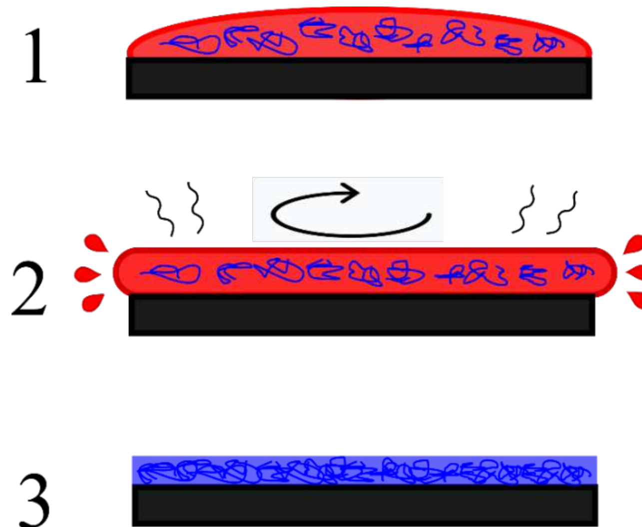

Figure 24 *The primary spin-on method for polymer thin film casting. The solvent is depicted in red, and the solute as blue lines representing polymer chains. 1. A substrate is coated with a solution. 2. The substrate is spinning, and the solvent evaporates simultaneously. 3. The solute remains and is the resulting thin film, shown in blue.*

The most significant factors influencing the resulting film thickness are the solute concentration (which affects the viscosity of the solution) and the spinning speed. Higher solute concentrations lead to thicker films and higher speeds to thinner films.[101]

The films can exhibit defects, such as bubbles or uncoated areas, which are the most important artefacts. The first defect arises if air bubbles are present in the solution, which are then also present in the thin film. The bubbles can be pre-emptively extracted from the solvent with a vacuum or filtered out with a very fine filter. The second defect mainly arises when the amount of solvent applied to the substrate is too low and as such, using more solvent fixes the problem in most cases. The second defect can also appear when the solvent is highly viscous. The solution here is to cover as much substrate as possible with the solvent before starting the rotation.

The wafer chuck can also be heated during the spin-on procedure, which results, at higher temperatures, in a higher evaporation rate of the solvent, which has a significant impact on the microstructure of the deposited thin film.

Die approbierte gedruckte Originalversion dieser Dissertation ist an der TU Wien Bibliothek verfügbar.
The approved original version of this doctoral thesis is available in print at TU Wien Bibliothek.
TU WIEN Bibliothek Your knowledge hub

3.2 Patterning techniques

An overview of the fabrication technologies and structural designs used for this work is given in this section.

The standard method for patterning in the semiconductor industry is by coating the substrate with a material, depositing a resist, which is patterned, and subsequently etching the sample. This standard method will not be discussed in detail, as it is ubiquitous and can be easily found in literature. We will first present the preferred micropatterning method when the used material cannot be etched easily. A standard procedure to pattern such thin films is the so-called lift-off process:

Lift-Off

For the lift-off process, an image-reversal resist is first patterned on the substrate such that the resist coats the areas where the resulting structure should not be, as depicted in *Figure 25*. The image reversal resist is needed so that the flanks of the structured resist are undercut (angled away from the final structure). Next, the material is deposited onto the wafer by evaporation or sputtering. After the deposition, the material-coated resist is removed, leaving material only in areas free of resist prior to lift-off.

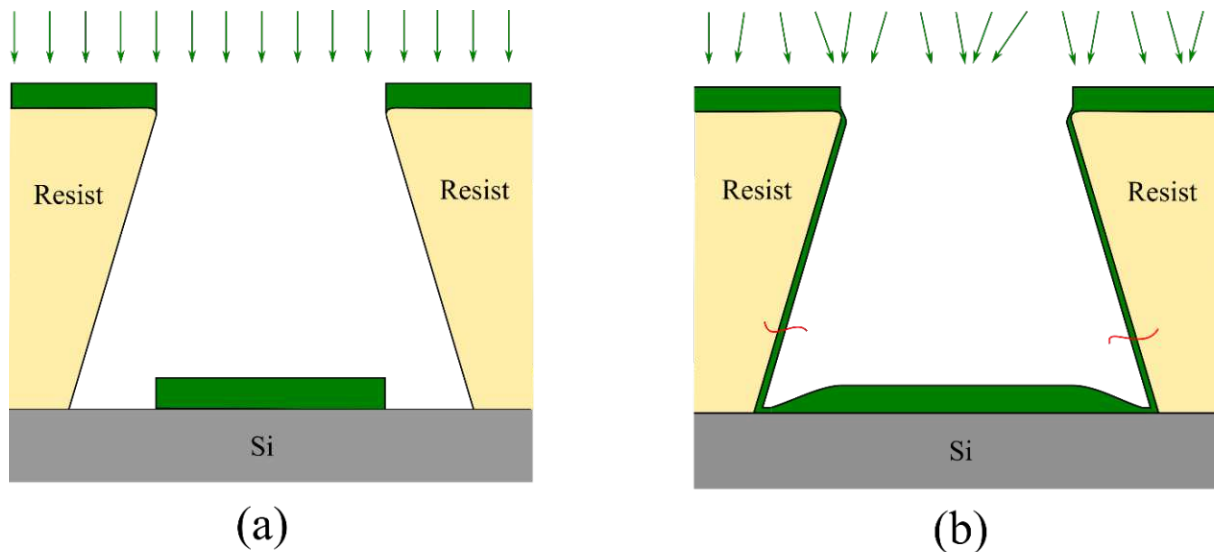

Figure 25 *Schematic illustrations of the cross-section of a Si wafer with a resist patterned for the lift-off process for either (a) evaporation or (b) sputtering. The green arrows indicate the angle of the impinging ions. When sputtering, unwanted protruding ridges at the edges of the final pattern can arise due to the coating of the flanks. The wiggly red lines indicate a possible fracture point of the coating, which leads to such ridges.*

Die approbierte gedruckte Originalversion dieser Dissertation ist an der TU Wien Bibliothek verfügbar.
The approved original version of this doctoral thesis is available in print at TU Wien Bibliothek.
TU Bibliothek WIEN Your knowledge hub

While thermal evaporation works fine in the lift-off process, sputter lift-off is problematic. As shown in *Figure 25*, the angular distribution of the incoming target atoms is wider than for evaporation. Due to this wider angular distribution, the negative flanks of the resist are also coated, which hinders the subsequent removal of the resist in acetone and leads to residue. This problem was especially pronounced for iridium oxide, which featured a stronger isotropic deposition characteristic and thus, a thicker flank coating than other materials due to the high gas pressures is needed to realise low-stress films. As IrO_2 has a high chemical resistance and no possible method for standard dry etching of the IrO_x films was found, a special resist (Nlof 20xx from Microchemicals) developed explicitly for sputter lift-offs was used. As spin-on parameters, a speed of 3000 rpm followed by a 6-minute soft bake at 100°C was used. The resist was then illuminated for 6 seconds with a subsequent 90-second post-exposure bake at 110°C. Then the resist was developed for 90 seconds with a puddle method[5].

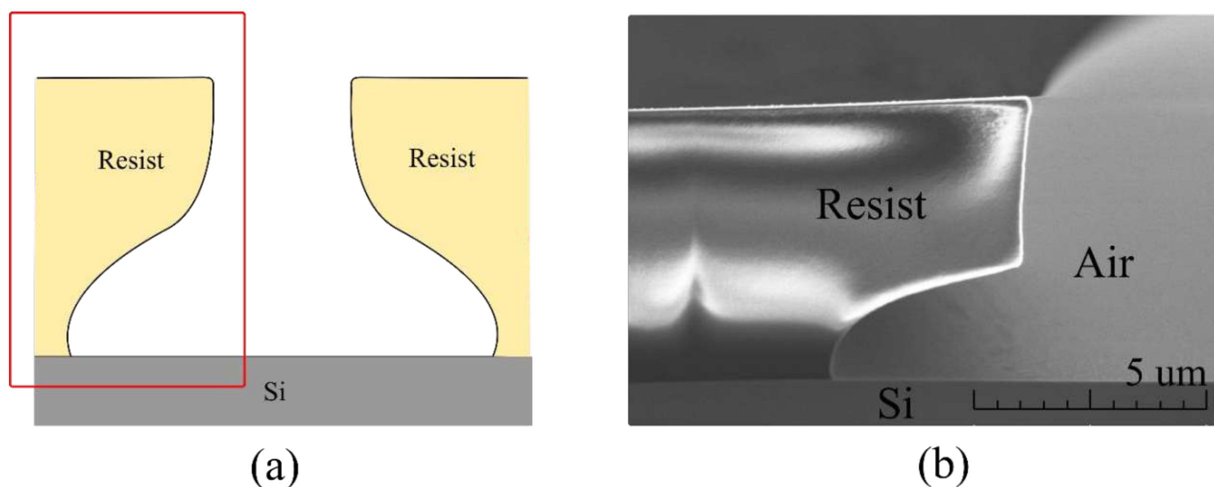

Figure 26 *A cross-sectional images of the Nlof 2070 edge characteristics on a Si wafer after processing. (a) Schematic cross-section of a part of a wafer. The red border indicates the image position of the SEM image. (b) SEM image of the Nlof resist used for the device fabrication. The deep undercut needed for the fabrication can be identified.*

Due to a gradient in developing rate over the thickness of the resist (i.e., closer to the substrate, the resist develops faster than further away), a pronounced undercut is created, allowing for better sputter lift-offs. The undercut of the resist, as used in this thesis, is shown in *Figure 26*. In *Figure 27*, it is shown that even for a large undercut, the flanks are still coated with IrO_x, and a subsequent resist removal leaves residue in form of protruding ridges.

[5] For the puddle method, the developer is applied evenly over the substrate, which is then wiggled clockwise and counterclockwise at very low speeds.

Die approbierte gedruckte Originalversion dieser Dissertation ist an der TU Wien Bibliothek verfügbar.
The approved original version of this doctoral thesis is available in print at TU Wien Bibliothek.
TU Bibliothek WIEN Your knowledge hub

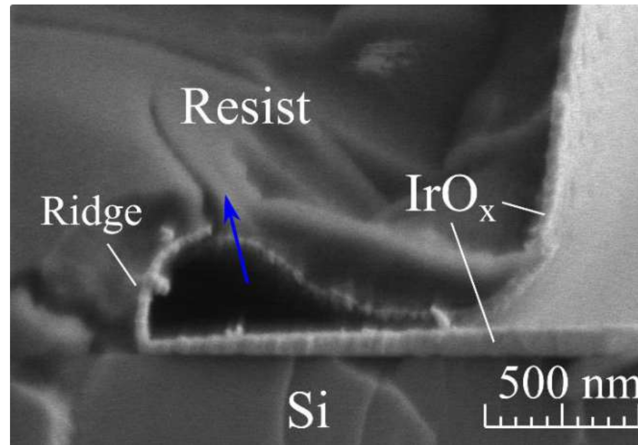

Figure 27 *SEM image of the cross-section of a wafer with a patterned Nlof resist and a sputtered layer of IrO_x. The IrO_x layer covers the whole surface of the resist. The resist can still be removed, as acetone can get through cracks of the IrOx film to the resist, as indicated by the blue arrow. However, when the resist is removed, ridges will be on the edges of the patterned electrode.*

These ridges can then facilitate a drop-like growth of the dielectrics layer, as seen in *Figure 28*, considerably changing the dielectric breakdown behaviour. Additionally, if the electrode has high thin film stress, the resist can be deformed and can, in the worst case, be pushed down onto the substrate, significantly reducing the large undercut.

Die approbierte gedruckte Originalversion dieser Dissertation ist an der TU Wien Bibliothek verfügbar.
The approved original version of this doctoral thesis is available in print at TU Wien Bibliothek.
TU WIEN Bibliothek Your knowledge hub

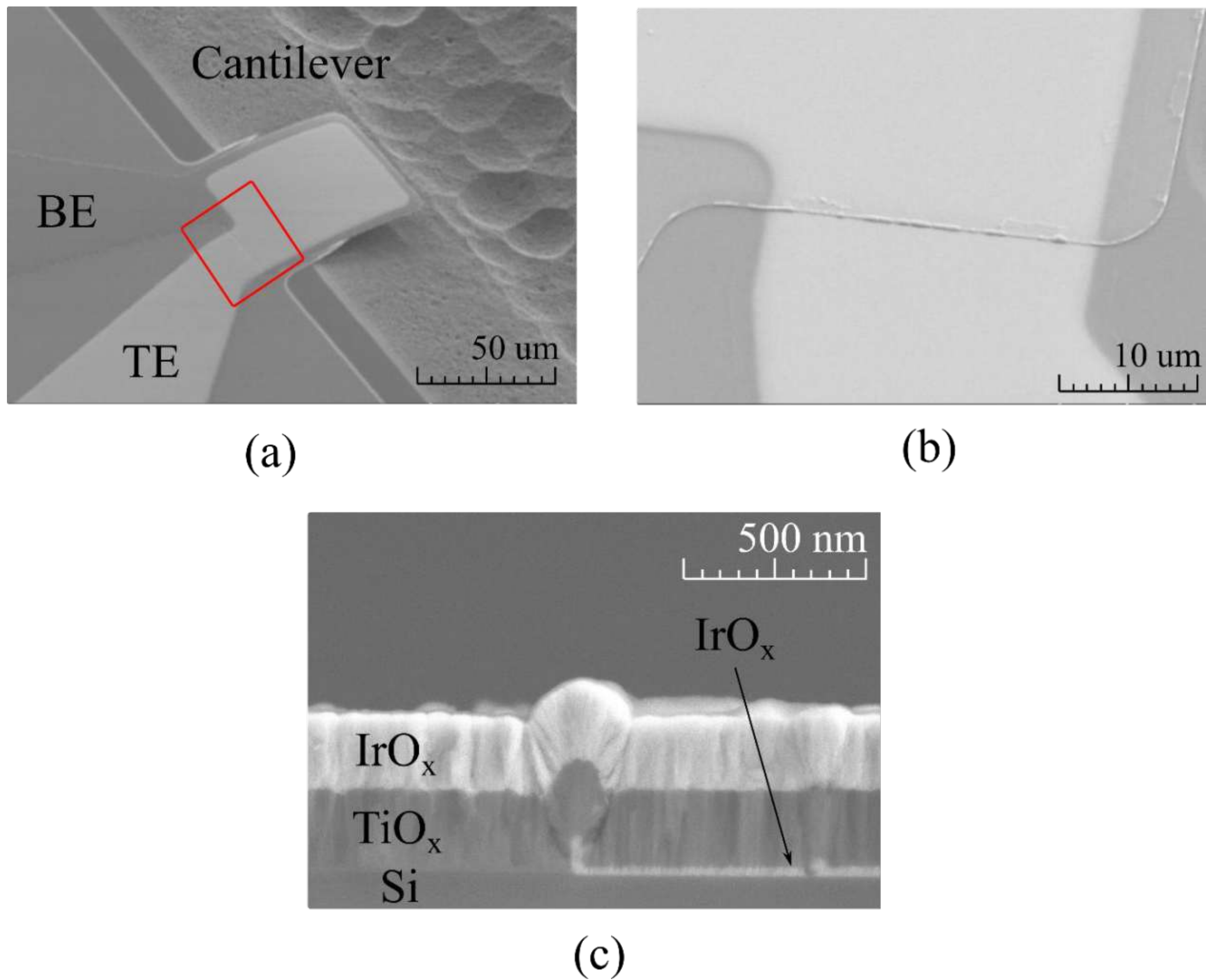

Figure 28 *Ridge analysis with SEM. (a) Top view on a cantilever device with a labelled bottom electrode (BE) and top electrode (TE). The red border indicates the area of the zoomed view of (b). (c) Cross-sectional view of such a ridge. The formation of droplet-like grains due to the protruding ridge can be seen.*

With the selection of tailored sputter parameters, the IrO_x lift-off can be achieved with minimal protruding ridges necessary for functioning devices.

RIE etch

Reactive ion etching is a dry etching technique where a gas or a gas mixture that gets chemically activated is introduced into a chamber together with the sample.[102] For this purpose, a DC or a high frequency electric field is applied, igniting a plasma. Due to the high frequency of the electric field, electrons are accelerated, while the heavier gas ions remain stationary. In this work, a DC RIE etch was used. With this technique, the bias voltage accelerates the ions from the plasma towards the sample. These radical ions can then react chemically with the sample atoms and remove material from the sample. There is also a physical etching component due to

Die approbierte gedruckte Originalversion dieser Dissertation ist an der TU Wien Bibliothek verfügbar.
The approved original version of this doctoral thesis is available in print at TU Wien Bibliothek.
TU WIEN Bibliothek Your knowledge hub

knock-on events of the accelerated gaseous particles, similar to sputtering, thus introducing anisotropy to the etching mechanism.

For the etching of TiO_2 films, an SF_6/O_2 gas mixture was used. In the plasma, typically, the sulphur hexafluoride breaks down to SF_4 and fluorine as:

$$SF_6 \Rightarrow SF_4 + 2F \tag{42}$$

The resulting fluorine reacts with the TiO_2 layer, thus removing material. The O_2 is introduced as it was shown that the fluorine atomic concentration gets substantially increased compared to a pure SF_6 gas composition.[103] The overall effect is that the etch rate increases with increasing O_2 concentration, and the lateral size of an etched hole is reduced. The etch rate of the fabricated TiO_x thin films was determined to be ~ 4 nm/s.

XeF_2 etch

Dry chemical etching with XeF_2 is a well-known method in MEMS device fabrication because of the high selectivity between silicon and many other commonly used materials (most notably, photoresist) and of high silicon etch rates. Sticking is also avoided.[104] The etching process with silicon is isotropic, meaning a constant etch rate in all crystal directions. At room temperature and atmospheric pressure, XeF_2 is solid. For this etching method, XeF_2 is vaporized by reducing the pressure below its vapour pressure in a so-called expansion chamber. The XeF_2 gas is then introduced into the sample chamber, where a chemical reaction with silicon occurs. The xenon and fluorine can dissociate on the silicon surface, whereas the highly electronegative fluorine can react with the silicon atoms.

When the XeF_2 is introduced into the chamber, the etch rate is initially high, as 100% of the fluorine ions can react. Over time, more and more fluorine atoms have already reacted, leading to a decrease in etch rate. This time-varying etch rate can be problematic for etch-depth control. A pulse etching method is commonly used to counteract this problem and gain better control of the etch depth. With this method, a small quantity of XeF_2 is introduced in the chamber and pumped out after some time (typically below one minute). After the evacuation of the chamber, the gas is introduced again. This process can be cycled multiple times.

For this work, XeF_2 etching with a XactiX Xetch E1 was used to release the cantilevers. Neither electrical nor mechanical properties of the TiO_x or IrO_x films were affected by this etch step in

TU WIEN Bibliothek Your knowledge hub
Die approbierte gedruckte Originalversion dieser Dissertation ist an der TU Wien Bibliothek verfügbar.
The approved original version of this doctoral thesis is available in print at TU Wien Bibliothek.

any measurable way. The etch rate varied from sample to sample, and for an etch depth of ~100 µm, 20-30 cycles at 5.33 mbar XeF_2 were needed.

3.3 Cantilever fabrication process

In this work, two main mask designs were developed. First, there are the masks for the characterization of TiO_x and PVDF cantilevers, and second, to increase the flexoelectric actuation by optimizing the top electrode design.

Mask designs

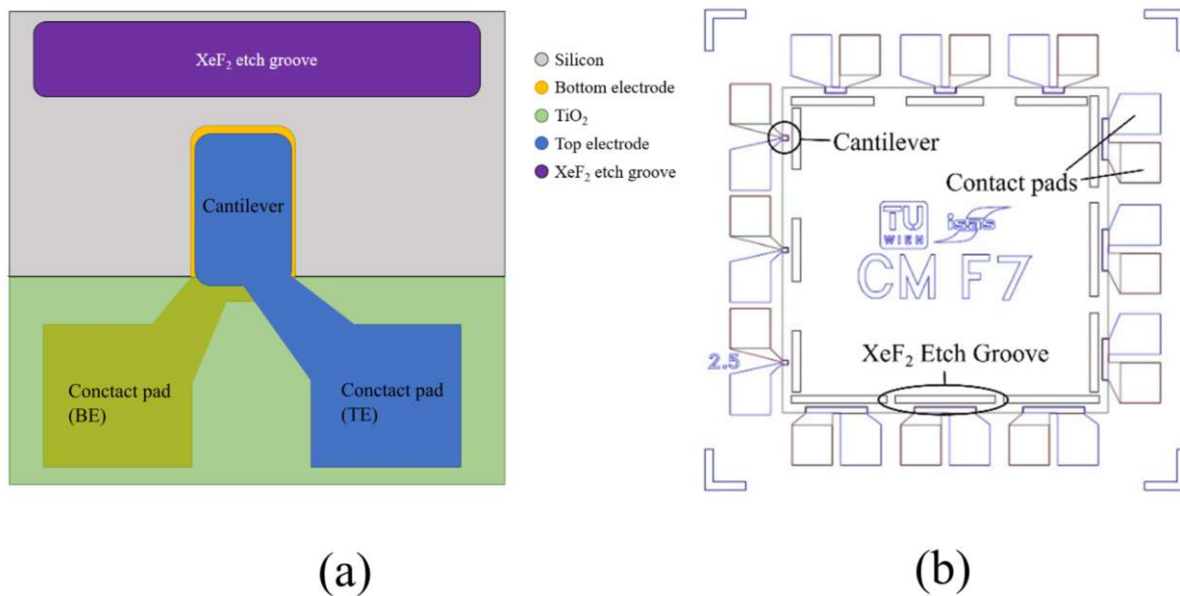

Figure 29 *Mask design to characterise the flexoelectric effect via MEMS cantilever. (a) Detailed schematic top-view on a typical cantilever design. (b) One chip of the wafer with several cantilever structures. The length of the cantilevers is 65 µm.*

The first design can be seen in *Figure 29*. This design consists of four masks, a bottom electrode (BE) lift-off mask, an RIE etch mask for the dielectric layer, a top electrode (TE) lift-off mask, and a XeF_2 etch mask. In *Figure 29 a*, important cantilever features are shown. The three most important building blocks are the cantilever, contact pads and XeF_2 etch groove. For the cantilever thickness, small dimensions are targeted as the flexoelectric is enhanced. Three different lengths were chosen such that resonance frequencies are 100/200/300 kHz, which results in the lengths of 45 µm, 65 µm and 100 µm, respectively. The values were chosen such

Die approbierte gedruckte Originalversion dieser Dissertation ist an der TU Wien Bibliothek verfügbar.
The approved original version of this doctoral thesis is available in print at TU Wien Bibliothek.
TU Bibliothek Your knowledge hub WIEN

that the structures are well measurable with the MSA, as the resonance frequency is well within the frequency range of the MSA. Additionally, the length of the cantilevers was chosen to be as short as possible, as otherwise static bends (due to thin film stress) result in an enhanced static tip deflection preventing MSA characterization. With these parameters, the mechanical behaviour of the cantilever is plate-like, meaning that two dimensions (length and width) are in a similar order of magnitude and much larger than the third (thickness).[105] This definition is in accordance with the theory of flexoelectric bending, which is based on the theory of plates.

On a single chip (shown in *Figure 29 b*), there are 12 cantilevers with four widths ranging from 45 to 500 µm. The width was varied to increase the cantilever area while having the same fundamental resonator mode. The larger area is favourable for measurements of the direct flexoelectric effect, as the area where charges are generated is also larger. In the design, the bottom electrode is wider than the top electrode to avoid lift off ridges parasitically connecting the BE and TE. Consequently, this design choice has a weakness (or strength, depending on the use case), as it was discovered that the neutral axis of the cantilever is not centric anymore. The resulting asymmetry is discussed in detail in section 4.1.

The contact pads were designed to be large enough to contact them with wafer prober needles. The feed line between the contact pad and cantilever was made as thick as possible to reduce electrical resistance. Lastly, the XeF_2 etch mask was designed with wide grooves at the front face of the cantilever, see *Figure 30 a*. Even though the XeF_2 etch of silicon is isotropic, a straight groove edge at the cantilevers' base can be achieved. If the resist is patterned to expose a wide bare silicon area, as shown in *Figure 30 a-b,* a straight groove edge in the cantilever's direction is achieved.

Die approbierte gedruckte Originalversion dieser Dissertation ist an der TU Wien Bibliothek verfügbar.
The approved original version of this doctoral thesis is available in print at TU Wien Bibliothek.
TU Wien Bibliothek Your knowledge hub

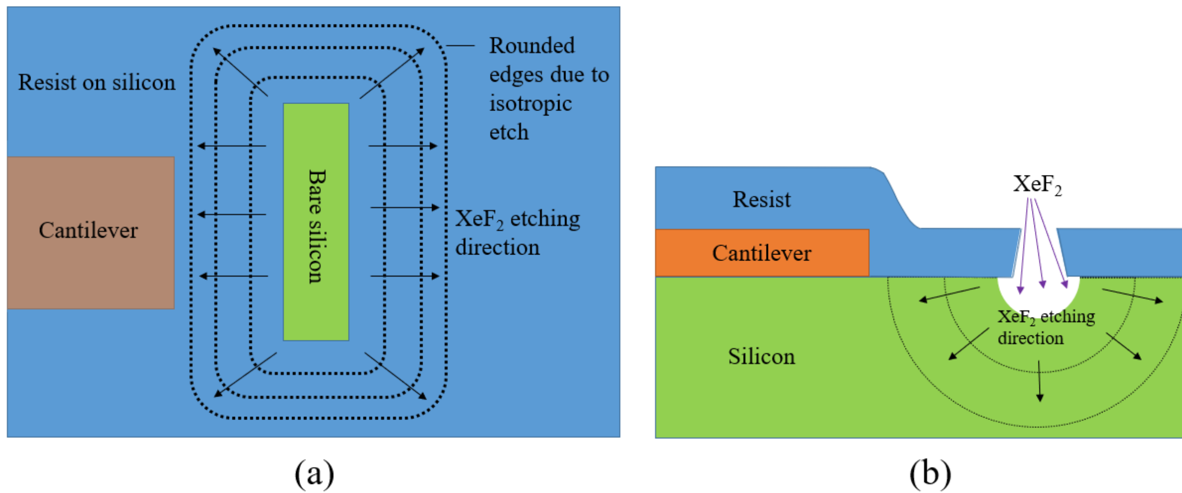

Figure 30 *Schematics of how the cantilever under-etch works. (a) Top view of a cantilever process at the XeF_2 etching step. When a long strip of resist is removed, the subsequent isotropic etch yields a straight etch. (b) Side-view of the process step. The XeF_2 comes into contact with the silicon through the removed strip of resist. The silicon is etched until the cantilever is free-standing.*

For the second design, seen in *Figure 31*, there are three main changes to the mask design. The most significant change is the top electrode design, which shows a ladder-like structure. The purpose of these structures is to increase flexoelectric actuation due to a high field gradient density. Furthermore, the electrode feed line design is changed. The smaller dimensions were designed to decrease the area where the top electrode overlaps with the edge of the bottom electrode. As shown in the lift-off chapter in section 3.2, ridges at the BE edges can lead to electrical shortcuts. With the optimized lift-off process, ridge formation can be reduced but not completely avoided. The device failure rate depends on the area of overlap where the top electrode spans over the bottom electrode edges. The newly designed smaller overlap area makes ridge formation less likely to occur in this critical region. The third change is not depicted, but the BE contact pads have a mask that allows for subsequent deposition of Cr/Au bi-layers across the whole contact pad. This additional mask is needed for wire bonding of the MEMS structure, as gold bonding directly on IrO_x is not possible.

Die approbierte gedruckte Originalversion dieser Dissertation ist an der TU Wien Bibliothek verfügbar.
The approved original version of this doctoral thesis is available in print at TU Wien Bibliothek.
TU WIEN Bibliothek Your knowledge hub

Figure 31 *Cantilever structures with ladder-like electrode design to achieve higher field gradients. Designs with decreasing ladder steps are shown from left to right. Importantly, each ladder design has the same electrode area. This figure does not show the actual positions of each cantilever design but was ordered side by side for illustration purposes.*

Die approbierte gedruckte Originalversion dieser Dissertation ist an der TU Wien Bibliothek verfügbar.
The approved original version of this doctoral thesis is available in print at TU Wien Bibliothek.
TU WIEN Bibliothek Your knowledge hub

TiO_x cantilevers

The process is shown step by step in *Figure 32*. As a substrate for the TiO_x cantilevers, undoped 4” Si wafers were used. Undoped wafers (with a bulk resistivity of >10.000 Ω·cm) were used to avoid excessive lateral leakage currents between the top and bottom electrode contact pads, as TiO_x is a relatively poor insulator. The native oxide on the Si wafer was removed with a hydrofluoric acid clean, and a subsequent ultrasonic de-ionized water rinse was performed.

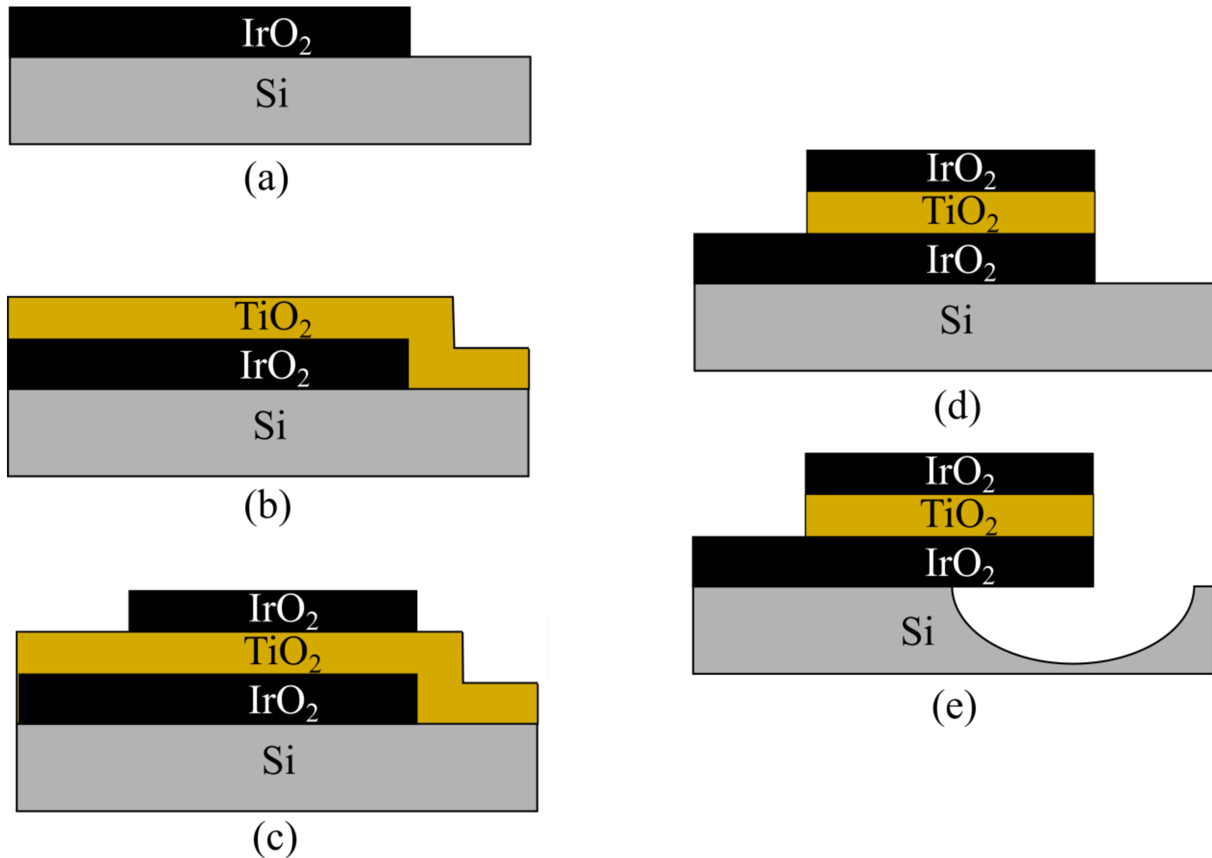

Figure 32 *Schematics of the cantilever fabrication process. a) The IrO_x bottom electrode is deposited on the wafer and patterned via lift-off. b) The wafer is covered with TiO_x. c) The IrO_x top electrode is deposited and patterned via lift-off. d) The TiO_x is patterned with an RIE etch. e) The cantilever is released by a XeF_2 etch.*

The IrO_x bottom electrode was then patterned with a lift of method. The IrO_x film itself was synthesised via reactive DC sputtering. A 4" iridium target with 99.9% purity was used. The plasma power was 500 W, and the deposition chamber back pressure was 60 µbar with a gas flow of 20/80 sccm O_2/Ar. The sputtering rate was 10 nm/s on average. With these settings, the film stress of the bottom electrode is below 100 Mpa. As a side note: When performing the resist strip, it is crucial to clean the sample with an ultrasonic DI water rinse to remove any residual debris.

Next, the TiO_x film was also deposited via reactive DC sputtering. The Ti target had a diameter of 6", and the purity was 99.995%. The plasma power was set to 800 W and the back pressure to 2 µbar. The deposition chamber gas flow was 20 sccm O_2. The sputtering rate averaged around 0.1 nm/s. The sputter values were chosen such to optimise the quality of the TiO_x films. However, these values led to a film with high tensile stress of ~1.2 GPa. The TiO_x layer was then patterned with an RIE SF_6/O_2 etch. Here a plasma power of 300 W was used with a back pressure of 150 mTorr. The etch rate averaged around 5 nm/s.

Die approbierte gedruckte Originalversion dieser Dissertation ist an der TU Wien Bibliothek verfügbar.
The approved original version of this doctoral thesis is available in print at TU Wien Bibliothek.
TU Bibliothek WIEN Your knowledge hub

The top electrode differs from the bottom electrode only in the sputter chamber back pressure, which was 80 µbar. These values were chosen such that the tensile stress of the TiO_x film was compensated.

Finally, when the top electrode is patterned, the XeF_2 etch resist is applied, and the sample is etched with a XeF_2 etch. The amount of XeF_2 cycles varied between 10 and 20 for a full release of the cantilevers. This variation in etch cycles did not affect the final length of the released cantilevers, as the under etch could be controlled by checking the size of the etch groove every three cycles via a microscope and stopping the process once the wanted under etch is achieved.

PVDF cantilevers

The PVDF cantilevers used the same masks as the TiO_x ones, but the fabrication process was different.

First, as PVDF has a lower electrical conductivity than the TiO_x, with $10^{-13}\ \Omega^{-1}cm^{-1}$ compared to $10^{-8}\ \Omega^{-1}cm^{-1}$ at room temperature respectively, using a standard p-doped 4” (100) silicon wafer was feasible.[106,107] The high resistance avoids stray capacitances and leakage currents between the contact pads of the top and bottom electrode. In a pre-step, a polymerized PVDF powder was dissolved using N,N-dimethylformamide (DMF). The weight ratio of PVDF to DMF was chosen such that the solution has a 4wt-% PVDF concentration.

After an ultrasonic clean with deionized water, the bottom electrode was fabricated and patterned by evaporating a 100 nm chromium and a 200 nm gold film and patterning it with a standard lift-off process. The chromium film is introduced as a silicon-to-gold adhesion promoter.

Next, the spin-coater chuck was placed on a hot-plate set to 170°C, as the PVDF should be cast under temperature (the reason for the elevated temperature is explained in section 3.5). The heated spin-coater chuck was inserted into the spin-coater, the wafer was fixated with a vacuum on the chuck, and the spin-coater was turned on. A slow ramp of the spin-coater revolutions per minute (RPM) was chosen. In detail, the RPM increased from 0 to 3500 in 5 s. This parameter was determined in a pre-study where the film thickness of PVDF thin films was recorded as a function of PVDF wt-% in the solution and spin-coater RPM. While the spin-coater RPM was ramping up, the PVDF-DMF solution was applied to the centre of the wafer with a dispenser

Die approbierte gedruckte Originalversion dieser Dissertation ist an der TU Wien Bibliothek verfügbar.
The approved original version of this doctoral thesis is available in print at TU Wien Bibliothek.
TU WIEN Bibliothek Your knowledge hub

syringe. As the film thickness is not dependent on the volume of the applied polymer solution, the maximum dispenser volume was chosen to 10 ml. The spin coater RPM was held for approximately 1 minute before turning off. The wafer was then placed on a hot-plate at 170°C for 2 hours to effuse any remaining solvent. The final film thicknesses averaged around 200 nm.

Next, the whole wafer is covered with 200 nm gold via evaporation. Standard lithography with the top electrode mask was done, and the wafer was submerged in potassium iodide for 2 minutes to etch the gold. At this step, the PVDF patterning is still missing. The deposited gold top electrode was used instead of a resist for PVDF patterning. Next, the wafer is exposed to an O_2 plasma in an STS 320 PC at 300 W for 1 minute. As a side note, the etch rate of PVDF in O_2 plasma is very high, and power and exposure time need to be tuned carefully to avoid device failures.

The cantilever was released from the substrate in a XeF_2 etching step, like the TiO_x cantilevers. At this stage, the cantilevers showed a static bend, which is not wanted in the final device. This static bend is predominantly due to the high stress in the chromium layer. Therefore, in the final step, the chromium was removed from the areas exposed to the air, mainly the bottom side of the free-standing part of the cantilever, eliminating the static bend.

3.4 Measurement methods

Laser interferometry

Laser vibrometry is a vital characterization tool for MEMS, as it can capture and record the dynamics (i.e. mode shape, displacements) down to the picometre range over time.[108] Laser vibrometers generally use the principle of laser interferometry, where the superposition of two coherent laser beams results in a fringe pattern. This fringe pattern comes from the cross term of the measured intensity $I_{E,ges} = \langle E \rangle^2$ of two superposed sinusoidal electric fields $E_{1,2}(x,t)$ with different path lengths L_1, L_2:

Die approbierte gedruckte Originalversion dieser Dissertation ist an der TU Wien Bibliothek verfügbar.
The approved original version of this doctoral thesis is available in print at TU Wien Bibliothek.
TU Bibliothek WIEN Your knowledge hub

$$E_i(x,t) = E_{0,i}\cos(\omega_i t - k_i x)$$

$$I_{E,ges} = I_{E,0}\, cos^2(k(L_1 - L_2)) \tag{43}$$

Where x is a cartesian coordinate, t the time, k is the wavenumber, ω the circular frequency, $E_{0,i}$ the electric field amplitude and $I_{E,0}$ the resulting field intensity amplitude. Looking at $I_{E,ges}$, the superimposed electric fields have an intensity function proportional to $\cos^2(\Delta L)$, giving the fringe pattern that is dependent on the difference in optical path length.

Laser-Doppler vibrometry

The laser Doppler vibrometry (LDV) approach is most prominent in the laser vibrometry methods. With normal laser vibrometry, the resolution is limited by the minimally achievable wavelength and the maximally possible optical path length difference. Achieving a picometre resolution with nanometre wavelength is challenging to achieve. With the LDV, picometre amplitude resolution and high-frequency ranges up to single-digit GHz can be typically achieved.[109] A typical LDV setup is depicted in *Figure 33*.

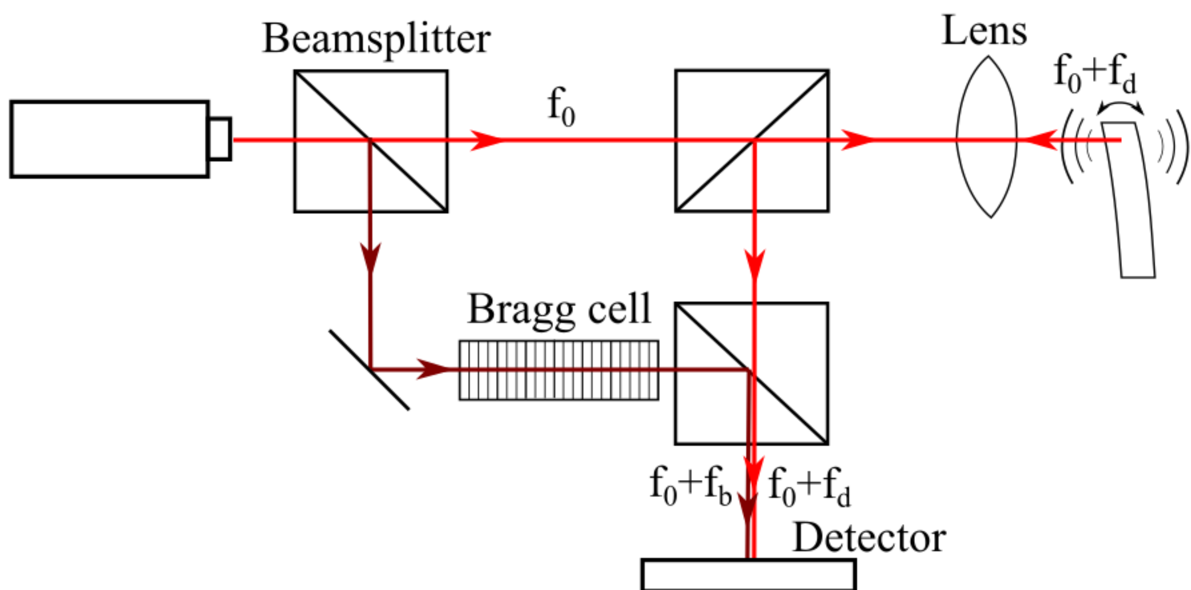

Figure 33 *Schematics of a laser Doppler vibrometry setup. It consists of a laser source split up by a beam splitter, where one optical path passes through a Bragg cell, and the other passes through a lens to focus on the sample. Both laser beams are superimposed, and a detector reads the corresponding interference pattern.*

The fundamental principle of the LDV is the Doppler effect, which describes the frequency shift $\Delta f(t)$ of a wave source when being in relative movement $\Delta v(t)$ to an observer.

Die approbierte gedruckte Originalversion dieser Dissertation ist an der TU Wien Bibliothek verfügbar.
The approved original version of this doctoral thesis is available in print at TU Wien Bibliothek.
TU Bibliothek WIEN Your knowledge hub

$$\Delta f(t) = \frac{\Delta v(t)}{c} f_0 \tag{44}$$

Here c is the speed of the wave in the medium, which for an electromagnetic wave is the speed of light in the corresponding medium.

This frequency shift can then be used to measure the velocity of an object. In detail, for the LDV, there is a laser source with frequency f_0, which gets first split up into two optical paths. One arm is the sample beam, and the other is used as a reference to obtain this superimposed fringe pattern. The sample beam exhibits a frequency shift f_d compared to the reference beam due to the Doppler effect, having a sum frequency of f_0+f_d. From the acquired superposed intensity profile, the velocity can be directly calculated. As the fringe pattern is the same for objects moving towards or away from the LDV, a Bragg cell is added to the reference beam. Now, the reference beam frequency is typically shifted by 40 MHz (but the shift can go up to 300 MHz) and is breaking this symmetry. The direction can now be determined, as the fringe patterns are now distinct in each direction.[110,111]

In this work, an LDV from Polytec is used. The equipment is called a microsystems analyser (MSA), where both MSA 400 and MSA 500 systems were used to characterize the cantilevered structures.

Thermal calibration

The thermal calibration method is used to determine the Young's modulus of the fabricated cantilevers. Every cantilever has a specific mechanical resonance frequency. At temperatures above 0 K, any object or particle, such as atoms forming the cantilever or the surrounding atmosphere have a certain kinetic energy due to the ambient temperature. The movement of the atoms creates a motion in the cantilever, effectively described as an applied load with a power spectral density approximated constant across the frequency (white noise).[112] A white noise excitation leads to the excitation of the cantilever in its resonances, which can, in turn, be seen in a Fourier-transformed amplitude measurement. The resulting thermally excited resonance spectrum of the cantilever can be described with the following formula:[113]

Die approbierte gedruckte Originalversion dieser Dissertation ist an der TU Wien Bibliothek verfügbar.
The approved original version of this doctoral thesis is available in print at TU Wien Bibliothek.
TU Bibliothek WIEN Your knowledge hub

$$\frac{\delta^2(f)}{\Delta f} = \frac{2\,k_B T}{\pi\,Q\,f_0\,\kappa}\frac{1}{[1-(f/f_0)^2]^2+(f/f_0 Q)^2} \tag{45}$$

Where κ is the spring constant, δ is the deflection amplitude of the cantilever at the tip, Δf is the spectral resolution, k_B is the Boltzmann constant, T the temperature in Kelvin, Q the quality factor and f_0 the resonance frequency. It has to be noted that the latter formula is only applicable to cantilever structures. This equation can be fitted concerning the spring constant and the Q-factor. With a simple harmonic oscillator model, the Young's modulus E_{mod} can then be calculated:[114]

$$\kappa = \frac{3\,E_{mod}\,b\,h^3}{12\,l^3} \Rightarrow E_{mod} = \frac{4\,\kappa\,l^3}{b\,h^3} \tag{46}$$

Where h is the total thickness, l the length and b the width of the cantilever. The Young's modulus determination is straightforward for cantilevers made from a single material. For a cantilever consisting of multiple layers of different materials, the method results in a weighted averaged E_{mod}, which we call effective Young's modulus E_{eff} in this work. The weighted average E_{eff} is calculated as follows:

$$E_{eff} = \frac{\sum_{i=1}^{n} h_i\,E_{mod,i}}{\sum_{i=1}^{n} h_i} \tag{47}$$

Where the index i denotes the layer number and n the total number of layers.

Spectral acquisition and lock-in measurements

Using the MSA, there are two methods to measure the resonance spectrum of a cantilever. The first is to apply a frequency signal with a wide bandwidth and measure the mechanical amplitude spectrum. There are different characteristic signal types, like white noise or a periodic chirp. For this work, the periodic chirp was used. The chirp signal features a pure sine tone with constant amplitude and linearly increasing frequency over time, thus covering a predefined frequency range. When the maximum frequency is reached, the chirp periodically restarts from the starting frequency.

For more precise measurements, a lock-in amplifier can be used as the signal-to-noise ratio is increased. The excitation signal (pure sine tone) is generated using the Zurich HF2LI lock-in amplifier, and the measurement signal from the LDV modulated by the velocity of the

Die approbierte gedruckte Originalversion dieser Dissertation ist an der TU Wien Bibliothek verfügbar.
The approved original version of this doctoral thesis is available in print at TU Wien Bibliothek.
TU WIEN Bibliothek Your knowledge hub

cantilever surface is fed into the input of the lock-in amplifier. The frequency of the sine tone is swept across a defined frequency range, and the input signal is demodulated at multiples of that frequency. With this approach, the first and second harmonics can be measured by demodulating the measurement signal at both single and double values of the excitation frequency. Measuring the first and second harmonics separately is recommended to distinguish between the linear and the quadratic electromechanical mechanisms, as explained in section 2.4.

Extracting the curvature

The curvature calculation scheme is the following. First, the cantilever tip deflection is measured under sinusoidal electrical excitation ($E_{ex}(t) \propto sin(ft)$) in a raster grid by the MSA, as shown in *Figure 34 a*. The surface of maximum deflection in the time-dependent signal is taken to calculate the curvature. The MSA surface scan is separated into several line scans along the x-direction, equally spaced across its width. For small deflections, the curvature can then be approximated by the second derivative of the deflection with respect to the *x*-coordinate.

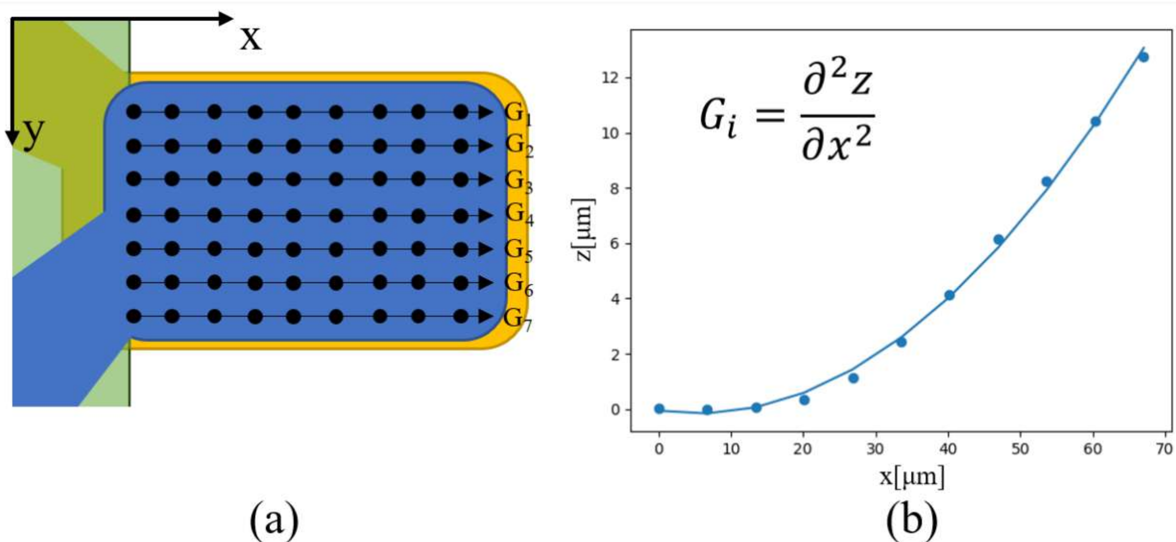

Figure 34 *(a) Schematics of the raster principle and the calculation scheme. Black dots denote one MSA measurement at that position on the cantilever. Lines are scanned, and each line in the x direction gives one curvature value, G_i. (b) Deflection along the x-direction of one line on a cantilever, as measured by the MSA. Here the measurement is fitted with a 2nd-order polynomial.*

This work used two methods to calculate the curvature from the measurement data. One method is to fit the line scans with a 2nd-order polynomial $z = a + b\,x + c\,x^2$ (see *Figure 34 b*). The polynomial's 2nd derivative (curvature) gives the constant $2 \cdot c$.

Die approbierte gedruckte Originalversion dieser Dissertation ist an der TU Wien Bibliothek verfügbar.
The approved original version of this doctoral thesis is available in print at TU Wien Bibliothek.
TU WIEN Bibliothek Your knowledge hub

In the other method, we calculate the curvature numerically from the second derivative:

$$G_i = \frac{z(x_{i+1}) + 2\, z(x_i) - z(x_{i-1})}{(x_{i+1} - x_i)^2} \quad (48)$$

Figure 35 shows a cantilever measurement with the indexing used for the calculation. The maximum curvature of a line (along x) is then averaged over the lines corresponding to a line number along the y coordinate. Finally, the curvature values of the different line scans are averaged. The error in the curvature between different lines is below 1%.

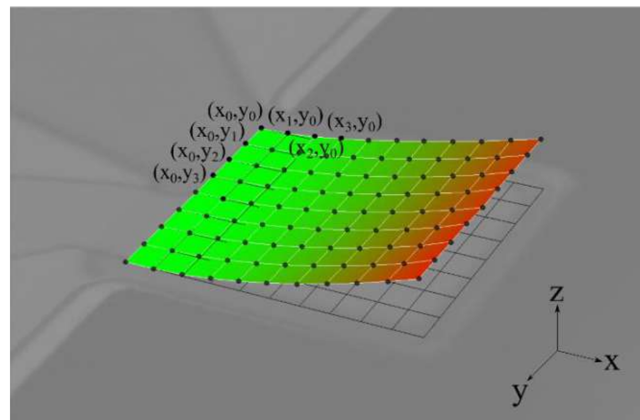

Figure 35 *A MSA surface scan of a sinusoidally excited cantilever. Each dot of the surface represents the maximum measured deflection. The method of indexing is shown in brackets next to the respective dots.*

Both methods have advantages and disadvantages. The numerical method is the more accurate, as it correctly reflects the measured deflection values. However, if the measurement is noisy or the data are scattered, the curvature values can vary significantly within one cantilever. The fitting method is the better choice for measurements exhibiting a higher noise floor, as a fit can be found, which varies less than 1 % between each line across the cantilever.

In principle, a circular segment can also be fitted in the region of highest deflection:

$$z(x) = \sqrt{r^2 - x} - r_0 \quad (49)$$

Where r is the radius and r_0 is the centre of the circle. However, as the fitting region is close to the anchor of the cantilever, $x \approx 0$, and as such:

Die approbierte gedruckte Originalversion dieser Dissertation ist an der TU Wien Bibliothek verfügbar.
The approved original version of this doctoral thesis is available in print at TU Wien Bibliothek.
TU Bibliothek WIEN Your knowledge hub

$$z(x) \approx r + r_0 - \frac{1}{r}x^2 + ..$$ (50)

Which is a polynomial of degree 2 and, therefore, should not yield a different result than the 2nd-order polynomial fit.

Impedance measurement

The real and imaginary parts of the electrical impedance can be used to calculate various electric parameters. The impedance is gained by applying a sine wave voltage across the device and measuring the current and the current/voltage (*J/V*) phase shift.

For this work, the most important electrical parameters are the capacitance and the loss angle, which are related to the permittivity and the electrical losses, respectively. The permittivity is especially important for this work (see section 2.3), which is why this method was employed extensively. To calculate the capacitance from the impedance, the electrical equivalent circuit of the tested device must be known. For a perfect capacitance, the impedance is $Z_C = 1/i\omega C$, where Z_C is the impedance, i is the imaginary number, ω the angular frequency and C the capacitance. This relationship is only valid if the capacitor exhibits an infinitely high resistive impedance ($Z_R = R_p = \infty$), so the current only flows through the capacitive equivalent circuit element.

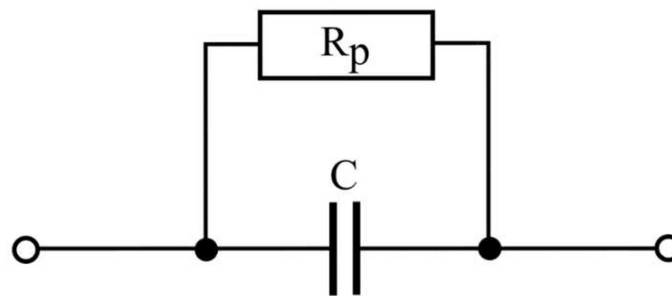

***Figure 36** The equivalent circuit of a capacitor with a leaky insulator is a resistance R_p parallel to the capacitance C.*

For real capacitors, Z_R has a finite value and has to be included and hence

$$Z = \frac{1}{{}^{1}/_{R_p} + i\omega C}$$ (51)

Die approbierte gedruckte Originalversion dieser Dissertation ist an der TU Wien Bibliothek verfügbar.
The approved original version of this doctoral thesis is available in print at TU Wien Bibliothek.
TU WIEN Bibliothek Your knowledge hub

From the capacitance, the permittivity can be calculated with the equation for a parallel plate capacitor as described in *equation 3*.

A Hioki IM3533 LCR meter and an Agilent Precision Impedance Analyzer 4294A were used for this work. With the latter, the impedance spectrum with respect to excitation signal amplitude and DC-bias was determined. The Hioki was used for low-frequency measurements (< 300 kHz), whereas the Agilent was used for DC-Bias measurements and high-frequency measurements (> 300 kHz).

Leakage current setup

To measure leakage currents of capacitors, two methods can be used. For the first method, a voltage is applied to the capacitor, while the current is measured with an ampere meter in series. In the second method, a voltmeter is used in parallel with a resistor, which is then connected in series to the capacitor and a voltage is applied. For the low capacitance capacitors (<1 µF) used in this thesis, the first method is more suitable, as such capacitors have very low leakage currents, and ampere meters offer the needed high precision. In addition to the ampere measuring precision, the ampere meter also offers a high measurable range from femtoampere to ampere. The source of modern ampere meters also has a high resolution down to nanovolt. In this thesis, a Keysight B2911A precision SMU was used, which features 10 fA current and 100 nV voltage resolutions.

To get the most accurate measurement, any other sources of leakage currents, such as induced from external radiation, must be reduced to a minimum. Additional leakage currents can also arise from the measurement set-up. To get the best possible results, following setup was realized. The measurement setup consists of a wafer probe station (Süss PM8 in our case), two 3-axis micrometre manipulators, wolfram needles to contact the samples and cables connecting the needles to the source measuring unit (SMU). The wafer prober station consists of a platform for the needles, which are attached to the 3-axis manipulators, a heat-able sample chuck with vacuum-based sample fixation and a microscope for precise contacting of the needles, which are electrically isolated to the tip. A schematic of the electrical wiring within the measurement setup is shown in *Figure 37*.

Die approbierte gedruckte Originalversion dieser Dissertation ist an der TU Wien Bibliothek verfügbar.
The approved original version of this doctoral thesis is available in print at TU Wien Bibliothek.
TU Bibliothek WIEN Your knowledge hub

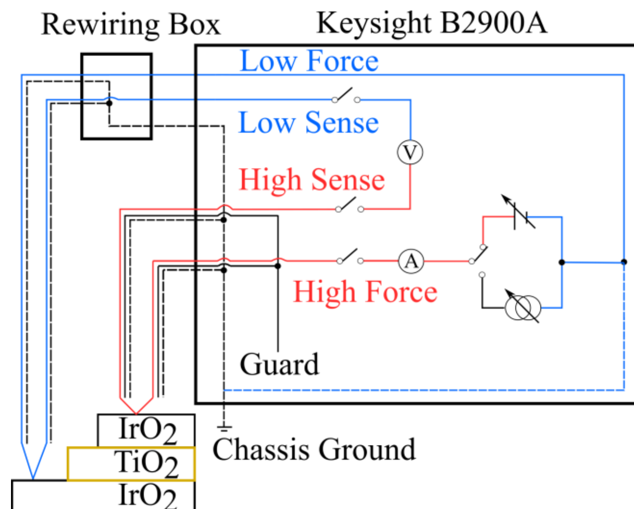

Figure 37 *Schematic of the measurement setup. For the low force/sense, biaxial cables and for the more precise high force/sense, triaxial cables were used. The dashed lines indicate grounded wires.*

The largest source of parasitic leakage current comes from the cables connecting the SMU with the needles. If, for example, coaxial cables are used, there is a potential difference between the outer shield and the inner core, which is prone to leakage currents through the cable insulation, increasing the total leakage current level. This error can be minimized by using triaxial cables, which have an additional guard. The guard is kept at the same voltage level as the core; thus, no parasitic leakage currents are created between the guard and the shield.

Measurements, where the voltage is cycled stepwise and the current is measured at each voltage step is called cyclic voltammetry. This method was mainly used for the measurements in this thesis. A python script was written to enable a software-based data read-out of the leakage current measurements. With this program, the number of voltage steps V_{step}, voltage step time t_{step} and the number of measurement points at each voltage step can be defined, as shown in *Figure 38*.

Die approbierte gedruckte Originalversion dieser Dissertation ist an der TU Wien Bibliothek verfügbar.
The approved original version of this doctoral thesis is available in print at TU Wien Bibliothek.
TU WIEN Bibliothek Your knowledge hub

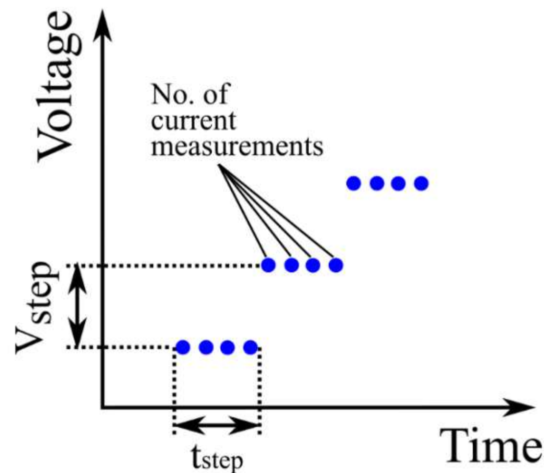

Figure 38 Current/voltage measurement scheme. Shown are the current measurements (one blue dot represents one measurement) with respect to voltage level over time.

Additionally, the temperature can be controlled via a heat-able sample chuck between room temperature and 300°C in air.

X-ray diffraction

X-ray diffraction is a powerful tool that can measure a solid's crystal structure.[115] The principle is based on Bragg scattering of X-rays at the crystal lattice. X-rays scattered at different crystal lattice planes can have coherent or incoherent interference, dependent on the lattice plane spacing, the wavelength and the incoming angle of the incident beam.

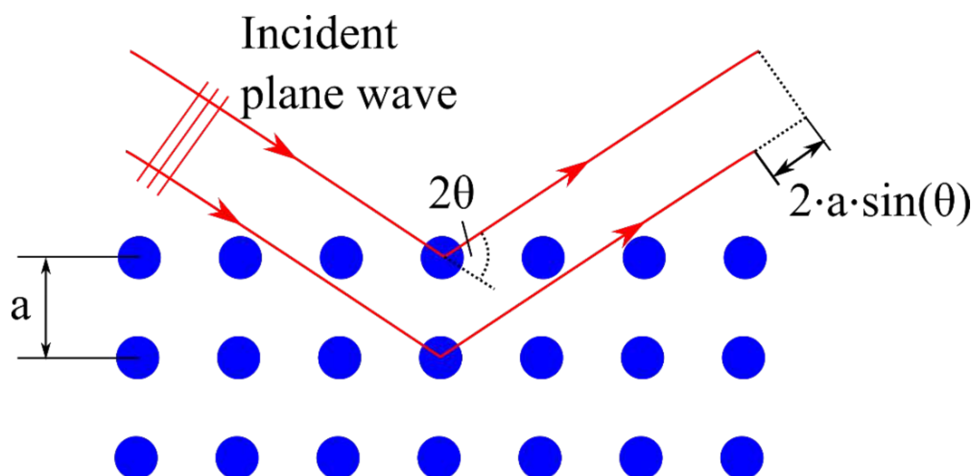

Figure 39 Schematic illustration for Bragg's law. Depending on the incident beam angle, lattice constant and wavelength, constructive or deconstructive interference patterns are obtained and are defined by Bragg's law.

Die approbierte gedruckte Originalversion dieser Dissertation ist an der TU Wien Bibliothek verfügbar.
The approved original version of this doctoral thesis is available in print at TU Wien Bibliothek.
TU Bibliothek Your knowledge hub WIEN

This means that the X-rays scatter at specific angles, schematically shown in *Figure 39*. The Bragg law is given as follows:

$$2\,a\sin(\theta) = n\,\lambda \tag{52}$$

Where θ is the angle of the incoming x-ray, n is a natural number, λ is the wavelength of the X-rays, and a is the lattice constant. For the actual XRD measurements, a 2θ scan is performed to see the different lattice spacings. For polycrystalline samples, the resulting 2θ scan has a broader peak (meaning higher angular distribution and lower total intensities than a single crystal), due to the wider variety of orientations of the grains.

There are several XRD methods, but one used in this work is the grazing incidence XRD (GIXRD). With this method, the angle of the incoming X-rays is very shallow, almost parallel to the sample surface, hence grazing incidence. The shallow angle is advantageous for thin films, as the penetration depth of the X-rays is much lower, and the influence of the substrate signal does not obscure the thin film signal.

The XRD method proved helpful in the identification of crystalline phases and the degree of crystallinity for the IrO_x, TiO_x and PVDF films for the various fabrication methods and parameters. These analyses were performed with a PANalytical XPert Pro MPD. As a source for the X-rays, a Cu Kα anode with a wavelength of λ=1.540 Å was used. The angular step size of the goniometer was set to $\Delta 2\theta$ = 0,001°. The divergence slit was set to 0.76mm.

Atomic force microscopy

Atomic force microscopy (AFM) is a technique to characterize the topography of a given sample.[116] In principle, a cantilever with a sharp tip with a radius in the nanometre range is brought close to the surface. Van-der-Waals forces, dipole interactions and electrostatic forces of the surface then act on the cantilever by deflecting it. A laser scanning system is used to measure the tip deflection, which is fed into a phase-locked loop, thus keeping, for example, in the contact mode, the distance from the AFM needle to the sample surface constant. The resulting control signal from the phase-locked loop gives information about the topography.

Die approbierte gedruckte Originalversion dieser Dissertation ist an der TU Wien Bibliothek verfügbar.
The approved original version of this doctoral thesis is available in print at TU Wien Bibliothek.
TU WIEN Bibliothek Your knowledge hub

There are different modes in which the AFM can be used, mainly the contact, non-contact and tapping modes. In contact mode, the AFM tip is in contact with the surface and then scanned across the surface. While rastering the surface, the tip deflection is measured. The disadvantages of this method are tip and sample degradation due to the acting forces, also called sticking. Even more, soft samples, like biological ones, are typically damaged with this method.

In non-contact mode, the cantilever is brought into resonance by either an external piezo or integrated piezoelectric transducer on the cantilever. When the resonating cantilever is near the sample's surface, the resonance frequency changes. A closed-loop feedback keeps the resonance frequency constant by changing the distance to the sample. This results in a topography image without damaging the sample or the tip; therefore, soft samples can also be measured. However, if the resonance shift is not measured correctly, the cantilever tip could be too close to the sample, thus being attracted to the surface by the Van-der-Waals forces and subsequently getting damaged by the surface. Therefore, this mode is favourably used in vacuum, as resonance shifts can be measured more precisely due to greater deflection amplitudes.

The third mode, the tapping mode, is a mixture between the contact and non-contact mode. Here a cantilever is brought into resonance, and the amplitude and frequency are kept constant. The tip then is only tapping the surface once each oscillation cycle, which combines the advantages of the contact and non-contact mode by reducing the strength of lateral forces on the sample and tip while solving the sticking problem.[117]

A Bruker Dimension Edge AFM was used in tapping mode with NCHV-A type cantilevers to characterize the PVDF's morphology and measure the roughness of the various materials used in this work. The PID controller values varied between individual samples and cantilevers. The P_{PID} value varied between 10 and 20 while the I_{PID} value varied between 0.5 and 2.

Fourier-transformed infrared spectroscopy

Fourier-transformed infrared spectroscopy (FTIR) is a method to determine the composition of chemical bonds of a material.[118] In principle, the vibrational energies of molecules are measured with the FTIR method. Here the spring-like behaviour of molecular bonds leads to

Die approbierte gedruckte Originalversion dieser Dissertation ist an der TU Wien Bibliothek verfügbar.
The approved original version of this doctoral thesis is available in print at TU Wien Bibliothek.
TU WIEN Bibliothek Your knowledge hub

mechanical eigenfrequencies, which can absorb an electromagnetic field with the same frequency as the given vibrational eigenfrequency.

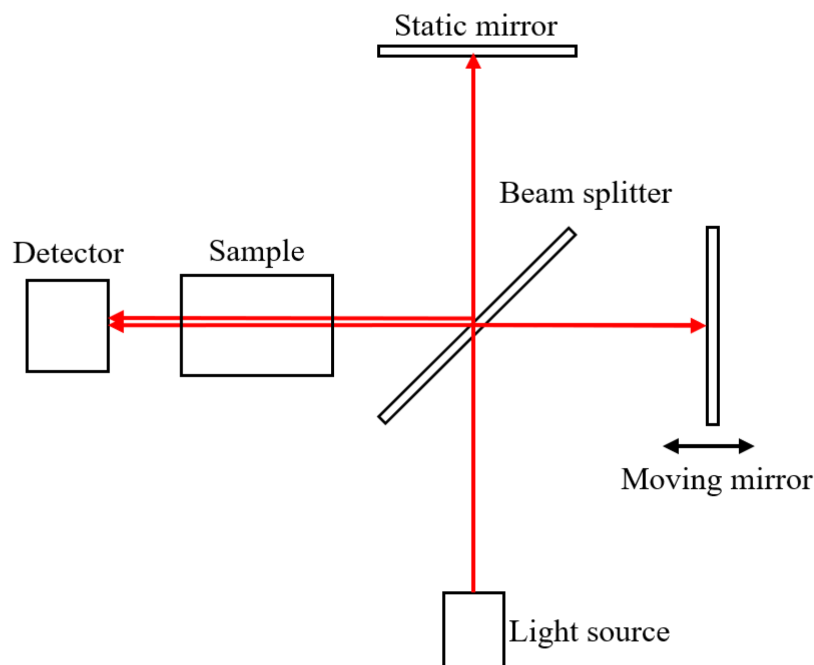

Figure 40 *The light path shown schematically for an FTIR. The light exits the light sources and passes a beam splitter. At the splitter, the light is split into a path to a static mirror and another to a moving mirror. Due to the beam splitter properties, both light paths overlap and point to the detector. Before reaching the detector, the light passes through the sample, where specific wavelengths are absorbed.*

The sample is exposed to a broadband infrared light source in the FTIR. A Michelson-Interferometer is between the source and the sample, as shown in *Figure 40*. This Michelson-Interferometer splits the source light into two paths, where one path can change the length (for example, the mirror can be moved with a one-axial stepper motor), and the other is fixed. Then the two light paths are superimposed and pass through the sample onto a detector. The detector then sees an interferometric fringe pattern. The movable arm changes its path length, and then through a Fourier transformation from the real space to the wavenumber space, an FTIR spectrum is obtained. The wavenumber resolution linearly depends on the individual step size the movable arm can travel. As the molecules absorb some energy of the source emission, a drop in light intensity at the rovibrational frequencies is observed. From this absorption pattern, the composition of the sample can be identified.

The FTIR method is limited to samples which do not entirely absorb or reflect the source light; metals, for example, cannot be characterized with this method. In this work, FTIR proved

Die approbierte gedruckte Originalversion dieser Dissertation ist an der TU Wien Bibliothek verfügbar.
The approved original version of this doctoral thesis is available in print at TU Wien Bibliothek.
TU Bibliothek WIEN Your knowledge hub

helpful in characterising the PVDF samples' microstructure. A Bruker Tensor 27 FTIR spectrometer was used with the accuracy set to 4 cm^{-1} and the detector was at room temperature. For each measurement, the background was measured first (i.e. the measurement was performed without a sample) and then subtracted from the sample measurement to filter out the spectrum of elements that are present in the atmosphere, like water or CO_2.

Scanning electron microscope

With the scanning electron microscope (SEM), surface features of the sample can be depicted down to scales of 10^{ths} of nanometres.[119] Compared to AFM, the SEM technique offers larger scanning areas to analyse *e.g.* the whole MEMS device. In addition, sample composition can be obtained with an energy-dispersive x-ray spectroscope (EDX). Generally, for SEM operation, electrons are accelerated and focused onto the sample surface. A compact description is given in the following.

For this work, a tungsten wire for field electron (FE) emission was used as an electron source. Field emission describes the emission of electrons from a solid due to a high electric field, giving the electrons more energy than the work function of the solid. A high electric field between a tungsten wire and the sample holder is applied for an FE-SEM, high enough to emit electrons. These electrons are then focused on the sample with electromagnetic lenses. When the electrons hit the sample, they interact with it and produce secondary electrons, back-scattered electrons, characteristic x-rays, cathodoluminescence, absorption current and transmitted electrons (only for very thin samples in the nanometer thickness range). These effects happen in different areas in the sample and are shown in *Figure 41*. The teardrop-shaped interaction volume of the electrons with the sample depends on the acceleration voltage and the sample composition and is generally in the range of several µm.

TU Bibliothek WIEN Your knowledge hub
Die approbierte gedruckte Originalversion dieser Dissertation ist an der TU Wien Bibliothek verfügbar.
The approved original version of this doctoral thesis is available in print at TU Wien Bibliothek.

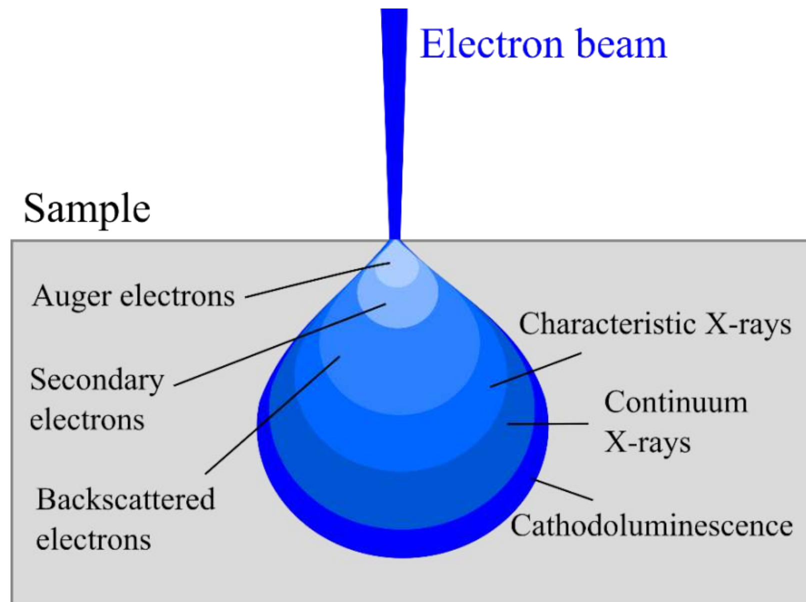

***Figure 41** Schematic of the different effects when an electron beam is focused on a sample. The scale of the bulb shape is several micrometres and depends predominantly on the electron acceleration voltage.*

In a typical SEM, secondary electrons are recorded for imaging. They have comparatively low energy (below 50 eV) and can, therefore, only travel a small distance in the sample before they are either ejected from the surface or absorbed. This means that only electrons from the surface (in a depth of a few nanometres from the surface) can escape and reach the detector, making this technique very surface sensitive.

The chemical composition of a sample can also be measured with the SEM. Here, the characteristic X-rays, as shown in *Figure 41*, are often measured with an energy-dispersive X-ray spectroscopy (EDX) sensor. The measured characteristic X-rays originate from the interaction of primary electrons with the sample atoms. A core hole is produced when the incoming electron knocks an electron out of the atom's inner orbital shell. Another higher-energy electron immediately fills this energy level. The resulting loss in energy for the electron hopping down from a higher energy state results in an emitted X-ray. This interaction happens at depths of several micrometres in the sample. When the thin film to be measured is thinner than several micrometres, the obtained EDX spectrum contains information on layers beneath the topmost layer and the substrate. This poor resolution, especially in depth, can make the analysis of e.g. the local oxygen concentration problematic.

For this work, the SEM was used to image the MEMS structures and observe cross-sections of the structures. It proved vital in understanding the origin of most device failures. The scanning

Die approbierte gedruckte Originalversion dieser Dissertation ist an der TU Wien Bibliothek verfügbar.
The approved original version of this doctoral thesis is available in print at TU Wien Bibliothek.
TU WIEN Bibliothek Your knowledge hub

electron microscopy (SEM) micrographs were recorded with a Hitachi SU8000 at acceleration voltages in the range from 2 to15 kV.

Transmission electron microscope

With the transmission electron microscope (TEM), nanometre scale sample imaging is possible, and with modern TEMs, even atomic scale resolution can also be reached.[120] The basic structure of a TEM microscope is very similar to an SEM. There is an electron gun, electromagnetic lenses, and various detectors. The fundamental difference is that the transmitted electrons are analysed in a TEM after passing through the sample. For this method to work, the samples must be thin enough for electrons to pass through. In the best case, the sample thickness where the electron beam passes through is only several atomic layers thick. Such thin layers can be achieved by *e.g.* ion milling of the sample. When electrons pass through the sample, they can be reflected, absorbed, or transmitted. There are several imaging modes, such as bright-field imaging, dark-field imaging, diffraction imaging or convergent beam electron diffraction. The most common one, and the one that was used in this work, is the bright-field imaging mode. In this mode, the electrons that pass through the sample non-scattered are recorded. Regions where electrons have a low absorption rate appear brighter in the recorded picture, and regions where electrons are more likely to be absorbed, appear darker.

The electrons that pass through can also be characterized with an electron energy-loss spectrometer (EELS). Here the electrons are fired from the electron gun with a narrow range in kinetic energy, and the energy loss of the electrons when passing through the sample is measured. The electrons are more likely to be absorbed at specific energies, as those energies correspond to different excitations. These can be core-shell excitations, band transitions, phonon excitations, plasmon excitations or Cherenkov radiation, where core-shell excitations are mainly used for recording the chemical composition.

In this work, the TEM, in combination with EELS, was used to analyse the oxygen vacancy distribution in the TiO_x using a TECNAI TF20 (scanning) transmission electron microscope (S/TEM) operated at 200 keV and the electron beam was converged to a diameter of 0.15 nm.

Die approbierte gedruckte Originalversion dieser Dissertation ist an der TU Wien Bibliothek verfügbar.
The approved original version of this doctoral thesis is available in print at TU Wien Bibliothek.
TU Bibliothek WIEN Your knowledge hub

X-ray photoelectron spectroscopy

X-ray photoelectron spectroscopy (XPS) is based on the photoelectric effect; a schematic of the equipment is shown in *Figure 42*. This method is used to determine the spectrum of binding energies of electrons exciting the surface of a sample due to the photoelectric effect. The resulting spectrum determines which chemical composition is present at the sample's surface.

To do so, a sample is exposed to high-energy photons. When the energy of the photons is high enough, shell electrons of the sample atoms can escape the ion core potential. The escaping electrons are most often measured with a hemispherical electron energy analyser.[121]

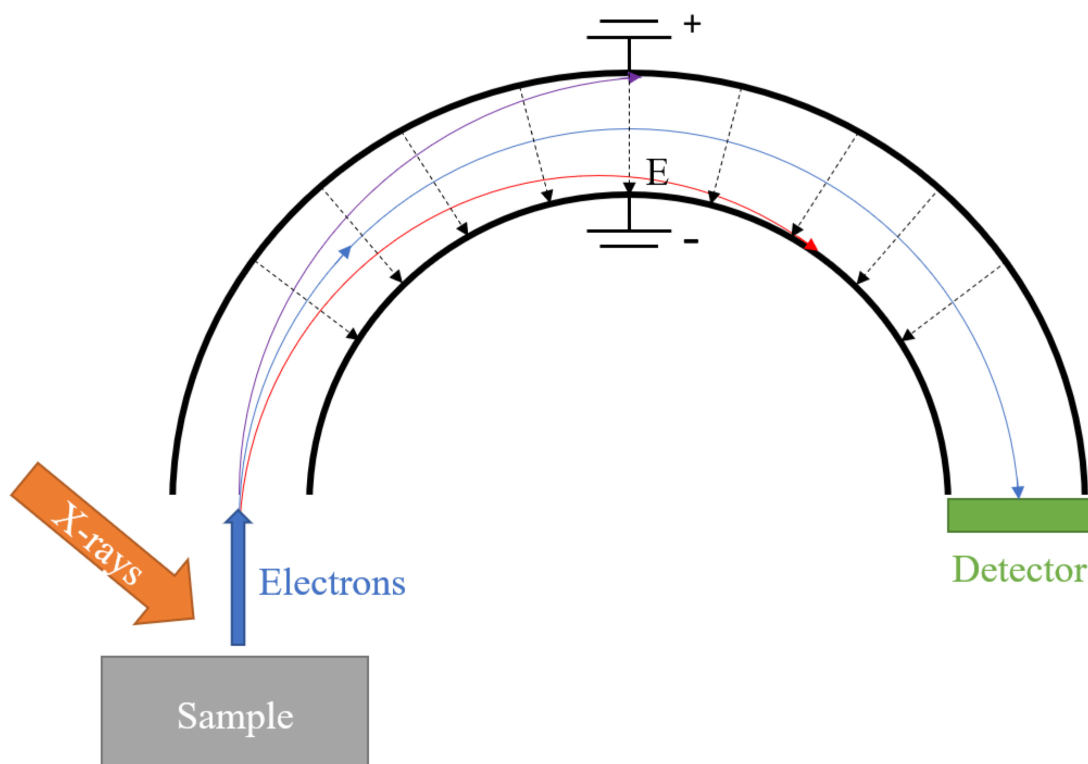

Figure 42 *Schematics of the XPS measurement. X-rays are accelerated onto a sample surface. Subsequently, electrons are ejected and deflected by the electrostatic force (dotted arrows) of the hemispherical electron energy analyser. The resulting trajectory of the electrons is dependent on the electron's velocity. Three different velocities are shown schematically with red, blue, and purple paths. Only electrons within a certain velocity window (in this case only the blue one) arrive at the detector. The velocity determines the electron's kinetic energy. By changing the amplitude of the electric field, the velocity window can be changed.*

The hemispherical electron energy analyser is essentially a hemispherical plate capacitor with a defined voltage across the hemispheres. Electrons with different velocities have different

Die approbierte gedruckte Originalversion dieser Dissertation ist an der TU Wien Bibliothek verfügbar.
The approved original version of this doctoral thesis is available in print at TU Wien Bibliothek.
TU Bibliothek WIEN Your knowledge hub

trajectories through the hemispherical capacitor due to the constant deflection of the electrostatic force F_E:

$$\vec{F}_E = q\vec{E} \tag{53}$$

Where q is the elementary charge, E the electric field. Since the gap between the two hemispheres is narrow, only electrons within a narrow velocity window will pass through the hemispherical analyser. Faster or slower electrons will hit the walls of the analyser, essentially acting as a velocity filter. This filter window can be swept by changing the electric field amplitude and therefore the kinetic energy spectrum can be determined. Equating the energy of the X-ray (*XE*) to the kinetic energy (*KE*) of the exiting electron plus the binding energy (*BE*) plus a spectrometer work function ($\varphi_{spec,}$ which is an apparatus-dependent known constant) yields the binding energy:[122]

$$BE = KE - XE + \varphi_{spec} \tag{54}$$

Measuring the binding energy has the advantage that the chemical environment of an atom is included. For example, the binding energy of an electron in the oxygen 1s shell is different in a TiO_2 configuration compared to TiO.

The surface composition of the samples in this thesis was measured in an ultra-high vacuum with an AXIS Supra photoelectron spectrometer (Kratos Analytical Ltd., UK) equipped with a hemispherical analyser and monochromatic AlKα X-ray source (1486.6 eV).

Wafer bow

A wafer bow measurement is a valuable method for measuring the thin film stress of a sample. Knowing the thin film stress is vital when fabricating MEMS to minimize static bending of cantilevers and to avoid delamination or cracking of the films. When a wafer is coated with a stressed film, the curvature of the wafer changes. This curvature change can then be measured, and the film stress can be calculated via the Stoney equation:[123]

TU Bibliothek WIEN Your knowledge hub
Die approbierte gedruckte Originalversion dieser Dissertation ist an der TU Wien Bibliothek verfügbar.
The approved original version of this doctoral thesis is available in print at TU Wien Bibliothek.

$$\sigma_f = E_{mod}\frac{h_s^2}{6h_f}\left(\frac{1}{G_1}-\frac{1}{G_0}\right) \tag{55}$$

Where h_s is the substrate thickness, h_f the film thickness and G_0 as well as G_1 are the pre- and post-coated sample curvature.

In our case, the curvature is measured with an MX 203-6-33 from E+H Metrology. It features an array of capacitive sensors across the wafer. The capacitance depends on the distance of the sensors to the wafer; hence, the curvature can be obtained. In this thesis, the wafer bow measurement technique was used extensively to optimize deposition parameters.

3.5 Used materials

TiO_2

Titanium dioxide is a material with attributes that make it interesting for a wide field of applications. Additionally, it is inexpensive and readily available, making it an excellent option for not only scientific purposes but also for industrial applications. Its properties range from high permittivity (< 60) and resistive switching effects to catalytic effects.[40,43,124] These outstanding features can be used in applications for resistive switching random-access memory, hydrogen sensors, supercapacitors and solar cells, for example.[125] The permittivity of a TiO_2 sample is dependent on its crystal structure and can vary strongly within the same crystal structure, depending on the fabrication technique and the electrode material.[43] Four crystallographic phases of titanium dioxide have been identified: rutile, anatase, akaogite and brookite.[126] The rutile crystal structure is the most common of the four phases, is the only stable phase above 500°C and has the lattice parameters (i.e. length of the unit cell) $a = b =$ 4.5937 Å and $c = 2.9587$ Å, see *Figure 43*. Anatase is the second most common phase, but is metastable and converts to rutile at higher temperatures (above 500°C). Brookite and akaogite are the rarest of the crystallographic phases, are only stable under extreme conditions, and are of no importance in this work.

The permittivity of TiO_2 is more favourable in rutile, as it shows a higher permittivity than the anatase phase. Rutile TiO_2 can range from ~60-250, whereas anatase TiO_2 has values up to

Die approbierte gedruckte Originalversion dieser Dissertation ist an der TU Wien Bibliothek verfügbar.
The approved original version of this doctoral thesis is available in print at TU Wien Bibliothek.
TU WIEN Bibliothek Your knowledge hub

~40.[127] As the flexoelectric effect scales linearly with the permittivity (see *equation 18*), the rutile phase is favoured for flexoelectric MEMS applications. The permittivity varies with the crystallographic direction within the rutile crystal structure. The *c*-axis has a significantly higher permittivity compared to the *a*- and *b*-axis. This was shown in a study by Sabisky *et al.*, where the permittivity approaches 256 in *c*-axis and 131 in the *a*-direction at low temperatures.[128] As such, a *c*-axis-oriented growth for the flexoelectric thin film is desired. The *c*-axis orientation can be identified in XRD measurements by the (110) direction.[129] On most electrode materials, *c*-axis oriented rutile growth is favoured, as our study shows, and will be discussed in the results section 4.2.[130]

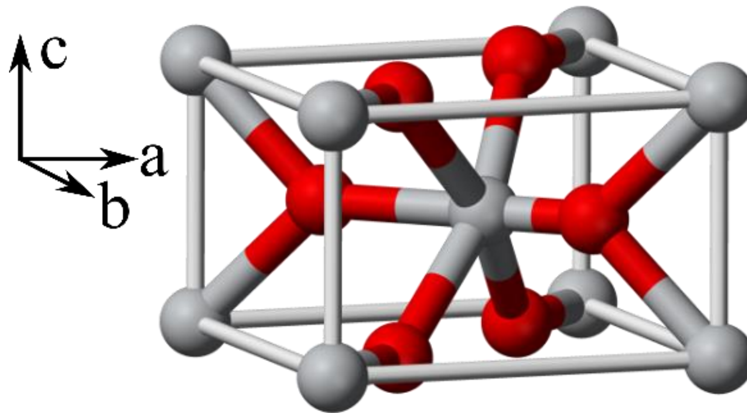

Figure 43 *The rutile unit cell of TiO_2. The titanium atoms are depicted in grey, and the oxygen atoms in red.*

Titanium dioxide in its stoichiometric form is rarely synthesized in sputtered thin films. The film is often sub-stoichiometric, meaning there is less than twice the amount of oxygen compared to titanium in the "TiO_2" layer. The missing oxygen results in so-called vacancies, which are electrically active and lead to various phenomena, such as resistive switching properties, as discussed in section 2.2. The films fabricated in this work are not perfectly stoichiometric, which is why these films are denoted as TiO_x throughout this work. Any theoretical considerations and citations to other sources still refer to TiO_2.

Titanium dioxide is also often investigated for its photoelectric activity under UV light, for example, in photovoltaic cells. However, such effects were not investigated in this work.

Die approbierte gedruckte Originalversion dieser Dissertation ist an der TU Wien Bibliothek verfügbar.
The approved original version of this doctoral thesis is available in print at TU Wien Bibliothek.
TU WIEN Bibliothek Your knowledge hub

IrO_2

Iridium dioxide is a black solid and an oxide of one of the rarest metals – iridium. Even though most metal oxides are non-conductive, iridium oxide is one of the few conductive metal oxides, which makes it the preferred choice as an electrode material when specific requirement. A conductive oxide as an electrode is beneficial when used in oxidizing surroundings, as oxidation effects are considered to have less impact. IrO_2 is also suitable as a thermal barrier layer between the capacitor stack and the Si wafer, allowing for thermal treatment without the problem of diffusing capacitor layers.[131] Even more, the crystal structure of IrO_2 is the tetragonal rutile phase, which is also present in TiO_2, with slightly different lattice constants. With XRD measurements, a difference of 0.086 Å in *a/b* (approx. 2% difference) and 0.039 Å in the *c*-axis direction (approx. 1.3% difference) has been identified. The similarity in crystal structure to the rutile TiO_2 phase, which is the desired phase for flexoelectricity, makes IrO_2 most suitable as a seed layer.

It was shown that using IrO_2 electrodes leads to a higher permittivity of the TiO_x in the $IrO_x/TiO_x/IrO_x$ capacitor stack compared to other tested electrode metals like pure iridium, platinum, and gold.[130] The resulting dielectric constant of capacitors with different bottom electrode metals can be seen in *Figure 44*. All films were fabricated by sputtering.

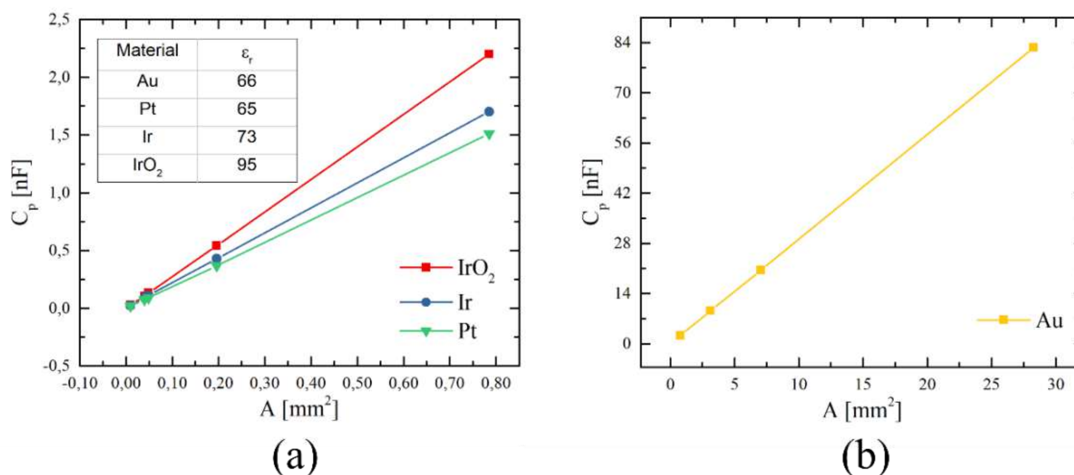

Figure 44 *Measured parallel capacitance of parallel plate TiO_x capacitors with varying sizes and electrode materials. (a) C_p-A plot for the electrode materials IrO_x, Ir and Pt. The resulting relative permittivity for the tested electrode materials is shown in an inlay. (b) C_p-A plot for gold as electrode material. The tested capacitor devices have larger areas for the gold samples.*

We also performed an XRD study to compare the IrO_x electrode to other common electrode metals. All produced samples were fabricated by sputtering a metal (Ir, Pt, IrO_x and Au) onto a

Die approbierte gedruckte Originalversion dieser Dissertation ist an der TU Wien Bibliothek verfügbar.
The approved original version of this doctoral thesis is available in print at TU Wien Bibliothek.
TU Bibliothek WIEN Your knowledge hub

standard p-doped Si wafer. On top of this bottom electrode, the TiO_x was sputtered. These samples, in addition to a single crystal rutile TiO_2 sample, were then measured with the XRD. The result is shown in *Figure 45*. [130]

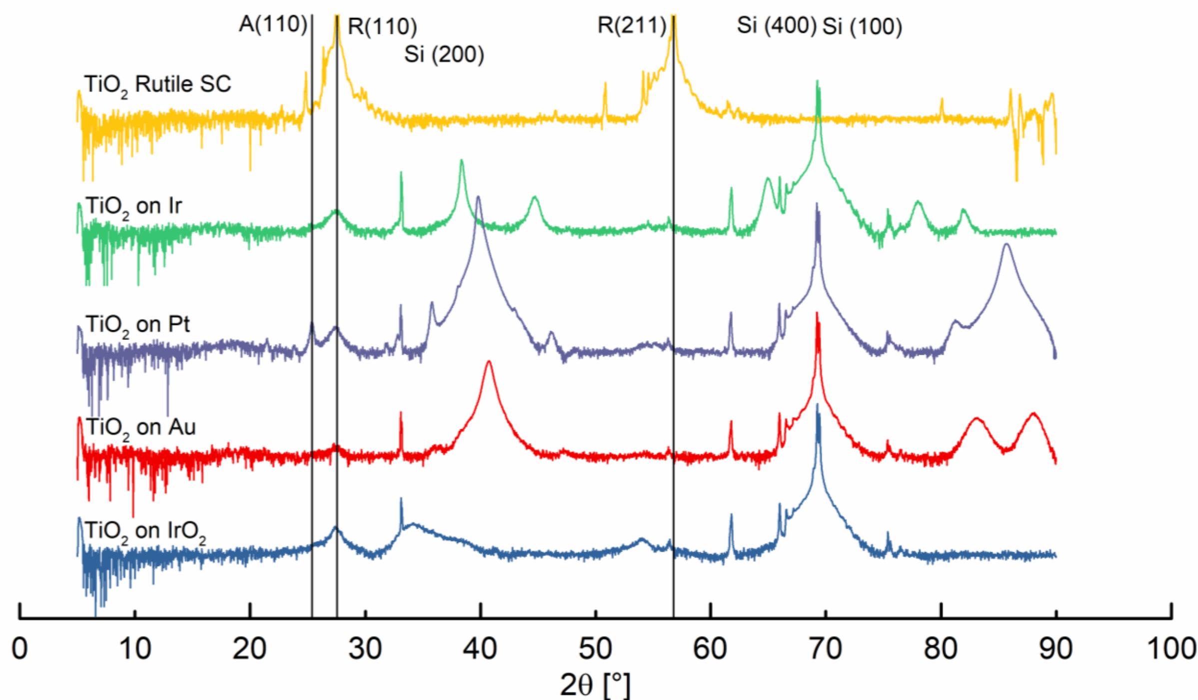

Figure 45 *An XRD analysis of TiO_x grown on different bottom electrode materials is shown. A single crystal bar of rutile TiO_2 is also shown as reference. The main peak of anatase A(110) and of rutile R(110) and R(211) are labelled. The substrate Si peaks Si(100), Si(200) and Si(400) are also marked. The other peaks in each XRD measurement correspond to the respective bottom electrode material.*

A detailed analysis of the (110) peak of all samples is given in *Table 2*.

Electrode Material	*Peak Intensity [Counts]*	*FWHM (110) [°]*
Bulk SC TiO_2	$1{,}5 \cdot 10^7$	0,12 ± 0,002
IrO_x	4000	0,89 ± 0,03
Ir	3000	1,1 ± 0,06
Pt	4000	0,91 ± 0,03
Au	1100	0,92 ± 0,07

Table 2 *Peak intensity and a full-width half maximum of the R(100) peaks measured with XRD in Bragg-Brentano configuration.*

Die approbierte gedruckte Originalversion dieser Dissertation ist an der TU Wien Bibliothek verfügbar.
The approved original version of this doctoral thesis is available in print at TU Wien Bibliothek.
TU WIEN Bibliothek Your knowledge hub

From this result, it is clear that IrO_x stimulates the best TiO_x material quality according to peak intensity and FWHM. Platinum electrodes showed very similar results, but suffered from the anatase phase also being present. Accordingly, the permittivity in the TiO_x layer is highest when integrating IrO_x as bottom electrode. Any further details are discussed in the results section 4.2.

When iridium dioxide is exposed to H_2O containing atmosphere, OH groups and H_2O molecules adhere to the surface.[132] Iridium dioxide also shows catalytic activity towards one half-reaction of the water-splitting process.[50] This half-reaction is called an oxygen evolution reaction (OER) and is:

$$2H_2O \rightarrow 4e^- + 4H^+ + O_2 \quad (56)$$

This equation describes that at the surface of IrO_2, two H_2O molecules are split into one O_2 molecule, four H^+ atoms and four electrons. This specific reaction is not a one-step reaction and has some more steps in between, but those are of no importance to this work. It must be noted that this equation is valid for IrO_2 films in direct contact with water and likely differs at the IrO_2/TiO_2 interface. In the case of the analysed capacitors, TiO_x is also present at the interface, likely changing the reaction dynamics. To the best of the author's knowledge, there are no studies of the catalytic reaction of OH-bonds at the IrO_2/TiO_2 interface. The reactiveness towards water gives the material a complex electrical temperature dependency, as was examined in this work and is described in section 4.3.

Die approbierte gedruckte Originalversion dieser Dissertation ist an der TU Wien Bibliothek verfügbar.
The approved original version of this doctoral thesis is available in print at TU Wien Bibliothek.
TU Bibliothek WIEN Your knowledge hub

Polyvinylidene fluoride (PVDF)

Plastics are a conglomeration of long molecules (so-called macromolecules) consisting of many chained basic components (monomers). This chain of monomers is then called polymer and the length of the chain is given by the degree of polymerization.

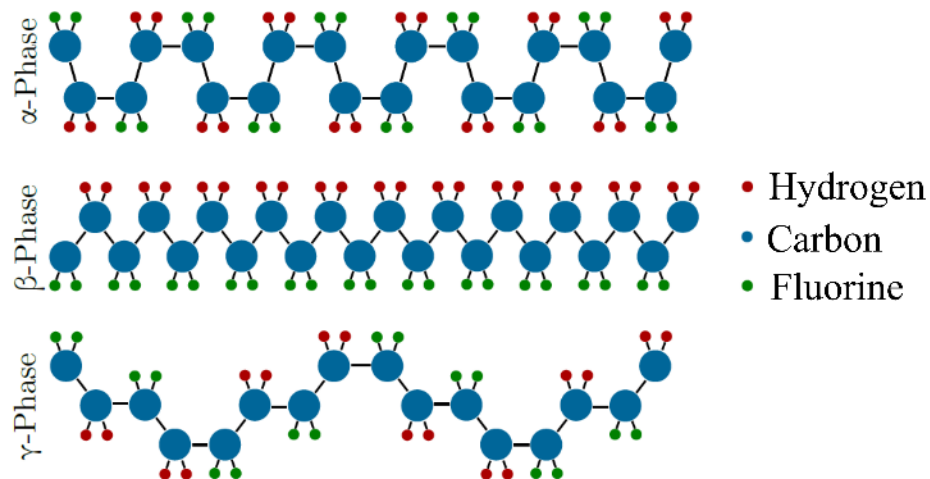

Figure 46 *Three of the most prominent chain configurations of PVDF, namely the α-, β- and γ-phase.*

For PVDF, there are different chain conformations. The three main configurations are shown in *Figure 46*. The α-phase of PVDF is non-polar and is achieved by crystallising the polymer solution. Here the monomers are chained such that no net polarization exists. Therefore, this chain structure does not exhibit any piezoelectric effect. The β-phase, in comparison, is chained such that the high-electronegativity fluorine atoms are oriented on one side of the chain and show a significant dipole moment.

There are mainly two ways of achieving the β-phase. The first method is to stretch the α-phase PVDF film and simultaneously apply an electric field. When the polymer is stretched, the chains are elongated and can orient themselves parallel. The second method is to add the co-polymer trifluroethylene (TrFE). With this co-polymer, the β-phase is achieved without stretching the film, which is vital for MEMS applications. The γ-phase is a high-temperature phase that exhibits some piezoelectricity but is not stable at room temperature and atmospheric pressure.

These chains form the basis for an amorphous, crystalline or semi-crystalline microstructure in a polymer film. In the amorphous regions, the polymeric chains are randomly oriented. In the crystalline regions, the polymeric chains are oriented in a specific way to each other, depending on the type of polymer and the fabrication technique.

TU Bibliothek WIEN Your knowledge hub
Die approbierte gedruckte Originalversion dieser Dissertation ist an der TU Wien Bibliothek verfügbar.
The approved original version of this doctoral thesis is available in print at TU Wien Bibliothek.

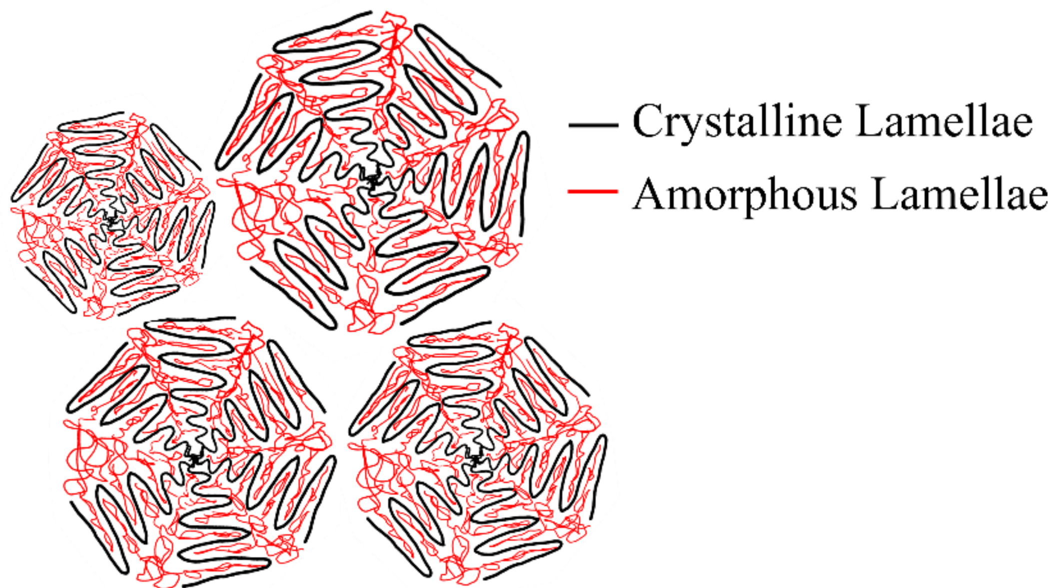

Figure 47 *Spherulitic structure of PVDF films. The structure consists of a mix of ordered chains (black) which make up the crystalline part, and non-ordered chains (red) which make up the amorphous part.*

Specifically, polyvinylidene fluoride is a semi-crystalline polymer, meaning that amorphous and crystalline phases are simultaneously present in the polymer microstructure. In detail, the chains are arranged in a spherulitic-type structure, as depicted in *Figure 47*. These spherulites consist of ordered chains that are mixed with non-ordered chains. The film consists of several of these spherulites with initially random orientation.

In *Figure 48*, a SEM image illustrates part of a fabricated cantilever. The spherulite structure can be identified.

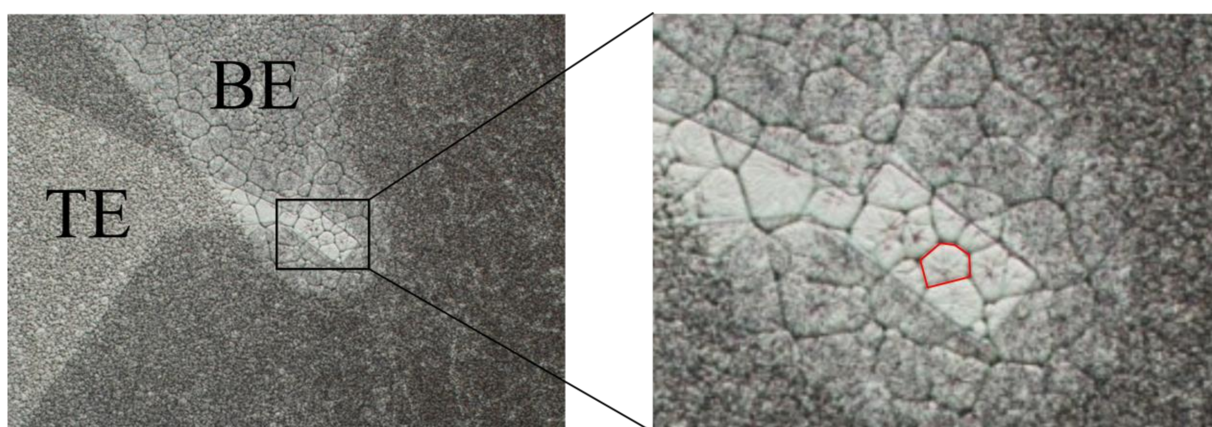

Figure 48 *A top-down SEM image of a PVDF cantilever sample mid-processing. Here, the bottom electrode, PVDF layer and top electrode are finished. A spherulitic structure that formed on and close to the bottom gold electrode (BE) is detected. In the zoomed picture on the right, a spherulite is indicated by red borders.*

Having a well-crystallized film is, however, not always wanted. Such large crystals also lead to high roughness values of e.g., 1.5 µm for 2.5 µm thick PVDF layers.[133] In the aim of this

Die approbierte gedruckte Originalversion dieser Dissertation ist an der TU Wien Bibliothek verfügbar.
The approved original version of this doctoral thesis is available in print at TU Wien Bibliothek.
TU Bibliothek WIEN Your knowledge hub

work, thinner films are preferred. As one can see from the example, reducing the film thickness to 200 nm while simultaneously avoiding electrical short-cuts is very challenging. This is why the PVDF in this work was deposited by spin coating under elevated chuck temperature. This method increases the evaporation rate from the solution, disrupting the crystal growth. The resulting decrease in crystal size is beneficial to achieve low surface roughness.[134] In detail, PVDF thin films at a thickness of 400 nm show a very low roughness below 10 nm when synthesized at 100°C substrate temperature.[135]

Having a deposition temperature above room temperature is also beneficial for reproducibility. Unfortunately, quality of PVDF films strongly depends on the atmospheric moisture when depositing at room temperature. If the conditions are not carefully selected, the films appear white instead of translucent, and it becomes very brittle with a high tendency for crack formation.[133]

As the β-phase PVDF was shown to be piezoelectric, a property that is not usual for polymers, this polymer gained particular attention. Especially interesting is that the longitudinal piezoelectric d_{33} coefficient is negative, meaning that there is a contraction when a field in the direction of the polarization is applied.[136] This contrasts with most other piezoelectric materials, which feature a positive d_{33} coefficient. Much research has been conducted to understand this behaviour for the co-polymers of PVDF. At the time of writing, there are several theories about where this negative piezoelectric constant behaviour comes from. First, there is the theory that the piezoelectric effect originates from electrostrictive deformation in the crystalline domains. This was shown by Liu *et al.* by investigating the PVDF-TrFE behaviour at the morphotropic phase boundary.[137] There, the behaviour can be best modelled with a crystalline model, whereas the so-called dimensional model (where the effect comes from the amorphous part of the structure) does not predict the behaviour very accurately. There is also the idea that piezoelectricity originates the interplay of amorphous and crystalline regions.[136] In the crystalline part, the contraction perpendicular to the applied electric field comes from stretching the spherulites' polymer chains in the direction of the applied field. This behaviour is analogous to the decrease in thickness when a beam, for example, is stretched length-wise.

In a recent study, two slightly different mechanisms for PVDF-based polymers are proposed.[30] In this study, the electromechanical response is split into two contributions: mechano-electrostriction and electric repulsion. Mechano-electrostriction is due to the conformation transformation of twisted polymer chains to extended ones when subjected to an electric field

Die approbierte gedruckte Originalversion dieser Dissertation ist an der TU Wien Bibliothek verfügbar.
The approved original version of this doctoral thesis is available in print at TU Wien Bibliothek.
TU Bibliothek WIEN Your knowledge hub

and is responsible for the linear behaviour of up to 400 kV/cm. The second contribution, which causes non-linearities above 400 kV/cm, comes from the repulsion of electrically aligned nanodomains. It must be noted that the above cited studies use PVDF-baser polymers, such as PVDF-TrFe but did not use PVDF itself. Therefore, not all conclusions from these studies can be readily extended to PVDF. For example, the above-mentioned nano-domains occur in relaxor ferroelectric materials such as PVDF-TrFE but do not contribute to the paraelectric ∝-phase PVDF.

From our results, it is unclear which of the two theories, piezoelectricity or mechano-electrostriction, describes linear electromechanical behaviour more accurately. It was therefore chosen to describe the effects with piezoelectricity, as this is more commonly found in the literature.

Even though ∝-phase PVDF is supposed to be non-polar, in real systems, this is not always the case. Polarization hysteresis effects have been shown at fields >200 kV/cm, where it was concluded that ferroelectricity is the cause of the hysteresis.[138] This means that even in linear electromechanical coupling effects, such as piezoelectricity, a non-linear response of the system can be expected.

TU Bibliothek WIEN Your knowledge hub
Die approbierte gedruckte Originalversion dieser Dissertation ist an der TU Wien Bibliothek verfügbar.
The approved original version of this doctoral thesis is available in print at TU Wien Bibliothek.

4 Results and Discussion

This chapter presents and discusses the results of the material characterization of the two materials, α-phase PVDF and TiO_x. The electro-mechanical properties of these materials are analysed with LDV measurements by applying MEMS cantilever structures. For PVDF, the flexoelectric contribution needs to be investigated. However, a significant electrostrictive actuation was measured. For the TiO_x, the primary electro-mechanical response can be attributed to the flexoelectric effect. Further studies on the TiO_x are also shown, such as measurements of devices using a segmented top electrode (to locally enhance electric field gradients), the electrical properties of TiO_x (mainly the capacitive and leakage current behaviour) and the cantilever behaviour at different temperatures and atmospheres.

First, the challenges of the flexoelectric coefficient determination of PVDF cantilevers are presented. Second, it is shown that the PVDF cantilever proves to be a viable electrostrictive MEMS actuator. Third, the actuation behaviour, the Young's modulus and the Q-factor are analysed at various temperatures ranging up to 190°C.

4.1 α-phase PVDF MEMS cantilevers

As discussed in the introduction chapter, PVDF was chosen as a potential flexoelectric material because the literature shows that the material's electromechanical activity promises a large flexoelectric component. [54] Additionally, PVDF is often cited as a suitable functional material for MEMS applications, as it is cost-effective, lightweight and chemically robust. [139–141] MEMS applications include cantilevers used in AFMs or in sensors that can measure particle mass, viscosity, or flow. Besides MEMS, other common application scenarios for PVDF also include high-energy-density capacitors, memory devices, energy harvesters and sensors. [142–144]

Adding a co-polymer, TrFE, is vital for most of these applications. The reason is that the as-cast PVDF (as described in section 3.5) is in the non-polar α-phase, and a special technique is

Die approbierte gedruckte Originalversion dieser Dissertation ist an der TU Wien Bibliothek verfügbar.
The approved original version of this doctoral thesis is available in print at TU Wien Bibliothek.
TU Bibliothek Your knowledge hub WIEN

needed to change the non-polar α-phase to the polar β-phase. This technique stretches the PVDF film while a strong electric field (in the 100s of MV/m) is active. The addition of TrFE causes the polymer to form the β-phase at room temperature primarily. [145]

However, when investigating the flexoelectric effect, having the non-polar phase is beneficial. The non-polarity ensures that there is no piezoelectric contribution to the total electromechanical response of the functional film. In some applications, using the flexoelectric effect in PVDF is preferred, as using the d_{33} of copolymers like TrFE limits the temperature range to the Curie temperature of 120°C and therefore limits the application range. [146]

A non-piezoelectric α-phase PVDF cantilever with a symmetric cantilever design was fabricated to measure the flexoelectric coefficient in PVDF. The symmetric design, where the neutral axis is in the centre (out-of-plane direction), is supposed to cancel out the electrostrictive and the residual piezoelectric contributions compared to the electromechanical actuation, as shown in *Figure 49 a*. However, when measuring the PVDF devices with the MSA and demodulating the signal into its 1st and 2nd harmonics (explained in section 3.4), a significant quadratic mechanical response is present in addition to a linear actuation signal with a comparatively low deflection. A quadratic contribution to the actuation implies that there is an enormous non-linear flexoelectric effect in PVDF or that the cantilevers do not fulfil the symmetry requirement, which is needed to suppress the electrostriction and piezoelectricity.

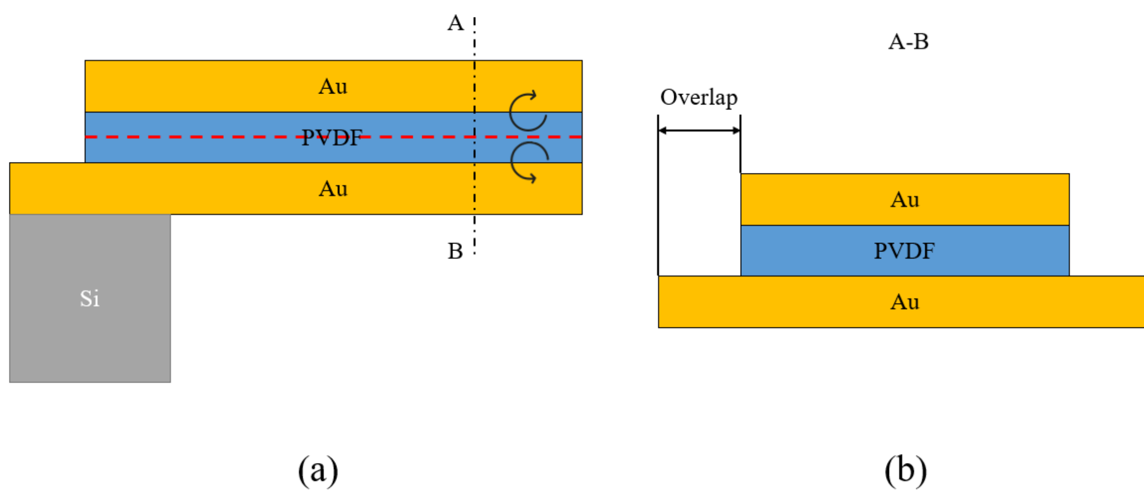

Figure 49 *(a) The side view of the cantilever. The neutral axis is shown as a dashed red line. The circular arrows indicate the direction of the torque that results from the piezoelectric/electrostrictive effect. (b) Cross-section of the cut A-B. The overlap is the difference between the lateral size of the bottom electrode and the top electrode.*

To check whether the latter influence is significant, frequency-dependent COMSOL simulations were performed and showed that the neutral axis is off symmetry due to the

Die approbierte gedruckte Originalversion dieser Dissertation ist an der TU Wien Bibliothek verfügbar.
The approved original version of this doctoral thesis is available in print at TU Wien Bibliothek.
TU Bibliothek WIEN Your knowledge hub

difference in lateral size of the bottom electrode and the top electrode. In this investigation, this difference in size is called overlap and is defined as shown in *Figure 49 b*.

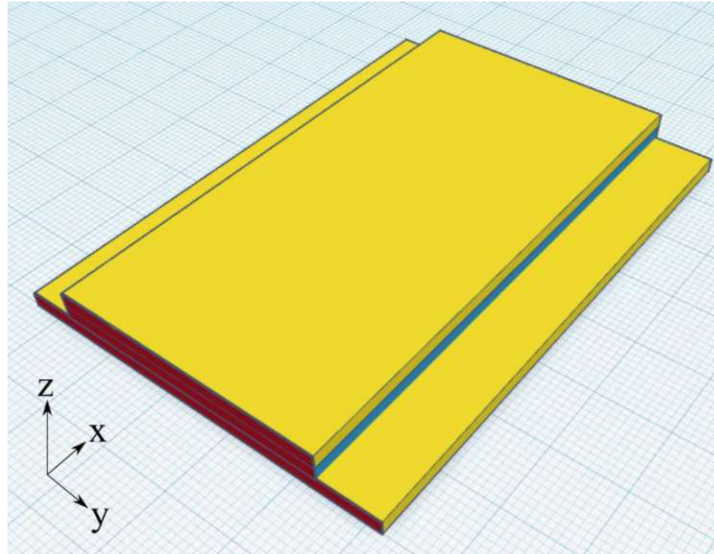

Figure 50 *A sketch of the 3D model used in COMSOL. Three rectangular plates can be seen. The yellow plates represent the gold electrodes, and the blue plate represents the PVDF film. The red area shows where the fixed boundary condition of COMSOL applies.*

The simulation was performed in 3D, and the model was a simple stack of three rectangular plates, where the bottom plate was laterally more extended than the other two, see *Figure 49 b* and *Figure 50*. The cantilever clamping was approximated by setting the front facet (red area in the sketch) as a fixed boundary condition (i.e., restricting any movement of the corresponding nodes in any direction). The plate thicknesses are rounded values of a measured cantilevered device, namely 200/190/200 nm. The width and length of the simulated cantilever are 50 µm and 150 µm, respectively. The bottom electrode width varies from 50 µm to 57 µm.

The first step of the simulation procedure was to find the resonance frequency of an undamped cantilever with a given overlap. Then, to obtain a comparative amplitude value between the different overlap values, a sinusoidal actuation with amplitude of 1 V was applied, where the actuation frequency is slightly below the actual resonance frequency ($0.999 \cdot f_0$). This is necessary, as the simulation at resonance of an undamped system is unstable. The resulting amplitude δ is normalized to the highest amplitude δ_{max} resulting from the different overlap values. This framework is reasonable for proofing that the overlap causes the off-axis symmetry of the neutral axis.

For the electrostrictive coefficients of PVDF, Q^e_{11} = -11 m^{4}C^{-2}, Q^e_{12} = 6.7 m^{4}C^{-2} and ε_r = 16 were used. The mechanical parameters were taken from the COMSOL standard library.

Die approbierte gedruckte Originalversion dieser Dissertation ist an der TU Wien Bibliothek verfügbar.
The approved original version of this doctoral thesis is available in print at TU Wien Bibliothek.
TU Bibliothek WIEN Your knowledge hub

[147,148] These are $E_{mod,PVDF}$ = 2.42 Gpa, ρ_{PVDF} = 1.76 g/cm^3 and v_{PVDF} = 0.34 and $E_{mod,Au}$ = 70 Gpa, density ρ_{Au} = 19.3 g/cm^3, Poisson ratio v_{Au} = 0.44. For the piezoelectric coefficients, standard COMSOL values for PVDF were applied.

The resulting normed tip deflection at various overlaps can be seen in *Figure 51*. Both piezoelectric and electrostrictive excitation were simulated for reasons of comparison.

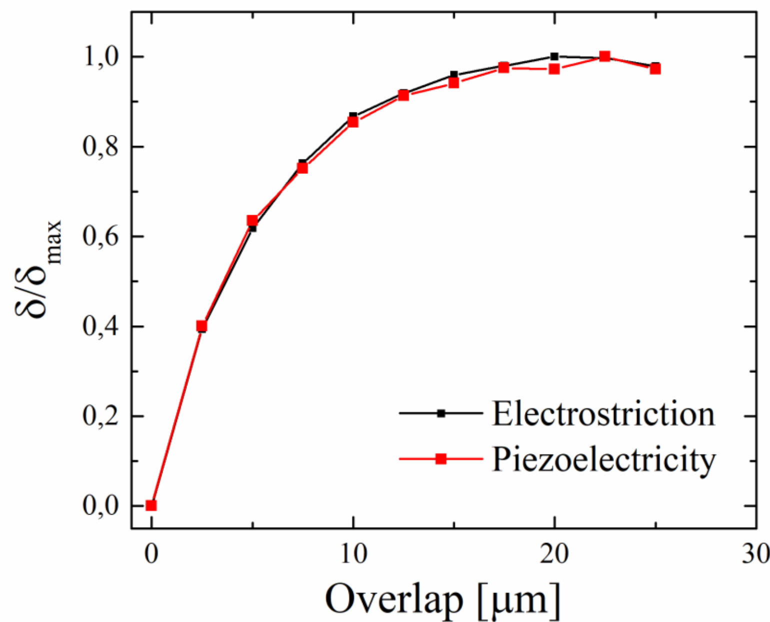

Figure 51 *The normalized tip deflection of the simulated cantilever at different overlap values. At no overlap, the tip deflection is zero. When an overlap is introduced, a resonance mode is excited, and the tip deflection increases with increasing overlap. No significant difference in deflection when comparing piezoelectric and electrostrictive actuation is detected.*

The simulation limit for the overlap was set to 25 μm, as at higher values, the mode shape changes as in-plane modes occur. As shown in *Figure 52 a*, at 0 overlap, the cantilever has no tip deflection and only shows changes in volume, as is expected for piezoelectric materials. Even the lowest overlap investigated (i.e., 1 μm in this case) leads to a tip deflection > 0. With increasing overlap, the amplitude increases up to the point where in-plane modes are introduced into the cantilever oscillation. The resulting tip deflection can be seen in *Figure 52 b*.

Die approbierte gedruckte Originalversion dieser Dissertation ist an der TU Wien Bibliothek verfügbar.
The approved original version of this doctoral thesis is available in print at TU Wien Bibliothek.
TU Bibliothek Your knowledge hub WIEN

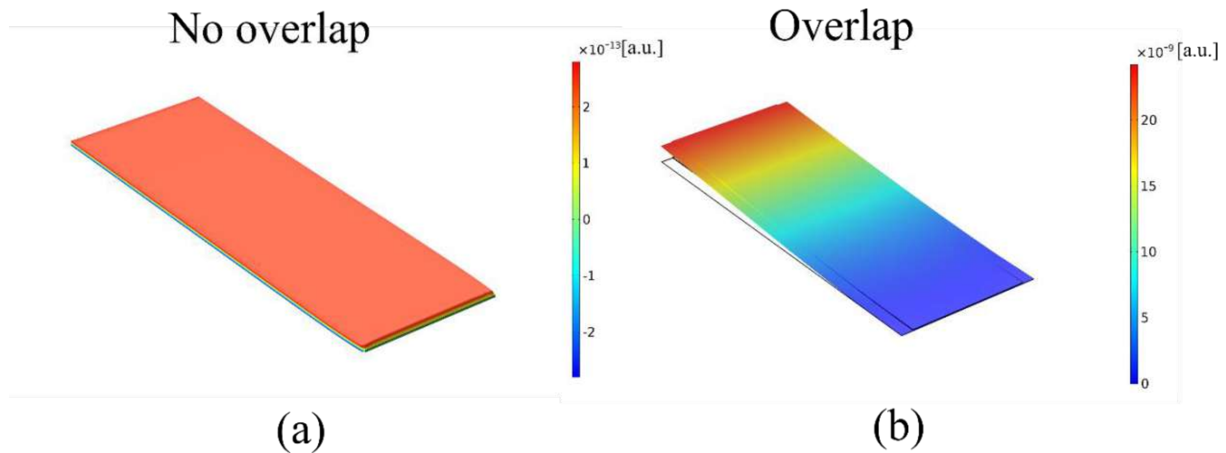

Figure 52 *The obtained mode shape from COMSOL simulations of a PVDF cantilever. (a) No overlap between the top and bottom electrode leads to an expansion of volume, but no tip deflection, (b) having an overlap > 0 leads to an out-of-plane mode shape with a tip deflection.*

Due to this overlap effect, and the fact, that 0 overlap leads to a drastic increase in the probability of bottom-to-top electrode short-cuts (see section 3.2), no methods were found that could sufficiently decouple the piezoelectric signal from the flexoelectric signal in these cantilevers. Additionally, as the actual value of the residual piezoelectric coefficient is not known, the piezoelectric portion of the linear actuation signal cannot be simulated and subsequently subtracted from the measured actuation signal.

However, we found a significant actuation based on the electrostrictive effect, and with this approach, no device layer is needed to break the symmetry. Therefore, as the cantilever stiffness is lower, a higher deflection is possible. This discovery leads to an exciting possibility for using the electrostrictive effect of α-phase PVDF in MEMS applications. The electrostrictive effect in PVDF is generally pronounced and even dominates the piezoelectric contribution at higher electric fields in β-phase PVDF.[149,150] Due to the quadratic dependency of the actuation to the applied electric field, electrostriction is generally outperformed by piezoelectric contributions at lower electric fields. [151] Before this discovery, two main strategies for increasing the actuation performance of an electrostrictive device were followed. One approach is to decrease the film thickness as much as possible while keeping the applied voltage level the same. This increases the electric field strength inside the functional material, which leads to more actuation. Unfortunately, there is a limit in film thickness, which is defined by the breakdown field strength. This limit for PVDF is about 8 MV/cm, which is comparable to the piezoelectric ceramic aluminium nitride (~ 9 MV/cm).[23,152]

Die approbierte gedruckte Originalversion dieser Dissertation ist an der TU Wien Bibliothek verfügbar.
The approved original version of this doctoral thesis is available in print at TU Wien Bibliothek.
TU WIEN Bibliothek Your knowledge hub

By omitting the device layer, the cantilever thickness can be reduced without being limited by the breakdown field strength. One potential application for a cantilever of this design as characterized in this thesis is to use them as probes in AFM measurements of biological samples. Compared to AFM probes made from silicon ($E_{mod,Si}$ of *140 Gpa)*, the Au/PVDF/Au cantilevers are much softer ($E_{mod,PVDF} \sim 2$ *Gpa* and $E_{mod,Au} \sim 69$ *Gpa)* [153–155]. This lower stiffness is required for biological samples; otherwise, the samples can get damaged.[156] The measured *Q*-factor of the Au/PVDF/Au cantilevers is also relatively low (~ 60), as is shown in the following section. A low *Q*-factor of the cantilever means that the response time regarding sharp changes in amplitude is much faster. A higher resonance frequency is also beneficial, and a good approximation for the response time is Q/f_0. [157]

Experimental results

The PVDF cantilever device was fabricated as described in section 3.3, and an SEM image of such a cantilever is shown in *Figure 53.*

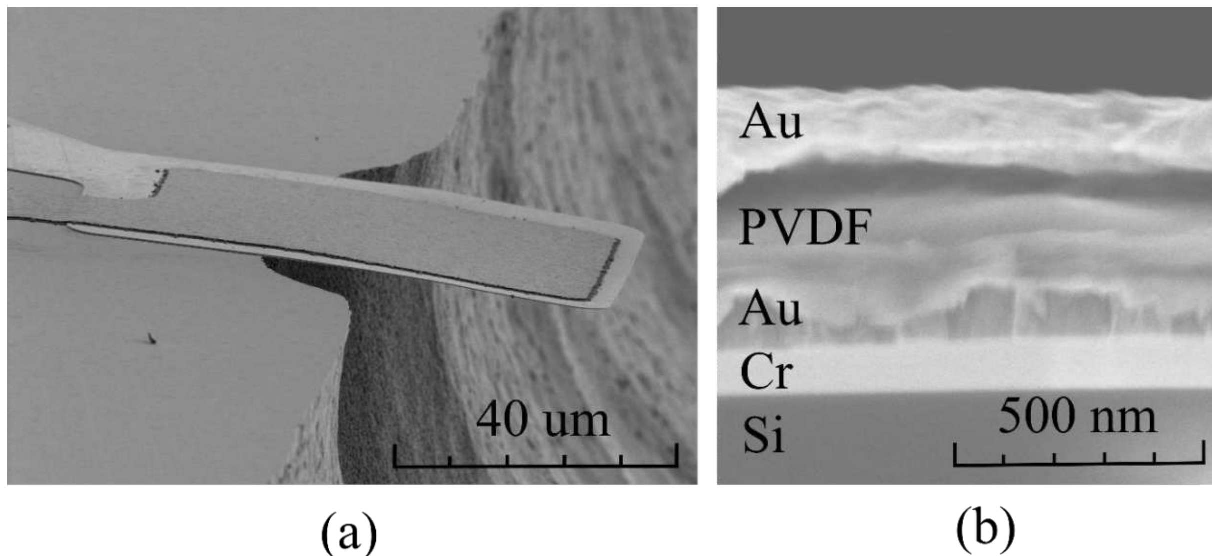

Figure 53 *SEM images of a PVDF cantilever. (a) Side view of a released cantilever. (b) Cross-section of the cantilever film stack. In a post-release etch, the chromium layer is removed and is, therefore, not present in the free-standing parts of the cantilever.*

As expected, no significant static bends can be observed. The XeF_2 under etch did not yield a perfectly straight anchor region, demonstrating that the etch rate close to the cantilever was higher than in the vicinity. No apparent reason was found; however, the anchor below the cantilever is reasonably straight and is thus still useful for characterization. In the SEM image, the surface roughness seems low. To prove that, an AFM characterization of PVDF deposited

Die approbierte gedruckte Originalversion dieser Dissertation ist an der TU Wien Bibliothek verfügbar.
The approved original version of this doctoral thesis is available in print at TU Wien Bibliothek.
TU WIEN Bibliothek Your knowledge hub

on gold was performed, which is shown in *Figure 54*. The annealing temperature of the film was 130°C.

As expected, a spherulitic structure can be identified (see section 3.5). However, the spherulites are comparatively small in lateral size (1-4 µm compared to <30 µm for room temperature deposition), resulting in a much smoother film.[158] The RMS roughness is very low, with 18.51 nm, whereas at grain boundaries, the thickness drops significantly down to 172 nm. This drop is due to the presence of deep troughs that can almost extend down to the bottom electrode. However, no effect on the electrical breakdown field strength was observed. A likely explanation is that the troughs are very small in lateral size, so the gold top electrode does not fill them, so that the bottom electrode gets connected.

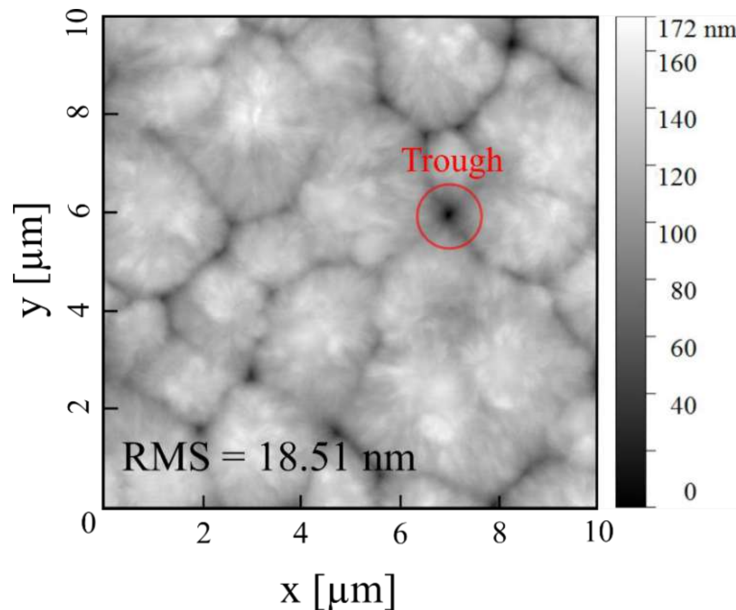

Figure 54 *An AFM measurement was performed on an AU/PVDF sample annealed at 130°C. The AFM was set to the tapping mode, and the forward height sensor signal was recorded. The total scanning area is 10x10µm^2. The trough with the steepest decline is marked with a red circle.*

Obtaining the effective cantilevers' Young's modulus is vital for determining the electromechanical coefficients. The Young's modulus was obtained as described in the methods section 3.4. In this measurement, the sinusoidal excitation frequency was swept from 10 to 200 kHz, and the sampling point of the MSA was put in the middle of the cantilevers' tip. The values determined with this approach were $\kappa = 0.3$ and $E_{eff} = 65$ *Gpa*. Using the literature values mentioned earlier in this section, and calculating the weighted sum for the cantilever results in an $E_{bulk,eff} = 46.6$ Gpa.[153–155] With a discrepancy of ~30%, this is reasonably close. As thin

Die approbierte gedruckte Originalversion dieser Dissertation ist an der TU Wien Bibliothek verfügbar.
The approved original version of this doctoral thesis is available in print at TU Wien Bibliothek.
TU Bibliothek Your knowledge hub WIEN

films have substantially different morphology and stress depending on factors like deposition method and used parameters, such a deviation is reasonable.[159]

To ensure that piezoelectric contributions from the β-phase are as minimal as possible, the PVDF film must consist predominantly of the α-phase. To confirm this, a combination of FTIR and XRD measurements was performed. As both methods benefit from thicker samples and 200 nm thick samples have a very low signal-to-noise ratio, 1 µm thick samples at different annealing temperatures were fabricated. As explained in section 3.5, the room-temperature deposition samples show a significant difference in film quality, also shown in *Figure 55*. Due to the low film quality, the sample at room-temperature deposition was omitted.

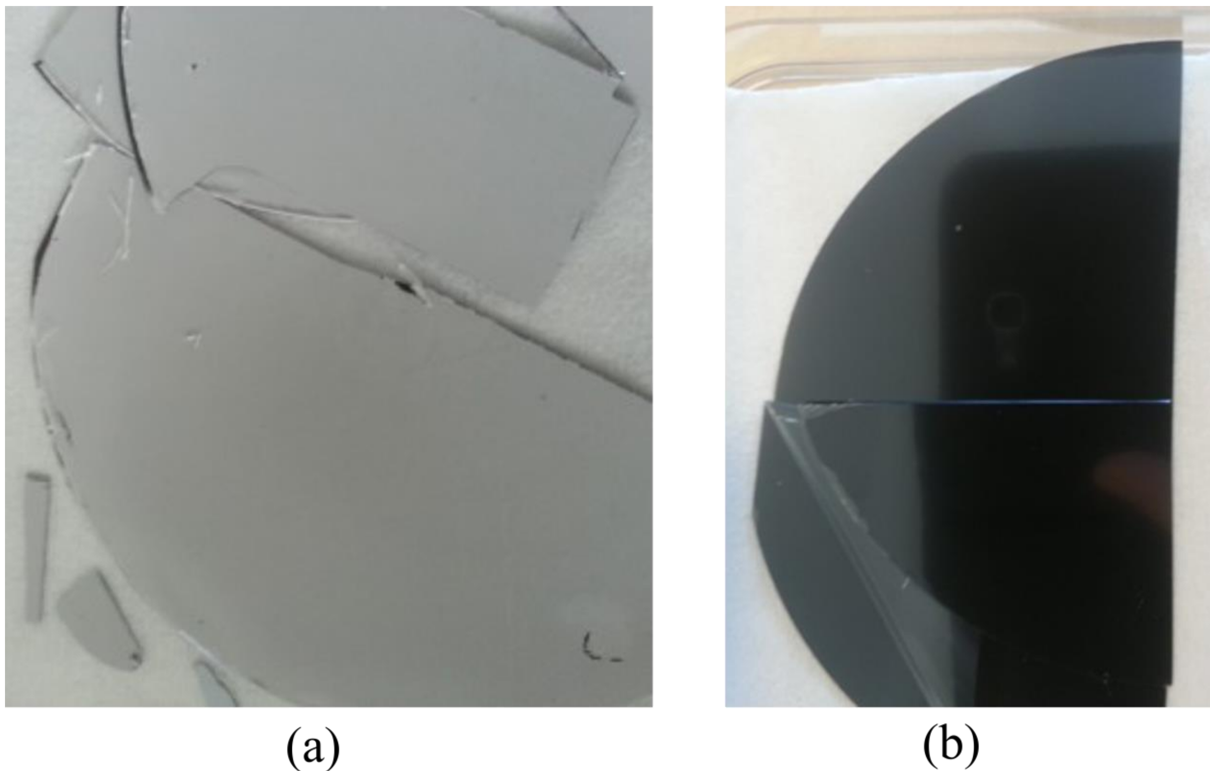

Figure 55 *PVDF films deposited on silicon wafers at different temperatures. (a) At room temperature, the PVDF film is white and brittle. (b) At deposition temperatures above 70°C, a translucent and soft film is formed.*

In *Figure 56 a*, the measured FTIR spectrum can be seen. The specific peaks for α-phase PVDF are at 763 and 614 cm^{-1}. For the β-phase, the peak location is at 1275, 841 and 510 cm^{-1} and for the γ-phase at 1234 cm^{-1}.[160] All three phases are present at room temperature and 70°C deposition temperature. Above this temperature, the α-phase specific peaks remain, while the β- and γ-phase characteristic peaks disappear.

Die approbierte gedruckte Originalversion dieser Dissertation ist an der TU Wien Bibliothek verfügbar.
The approved original version of this doctoral thesis is available in print at TU Wien Bibliothek.
TU Bibliothek WIEN Your knowledge hub

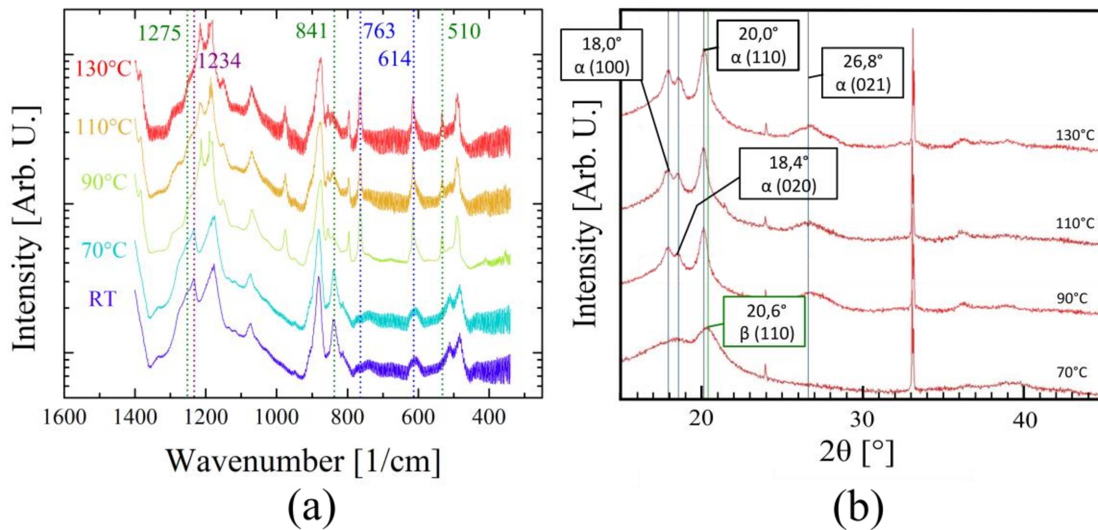

Figure 56 *(a) The measured FTIR spectrum for samples fabricated at deposition temperatures ranging from room temperature to 130°C. FTIR peaks which are identifiers of the α-phase, are labelled in blue, the β-phase specific peaks are labelled in green, and the γ-phase specific peak is labelled in purple. (b) XRD spectra for samples fabricated at deposition temperatures ranging from 50 to 130°C. α-phase and β-phase specific peak locations and corresponding crystallographic planes are labelled.*

The XRD measurement, shown in *Figure 56 b*, confirms the results from the FTIR measurements. The β-phase specific peak at 20.6° is only present at a deposition temperature of 70°C. This peak also has a low intensity and is broad, indicating a poor presence of this phase. The α-phase specific peaks at 17.9°, 18.4°, 20° and 26.8°, which represent the (100), (020), (110) and (021) crystallographic planes are pronounced at the samples synthesized at a substrate temperature above 70°C. [161]

The actuation behaviour of the cantilevers is studied with the MSA measurement approach, as described in section 3.4. This method can split the mechanical response into terms with linear and quadratic dependence on the electric field. The cantilevers are excited with a sinusoidal voltage at frequencies $f_m = f_a$ and $f_m = 2{\cdot}f_a$, and both the tip deflection across the frequency spectrum 10-200 kHz and the curvature at resonance were measured with the MSA. The resulting tip deflection concerning the actuation frequency is shown in *Figure 57 a*. The cantilever tip deflection in resonance at low electric fields (<600 kV/cm) is shown in *Figure 57 b*. As expected, the 2nd harmonic excitation ($f_m = 2{\cdot}f_a$) leads to higher tip deflection than when the 1st harmonic is applied ($f_m = f_a$). This is true across the whole analysed frequency spectrum. As explained in section 2.3, the significant actuation at the 2nd harmonics strongly indicates that

Die approbierte gedruckte Originalversion dieser Dissertation ist an der TU Wien Bibliothek verfügbar.
The approved original version of this doctoral thesis is available in print at TU Wien Bibliothek.
TU Bibliothek WIEN Your knowledge hub

the electrostrictive effect is the cause of this actuation. This is further supported by the expected quadratic dependence of the tip deflection as the case of electrostriction shown in *Figure 57 b*.

The measurement at the 1st harmonics has a comparatively low amplitude (roughly an order of magnitude) and shows a linear dependence on tip deflection as a function of actuation voltage. The linear behaviour of the tip deflection vs. actuation voltage at the 1st harmonics leads to the conclusion that this actuation originates either from the piezoelectric effect or the flexoelectric effect. As it was impossible to isolate those two effects by symmetric cantilever design, there is no final conclusion of what effect causes the 1st harmonics actuation. To make matters more complicated, some measured cantilevers also show the quadratic dependency of the tip deflection in the 1st harmonics measurement. However, in the author's opinion, it is most likely that the actuation is caused by the piezoelectric effect, as a piezoelectric contribution in α-phase PVDF was repeatedly reported. [27,162]

Die approbierte gedruckte Originalversion dieser Dissertation ist an der TU Wien Bibliothek verfügbar.
The approved original version of this doctoral thesis is available in print at TU Wien Bibliothek.
TU WIEN Bibliothek Your knowledge hub

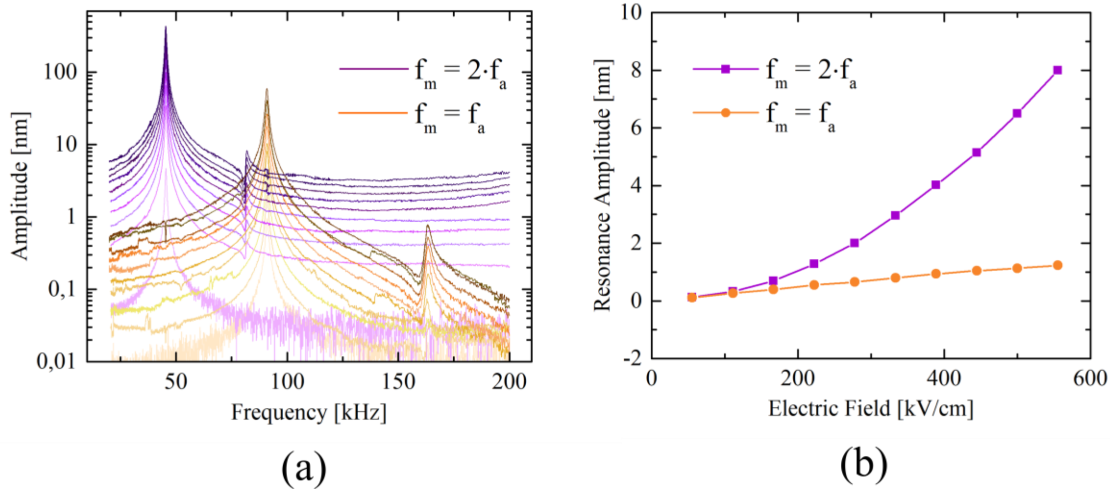

***Figure 57** MSA measurements of a PVDF cantilever. A lock-in amplifier was used to capture the tip deflection amplitude. The measured frequency f_m equals the excitation frequency f_a or twice the value of f_a. (a) A frequency sweep was measured. The excitation field was varied between 250 and 2750 kV/cm in steps of 250 kV/cm. (b) A plot of the corresponding tip deflection amplitude at resonance and low excitation fields.*

In addition to the previous measurement, a surface scan at varying sinusoidal excitation voltages was performed. With the surface scan, a more precise measurement is obtained. A 3D surface plot of the raw data of all surface scans is shown in *Figure 58 a*. The derived curvature of the MSA surface scan of the first mode at different applied electric fields at $f_m = 2{\cdot}f_a$ and $f_m = f_a$ is shown in *Figure 58 b*. The $f_m = 2{\cdot}f_a$ shows a quadratic dependency regarding the electric field, which is expected for this type of measurement. The measurement with $f_m = f_a$ shows linear dependence at lower electric fields and non-linearities at higher electric fields. The possible origin of this non-linearity comes from the presence of ferroelectric phases at higher electric fields, as explained in section 3.5.

Die approbierte gedruckte Originalversion dieser Dissertation ist an der TU Wien Bibliothek verfügbar.
The approved original version of this doctoral thesis is available in print at TU Wien Bibliothek.
TU WIEN Bibliothek Your knowledge hub

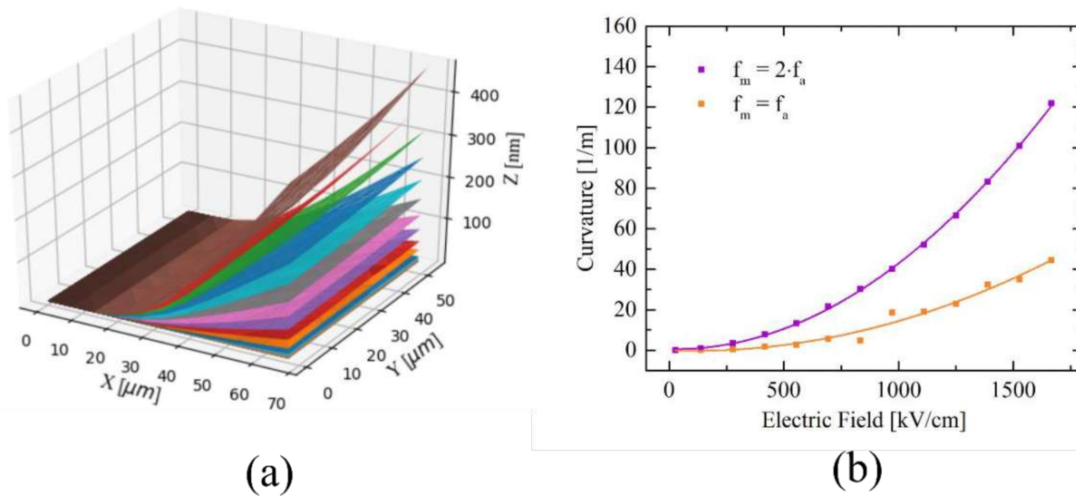

Figure 58 *(a) A surface scan of the first mode measured with the MSA at $f_m = 2{\cdot}f_a$. The electric field amplitude varied from ~30 kV/cm to ~1700 kV/cm resulting in deflection surfaces, ordered from the lowest to the highest Z values at the tip (b) The derived curvature at varying excitation fields. A quadratic fit of the two measurements is also shown to identify better the quadratic dependency of both $f_m = f_a$ and $f_m = 2{\cdot}f_a$.*

A typical maximum tip deflection Z at resonance of the presented cantilevers is ~450 nm at 60 V for a 60 µm long and 600 nm thick cantilever.

A comparison to other cantilevers found in literature would be beneficial here. However, to our knowledge, no other electrostrictive semiconductor-technology-compatible MEMS cantilever with such small dimensions has been published. The research of electrostrictive cantilevers focuses generally on much larger devices, ranging from a few millimetres to several centimetres.[163,164] Other electrostrictive MEMS devices are from a different type, such as membranes or textile fibres.[165,166] Also, the piezoelectric effect for MEMS cantilevers is generally favourable, as it produces a larger strain at lower electric fields[6] and is therefore attracting more attention.[167]

To benchmark the performance of these cantilevers, the best comparison that can be done is to compare the α-phase PVDF cantilevers with β-phase PVDF-TrFE cantilevers that our group published most recently [150], as similar methods, equipment and materials are used. For that comparison, the β-phase piezoelectric MEMS resonator achieved a deflection at the tip of 1.2 µm @ 30 V with a length of 400 µm and a total thickness of 3 µm, whereas an exemplary electrostrictive cantilever reached ~150 nm @ 30 V with a length of ~60 µm and 600 nm total

[6] The exact electric field values where the piezoelectric effect dominates the electrostrictive effect are material dependent, but in the next paragraph such a comparison between electrostrictive PVDF and piezoelectric PVDF-TrFE is given.

Die approbierte gedruckte Originalversion dieser Dissertation ist an der TU Wien Bibliothek verfügbar.
The approved original version of this doctoral thesis is available in print at TU Wien Bibliothek.
TU WIEN Bibliothek Your knowledge hub

thickness. From a geometry point-of-view, the tip deflection scales with $\propto L^3/h^3$. When comparing these different geometries, the 150 nm tip deflection must be multiplied by 2.3 if the cantilever is scaled to the dimensions of the piezoelectric PVDF-TrFE cantilever. This means that the tip deflection of the electrostrictive cantilever is only 1/3.4 compared to the tip deflection of the piezoelectric cantilever. This rough estimate does not take any consideration of, *e.g.* the *Q*-factor or other resonator-specific parameters into account, which has a high impact on the resulting tip deflection. Also, the quadratic field dependency favours the electrostrictive cantilever approach when going to higher fields. Calculating with the numbers above, one would need roughly 110 V (5500 kV/cm) to reach comparable deflection values from electrostrictive and piezoelectric actuation. As the dielectric breakdown strength can be as high as 8000 kV/cm (for thicker films, as mentioned before), the device could outperform piezoelectric devices. However, we could not achieve such high breakdown strengths and can, in direct comparison, not outperform the piezoelectric counterpart. With all this information combined, we can say that electrostrictive cantilever may be comparable to piezoelectric counterparts, if thick, high-quality PVDF is used.

For sensing purposes, the resonance amplitudes do not need to be very large (e.g., an AFM works with amplitudes of ~30 nm), and hence, the cantilever is considered suitable for sensing purposes. As PVDF has a higher melting point as PVDF-TrFE and α-phase PVDF do not need poling, the latter material offers benefits for electroactive devices.

Temperature-dependent measurements

The temperature-dependent performance of cantilevered resonators was also measured. In principle, the electrostrictive coefficient should not be dependent on temperature. On the other hand, the piezoelectric and flexoelectric effects were shown to increase with temperature. [168,169] In theory, the flexoelectric effect is present at temperatures above the Curie temperature, while the piezoelectric effect is not. Measuring actuation above Curie-temperature could prove that the flexoelectric effect exists in a measurable range in α-phase PVDF.

For this purpose, the cantilever was placed on a hot plate below the MSA. This hot-plate also had a vacuum chuck to fix the sample. The temperature of the hot-plate was set to the wanted temperature, and the cantilever's resonance frequency was monitored. In detail, a continuous periodic frequency sweep of a sinusoidal actuation voltage was applied, while the tip deflection

Die approbierte gedruckte Originalversion dieser Dissertation ist an der TU Wien Bibliothek verfügbar.
The approved original version of this doctoral thesis is available in print at TU Wien Bibliothek.
TU WIEN Bibliothek Your knowledge hub

was constantly measured with the MSA. Once the resonance frequency was stable for 15 minutes, the actual surface scan of the cantilever was performed. For each temperature, two measurements were made, one without electrical excitation for thermal calibration (see section 3.4) and one with electrical excitation, where the excitation amplitude was increased from 0 to ~300 kV/cm. The deflection amplitude dependent on the applied electric field was fitted with either a first- or a second-degree polynomial, $f = a_1 + b_1 x$ and $f = a_2 + b_2 x^2$, respectively. This corresponds to a 1st and 2nd harmonics behaviour, as previously explained. The temperature was varied from 25 to 160°C. Unfortunately, at higher temperatures, the PVDF devices started to bend downwards, and the PVDF film began to show bubble formation and could not be measured with the MSA anymore. This device failure is unfortunate, as the Curie temperature for α-phase PVDF is above 160°C, and this method to discern the piezo- and flexoelectric effect was not possible.

It Is Important to note that these fitting coefficients are evaluated at the resonance frequency and cannot be equated to material coefficients. However, as the cantilevers do not show any non-linear resonance behaviour[7], the fitting coefficient's general trend matches the material coefficient's trend.

The resulting fitting coefficient over temperature when measuring at $f_m = 2 \cdot f_a$ is shown in *Figure 59 a*. Also shown is the fitting coefficient normalized by the Young's modulus at the respective temperature. *Figure 59 b* depicts the $E_{mod,eff}$ and Q-factor obtained from the thermal calibration. A direct correlation of the 2nd harmonics fitting coefficient with the effective Young's modulus is identified.

[7] A non-linear resonance behaviour refers to cases, where the resonance frequency is dependent on the tip-deflection. When such a system is actuated, the resonance frequency changes. If the actuation frequency stays the same while the resonance frequency changes, the resonance amplitude can decrease even though the excitation amplitude increases.

Die approbierte gedruckte Originalversion dieser Dissertation ist an der TU Wien Bibliothek verfügbar.
The approved original version of this doctoral thesis is available in print at TU Wien Bibliothek.
TU Bibliothek WIEN Your knowledge hub

Die approbierte gedruckte Originalversion dieser Dissertation ist an der TU Wien Bibliothek verfügbar.
The approved original version of this doctoral thesis is available in print at TU Wien Bibliothek.
TU Bibliothek WIEN Your knowledge hub

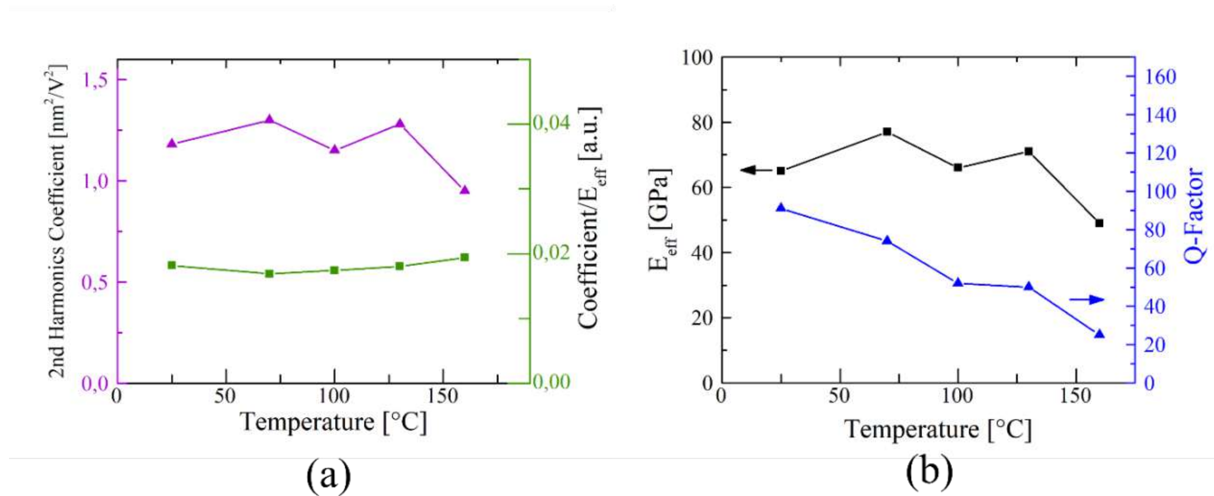

Figure 59 *Evaluation of the temperature-dependent MSA measurements of a PVDF cantilever. (a) The fi coefficient of the 2nd harmonics signal (purple) at temperatures ranging from 25 to 160°C. The coefficient is also plotted normalized to E_{eff} to demonstrate that the coefficient is almost constant over temperature. (b) The obtained E_{eff} from the thermal calibration method at various temperatures. The Q-factor of the cantilevers as a function of temperature is also shown.*

The $E_{mod,eff}$ decreased from 71 to 49 Gpa, which is close to the temperature dependent Young's modulus of gold nanofilms.[170] Compared to gold, PVDF has a much lower $E_{mod,eff}$ (71 Gpa to 2 Gpa), and therefore a direct comparison to pure gold films is reasonable. The *Q*-factor decreases from 80 to 20, most likely caused by a reduction in storage modulus with increasing temperature, which increases viscoelastic losses.[171]

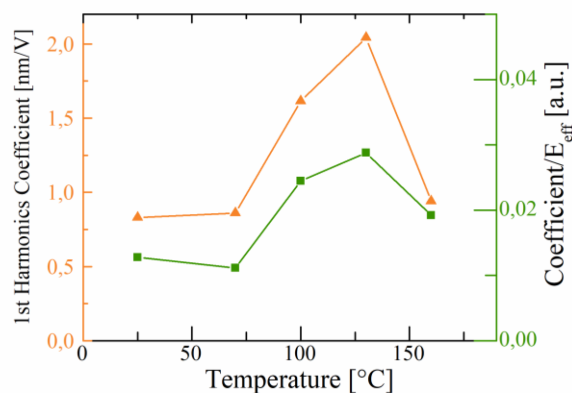

Figure 60 *The 1st harmonic quadratic fit coefficients (orange) at different temperatures and when normalized by E_{eff} (green).*

When analysing the 1st harmonics signal, the coefficient doubles from 70°C to 130°C, shown in *Figure 60*. Also, the coefficient is not directly correlated to the effective Young's modulus of the cantilever. The different temperature-dependent behaviour of the 1st and 2nd harmonics

could be due to increased polarization in the PVDF as the temperature increases. This is a reasonable assumption as the electrostriction is not dependent on the polarization, but the piezoelectric and flexoelectric effects are.[136]

To summarize, it was impossible to determine the flexoelectric coefficient in α-phase PVDF films quantitatively. With these investigations, however, these insights were obtained:

- A difference in bottom to top electrode width shifts the neutral axis off-centre, eliminating the need for a device layer, which reduces fabrication complexity and increases tip deflection amplitude.
- Electrostriction represents the most significant contribution to actuation.
- Electrostrictive α-phase PVDF cantilevers show comparable tip deflections to the piezoelectric counterpart β-phase PVDF-TrFE and theoretically can even outperform at high excitation fields above 5500 kV/cm.
- The temperature dependence of the tip deflection when excited at $f_m = 2 \cdot f_a$ is mainly correlated to the effective Young's modulus of the cantilever.
- The PVDF devices are stable up to ambient temperatures of 160°C in air.

4.2 Flexoelectric TiO_x cantilever

As introduced in section 3.5, another interesting material for flexoelectric device applications is TiO_x. There is no piezoelectricity due to the material's centrosymmetric crystal structure, and the electrostrictive effect is very weak, which will be demonstrated later. Based on these properties, this material was chosen for further investigations into the flexoelectric effect. First, the fabrication and the cantilever behaviour are analysed regarding different geometries and applied electric fields. Even more, analysis of the latter material was performed, where the crystal structure was determined with GI-XRD, and the film composition was analysed with XPS method. The flexoelectric effect of such a cantilever is calculated and presented in the context of other cantilever structures. Furthermore, different top electrode designs were tested to increase the flexoelectric actuation potential.

Die approbierte gedruckte Originalversion dieser Dissertation ist an der TU Wien Bibliothek verfügbar.
The approved original version of this doctoral thesis is available in print at TU Wien Bibliothek.
TU Bibliothek WIEN Your knowledge hub

Die approbierte gedruckte Originalversion dieser Dissertation ist an der TU Wien Bibliothek verfügbar.
The approved original version of this doctoral thesis is available in print at TU Wien Bibliothek.
TU Bibliothek WIEN Your knowledge hub

P-E curve and permittivity measurements

As a basis for investigating the flexoelectric effect in TiO_x, the dependence of the polarization to the electric field, the *P-E* curve, was measured. In principle, TiO_2 shows a temperature behaviour which indicates a phase transition into a ferroelectric phase, but the actual transition does not happen. This is why TiO_2 is sometimes called an incipient ferroelectric.[34] To rule out the possibility of any ferroelectric effects, the *P-E* curve of the TiO_x was measured with a Sawyer-Tower bridge circuit. Circular capacitor structures with the same fabrication parameters as the cantilevers were realized for these measurements. The resulting *P-E* curves at different frequencies can be seen in *Figure 61 a*. The polarization has a linear relationship with the applied sinusoidal electric field and does not vary significantly for various frequencies. The linearity shows that the TiO_x fabricated is paraelectric for the range of excitation voltages and frequencies used, and no additional polarization effects are expected.

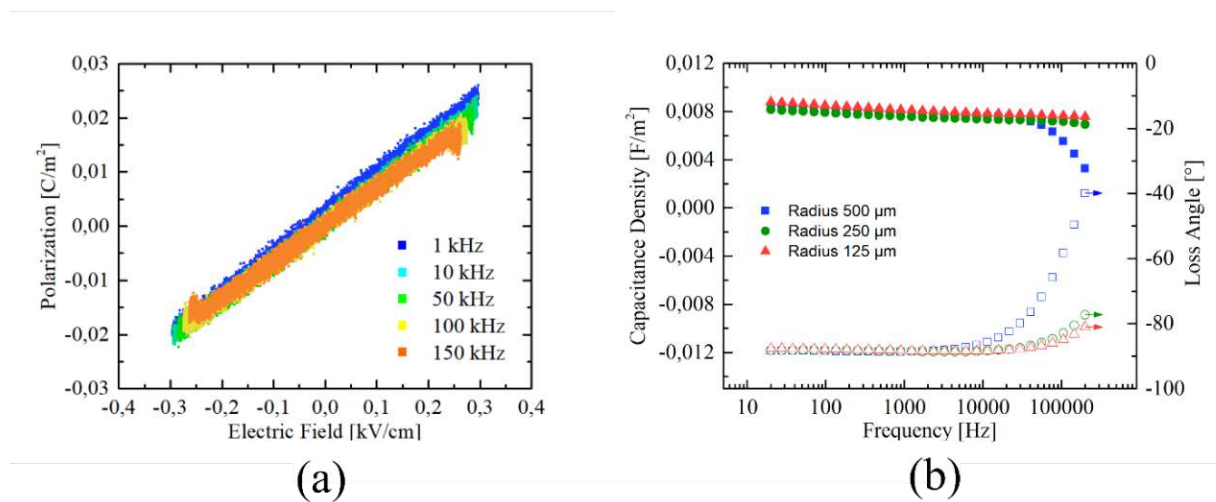

Figure 61 *Measurement of dielectric properties of $IrO_x/TiO_x/IrO_x$ parallel-plate capacitors. (a) The polarization vs. applied electric field plotted at various frequencies. (b) The measured capacitance density of capacitors over the frequency with varying capacitor radii. The loss angle is derived as shown in section 3.4.*

The dielectric constant must be known to calculate the flexoelectric coefficient and is calculated from the capacitance of the capacitors. The capacitance was measured in a frequency range between 20 Hz and 200 kHz with varying electrode radii of 125 µm to 500 µm. The resulting capacitance density and loss angle over frequency are depicted in *Figure 61 b*. The capacitance density does not change much as a function of frequency or electrode radius. For each radius, five devices were analysed, showing a variance in capacitance at a given frequency below 0.1 %. One exception is the 500 µm device at higher frequencies < 10kHz. Here, the capacitance

density drops, and the loss angle increases. This is likely due to increased leakage currents at higher radii and frequency (see section 3.4 for details). The loss angle shows values of -88° (close to the ideal -90°) at lower frequencies and increases at higher frequencies. The corresponding slope depends on the device radius and shows higher loss angles at larger electrode areas. However, the largest cantilever areas (4500 μm^2) are ten times smaller than the 125 µm capacitor devices (49000 μm^2) and hence, a drop in capacitance is not expected.

The derived dielectric constant for the analysed TiO_x films equals about 90 at 100 kHz (see section 3.5), which is a high value for sputtered TiO_x films, where values of 50-70 are reported. [172–174]

Determination of crystallographic and stoichiometric properties

The crystallographic microstructure of the IrO_x and TiO_x thin films was analysed with the grazing incidence X-ray diffraction method. As explained in section 3.4, the crystalline phases of thin films can be measured with a good signal-to-noise ratio. This is important for diffraction peak identification, as the IrO_x and TiO_x have reflections at very similar angles. For these measurements, a set of silicon (100) wafers were coated by sputtering either with a single IrO_x film or a double layer consisting of TiO_x on IrO_x. For reasons of comparison, the same sputter parameters as for the cantilever fabrication (section 3.3) were used for these samples.

The result of the analysis of these samples is shown in *Figure 62 a*. The two most prominent peaks, at 26° and 56°, show the common *c*-axis oriented rutile phase and correspond to the (110) and (220) crystal planes, respectively. [131,175] Reflections from other phases, such as anatase for TiO_2, cannot be identified. This is also in line with our pre-study on the influence of the bottom electrode material on the crystal structure of the deposited TiO_x, shown in section 3.5. However, a slight shift is determined between the TiO_x and IrO_x peaks. For the rutile (110) crystal plane, the shift is $\Delta 2\theta = 0.25°$, which translates to a lattice mismatch of ~ 0.03 Å. The literature shows that the lattice mismatch between IrO_2 and TiO_2 is 0.086 Å in the *a*/*b*-axis direction and 0.039 Å in the *c*-axis direction for single crystals. [176,177] Additionally, the polycrystalline nature of the double-layer samples was confirmed via SEM, shown in *Figure 62 b*, where an average grain size below 50 nm is identified.

Die approbierte gedruckte Originalversion dieser Dissertation ist an der TU Wien Bibliothek verfügbar.
The approved original version of this doctoral thesis is available in print at TU Wien Bibliothek.
TU WIEN Bibliothek Your knowledge hub

These results show that two goals were reached: First, the low permittivity anatase phase is not present, which means that the resulting flexoelectric actuation is expected to have the maximum value for this material. Secondly, the lattice mismatch between the IrO_x and TiO_x film is minimal, which lowers interfacial film stresses and avoids resulting static bends of the cantilever devices.

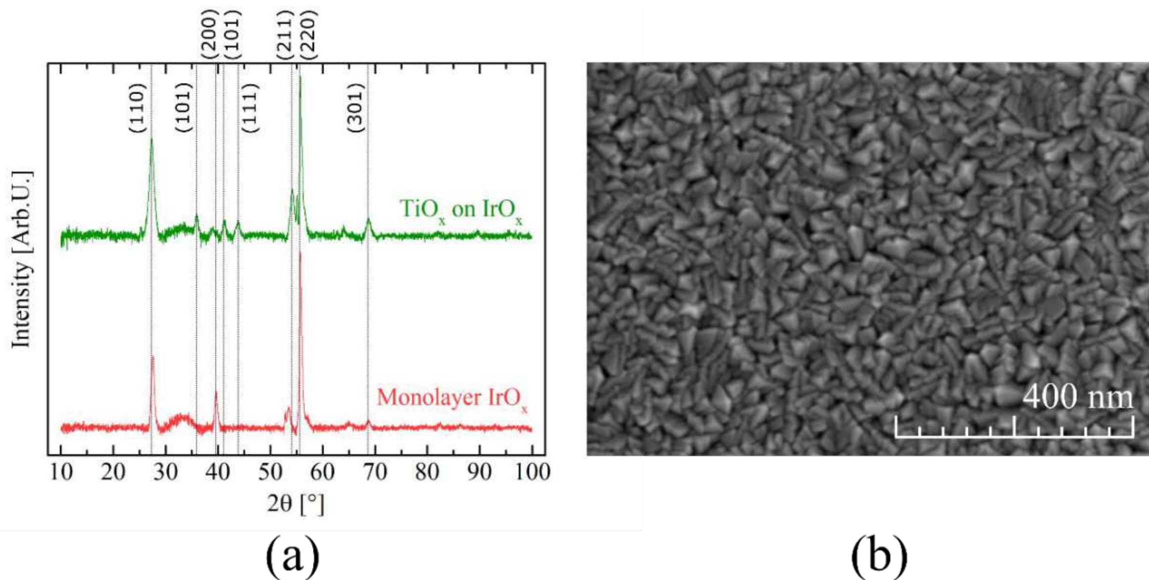

Figure 62 *The crystallographic investigations of sputtered IrO_x and TiO_x thin films. (a) GIXRD spectra of a single layer of IrO_x and an IrO_x/TiO_x bilayer deposited on a Si wafer. The rutile peaks are labelled with their corresponding crystallographic plane. (b) The surface morphology of a TiO_x thin film was recorded with the SEM. The sputtered films are polycrystalline with an average grain size of 40 (±10) nm.*

The chemical composition of the films was analysed with XPS. Three types of samples were compared:

- TiO_x on IrO_x sputtered on a Si wafer
- TiO_x sputtered on a Si wafer
- A piece from a single crystal rutile TiO_2 substrate

The bond concentrations were derived from the deconvolution of the Ti 2p XPS peaks, as shown in *Figure 63*. The TiO_x peak is also labelled with a C-OH compound, as the bond energies are similar. The respective bond energies are 533 eV for TiO_x and 533.3 eV for C-OH.[178,179] However, the C-OH peak is predominant materials such as carbon nanotubes with a high carbon content.[180] Given that our functional film does not contain carbon, it is reasonable to assume that this peak is related to TiO_x.[181]

Die approbierte gedruckte Originalversion dieser Dissertation ist an der TU Wien Bibliothek verfügbar.
The approved original version of this doctoral thesis is available in print at TU Wien Bibliothek.
TU Bibliothek Your knowledge hub WIEN

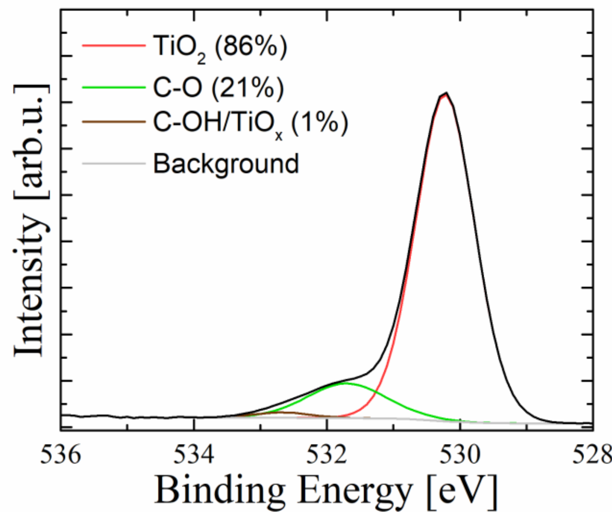

Figure 63 *XPS measurement of a TiO_x film deposited on IrO_x. The signal was deconvoluted into three peaks. The main contribution comes from the compound associated with TiO_2. The second largest contribution is C-O which stems most probably from surface contaminations due to the handling of the sample (no Ti-C bond was found). The third contribution is related to TiO_x.*

The Ti^{4+} component (= TiO_2) of the deconvolution is compared to the Ti^{3+} component (= TiO_x). The latter corresponds to oxygen vacancy presence in the material. The result is shown in *Table 3*.

	Ti^{4+} (TiO_2) [%]	*Ti^{3+} (TiO_x) [%]*
TiO_x/IrO_x on Si	95.1	4
TiO_x on Si	95	3.9
Single crystal TiO_2	95.5	3.3

Table 3 *The proportion of Ti^{4+} and Ti^{3+} bonds in the deconvolution of the Ti 2p peaks of samples obtained from XPS. A ratio of 100% Ti^{4+} bonds indicates stoichiometric TiO_2. The percentages do not add up to 100%, as the convolution contains trace amounts of pure Ti and Ti-C.*

The fraction of bonds associated with TiO_x (Ti^{3+}) is, for all samples, very similar and low, showing that the fabricated TiO_x films are close to the single crystal equivalent. If this was not the case, and the TiO_x films have a higher vacancy amount, there might be issues with the electrical insulating properties of the TiO_x layers. The resulting losses from the higher leakage currents would have a negative impact on the cantilever device performance. The effect of the oxygen vacancies in the TiO_x films on the leakage currents is analysed in-depth in section 4.3.

Die approbierte gedruckte Originalversion dieser Dissertation ist an der TU Wien Bibliothek verfügbar.
The approved original version of this doctoral thesis is available in print at TU Wien Bibliothek.
TU WIEN Bibliothek Your knowledge hub

Cantilever characterization

Using the recipe shown in section 3.3, IrO_x/TiO_x cantilevers were successfully fabricated. The analysed devices had a width of 45 µm and a varying length of either 35, 60 or 100 µm nominally. The actual length of the cantilevers varied up to ± 5 µm due to the process tolerances of the XeF_2 etching step. It is noted that a variation in length due to fabrication intolerances correlates to a change in device geometry that results in a variation in resonance frequency of up to 50 kHz across different devices. An exemplary device was recorded via SEM and is depicted in *Figure 64 a*. The fabricated devices did not show static bending, which would interfere with the MSA measurements.

Interestingly, the XeF_2 etch produced straight and smooth trenches compared to the α-phase PVDF cantilevers. It is not known where this difference in etch behaviour originates. In *Figure 64 b*, the cross-section of the thin film stack is shown. The TiO_x films show very low roughness, and columnar film growth.

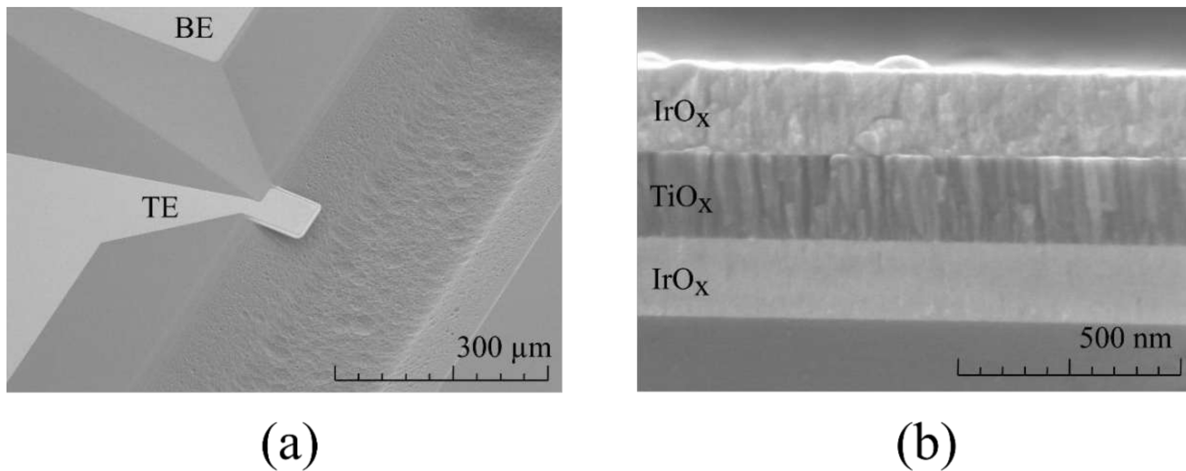

Figure 64 *SEM imaging of the TiO_x cantilevers. (a) An isometric view of one of the measured cantilevers. The top-electrode (TE) and bottom-electrode (BE) are also labelled. (b) Cross-section of the device layer stack. The TiO_x film shows columnar growth.*

The cantilevered devices were placed in the MSA and were excited with a sinusoidal voltage. A surface scan was performed at each excitation voltage step, where the voltage was varied from 0.2 to 2 V in 0.2V steps. Basically, the measurement frequency equalled the excitation frequency, except where the electrostrictive effect in TiO_x was determined. The raw data of a surface scan is shown in

Die approbierte gedruckte Originalversion dieser Dissertation ist an der TU Wien Bibliothek verfügbar.
The approved original version of this doctoral thesis is available in print at TU Wien Bibliothek.
TU Bibliothek WIEN Your knowledge hub

Figure 65. Here, the excitation frequency was at 10 kHz, far off the resonance frequency (~151 kHz), and the off-resonance modal shape corresponded to the 10 resonance mode. [182]

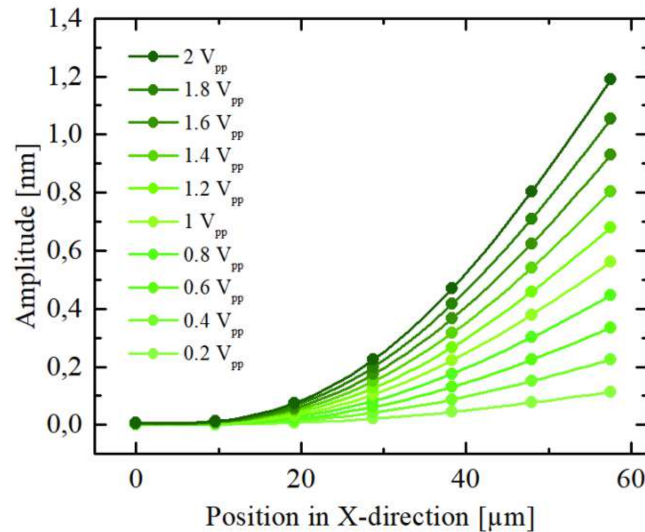

Figure 65 *Deflection amplitude of one line along a cantilever which is excited at different sinusoidal peak-peak voltages. The data was recorded with the MSA and corresponded to the maximum deflection at each location. A spline interpolation was added as a guide for the eye.*

Five cantilevers were measured, three with a nominal length of 60 µm and two with nominal lengths of 35 and 100 µm each. This set of cantilevers was chosen to check for the reproducibility of measurement results and to confirm the independence of the flexoelectric coefficient with regards to the cantilever length. In detail, the thermal calibration method was used on all five cantilevers. The individual effective Young's modulus of each cantilever was used to evaluate the flexoelectric coefficient. The power spectral density of one cantilever (derived from the cantilever tip deflection) in a frequency spectrum from 120 to 180 kHz is shown in *Figure 66*. The resonance peak in this measurement corresponds to the 10 out-of-plane mode of the cantilever, and the resonance frequency is 151.85 kHz.

Die approbierte gedruckte Originalversion dieser Dissertation ist an der TU Wien Bibliothek verfügbar.
The approved original version of this doctoral thesis is available in print at TU Wien Bibliothek.
TU WIEN Bibliothek Your knowledge hub

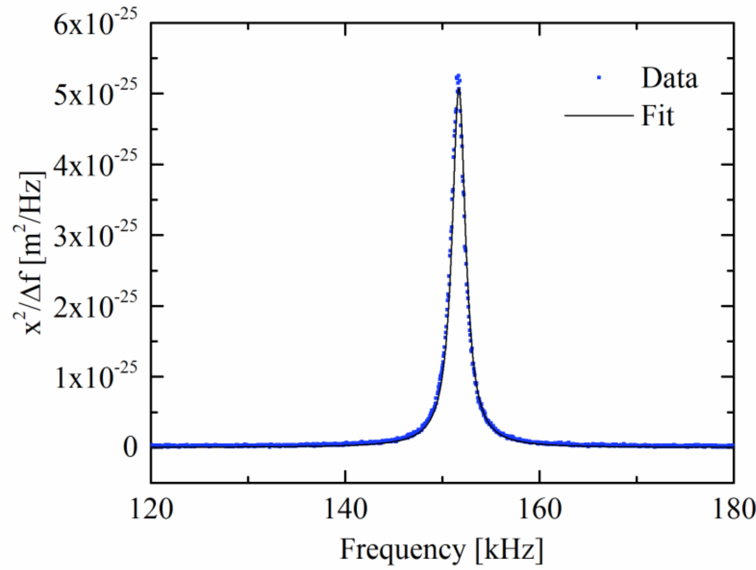

Figure 66 *The power spectral density at frequencies close to the first out-of-plane mode of the cantilever. The power spectral density is derived from the amplitude measured with the MSA without any external actuation. The thermal calibration fit, as explained in section 3.4, is also shown.*

Three different methods to obtain the $E_{mod,eff}$ are compared in the following. First off, the value is obtained from the equation for the resonance frequency of a cantilever:[26]

$$f_0 = \frac{1.875^2}{2\,\pi\,l^2}\sqrt{\frac{E_{mod,eff}}{12\,(1-\nu^2)\,\rho}} \tag{57}$$

The measured resonance frequency f_0 results when using $E_{mod,eff}$ = 217 GPa. The $E_{mod,eff}$ can be obtained from bulk literature values as a second method. The weighted sum of the individual $E_{mod,eff}$ when E_{IrO2} = 260 GPa and E_{TiO2} = 157 GPa, results in a $E_{mod,eff}$ = 225 GPa.[183,184] The third method is the aforementioned thermal calibration. This method, applied on all cantilevers, results in an average $E_{mod,eff}$ = (206.5± 11) GPa. As the thermal calibration values are close to the other two methods, the validity of this method is demonstrated.

Die approbierte gedruckte Originalversion dieser Dissertation ist an der TU Wien Bibliothek verfügbar.
The approved original version of this doctoral thesis is available in print at TU Wien Bibliothek.
TU WIEN Bibliothek Your knowledge hub

Electromechanical response

To assess the flexoelectric coefficient of TiO_x, it must be known what type of electromechanical effects are contributing in total to the actuation. Otherwise, the flexoelectric coefficient is overestimated.

Bulk piezoelectricity

Bulk piezoelectricity is not expected in TiO_2, as its crystalline phases do not have the necessary point group symmetry needed for a piezoelectric effect to occur. In principle, it is possible that so-called nano-polar regions can be present in ferroelectric materials. [185] However, we do not see any ferroelectric or paraelectric behaviour in the P-E measurements, shown in *Figure 61 a*. With these arguments, any bulk piezoelectric effect can safely be ruled out.

Field gradients in bulk (bulk flexoelectricity)

It has been shown that bending a curved beam can induce a flexoelectric effect due to geometry changes.[186] Consider a beam bent upwards (see *Figure 17* in section 2.3). Due to the bending, one beam surface gets stretched while the opposite surface is compressed. This difference in the surface area of the opposing electrodes leads to a field gradient in the bulk. However, in the case of the fabricated TiO_x microcantilevers, the spatial difference between the two electrodes is $6 \cdot 10^{-7}$ m. This is a minimal difference compared to the bending radius of ~2.5 m, making the effect negligible.[187]

Another factor to consider is the field gradients due to geometrical imperfections in the TiO_x. Such imperfections include micro-cracks, grain boundaries and lattice dislocations. No micro-cracks can be identified from SEM cross-sectional measurements (see *Figure 62 b*). Grain boundary effects and lattice dislocations are not easily determined and are assumed to be small due to their high local restriction.

Dynamic flexoelectricity

The dynamic flexoelectric effect is present when the geometric dimension of the bulk of the functional material is significantly larger than the acoustic wavelength of the excitation signal. In our case, the determining geometric dimension is the thickness of the TiO_x with 200 nm. The

Die approbierte gedruckte Originalversion dieser Dissertation ist an der TU Wien Bibliothek verfügbar.
The approved original version of this doctoral thesis is available in print at TU Wien Bibliothek.
TU WIEN Bibliothek Your knowledge hub

excitation frequency when determining the flexoelectric coefficient is 10 kHz, meaning that the acoustic wavelength is 0.5 m. Due to this large difference in size, this effect can be disregarded for this analysis.[6]

Surface flexoelectricity

In section 2.3, the general problem of the existence of the surface flexoelectric effect was discussed.[90] However, for the following estimation of the surface flexoelectric effect, it is assumed to exist and scales as proposed initially.[6] The scaling of the flexoelectric coupling coefficient is estimated to scale with the inverse of the permittivity χ and lattice constant a, $\Gamma_{surf} \sim \frac{q}{a\,\chi}$. The bulk- and surface-flexoelectric effect scales with $\Gamma \sim \frac{q}{a}$. Assuming that the pre-factors are the same, which is reasonable as the material is the same, a difference of 2 magnitudes ($\chi_{TiOx} \sim 100$) is observed. The surface flexoelectric effect is thus also negligible.

Electrostriction

The electrostrictive effect is, in theory, present in the analysed device and can be measured directly. This is done with the measurement method described in section 3.4, where the first and second harmonics are measured separately. The result of this measurement is illustrated in *Figure 67*. It can be seen clearly that the magnitude of resonance amplitude of the second harmonic is significantly lower than the first harmonic actuation. In detail, the resonance amplitude is lower by a factor of about 1/50.

Die approbierte gedruckte Originalversion dieser Dissertation ist an der TU Wien Bibliothek verfügbar.
The approved original version of this doctoral thesis is available in print at TU Wien Bibliothek.
TU Bibliothek WIEN Your knowledge hub

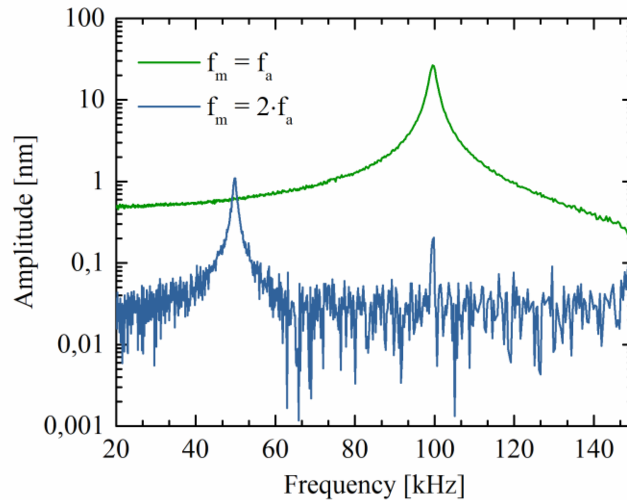

Figure 67 *Deflection amplitude of* TiO_x *cantilevers measured with the MSA at* $f_m = f_a$ *and* $f_m = 2{\cdot}f_a$*. The signal related to the electrostrictive effect (blue) is significantly lower than the flexoelectric actuation (green).*

Surface piezoelectricity

Section 2.3 showed that the surface piezoelectric effect could be easily mistaken with the flexoelectric bending (or interface flexoelectric effect). The main reason for this is the similar scaling of the surface piezoelectric coefficient and having a similar magnitude to the flexoelectric coefficient.

The surface piezoelectric effect exists because the unit cell at the surface differs from the bulk unit cell. In the case of the analysed IrO_x/TiO_x cantilever, the unit cells of both materials are in the rutile phase and have very similar lattice spacing (shown in *Figure 62 a*). It is reasonable that the change in unit cell structure at the interface of TiO_x/IrO_x is less than in the TiO_x/Air case. [8]

[8] In detail, the change of unit cell atom positions when TiO_x is in contact with IrO_x as compared to when in contact with air.

Die approbierte gedruckte Originalversion dieser Dissertation ist an der TU Wien Bibliothek verfügbar.
The approved original version of this doctoral thesis is available in print at TU Wien Bibliothek.
TU Bibliothek Your knowledge hub WIEN

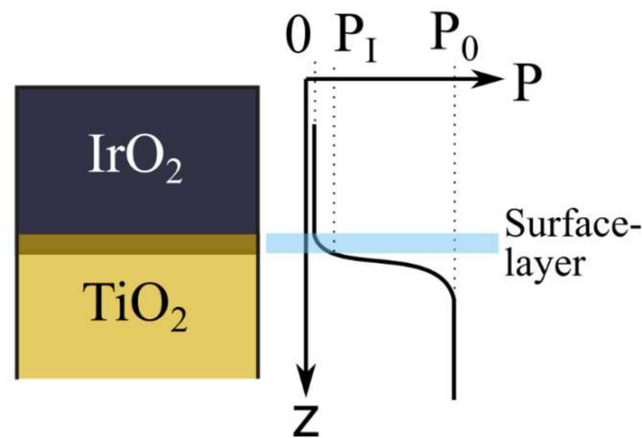

Figure 68 *Schematics of the TiO_2 surface layer when in contact with IrO_2. The proposed polarization in the spatial direction along the thickness of the cantilever. As this surface layer is only a few nm thin, the polarization at the interface P_I is much lower than the polarization inside the bulk of the TiO_2, P_0.*

Even more, the thickness of the reconstructed surface layer is in the low nm range. However, the proposed polarisation change at the interface spans a much larger space. This was shown by Abdollahi *et al.*, where the electric field of a beam of a single material exposed to an external electric field was simulated.[188] This study finds that the polarization gradient at the interface spans as wide as 10% of the beam's thickness. *Figure 68* shows a schematic of the polarization curve in such a case. The total polarization at the interface P_I is much lower than the polarization in the bulk P_0.

An estimation for the piezoelectric surface effect of a beam with thickness 200 nm is done. It is assumed, that the piezoelectric surface coefficient is the same as the flexoelectric coefficient. Also, a linear increase of the polarization from 0 in the IrO_x to P_0 in the TiO_x over a length of 20 nm (10%) is assumed. Only the uppermost unit cell layer of the TiO_x is reconstructed. This layer has a width of one unit cell width which is approximately 0.4 nm. The polarization P_I in these 0.4 nm is less than 2% of the bulk value P_0.

This means, that even though the coefficient of the piezoelectric surface effect equals the flexoelectric effect, the piezoelectric surface effect is a lot weaker than the flexoelectric effect. In this case, scaling with a polarization gradient yields higher actuation than scaling with the absolute value of the polarization.

Die approbierte gedruckte Originalversion dieser Dissertation ist an der TU Wien Bibliothek verfügbar.
The approved original version of this doctoral thesis is available in print at TU Wien Bibliothek.
TU WIEN Bibliothek Your knowledge hub

Flexoelectricity at the interface

As other electromechanical effects can be ruled out reasonably as the main contributors to the total actuation of the cantilevers, the flexoelectric bending mechanism is the most likely cause for the electromechanical actuation of the cantilevers. The flexoelectric coefficient of TiO_x can therefore be derived from *equation 28* for flexoelectric bending.

Coefficient determination and comparison to theory

The resonating behaviour of the cantilevers was measured with the MSA surface scan method. For the results shown in *Figure 69 a*, an excitation frequency was set, and several surface scans at different excitation voltages were performed. The voltage at each frequency step was swept from 0 to 2 V in 0.2 V steps. The excitation frequency was set to four values, 10 kHz, 100 kHz, resonance frequency (~151 kHz) and 160 kHz. The curvature was extracted from the surface scans, as explained in section 3.4.

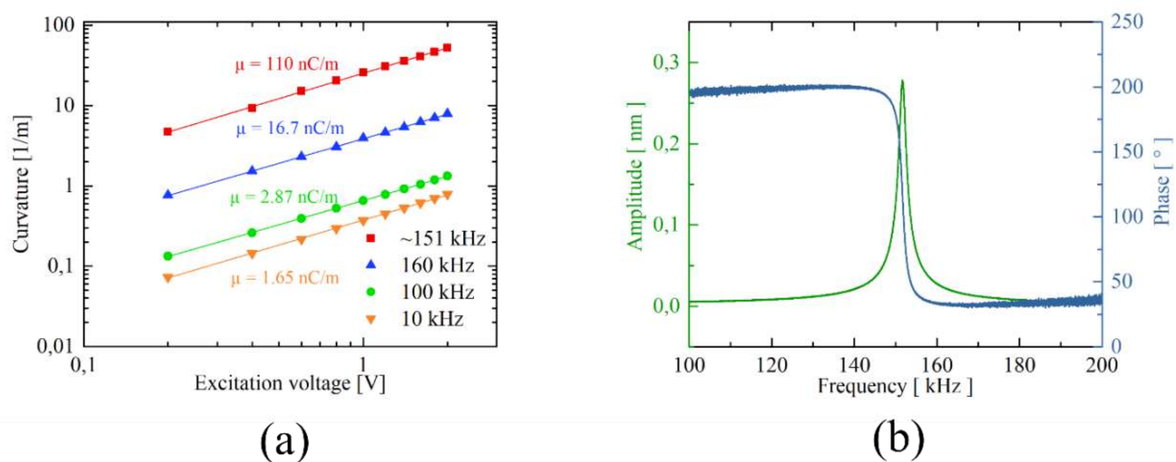

Figure 69 *Measurement of the flexoelectric coefficient and resonance behaviour of TiOx cantilevers. (a) The determined curvature at voltages up to 2 V at various frequencies. (b) Deflection amplitude and phase spectrum between 100 and 200 kHz.*

An additional measurement is shown in *Figure 69 b*, where the sinusoidal excitation frequency was set to a periodic chirp from 100 to 200 kHz, and the cantilever tip deflection was measured. The phase difference between the excitation signal and the measured deflection signal was also recorded. A *Q*-factor of 90 is calculated from this resonance curve. The phase shows the expected 180° phase shift when the frequency changes from a value lower than the resonance frequency to a value higher than the resonance.

Die approbierte gedruckte Originalversion dieser Dissertation ist an der TU Wien Bibliothek verfügbar.
The approved original version of this doctoral thesis is available in print at TU Wien Bibliothek.
TU Bibliothek WIEN Your knowledge hub

The effective flexoelectric coefficient μ_{eff} (where the main contributions are the longitudinal μ_{11} and transverse μ_{12} coefficient) is calculated from the curvature. It can be seen that the flexoelectric coefficient depends on the resonant behaviour of the cantilever. Measuring at resonance gives a much higher μ_{eff} compared to off-resonance. To avoid any unwanted amplification of the μ_{eff} due to a resonance behaviour, a measurement at an excitation frequency of 10 kHz was performed, far off-resonance.

To show that the influence of the resonance is sufficiently low, the tip deflection of a cantilever was measured with an applied periodic frequency chirp from 1 to 160 kHz. This results in the resonance curve shown in *Figure 70*. The tip deflection does not change significantly below 30 kHz. Additionally, surface scans at frequencies 1, 10 and 20 kHz were performed, showing flexoelectric coefficients of 1.98 nC/m, 1.65 nC/m and 1.67 nC/m, respectively. The coefficient increase at 1 kHz is most likely due to frequency interference with the ambient noise. From this data, it is concluded that 10 kHz is a suitable frequency to determine the flexoelectric coefficient, as this frequency is far enough off any resonance frequency and is not affected by ambient noise.

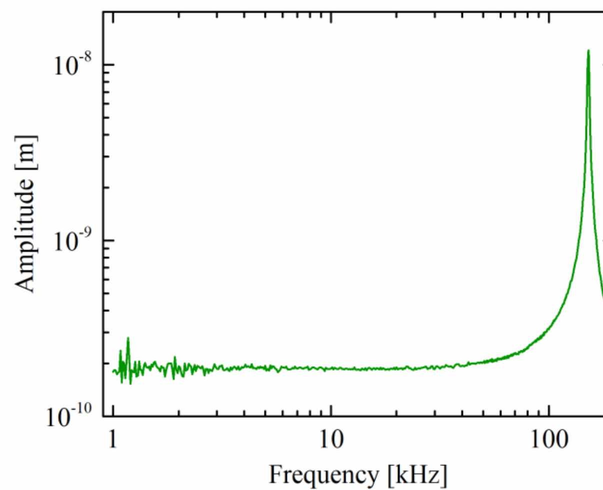

Figure 70 *Response characteristics of the cantilever as a function of excitation frequency represented by the tip amplitude. Low-frequency measurements demonstrate the plateau in the response characteristics at frequencies far below resonance.*

The flexoelectric coefficient of three cantilevers with a nominal length of 60 µm was determined at 10 kHz. The effective flexoelectric coefficient was determined as μ_{eff} = 1.78 ± 0.16 nC/m. The shorter cantilever at 35 µm nominal value yielded a flexoelectric coefficient of

Die approbierte gedruckte Originalversion dieser Dissertation ist an der TU Wien Bibliothek verfügbar.
The approved original version of this doctoral thesis is available in print at TU Wien Bibliothek.
TU WIEN Bibliothek Your knowledge hub

μ_{eff} = 1.61 nC/m, and the nominal 100 µm long cantilever resulted in a μ_{eff} = 1.97 nC/m. There seems to be a slight dependence of μ_{eff} with the cantilever length. Even though this dependence is small, a more in-depth study should be performed in future. The measured coefficients are close to the theoretically calculated 2.5 nC/m for single crystal TiO_2 with a permittivity of 90[9]. The lower measured value compared to the theoretical one most likely comes from crystallographic difference to a perfect TiO_2 single crystal. The TiO_x film of the measured cantilevers is polycrystalline and is not stoichiometric. This leads to intrinsic structural defects and higher leakage currents, leading to higher losses. The anchor of the cantilever also leads to additional losses.

The resulting coefficient is also very close to the measured coefficient of single crystal TiO_2 beams with a flexoelectric coefficient of ~ 1.7 nC/m, as performed by *Narvaez et al*.[36] But, a direct comparison is not straightforward. In the case of this study, the millimetre-sized beams were bent with a three-point bending method. In this method, the direct flexoelectric effect is used to generate the charges, which are measured. Here, the surface flexoelectric effect cannot be disregarded, as the surface will exhibit the largest deformation of the whole beam and contribute significantly to the total number of charges.

It was also checked if the resulting flexoelectric coefficient fits Kogan's estimate. Kogan's estimate indicates that any material's flexoelectric coupling coefficient Γ $(= \mu/\chi)$ lies in the range of 1 to 10 V. [83] Kogan's estimate yields 3.14/4.87 V for the TiO_2 a/c-axis lattice constants. For the characterized devices, the flexocoupling coefficient has a value of 2.75 V at 10 kHz. This shows that also the flexoelectric coupling coefficient is reasonably close to Kogan's estimate.

As discussed with the PVDF cantilevers in section 4.1, comparing cantilevers is not straightforward. However, from a geometry point of view, the TiO_x cantilevers are readily comparable to the electrostrictive PVDF cantilever. The PVDF cantilevers achieved a ~150 nm tip deflection @ 30 V with a length of ~60 µm and 600 nm total thickness. For the TiO_x cantilevers, a 231 nm tip deflection @ 2V was achieved. The break-even point between the linearly scaling TiO_x cantilevers and the quadratic scaling PVDF cantilevers is at around 70 V. This voltage is not achievable with the electrostrictive cantilever. To reach the same amplitude

[9] Calculated with Kogan's estimate as: $\mu = \frac{q\,\chi}{4\pi a}$

Die approbierte gedruckte Originalversion dieser Dissertation ist an der TU Wien Bibliothek verfügbar.
The approved original version of this doctoral thesis is available in print at TU Wien Bibliothek.
TU Bibliothek WIEN Your knowledge hub

(in resonance) as the flexoelectric cantilever at 2 V, 25 V have to be applied to the electrostrictive PVDF cantilever.

To further improve the flexoelectric actuation of the TiO_x cantilevers, an electrode design was developed with the goal to increase the field gradient density.

Segmented top electrode

By introducing a specifically patterned top electrode leads to a locally enhanced field gradients which extend also into the core region of the layer, thus increasing flexoelectric actuation. However, segmenting the electrodes always reduces the overall area of the electrode. As the basis for this actuation principle is an interface effect between the electrode and the functional insulator, one could potentially lose actuation potential when decreasing the electrode area. In this section, the main effect dominating the cantilever actuation is investigated.

The electrode segmentation idea is shown schematically in *Figure 71 a* and *b*.

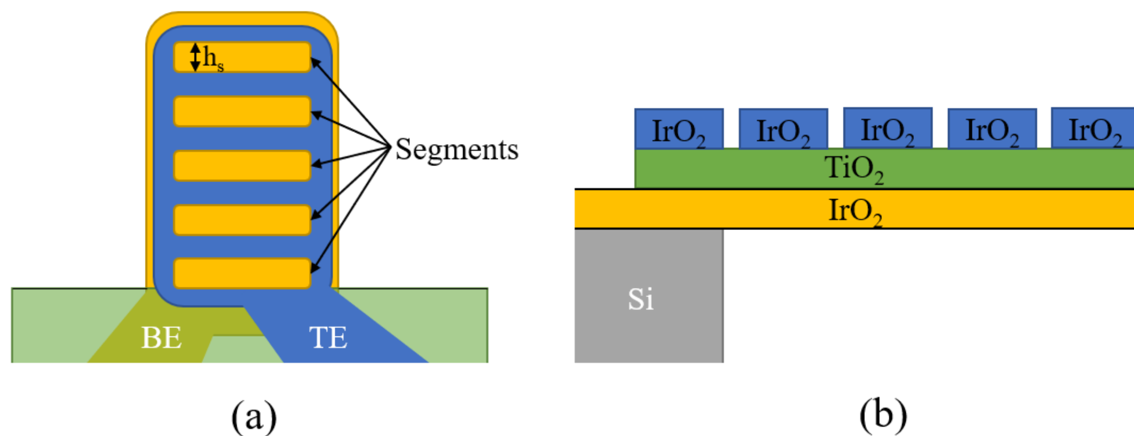

Figure 71 *(a) Top view of the cantilever design principle. Here, empty segments with gap size h_s are introduced into the top electrode (TE). (b) Cross-section of the cantilever. Gaps in the top electrode lead to gradients in the electric fields throughout the bulk of the TiO_2 layer.*

To properly determine the effect of this electrode segmentation, the TE was designed with a varying number of segments while keeping the total area of the TE constant. Varying the number of electrodes is used as a sweeping parameter, as it is hypothesised that more gaps lead to more field gradients due to the increased total length of edges.

However, when increasing or decreasing the number of segments, the TE area changes, affecting the resulting actuation. As such, the top electrodes with varying segment numbers

Die approbierte gedruckte Originalversion dieser Dissertation ist an der TU Wien Bibliothek verfügbar.
The approved original version of this doctoral thesis is available in print at TU Wien Bibliothek.
TU Bibliothek WIEN Your knowledge hub

change the segment gap size to keep the area covered by the top electrode constant while increasing the number of open segments. The gap size varied between 2 and 50 µm depending on the cantilever size and the number of segments. It must be noted that the all segments of the top-electrode are at the same electric potential and therefore they are not generating an additional lateral electric field between the segments. The TE edges act as a discontinuity, leading to an electric field gradient. Hence, the gap size is not a critical parameter, but the total length of the edges of the segments is. The resulting area and edge length versus the number of open segments is illustrated in *Figure 72*.

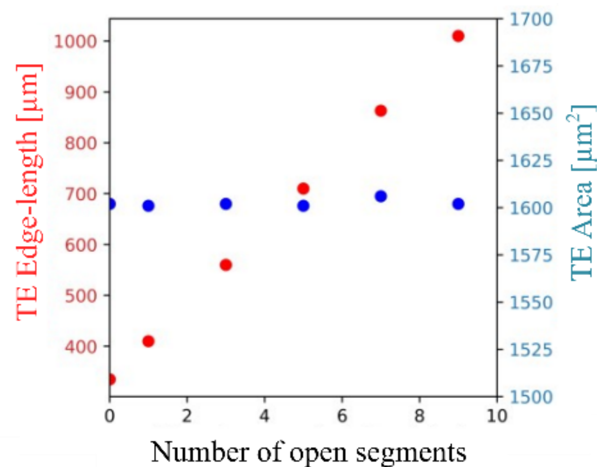

Figure 72 *The designed TE edge length as a function of the number of open segments as well as the TE area are shown. The edge-length increases with more segments, whereas the area stays approximately constant.*

The final design of the devices with different segment numbers can be found in section 3.3, *Figure 31*.

Figure 73 shows the side view of the cantilever with the calculated electric field (colour map) and the field gradient (black arrows). From these figures, the expected result is demonstrated that the segmented top electrode introduces field gradients. A careful analysis showed that only introducing these segments dampens the cantilever actuation and an etching step is necessary for the segments to have a positive effect on the actuation, as will be explained in the following. In *Figure 73 a*, coloured arrows were inserted to schematically illustrate in which direction the different field gradients in the *z*-direction (∇E_z) point. The *z*-direction is mainly analysed, as the field gradient in *x* direction is equal above and below the neutral axis, and therefore their bending moments cancel each other out. In *Figure 73 a*, the blue arrows show gradients where the bending moments are clockwise and superimpose. Violet arrows indicate gradients that lead to counterclockwise bending moments. The bending moment, where the most significant field

Die approbierte gedruckte Originalversion dieser Dissertation ist an der TU Wien Bibliothek verfügbar.
The approved original version of this doctoral thesis is available in print at TU Wien Bibliothek.
TU WIEN Bibliothek Your knowledge hub

gradient is (white), is counteracting both the moment from the interfacial effect and the electrode segmentation.

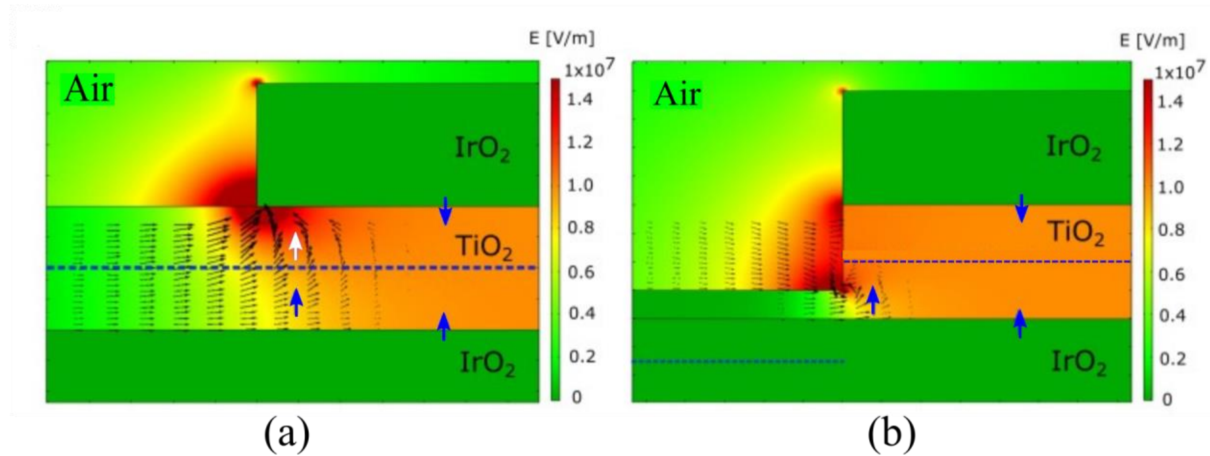

Figure 73 *(a) The simulated electric field (colour plot) and the electric field gradient (black arrows) of a segmented top electrode for no etch. (b) The electric field gradient for the etched case. The field gradients' general direction from the TE design and the IrO_x/TiO_x interface are shown as coloured arrows, and the neutral axis is shown as a blue dashed line. Blue arrows indicate gradients that lead to a clockwise bending moment and white arrows to a counterclockwise bending moment of the cantilever.*

This problem can be solved by anisotropically etching the TiO_x layer to a depth below the neutral axis prior to etching. This case is shown in *Figure 73 b*. Now, the electric field gradient is most significant below the neutral axis and all moments add up.

As a consequence, the thin film stress compensation had to be changed to realise this design. In the previous cantilever design, the stress was compensated by the TE, which is now more sophisticated as the TE geometry consists of different segmented electrodes. Sputter parameters were successfully adapted such that the stresses in both BE and TiO_x layers compensate each other while the TE layer stress should be as low as possible (in the fabricated devices, the stress was below 200 MPa generally).

Die approbierte gedruckte Originalversion dieser Dissertation ist an der TU Wien Bibliothek verfügbar.
The approved original version of this doctoral thesis is available in print at TU Wien Bibliothek.
TU WIEN Bibliothek Your knowledge hub

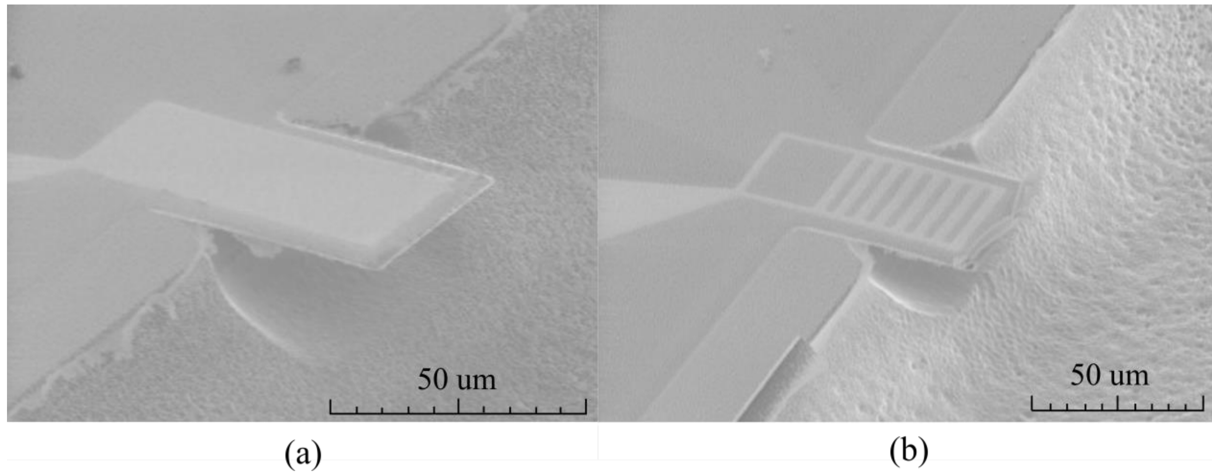

Figure 74 Microscope pictures of the tested devices. (a) A reference design with a fully covering TE is shown. (b) A cantilever with a segmented top electrode is shown. Similar to the PVDF cantilevers in section 4.1, the XeF_2 etch rate close to the cantilever is higher, resulting in an uneven under-etch. Also, a residual resist can be seen at the edges of the cantilevers. Both devices were functional, however.

In *Figure 74*, different stages of the cantilever process are shown. The segmented cantilever structures were produced successfully, although the yield was low due to the problematic IrO_x lift-off, which is especially challenging for the small gaps (~ 5 µm) at the TE.

The cantilever tip deflection with different segment numbers was measured with the MSA, and the result are shown in *Figure 75*. Here the resonance frequency of each cantilever was determined prior to any further analysis by a frequency sweep, so that the cantilevers were excited most precisely at the device-specific resonance frequency.

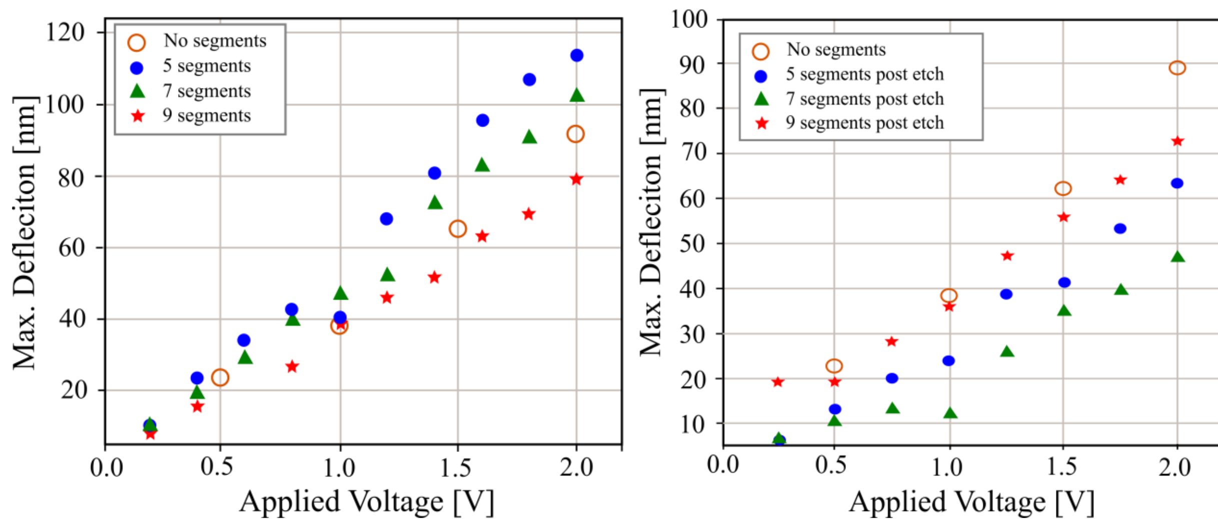

Figure 75 The cantilever tip deflection over the applied voltage measured with the MSA in resonance is shown. 4 different top electrode structures are compared, namely with 0/5/7/9 segments. While the 5/7/9 segment cantilevers are yielded from one wafer, the 0 segment structure was from a different wafer. (a) The maximum deflection before the TiO_x etch. (b) The maximum deflection after the TiO_x etch. The 0 segment device was not post-etched but is shown for reference.

Die approbierte gedruckte Originalversion dieser Dissertation ist an der TU Wien Bibliothek verfügbar.
The approved original version of this doctoral thesis is available in print at TU Wien Bibliothek.
TU Bibliothek Your knowledge hub WIEN

Figure 75 a shows the tip deflection vs. amplitude of the sinusoidal excitation of the unetched segmented cantilevers and a reference cantilever without segments. Unfortunately, the reference structures with no segments on the same wafer failed in compensating film stresses. This leads to static bends that make the devices unmeasurable in the MSA. However, the reference structures with no segments from another wafer is shown. At first glance it seems that the segmenting has a positive effect on the deflection amplitude when comparing the reference device to the 5 and 7 segment devices. However, when the number of segments is increased, a decrease in deflection amplitude is observed, according to the theory. It must be noted that resonator properties vary from wafer to wafer and hence, some uncertainty in direct comparison of devices can occur.

Using RIE, the same set of cantilevers was then etched with SF_6/O_2. The resulting tip deflection of the cantilevers after etching can be seen in *Figure 75 b*. The total tip deflection of all cantilevers decreased, whereas the one with 9 segments seems to be affected the least. This is evidence that etching the TiO_x leads to beneficial field gradients favouring more edge length. However, there are still many issues to be solved. First, the total deflection of all cantilevers decreased, which could be due to the different resonance behaviour of segmented and unsegmented devices. Secondly, the deflection dependent on the number of segments of the etched cantilevers is not following a clear trend, as the 5-segment cantilever showed more actuation than the 7-segment one. Therefore, more experimental data are needed to support the theoretical considerations.

4.3 Electric behaviour of $IrO_x/TiO_x/IrO_x$ capacitors

While increasing the flexoelectric actuation with geometric design optimization is an intuitive approach, it showed no consistent increase in the cantilever deflection. Also, the straight-up approach with fully covering electrodes and an interfacial field gradient is more reliable than the segmented electrode approach, as the fabrication process is simpler. As the interface effect is a promising way of actuating devices via the flexoelectric effect, it is essential to understand the electric behaviour of the pure capacitor. For this purpose, we focused on leakage current measurements supported by XPS, TEM and CV measurements.

Die approbierte gedruckte Originalversion dieser Dissertation ist an der TU Wien Bibliothek verfügbar.
The approved original version of this doctoral thesis is available in print at TU Wien Bibliothek.
TU Bibliothek WIEN Your knowledge hub

Die approbierte gedruckte Originalversion dieser Dissertation ist an der TU Wien Bibliothek verfügbar.
The approved original version of this doctoral thesis is available in print at TU Wien Bibliothek.
TU Bibliothek WIEN Your knowledge hub

Experimental details

All TiO_x capacitor devices were made with the same process parameters as the TiO_x cantilever devices presented in section 3.3. However, the capacitor devices differ according to the following points. The substrates for these samples were p-doped silicon wafers with a 50 Ω·cm bulk resistivity. The use of undoped wafers were not necessary, as the bottom electrode and the top electrode of the capacitor are both not arranged on the wafer surface side by side, as for the cantilever structure. In contrast, the bottom electrode has a contact pad for the capacitors, and the top electrode is contacted directly via a prober needle (as shown in section 3.4).

The set of samples that were compared vary according to the following parameters: Set 1 is most similar to the TiO_x cantilever fabrication. Here 100/*h*/100 nm $IrO_x/TiO_x/IrO_x$ capacitor devices with varying dielectric thickness and a top electrode diameter of 250 µm were fabricated. After depositing the bottom IrO_x electrode on the substrate, the sample was removed from the sputtering chamber and exposed to air for approximately one day. For the second set, the gas composition in the sputtering process of the TiO_x layer was varied and the bottom electrode was also exposed to air. For the third set, the sample was not removed from the sputtering chamber, and the TiO_x layer was sputtered without breaking the vacuum. The detailed parameters of the sets are shown in *Table 4*.

	Sputter chamber gas flow O_2/Ar [sccm]	*TiO_x layer thickness [nm]*	*Bottom interface exposure to air*
Set 1	20/0	50 100 150 200	Yes
Set 2	10/10 12/8 14/6 16/4	100	Yes
Set 3	20/0	100	No

Table 4 *Sample parameters of the three sets fabricated for evaluating the electrical properties of the IrO_x/TiO_x interface.*

These samples were mainly characterized by *JV* and CV measurements with the setup described in section 3.4. Characterization with the XPS and TEM methods was performed on samples

fabricated in addition to the ones in *Table 4*. These samples are IrO_x/TiO_x and $IrO_x/TiO_x/IrO_x$ samples without lithography and had fabrication parameters according to set 1.

Material characterisation

An investigation of the set 1 samples' cross-section in the SEM, as illustrated in *Figure 76*, shows a very similar structure compared to the samples presented in section 4.2. IrO_x and TiO_x films show a columnar polycrystalline microstructure with grain sizes below 50 nm. In the case of these samples, the IrO_x layer has a thickness of 120 nm instead of the nominal 100 nm. This deviation from the nominal value is likely due to the sputter parameters not being optimized to achieve a good thickness precision. A high sputter rate of 10 nm/s was reached with these parameters. As the total sputtering time of 10 seconds is relatively short, it is likely, that variations when igniting the plasma in the chamber lead to these thickness variations. However, the electrical behaviour of the fabricated capacitors is more likely to be determined by the dielectric thickness than the electrode thickness.

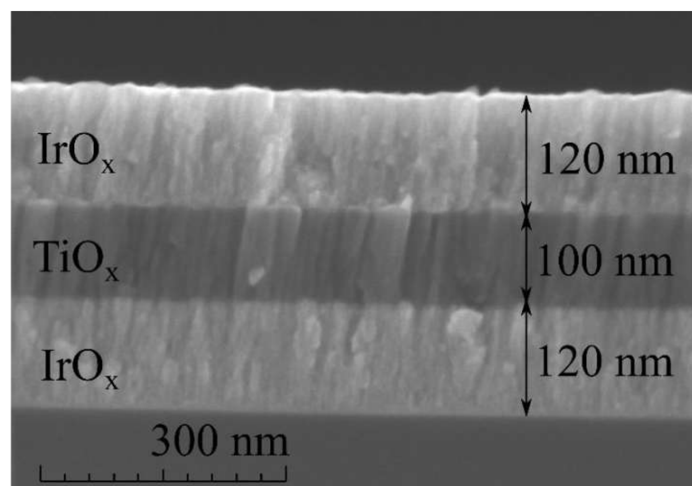

Figure 76 *Cross-section of the nominally 100 nm thick* TiO_x *parallel-plate capacitor. A columnar polycrystalline film morphology is identified.*

The electrical measurements in this study were performed at temperatures ranging from room temperature to 100°C. To check the chemical stability of the IrO_x electrode, the oxidation state under elevated temperatures in a vacuum was analysed with XPS. The measured Ir 4f peaks are illustrated in *Figure 77*. The 61.9 and 64.9 eV peaks correspond to the $4f_{7/2}$ and $4f_{5/2}$ peaks of IrO_2, respectively.[189] At temperatures below 150°C, only IrO_2 peaks are detectable. When

Die approbierte gedruckte Originalversion dieser Dissertation ist an der TU Wien Bibliothek verfügbar.
The approved original version of this doctoral thesis is available in print at TU Wien Bibliothek.
TU WIEN Bibliothek Your knowledge hub

increasing the temperature above 150°C, the IrO_2-associated peaks decrease in intensity, and new peaks at 60.8 eV and 63.8 eV emerge. These peaks are associated with the $4f_{7/2}$ and $4f_{5/2}$ peaks of unoxidized Ir. Since only the IrO_2 specific peaks are present below 150°C, it is shown that IrO_x layers do not decompose to Ir at temperatures up to 150°C in a vacuum environment. Consequently, it is even less likely that the functional material will reduce to Ir in an oxygen-containing environment such as in air when performing the *JV* measurements.

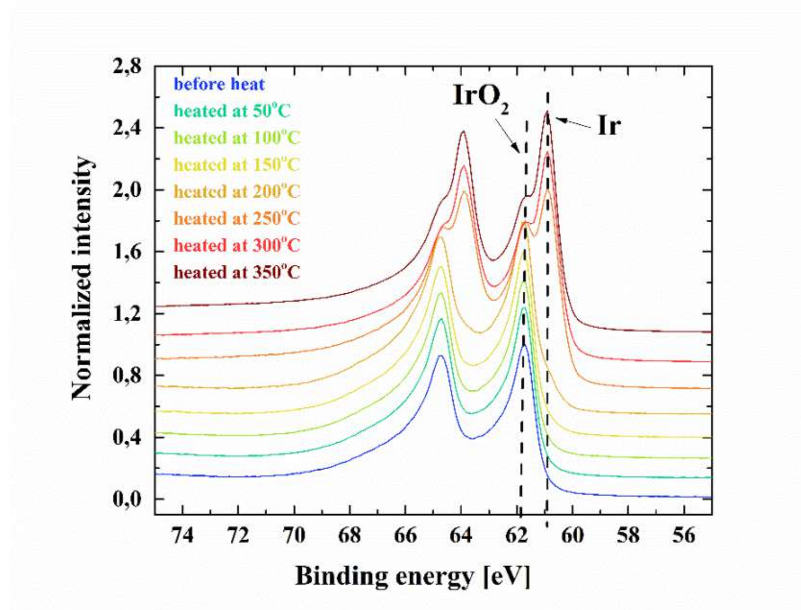

***Figure** 77 XPS spectra of Ir 4f of IrO_x samples measured at various temperatures in a vacuum chamber. At temperatures below 200°C, the Ir 4f peaks indicate IrO_2 bonds. At temperatures of 200°C and higher, the peak position shifts to a value typical for pure Ir.*

Like the XPS measurements shown in section 4.2, an XPS study was performed on the samples, including an analysis when water is present. The result of this measurement is shown in *Figure 78*. An energy spectrum from 526 to 538 eV was analysed, where oxygen related O 1s peaks are expected. The obtained signal for the IrO_x top electrode, seen in *Figure 78*, can be deconvoluted into four components. The components found from the deconvolution procedure are: [179,189–191]

- Oxygen in IrO_2 bonds.
- Oxygen in OH bonds.
- Oxygen in adsorbed water.

Die approbierte gedruckte Originalversion dieser Dissertation ist an der TU Wien Bibliothek verfügbar.
The approved original version of this doctoral thesis is available in print at TU Wien Bibliothek.
TU Bibliothek WIEN Your knowledge hub

- Oxygen in electrically isolated[10] H_2O, *i.e.*, moisture on the sample.

Comparing the relative occurrence of the components to each other, the surface of the IrO_x has a significant amount of OH bonds and adsorbed water on the surface. It is reasonable to assume that all IrO_x surfaces in contact with air show similar behaviour.

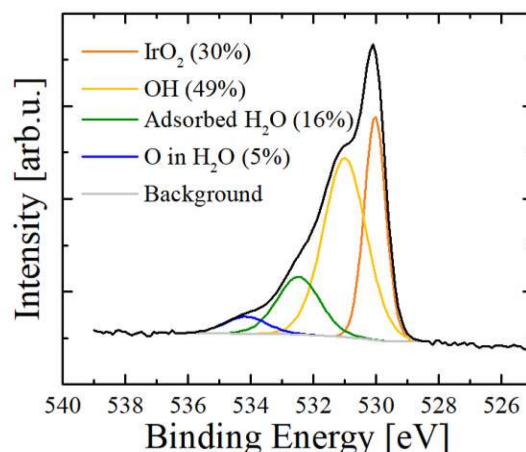

Figure 78 *XPS measurement of the O 1s spectrum of IrO_x samples. The signal is deconvoluted to the four peaks as labelled.*

When the same XPS measurement was performed on pure TiO_x samples, as shown previously in *Figure 63*, no peaks associated with OH or adsorbed water were identified. The prominent peaks aside from the expected TiO_2 oxygen peak are C-O peaks, most likely due to sample contamination, *i.e.*, dust. The absence of any OH or H_2O peaks means that water will not likely permeate through the TiO_x layer to the bottom electrode. This is important to ensure that the bottom electrode in sample set 2 does not experience any impact from humidity or water.

[10] Electrically isolated means that the H_2O molecule did not adsorb on the surface and therefore the oxygen did not form a bond with any of the sample material.

Die approbierte gedruckte Originalversion dieser Dissertation ist an der TU Wien Bibliothek verfügbar.
The approved original version of this doctoral thesis is available in print at TU Wien Bibliothek.
TU WIEN Bibliothek Your knowledge hub

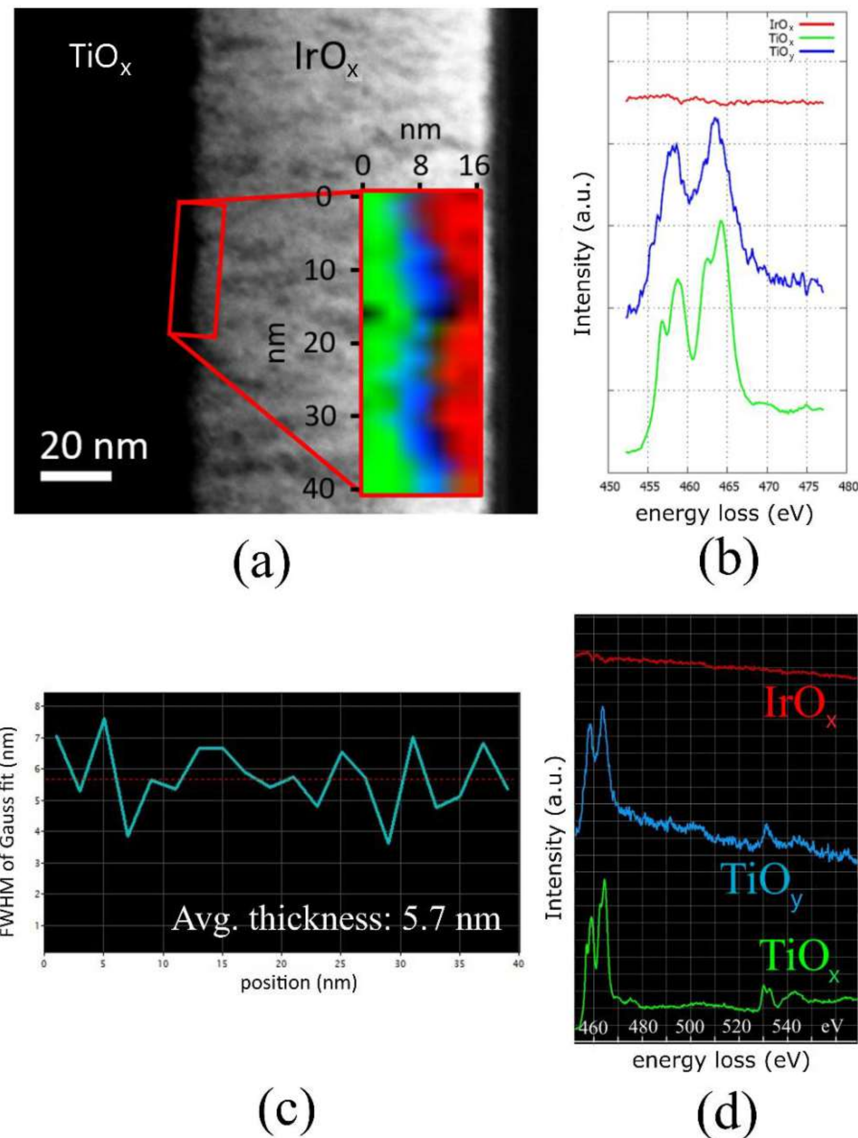

Figure 79 *STEM-EELS measurement at the Ti-$L_{3,2}$ edge of an IrO_x/TiO_x sample. (a) TEM image of the investigated sample. The interface area, which was analysed with the EELS method, is highlighted and shows the three measured compounds: IrO_x (red), TiO_x (green) and TiO_y (blue). (b) The electron energy loss spectrum around 460 eV. A significantly reduced TiO_y layer can be identified. (c) The measured thickness of the TiO_y layer. (d) Full recorded EELS spectrum with additional peaks at ~530 eV.*

To analyse the chemical composition of the TiO_x/IrO_x interface, STEM-EELS was applied, as well as a TEM image is presented in *Figure 79 a*. For details on the method, the reader is referred to section 3.4. A 16x14 nm^2 interface area was scanned with a beam diameter of 0.15 nm, as shown in the insert of *Figure 79 a*. *Figure 79 b* yields the resulting Ti-L edge Energy Loss Near Edge Structure (ELNES). First, the energy loss signal for TiO_x can be identified clearly. Unfortunately, as the measured spectrum is out of range for the IrO_x peaks, no information about this layer can be obtained. The TiO_x signal shows the expected peaks at distances > 6 nm from the IrO_x/TiO_x interface. At distances < 6 nm to the interface, the TiO_x

Die approbierte gedruckte Originalversion dieser Dissertation ist an der TU Wien Bibliothek verfügbar.
The approved original version of this doctoral thesis is available in print at TU Wien Bibliothek.
TU Bibliothek WIEN Your knowledge hub

signal is noisy, which indicates significantly reduced TiO_y, where $y < x$. As shown in *Figure 79 c*, the average thickness of the TiO_y layer is 5.7 nm. The whole measured EELS spectrum can be seen in *Figure 79 d*. The additional peaks at around 530 eV show the same noisy signal for the TiO_y layer. It can be concluded that a TiO_y layer with a high amount of oxygen vacancies is present at the IrO_x/TiO_x interface. For more information on fundamentals of oxygen vacancies, the reader is referred to section 2.2.

Capacitive behaviour

The permittivity behaviour of sample set 1 was investigated (for the methodology, see section 3.4). The applied sinusoidal frequency was swept from 30 to 300 kHz. The capacitance of the 100 nm thick sample was also recorded at varying temperatures ranging from 25 to 100°C. As shown in *Figure 80 a*, the permittivity at room temperature decreases from 78 to 64 when going to higher frequencies. When temperature increases, permittivity also decreases to roughly 90% of the initial value.

In *Figure 80 b*, the frequency-dependent relative permittivity at varying dielectric thicknesses is shown. At thicknesses above 50 nm, the relative permittivity is very similar and has values of 75 at 50 kHz. At 50 nm, a lower value of 70 is measured at 50 kHz. These values are lower and more frequency-dependent than those shown in the cantilever devices presented in section 4.2. The main difference is likely the significantly reduced TiO_x interface layer. Such an interface layer can substantially influence the electrical behaviour, and the oxidation state of the sputtered films depends on various factors such as the preconditioning state of the sputtering chamber, the residual gas composition in the chamber or the sputter target condition.

However, even these lower values are comparable to other studies, such as sputtered $Al/TiO_2/Al$ structures with an ε_r of ~60.[192]

Die approbierte gedruckte Originalversion dieser Dissertation ist an der TU Wien Bibliothek verfügbar.
The approved original version of this doctoral thesis is available in print at TU Wien Bibliothek.
TU WIEN Bibliothek Your knowledge hub

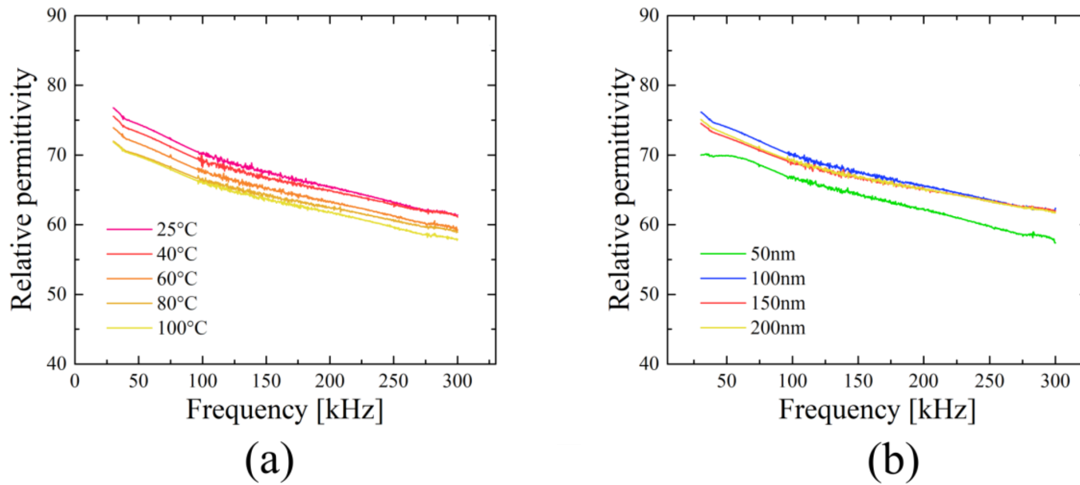

Figure 80 *The frequency-dependent relative permittivity of* $IrO_x/TiO_x/IrO_x$ *parallel-plate capacitors obtained from impedance measurements. The amplitude of the applied sinusoidal voltage was at 0.1 V. (a) Measurement of capacitors with a 100 nm thick dielectric at various temperatures. (b) Measurement of capacitors with varying thickness of the dielectric at room temperature.*

Time-dependent leakage current behaviour

First, the leakage current behaviour is analysed. Theoretically, for the $IrO_x/TiO_x/IrO_x$ capacitors, the band diagram, as shown in *Figure 81*, is expected. The values assumed for the work functions of both materials are $\varphi_{IrO2} \sim 4.2$ eV and $\varphi_{TiO2} \sim 4.4$ to 5.5 eV. [193,194] Another critical parameter is the electron affinity, which has a value of $\chi_{a,TiO2} \sim 3.9$ eV for TiO_2. As explained in section 2.2, the individual Fermi-energies of both materials equalize when the materials come into contact. As a consequence, the band structure is changed, and the interface forms an ohmic contact.

Die approbierte gedruckte Originalversion dieser Dissertation ist an der TU Wien Bibliothek verfügbar.
The approved original version of this doctoral thesis is available in print at TU Wien Bibliothek.
TU WIEN Bibliothek Your knowledge hub

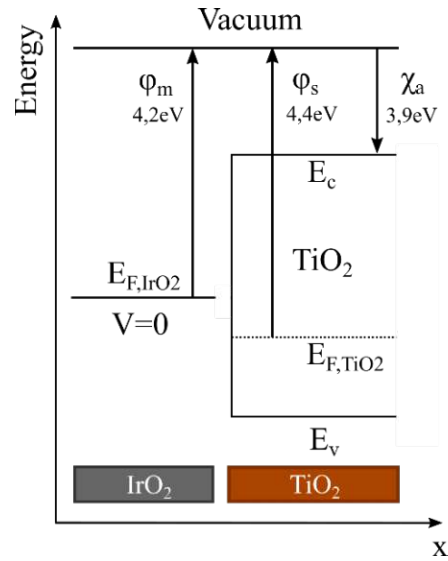

Figure 81 *Band diagram for $IrO_2/TiO_2/IrO_2$ capacitors with literature values for electron affinity and work function.* [193,194]

Additionally, the low bandgap of TiO_2 (roughly 3.2 eV at room temperature) also means that leakage currents will be higher compared to *i.e.,* SiO_2 (approximately 8.6 eV). The low bandgap and the ohmic contact means that there will be a high amount of charge carriers injected from the IrO_x cathode to the TiO_x when a sufficiently high electric field is applied. The high amount of injected charge carriers have a significant repulsive force that counteracts the applied field and therefore limits the injection of additional electrons. The current shows the characteristics of a space-charge-limited current as a result (see section 2.2).

Measurement at room temperature

The measurement setup and method, as shown in section 3.4, were used for the actual measurements of the leakage current. The first series show an *JV*-hysteresis measurement performed at room temperature on set 1 samples with a thickness of 100 nm. The hold time was set to 100 ms with 10 consecutive measurements at each step (i.e., every 10 ms). The last 10 measurements at each DC voltage step are used for the *JV* analysis. The voltage cycles in a hysteresis-like fashion from -3 V to 3 V, where one cycle has the following steps:

1. 0 V to 3 V
2. 3 V to 0 V
3. 0 V to -3 V
4. -3 V to 0 V

Die approbierte gedruckte Originalversion dieser Dissertation ist an der TU Wien Bibliothek verfügbar.
The approved original version of this doctoral thesis is available in print at TU Wien Bibliothek.
TU WIEN Bibliothek Your knowledge hub

This numbering of the sweeps will be used for the following sections. This voltage cycling method is also referred to as cyclic voltammetry.

In *Figure 82*, the cyclic voltammetry measurement performed on one of the 100 nm thick set 1 samples is shown. The arrows and numbering indicate how the curve was recorded. The inserts show 10 individual consecutive measurements at selected points of the *JV* curve.

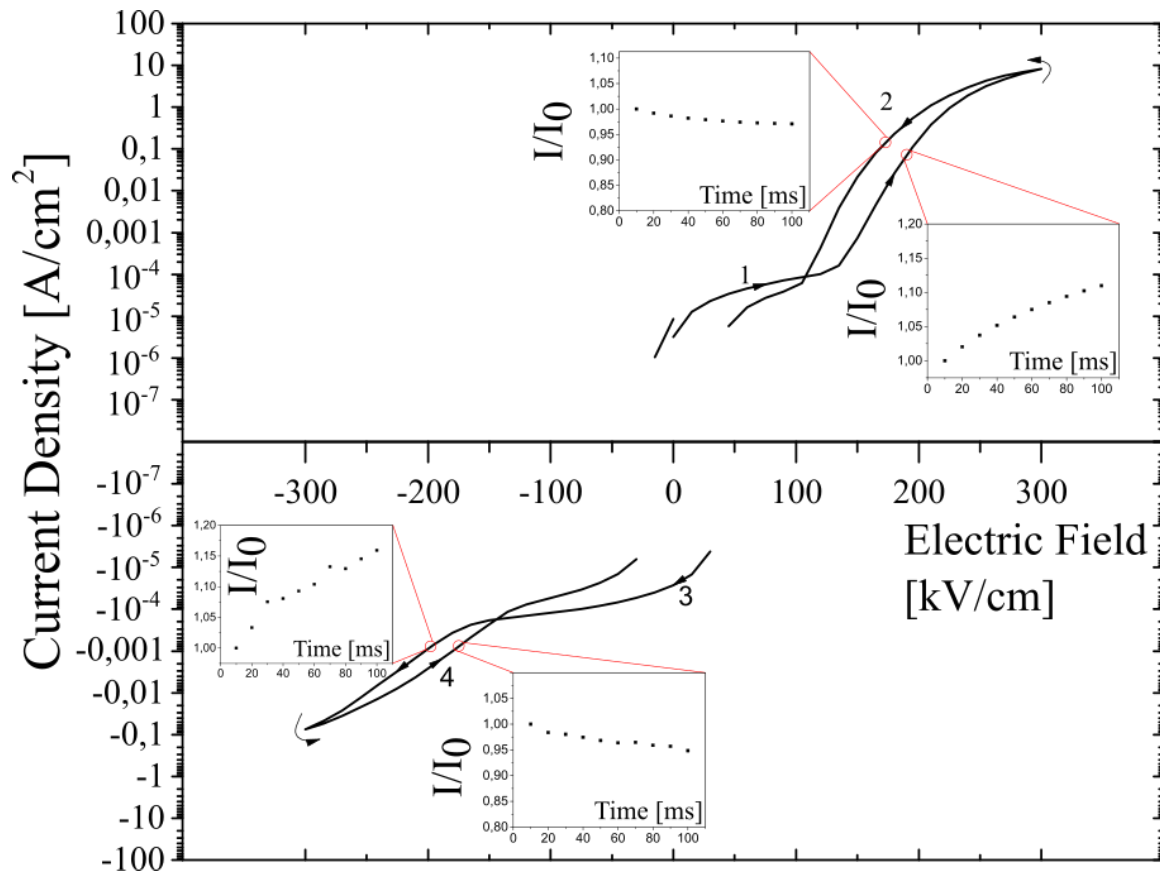

Figure 82 *Cyclic voltammetry measurements of an $IrO_x/TiO_x/IrO_x$ parallel-plate capacitor. The electric field was varied from -300 to 300 kV/cm in steps of 0.15 kV/cm and a hold time of 100 ms per step. For clarity, the plot is separated into two log plots, one containing the positive current values and one with the absolute negative current values. For this purpose, the negative plot is flipped upside down. One typical cycle of the JV curve where the trajectory of the curve is labelled. Inserts show the time evolution of the current at selected points of the JV curve.*

Three critical features are deduced from this measurement cycle. First, the leakage current shows a hysteresis-like behaviour, where the leakage current at each voltage depends on the history of the stressing. This means the leakage current values are different for sweep 1 compared to sweep 2. For example, when looking at the *J* value at 150 kV/cm, a difference of three orders of magnitude is observed when comparing the up-sweep to the down-sweep cycle. This means that the electrical resistance of the capacitor changes dynamically, depending on

Die approbierte gedruckte Originalversion dieser Dissertation ist an der TU Wien Bibliothek verfügbar.
The approved original version of this doctoral thesis is available in print at TU Wien Bibliothek.
TU Bibliothek WIEN Your knowledge hub

the history of electrical stressing. According to literature, this behaviour is typically called memristive- or resistive switching behaviour.[74]

Secondly, when looking at the time-transient behaviour in the different sweeps (inlays), sweeps 1 and 3, where the voltage magnitude is increasing, show an increasing current transient behaviour. In sweeps 2 and 4, where the voltage decreases in magnitude, the current decreases over time. This transient behaviour shows an asymptotic relaxation behaviour for voltages applied in this study. This relaxation behaviour indicates that the memristive mechanism also has a time-dependent component.

The last important observation to note is at the end of sweep 2. The voltage is back to 0 V again, but there is still a significant negative current with a magnitude of ~ 10^4 A/cm^2. A memristive hysteresis where the current is not zero at zero voltage is often referred to as non-pinched hysteresis.[195]

Die approbierte gedruckte Originalversion dieser Dissertation ist an der TU Wien Bibliothek verfügbar.
The approved original version of this doctoral thesis is available in print at TU Wien Bibliothek.
TU Bibliothek WIEN Your knowledge hub

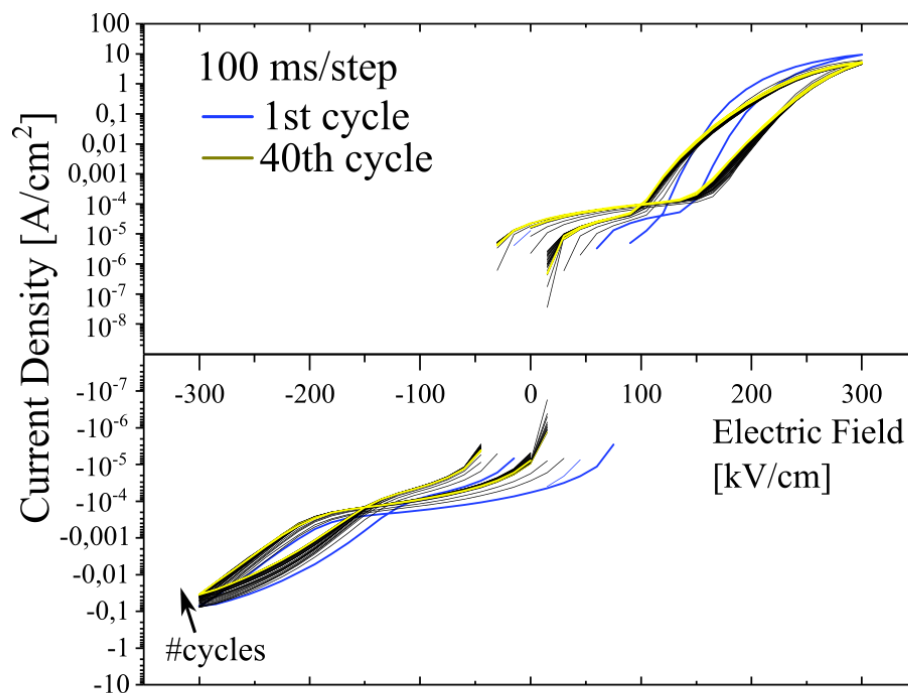

Figure 83 *Cyclic voltammetry measurements of an $IrO_x/TiO_x/IrO_x$ parallel-plate capacitor. The electric field was varied from -300 to 300 kV/cm in steps of 0.15 kV/cm and a hold time of 100 ms per step with multiple consecutive cycles. The first cycle is in blue, and the 40th is coloured in yellow.*

Figure 83 shows multiple voltage cycles repeated up to the 40th cycle. Only in the first three cycles noticeable changes in the *JV* behaviour are identified. From cycle three to 40 the *JV* values only differ slightly between each cycle. Over the 40 measured cycles, this change in

leakage current magnitude is adding up to almost an order of magnitude. Even though the absolute current values changed, no breakdown or change in the behaviour of the leakage current is observed and is therefore regarded as stable behaviour within these 40 cycles,.

Where this dynamic memristive behaviour is coming from is explained in the following.

Non-pinched hysteresis

The presented electrical behaviour is best modelled when assuming a parallel equivalent circuit consisting of a memristor and a capacitor. [196] In this configuration, leakage currents are caused by memristive and capacitive elements, which add to the total leakage current. The corresponding modelling and leakage current curves are published in the work of Sun *et al.*[76] The curve C_1M_3 looks similar to what is presented in *Figure 82*. Interestingly, as argued in the latter study, this C_1M_3 shape was not measured before and is the first of its kind. The capacitively induced leakage current is the cause of the non-pinched hysteresis. If only the memristive effect is targeted in a device, the capacitive effect must be avoided; otherwise, energy is lost by the capacitively induced opposing internal field.

In detail, this effect is due to the separation of charges with opposite sign in the dielectric. Consider a TiO_x capacitor with a voltage applied. As a consequence, oxygen which has captured two electrons and is negatively charged (O^{2-}), drift toward the positive electrode. Oxygen vacancies, however, are positively charged and drift towards the negative electrode. This charge separation builds up an internal electric field. When the applied voltage is turned off, the O^{2-}/V_0 ions slowly return to their initial distribution. Until this equilibrium distribution is reached, a leakage current can be measured, even though the applied voltage is zero.

A cyclic voltammetry measurement of set 1 samples with a thickness of 100 nm was performed at lower applied electric fields and at different hold times. The maximum field strength was 60 kV/cm, and the hold times were 1 ms/step, 100 ms/step and 15 s/step.

TU Bibliothek Die approbierte gedruckte Originalversion dieser Dissertation ist an der TU Wien Bibliothek verfügbar. The approved original version of this doctoral thesis is available in print at TU Wien Bibliothek. WIEN Your knowledge hub

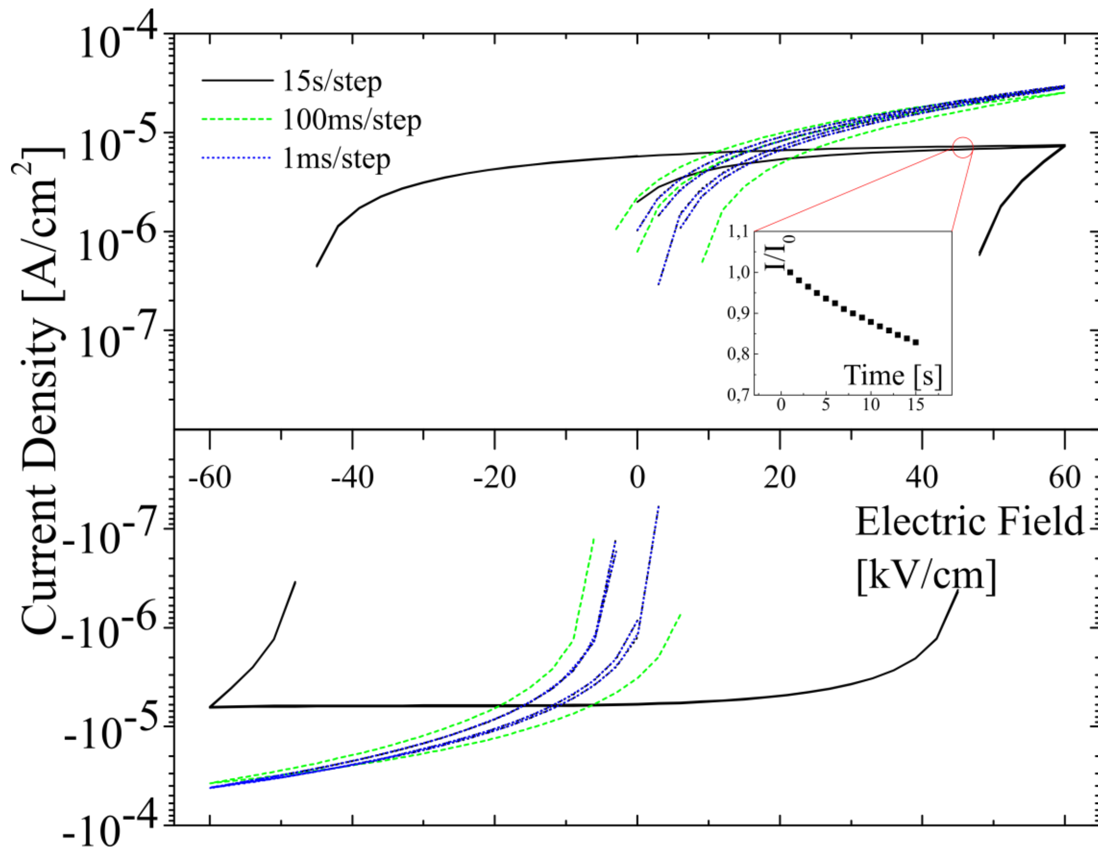

Figure 84 *Cyclic voltammetry of a 100 nm thick set 1 sample at different hold times and a maximum electric field of 60 kV/cm. The insert shows the time transient of a chosen point on the JV curve.*

The result can be seen in *Figure 84*. The first fact observed is that the longer the hold time, the more significant the hysteresis is. This is expected, as the longer biasing time leads to a more effective charge separation. Secondly, in the upward sweep 1, the current at each step is relaxing to a lower value (see insert). This decrease is different to the current transient of sweep 1 in Figure 82, showing that a lower bias value does not generate new V_0 (which would cause the memristive effect).

To see which type of charge carriers causes the capacitively induced leakage current, set 2 samples were measured again with the cyclic voltammetry method. The result is depicted in *Figure 85*.

Die approbierte gedruckte Originalversion dieser Dissertation ist an der TU Wien Bibliothek verfügbar.
The approved original version of this doctoral thesis is available in print at TU Wien Bibliothek.
TU WIEN Bibliothek Your knowledge hub

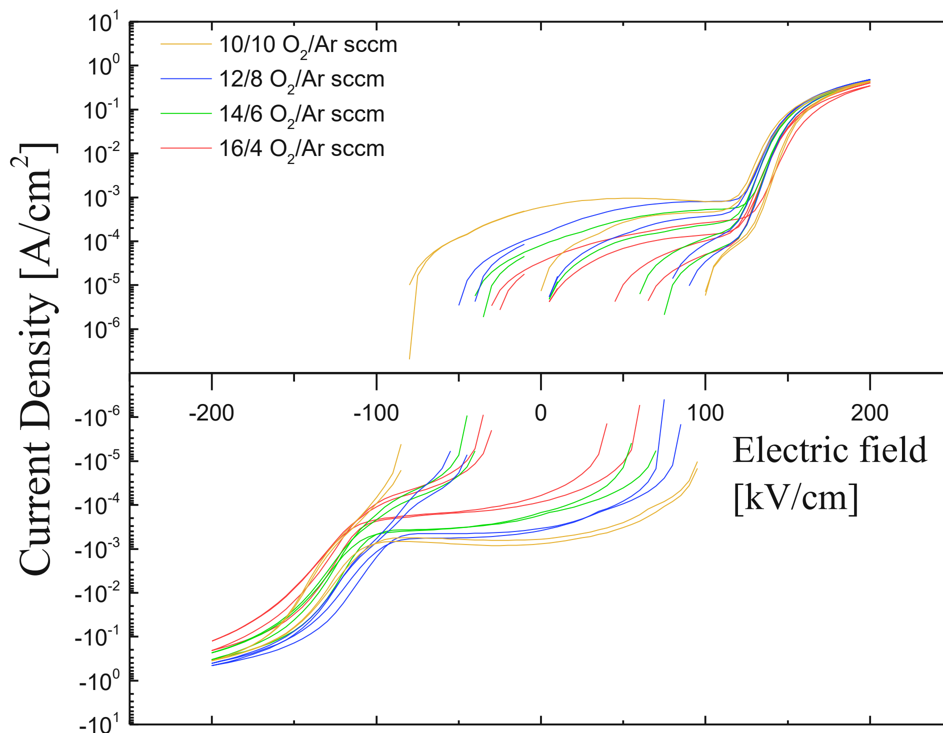

Figure 85 *Cyclic voltammetry measurements of set 2 samples with varying gas compositions during sputtering. Two consecutive cycles per gas composition are shown. The measurements were performed at room temperature with a 100 ms/step hold time.*

As explained in section 3.3, the TiO_x is fabricated by reactive sputtering. This means that the Ti atoms of the Ti target react with the oxygen in the sputtering plasma. To analyse the impact of deposition parameters, the gas composition of the plasma was changed so that the oxygen content was partially replaced with Ar, which reduces the amount of oxygen in the plasma, but keeps the total gas pressure in the deposition chamber constant due to reasons of comparison.

The measurement indicates that the hysteresis is less pronounced the higher the oxygen content in the plasma is. This correlates with existing literature, where a higher amount of oxygen flow corresponds to a higher oxidation grade of the TiO_x.[197] As the capacitive hysteresis effect is more pronounced in samples with a lower degree of TiO_x oxidation, it is reasonable to assume that the capacitive effect is indeed caused by the charge separation of O^{2-} and V_0.

Die approbierte gedruckte Originalversion dieser Dissertation ist an der TU Wien Bibliothek verfügbar.
The approved original version of this doctoral thesis is available in print at TU Wien Bibliothek.
TU Bibliothek WIEN Your knowledge hub

Memristive leakage current description

In general, not considering any traps, a space-charge-limited current (SCLC) is expected, as explained before. However, as the TiO_x is V_0 rich, the SCLC behaviour will be altered. Such a trap-dependent SCLC has been described in literature before and was also used to describe TiO_x devices with memristive effects. Such devices include Al/TiO_x/Al, Al/TiO_x/TiO_2/Al memristors, and Al/TiO_x-nanowire/Ti.[198–200] As Al has a very similar work function (~4.06 - 4.28 eV) as IrO_x (~4.2 eV), in theory, these devices should show similar behaviour.

For a complete analysis of the SCLC mechanism, the exponent *exp* in the $J \propto V^{exp}$ correlation has to be identified in addition to the free carrier density and carrier mobility. The exponent can be derived from the slope of the *log(J)-log(V)* plot. Determining the free carrier density and carrier mobility is, however, possible with Arrhenius plots. As the temperature dependence of the investigated devices does not show similarities to other devices in literature (to the best of the author's knowledge), these parameters could not be determined. The unusual temperature temperature dependence of the devices is discussed in detail later in this section.

However, the exponent is a good indicator if SCLC is the dominiating leakage current mechanism. As explained in section 2.2, the exponent should be equal to 1 for low voltages, increasing at medium voltages to high values of >3 and settling at high voltages to an exponent of 2. The ranges of low, medium and high voltages is material dependent, but for the investigated device, it is 0 to 1 V (0 to 100 kV/cm), 1 to 5 V (100 to 500 kV/cm) and >5 V (>500 kV/cm), respectively.

To confirm the theoretically expected SCLC behaviour, cyclic voltammetry measurements on set 1 samples with a thickness of 100 nm have been performed. One measurement spans a voltage range of 0 to 1.2 V and the other from 0 to 10 V. To keep stressing times similar, both measurements consist of 20 individual measurement points with a hold-time of 100 ms each. The result is depicted in *Figure 86 a* and *b* for the low and high voltage range, respectively. The obtained slopes are ~1 for low voltages, ~17 for medium voltage and ~2 for high voltages.

Die approbierte gedruckte Originalversion dieser Dissertation ist an der TU Wien Bibliothek verfügbar.
The approved original version of this doctoral thesis is available in print at TU Wien Bibliothek.
TU Bibliothek WIEN Your knowledge hub

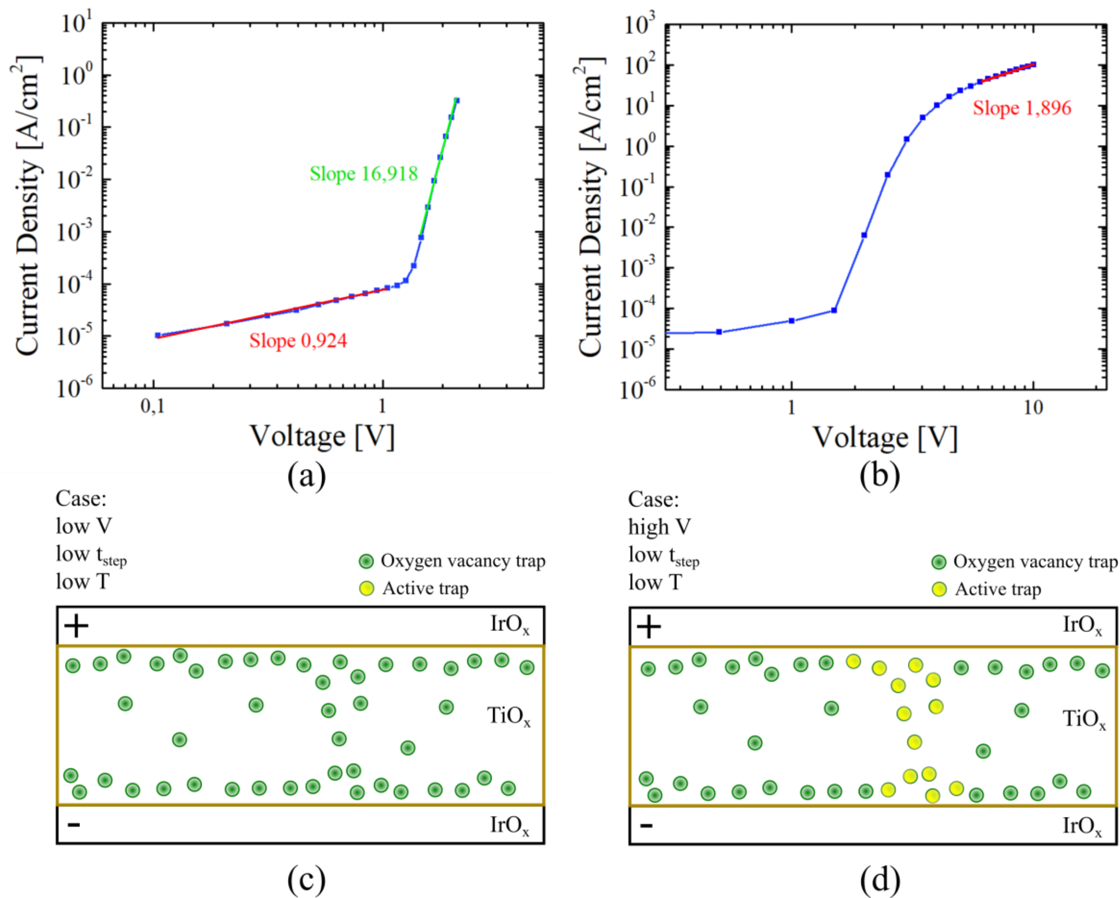

Figure 86 *Investigation of the SCLC behaviour of set 1 samples. (a) Log(J)-log(V) plot at small voltages up to 2 V with 0.1 V steps and a hold time of 100 ms. Below 1.2V, the slope is close to 1, and between 1.2 and 2 V, the slope is close to 17. (b) Log(J)-log(V) plot at higher voltages up to 10 V with 1 V steps and 100 ms hold-time. The high V slope is close to 2. (c) Schematic representation of the trapping behaviour for low voltages, step time and temperature. In the low voltage regime, the oxygen vacancy traps are not activated and do not contribute to conduction. (d) Trap behaviour at high voltages, low hold time and low temperature. Along a path of low resistance, traps are active.*

The individual regimes are explained as follows (see section 2.2):

- Low voltage range, exp = 1:

  Traps are inactive, and only ohmic behaviour is observed. No conductive channels are present. This is also depicted in *Figure 86 c.*

- Medium voltage range, exp > 3:

  Traps are activated and contribute to the electrical conduction. The trap-activation happens preferably through paths of low resistance, *i.e.* conductive channels throughout the capacitor, see *Figure 86 d.* Applying a steady voltage bias in this regime increases the current over time as new channels are formed (see insert of *Figure 82*).

- High voltage range, exp = 2:

Die approbierte gedruckte Originalversion dieser Dissertation ist an der TU Wien Bibliothek verfügbar.
The approved original version of this doctoral thesis is available in print at TU Wien Bibliothek.
TU WIEN Bibliothek Your knowledge hub

All traps are active and an excessive current flow is present. Also, no new channels of low resistance emerge and the current behaviour transitions to the SCLC typical squared exponent.

The exponential behaviour of the current for sweep 2 (high V to 0 V), shown in *Figure 87*, does not show any clear slope domains. As explained previsouly, when the voltage is ramped up, capacitive charge separation induces a leakage current that screens the memristively induced leakage current. This effect is hindering the analysis of the memristive leakage current.

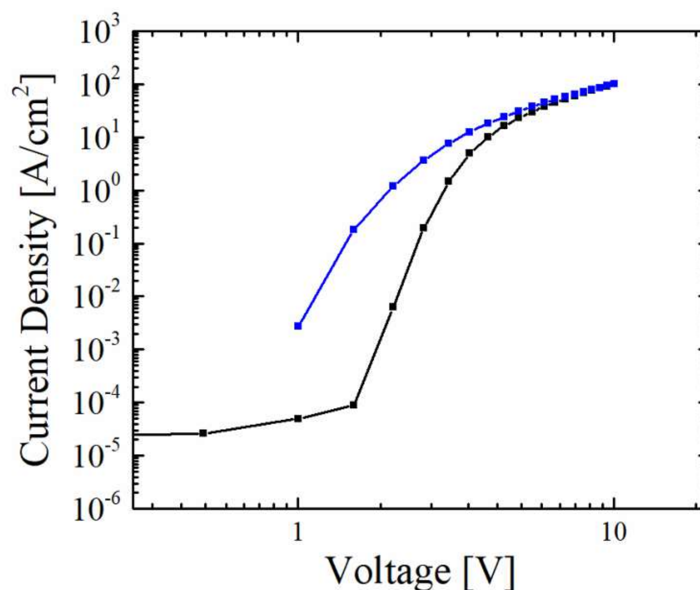

Figure 87 *Log(J)-log(V) plot of sweep 1 with voltages from 0 to 10 V (black) and sweep 2 from 10 to 0 V (blue) with 1 V steps and a hold time of 100 ms. Here only positive current values are plotted and therefore the resulting negative current values at voltages below 1 V in sweep 2 are not shown.*

The description of the memristive hysteresis so far is only of electronic nature. No new V_0 are generated. This hypothesis is supported by the measurement shown in *Figure 83,* where repeated cycles do not significantly change the leakage current levels. The measurement was repeated for lower hold times of 1 ms and showed similar results.

Given the nature of the SCLC, a space charge polarization should also be present in the dielectric. This is potentially of interest, as this polarization could cause electromechanical effects. However, the applied electric fields in the measurements shown in 4.2 are much lower (max. 200 kV/cm) than where a clear SCLC behaviour can be identified (<500 kV/cm) and

Die approbierte gedruckte Originalversion dieser Dissertation ist an der TU Wien Bibliothek verfügbar.
The approved original version of this doctoral thesis is available in print at TU Wien Bibliothek.
TU WIEN Bibliothek Your knowledge hub

therefore electromechanical contribution to the flexoelectric behaviour of the TiO_2 cantilevers can be ruled out.

Long hold-time measurements

For longer hold times, this picture changes. In the measurement shown in

a, the sample was stressed for several cycles with a hold-time of 15 s. Again, set 1 samples with a thickness of 100 nm were used. Striking is that the capacitively induced leakage current hysteresis is more pronounced than for shorter hold times, *i.e.* the electric field where the current is zero is larger than for shorter hold times (100 kV/cm vs. 50 kV/cm). This is in accordance with the measurement of the capacitively induced leakage currents shown in *Figure 84*.

In the first cycle, the behaviour is reminiscent of filament-forming behaviour. When a positive voltage is applied, V_0 are generated and filaments are formed, which lead to high leakage currents of up to several A/cm^2.[71,201] A schematic for a wide channel situation of V_0 is depicted schematically in

b. When the bias is reversed, however, these filaments erode. This is demonstrated as the maximum negative leakage current is not at the maximum negative bias but rather slightly before (at ~200 kV/cm). Between -200 and -300 kV/cm, the leakage current decreases in magnitude as the filaments erode, even though the magnitude of the external electric field increases.

A measurement where the voltage was cycled multiple times is shown in *Figure 89*. Each cycle shows that the switching behaviour decreases. In the 7th cycle, large jumps in leakage current are detected. In the 8th cycle, the memristive and capacitive hysteresis behaviour has vanished. Most likely, filaments formed, which are not reversible between high and low resistance states. This non-reversible breakdown behaviour is also called a hard breakdown.

TU Bibliothek Your knowledge hub WIEN
Die approbierte gedruckte Originalversion dieser Dissertation ist an der TU Wien Bibliothek verfügbar.
The approved original version of this doctoral thesis is available in print at TU Wien Bibliothek.

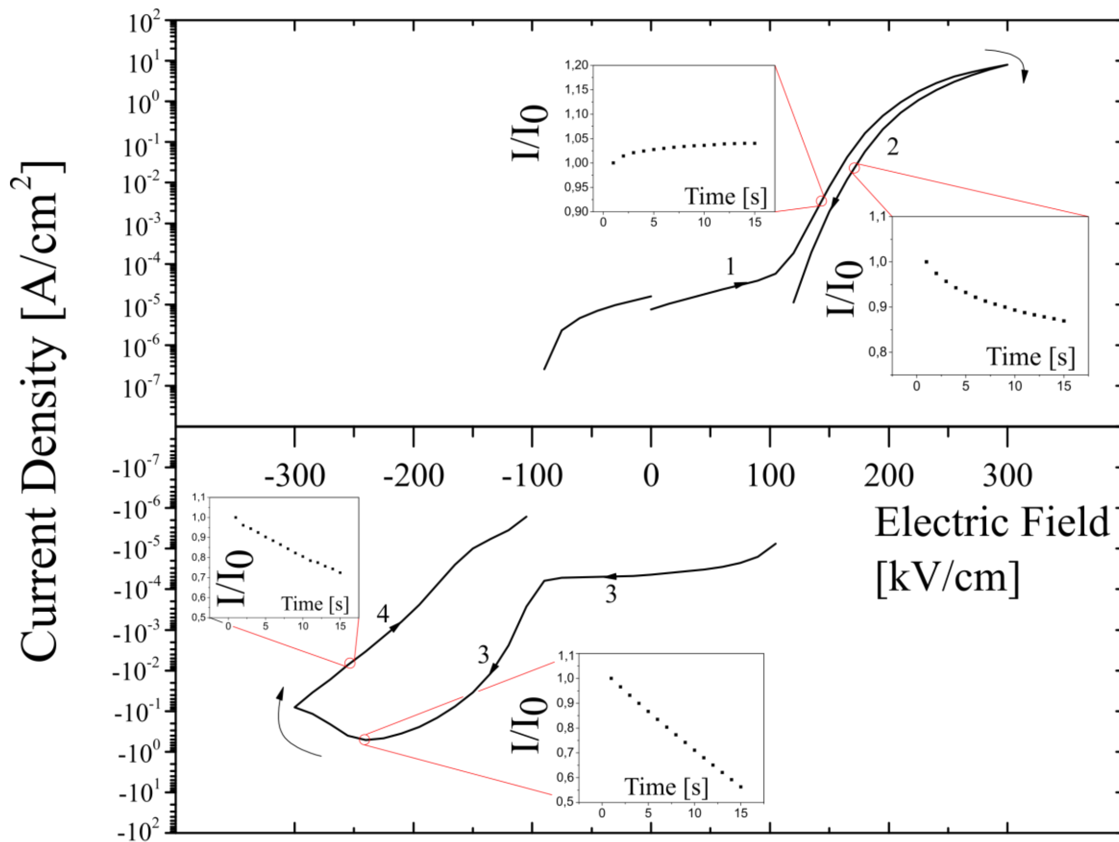

(a)

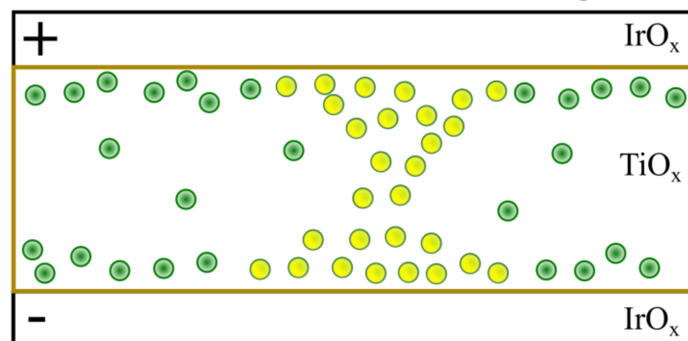

(b)

Figure 88 *(a) Cyclic voltammetry measurement of a set 1 sample with 100 nm thickness and a hold-time of 15 s. Black arrows indicate the voltage sweep order. Inserts show the time transient at specific points in the JV curve, and the red arrows indicate if the current is rising or falling over time. (b) Schematic of the origin of the JV hysteresis behaviour. At high V and high t_{step}, a V_0 filament forms and due to the high electrical stressing, new V_0 are created, thus widening the filament.*

Die approbierte gedruckte Originalversion dieser Dissertation ist an der TU Wien Bibliothek verfügbar.
The approved original version of this doctoral thesis is available in print at TU Wien Bibliothek.
TU Bibliothek WIEN Your knowledge hub

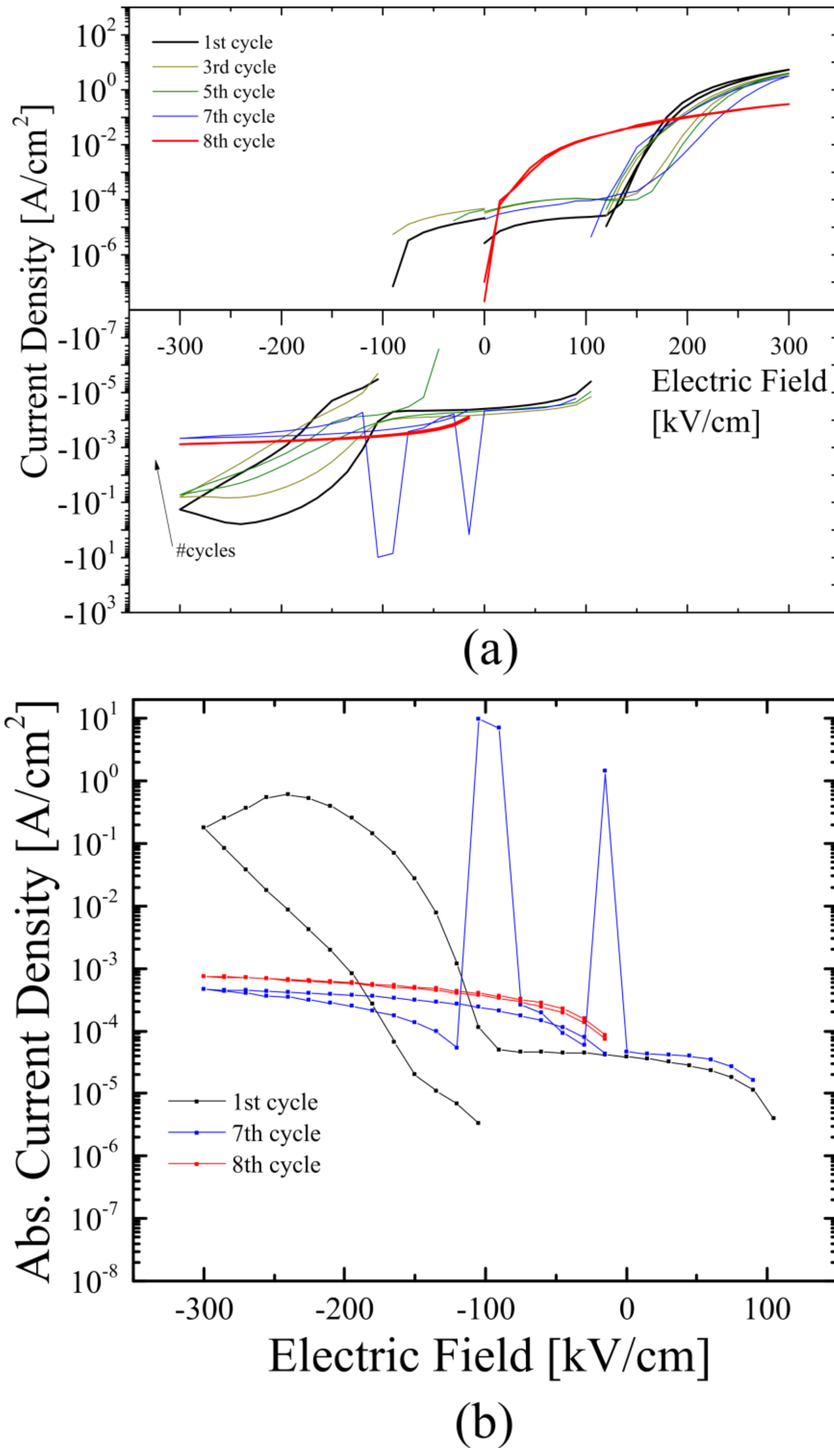

Figure 89 *Cyclic voltammetry measurement of a set 1 sample with 100 nm dielectric thickness and 15 s hold time per biasing step. The sample was repeatedly stressed in sweep order: 1, 2, 3, 4, until a dielectric breakdown, which happened at of 8 such cycles. (a) Selected cycles of the measurement are shown. (b) The absolute value of the current of cycles 1, 7 and 8 at negative electric field bias is shown. In the 7th cycle, the current shows large jumps in magnitude, resulting in a breakdown of the capacitive and resistive hysteresis, as seen in cycle 8. Most probably, a stable filament has established, causing this change in electrical performance.*

Die approbierte gedruckte Originalversion dieser Dissertation ist an der TU Wien Bibliothek verfügbar.
The approved original version of this doctoral thesis is available in print at TU Wien Bibliothek.
TU Bibliothek WIEN Your knowledge hub

Interestingly, the maximum leakage current after a hard breakdown (cycle 8) seems to be lower at electric fields >100 kV/cm than before the stressing (cycle 1). This might be due to a different leakage current mechanism after the dielectric breakdown.

TiO_x thickness dependent measurements

The *JV* behaviour was also analysed for samples with varying dielectric layer thickness, namely 50, 100, 150 and 200 nm. The result of the cyclic voltammetry for 1 ms, 100 ms and 15 s hold-time per voltage step is shown in *Figure 90* and *Figure 91*.

The capacitively induced *JV* hysteresis dominates the response characteristics for the 50 nm sample. Unfortunately, higher voltage bias, where a memristive hysteresis is most likely to occur, leads to hard breakdowns. It is reasonable to assume that the capacitive part is more pronounced in thinner samples, as the O^{2-} and V_0 ions are spatially closer together and therefore the magnitude of the internal electric field from charge separation is higher, according to $E = V/h$. This trend continues when analysing the other samples with different thickness values, where the field strength for zero-current condition is lower for thicker samples.

For the samples with thicknesses >50 nm, the memristive hysteresis is similar, as shown previously in *Figure 82*.

Die approbierte gedruckte Originalversion dieser Dissertation ist an der TU Wien Bibliothek verfügbar.
The approved original version of this doctoral thesis is available in print at TU Wien Bibliothek.
TU WIEN Bibliothek Your knowledge hub

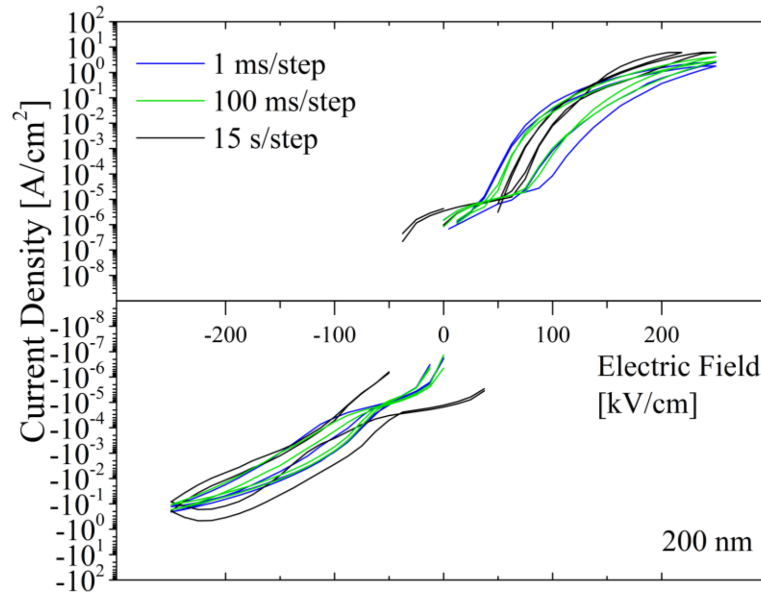

(a)

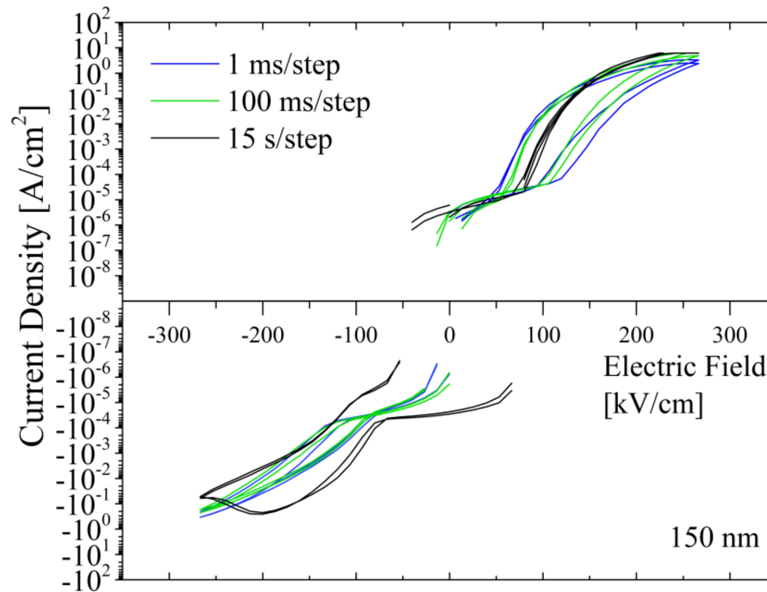

(b)

Figure 90 *Cyclic voltammetry of set 1 samples at hold times of 1 ms, 100 ms and 15 s. (a) A sample with 200 nm dielectric thickness. (b) A sample with 150 nm dielectric thickness. The leakage current characteristics are similar to the previously shown 100 nm thick samples.*

Die approbierte gedruckte Originalversion dieser Dissertation ist an der TU Wien Bibliothek verfügbar.
The approved original version of this doctoral thesis is available in print at TU Wien Bibliothek.
TU WIEN Bibliothek Your knowledge hub

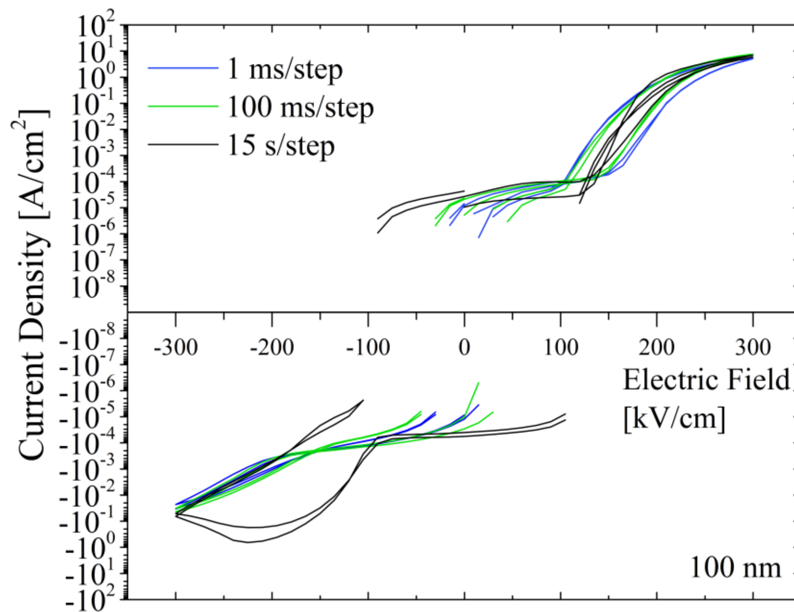

(a)

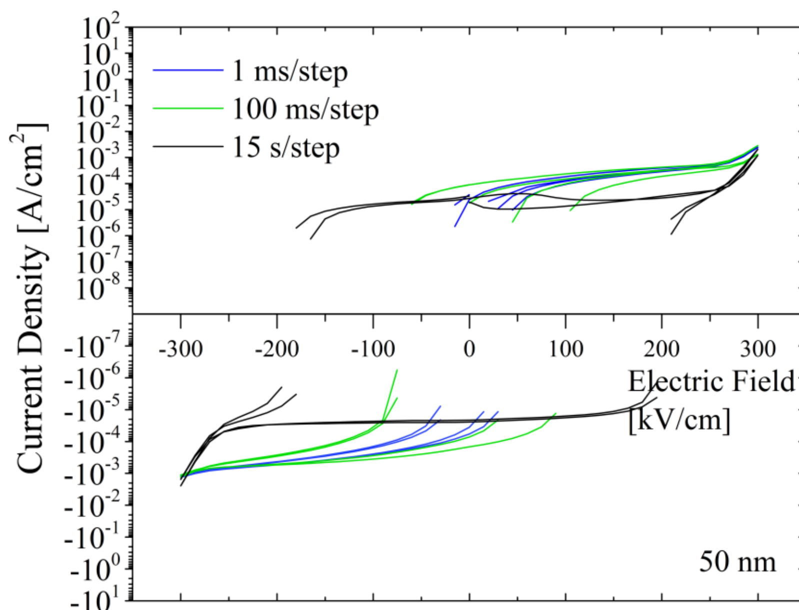

(b)

Figure 91 *Cyclic voltammetry of set 1 samples at hold times of 1 ms, 100 ms and 15s. (a) A sample with 100 nm dielectric thickness. (b) A sample with 50 nm dielectric thickness. The sample with 50 nm dielectric thickness is notably different to the other samples. Here, the capacitively induced leakage current hysteresis is dominating the signal.*

Die approbierte gedruckte Originalversion dieser Dissertation ist an der TU Wien Bibliothek verfügbar.
The approved original version of this doctoral thesis is available in print at TU Wien Bibliothek.
TU Bibliothek Your knowledge hub WIEN

Temperature-dependent leakage current measurements

A cyclic voltammetry measurement at temperatures varying from 30 to 100°C was performed in air on set 1 samples inclsuding all thickness variations. A maximum field strength of 200 kV/cm was chosen. This was done to ensure that there are no significant irreversible changes in the resistive properties of the dielectric layer when cycling over multiple temperature steps.

The following test was performed as proof that the material does not significantly change its resistive properties with the chosen electrical stressing parameters. A 100 ms hold-time was chosen, and a cyclic voltammetry measurement was performed on set 3 samples. The sample temperature was first swept from 30 to 100°C and then back from 100 to 30°C. The result can be seen in *Figure 92*.

While the total current values differ between the temperature up- and down-sweep up to one order of magnitude, the temperature dependence and capacitive-memristive leakage current behaviour are similar. Therefore, the chosen stressing values allow for an accurate analysis of temperature-dependent behaviour being free of any hysterises effects.

The cyclic voltammetry measurement at temperatures ranging from 30 to 100°C was also performed on set 1 samples with varying dielectric thickness, as illustrated in *Figure 93*. The results for thicknesses above 50 nm are similar and comparable to the thickness-dependent measurements shown in *Figure 90* and *Figure 94*. In detail, the capacitively induced electric field strength is reduced at higher thicknesses and the memristive leakage current behaviour is not changed significantly with increasing dielectric thickness.

Die approbierte gedruckte Originalversion dieser Dissertation ist an der TU Wien Bibliothek verfügbar.
The approved original version of this doctoral thesis is available in print at TU Wien Bibliothek.
TU WIEN Bibliothek Your knowledge hub

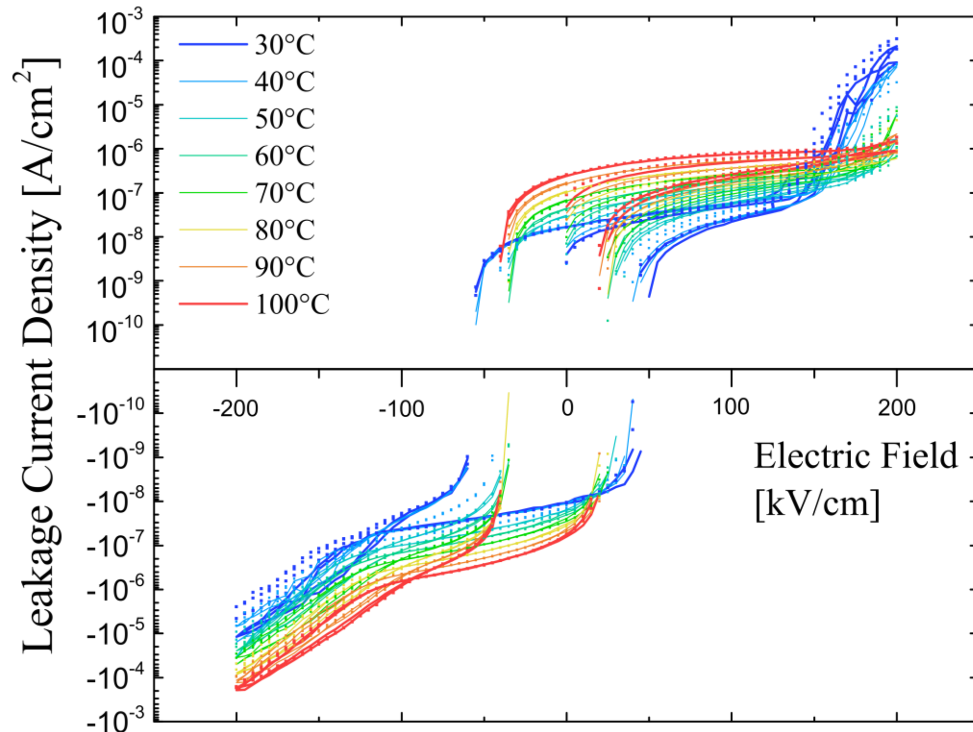

(a)

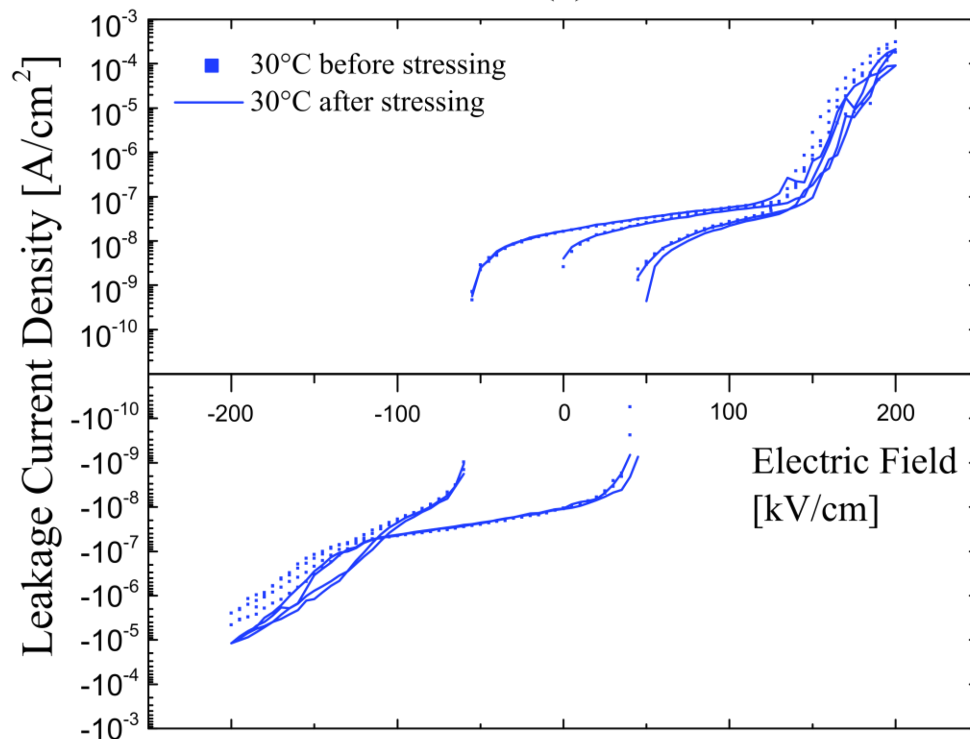

(b)

Figure 92 *Cyclic voltammetry of a set 3 sample at various temperatures and 100ms hold time. Two cycles per temperature step are shown. The temperature was swept from 30°C to 100°C and back down to 30°C. At each temperature step, 2 cycles were recorded. (a) The resulting leakage currents. Dots represent measurement points for the temperature up-sweep and lines represent measurements from the temperature down sweep. (b) Only the 30°C measurements are shown. It can be seen that the down-sweep JV curve is similar to the up-sweep JV curve in both current magnitude and temperature dependency.*

Die approbierte gedruckte Originalversion dieser Dissertation ist an der TU Wien Bibliothek verfügbar.
The approved original version of this doctoral thesis is available in print at TU Wien Bibliothek.
TU Bibliothek WIEN Your knowledge hub

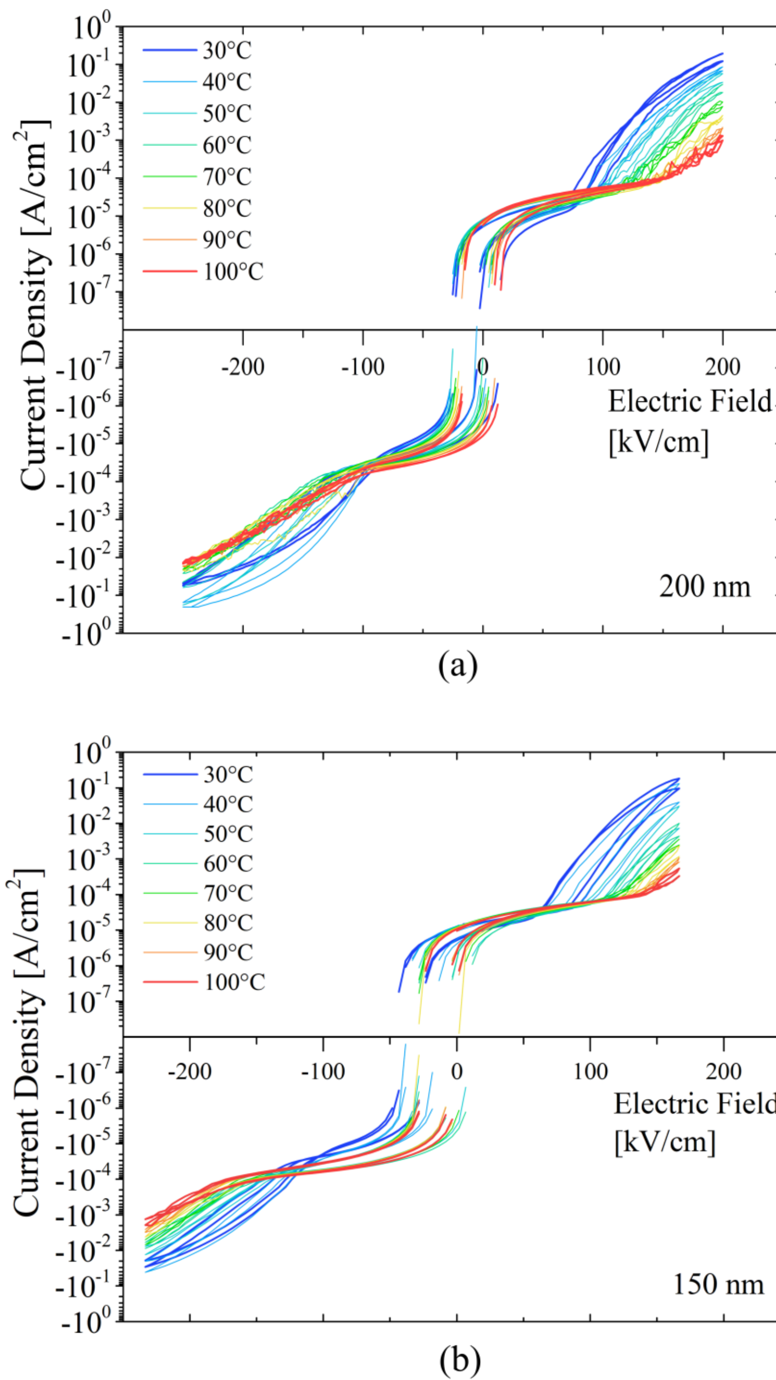

Figure 93 *Cyclic voltammetry of all set 1 samples at varying temperatures. The hold time was set to 100 ms, and two complete JV cycles were recorded at each temperature. (a) A sample with 200 nm dielectric thickness. (b) A sample with 150 nm dielectric thickness.*

Die approbierte gedruckte Originalversion dieser Dissertation ist an der TU Wien Bibliothek verfügbar.
The approved original version of this doctoral thesis is available in print at TU Wien Bibliothek.
TU Bibliothek Your knowledge hub WIEN

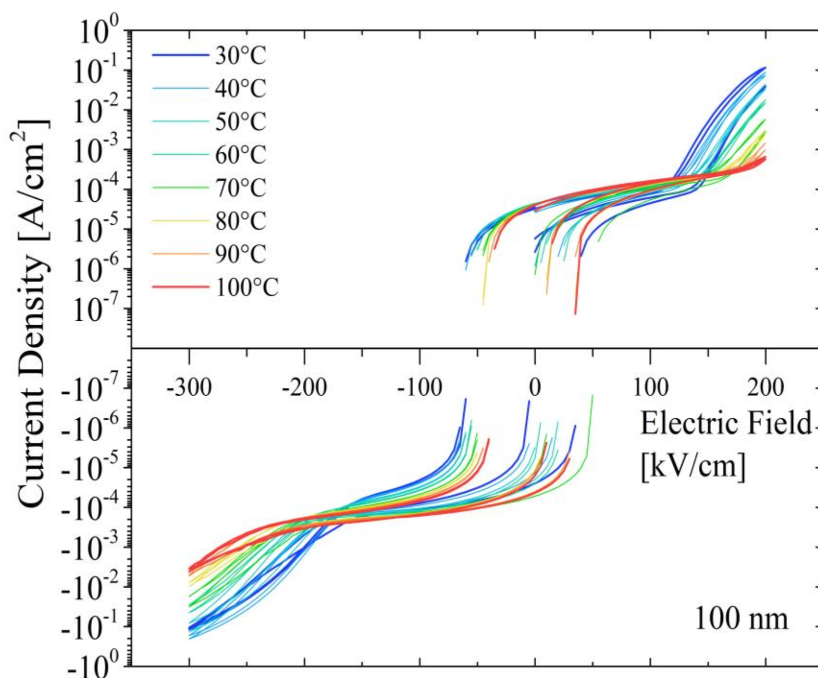

(a)

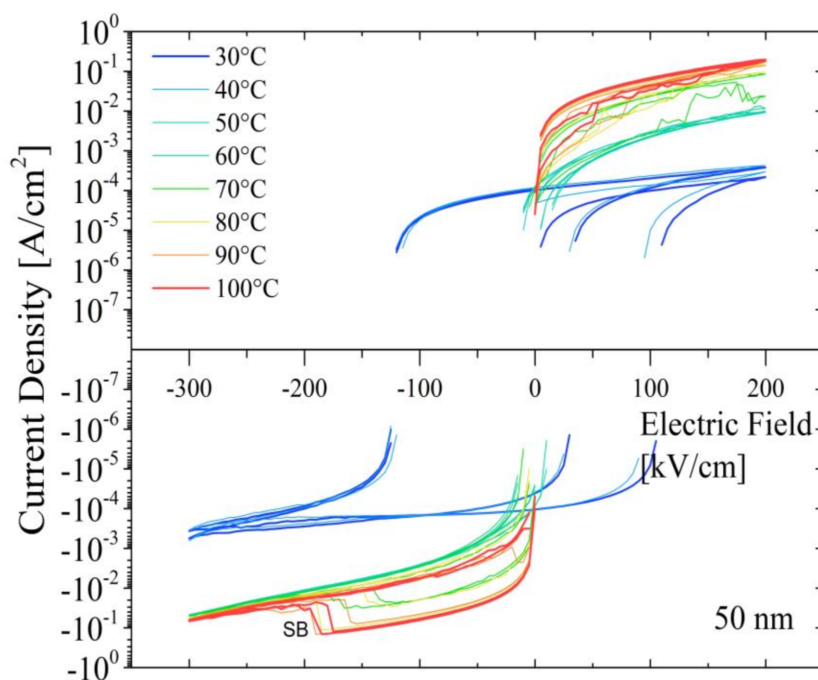

(b)

Figure 94 *Cyclic voltammetry of all set 1 samples at varying temperatures. The hold time was set to 100 ms, and two complete JV cycles were recorded at each temperature. (a) A sample with 100 nm dielectric thickness. (b) A sample with 50 nm dielectric thickness.*

Die approbierte gedruckte Originalversion dieser Dissertation ist an der TU Wien Bibliothek verfügbar.
The approved original version of this doctoral thesis is available in print at TU Wien Bibliothek.
TU Bibliothek WIEN Your knowledge hub

At 50 nm thickness, the resulting *JV* curve differs from the other samples. At room temperature, the *JV* curve is dominated by a capacitively induced leakage current (similar to *Figure 90*). At higher temperatures, the capacitive part vanishes, and a noisy transition to a filament-like *JV* behaviour is recorded. At temperatures above 70°C, a filament is formed, which is continuously being built and breaks down suddenly. This is event identified in the *JV* curve where the current suddenly jumps one order of magnitude, denoted with soft-breakdown (SB). Also, the capacitively induced electric field vanishes. It is reasonable to assume that a more pronounced filament-forming behaviour is present at samples with 50 nm dielectric thickness and at higher temperatures, respectively. The filament paths are shorter and hence, establish with a higher probability. Higher temperatures also increase the V_0 diffusion rate, leading to a faster filament build-up.

On the one hand, this is valid proof that filaments are indeed formed in the analysed capacitors. However, on the other hand, this means that the maximum applied field strength is too high for a reversible temperature cycling measurement. At lower maximum field values, the memristive behaviour is screened by the capacitively induced leakage current. As a consequence, it cannot be analysed with the same framework as the other samples with thicknesses above 50 nm.

When assessing the temperature dependence of samples with a film thickness >50 nm, a counterintuitive behaviour is determined. In most cases, the leakage current of a capacitor either increases with increasing temperature (see Schottky emission and Poole-Frenkel *equation 5* and *6*) or is independent of temperature (primarily seen in tunnelling effects such as Fowler-Nordheim tunnelling). Also, the free electron density, carrier mobility and oxygen vacancy forming rate increase with increasing temperature.[202,203] However, in the case of $IrO_x/TiO_x/IrO_x$ capacitors, none of these typical trends is observed, as the leakage current decreases almost three orders of magnitude with increasing temperature at electric fields <100 kV/cm.

TU Bibliothek WIEN Your knowledge hub
Die approbierte gedruckte Originalversion dieser Dissertation ist an der TU Wien Bibliothek verfügbar.
The approved original version of this doctoral thesis is available in print at TU Wien Bibliothek.

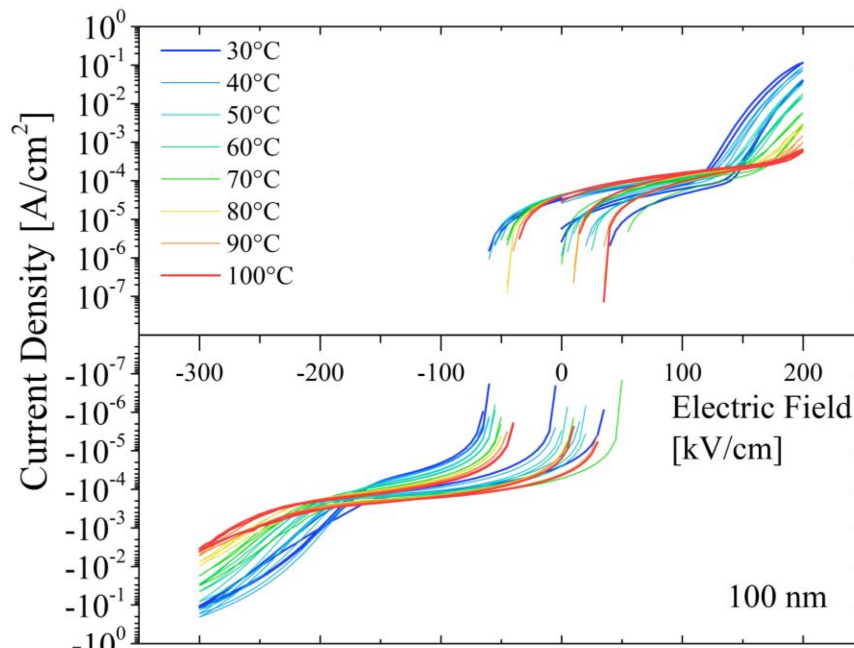

(a)

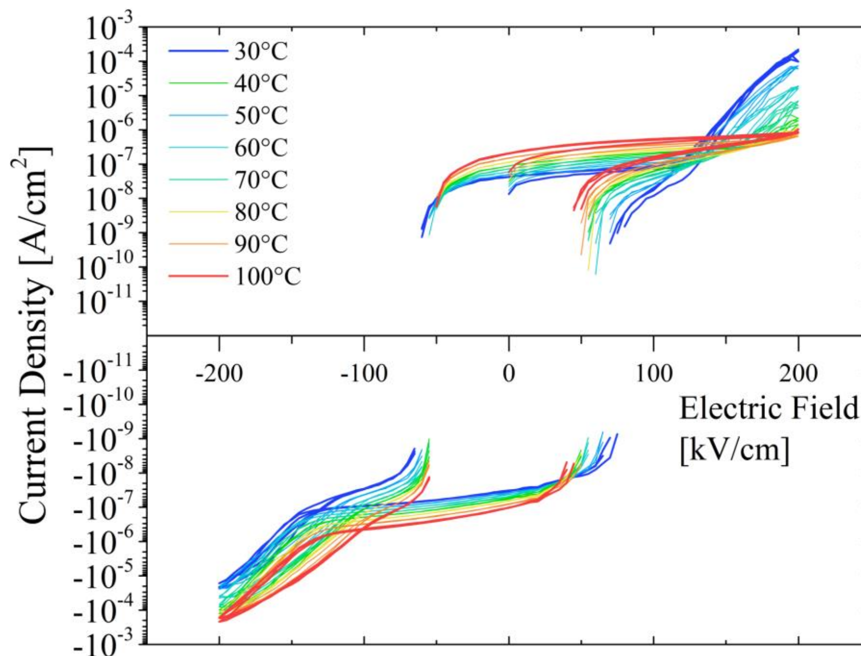

(b)

***Figure 95** Comparison of samples set 1, where the surface of the bottom electrode was exposed to air, to those of set 3, where this surface was not exposed to air. (a) Cyclic voltammetry measurement (two cycles) of a set 1 sample at various temperatures. At fields above 100 kV/cm, the current is inversely dependent on the temperature in both biasing directions. (b) Cyclic voltammetry (two cycles) of a set 3 sample. Notably, the current at negative bias is not inversely related to the temperature.*

Die approbierte gedruckte Originalversion dieser Dissertation ist an der TU Wien Bibliothek verfügbar.
The approved original version of this doctoral thesis is available in print at TU Wien Bibliothek.
TU WIEN Bibliothek Your knowledge hub

Where such a behaviour comes from can be seen when comparing sets 1 and 3 samples. The difference between these sets of samples is the exposure of the bottom electrode to air during fabrication. In *Figure 95 a*, a set 1 sample and in *b,* a set 3 sample was measured with cyclic voltammetry over temperatures ranging from 30 to 100°C. While the two samples show similar behaviour in the positive electric bias direction, the behaviour in negative electric bias direction differs significantly. While for the set 1 sample, where the bottom interface was exposed to the atmosphere, the leakage current decreased with increasing temperature, the opposite occurred in the set 3 sample, where the interface was not exposed to air. This represents strong evidence that the interface that forms when exposed to air is responsible for this counter-intuitive leakage current behaviour.

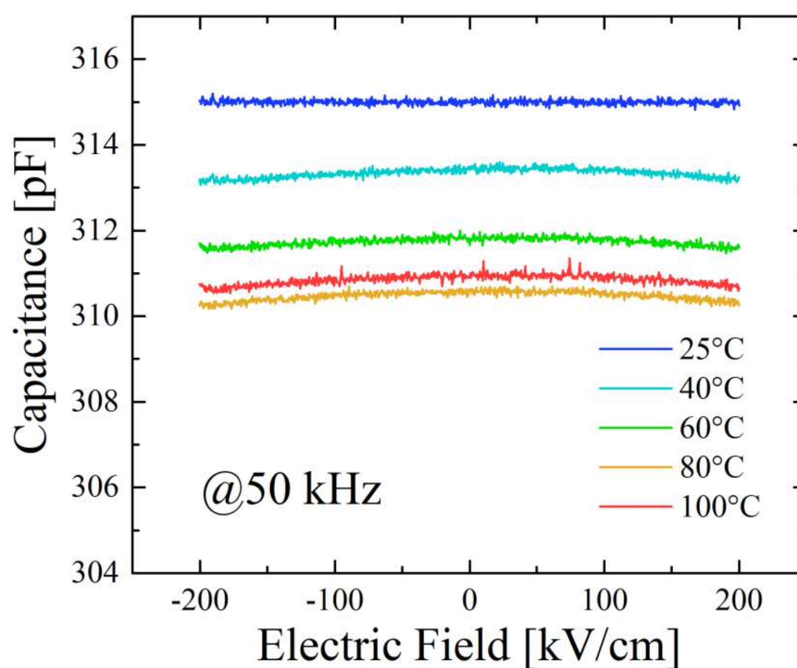

Figure 96 *Capacitance over biasing field measurement of a set 3 sample at temperatures ranging from 25 to 100°C at a biasing field frequency of 50 kHz. No electric field dependency can be identified. The temperature has minimal influence on the capacitance.*

The hypothesis is that due to the interface's exposure to air, a Schottky barrier formed, and the ohmic contact is not present anymore. Capacitance-voltage measurements of set 3 samples at temperatures from 30 to 100°C were performed to see if such a barrier exists. A diode-like *CV* curve is expected if a Schottky barrier is present. For a diode, the capacitance is dependent on the bias direction (positive bias or negative). In *Figure 96*, the *CV* measurement is shown. No

Die approbierte gedruckte Originalversion dieser Dissertation ist an der TU Wien Bibliothek verfügbar.
The approved original version of this doctoral thesis is available in print at TU Wien Bibliothek.
TU Bibliothek Your knowledge hub WIEN

such diode-like behaviour can be identified. The capacitance is constant with voltage and only changes ~5pF with increasing temperature. The formation of a Schottky interface is, therefore, unlikely.

Influence of atmosphere on the interface

A standard atmosphere contains mainly nitrogen, oxygen, and water (humidity). It is reasonable to assume that the interface that forms due to being in contact with these gaseous species is responsible for the unexpected temperature dependence of the leakage current.

One hypothesis is that the oxygen in the air passivates V_0 in the bottom interface, thus changing with respect to the top interface which is never in contact with air the oxygen vacancy distribution from a symmetric to an asymmetric one. As the oxygen vacancy density determines the overall electrical resistance, it is reasonable that the *JV*-curve is then also asymmetric.[42] The interface with less V_0 has a higher resistance than the that with a higher number of V_0. This hypothesis, however, would not explain the inverse temperature dependence, as a lower V_0 density leads to lower leakage currents at all temperatures and would not inverse this dependence.

Nitrogen can bind to the TiO_2 surface and, with the presence of water, is used for photocatalytic conversion of nitrogen to ammonia (NH_3).[204] In this process, the water is split and can interact with the V_0 at the interface. However, this process needs photons for activation, which are likely blocked by the top electrode IrO_x and dielectric TiO_x layer.

Water, on the other hand, can be adsorbed to both IrO_2 and TiO_2 surfaces and both materials are used as catalysts in an oxygen evolution reaction (OER). [49,50,204,205] It was also shown in this work that OH-bridges and adsorbed water are present at the investigated IrO_x surfaces. The presence of hydroxyl bridges when IrO_2 is exposed to water was also shown previously. [50] In addition, multiple works show the influence of water on leakage currents. More specifically, two works show such an influence on both Pt/$SrTiO_{3-\delta}$/Pt and Pt/TiO_2/Pt capacitors.[196,206] Similar to Pt, IrO_2 is also used for OER and is even a better catalyst for this reaction than Pt. [51,52] It was shown that the OH bridges for OER conditions deprotonate and passivate V_0 on the IrO_2 surface. [132] The OER favours higher temperatures, meaning that

Die approbierte gedruckte Originalversion dieser Dissertation ist an der TU Wien Bibliothek verfügbar.
The approved original version of this doctoral thesis is available in print at TU Wien Bibliothek.
TU Bibliothek WIEN Your knowledge hub

under these conditions , more V_0 can be passivated, which is similar to what was observed for Nb:$SrTiO_3$/$SrTiO_3$/Pt capacitors.[207]

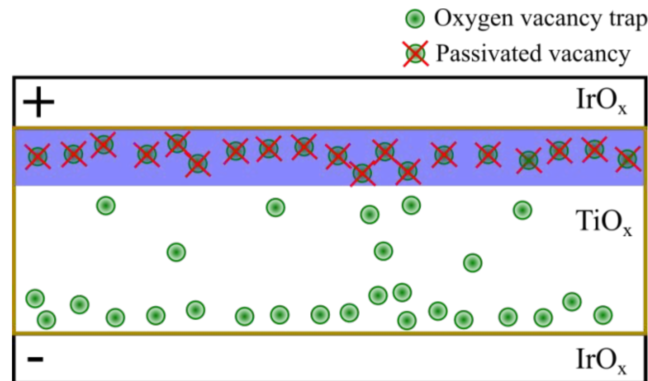

Figure 97 *Schematic representation of the mechanism causing the inverse temperature relationship.*

When taking these findings into consideration, the strong dependence of the leakage current on temperature can be estimated by an Arrhenius-type approach that the reaction rate of the OER follows. The so-called Tafel-slope of a catalyst is indicative of electrolytic cell efficiency. It has been shown previously that the Tafel-slope of IrO_2 decreases with temperature, which shows that the catalytic reaction rate increases.[208] Another study also linked higher temperatures to higher OER rates for IrO_2.[209] Therefore, the higher the temperature, the more the hydroxyl bridges deprotonate and the more V_0 are passivated.

Following these argumentations, the decrease in leakage current originates from the available oxygen from the deprotonation of the hydroxyl bridges at the interface. This additional oxygen can passivate oxygen vacancies and therefore, change the vacancy density at the interface. As depicted in *Figure 97*, the passivation of V_0 leads to the inhibition of the formation of low-resistance paths and filaments. This is seen in a decreased leakage current with increasing temperature when the interface was exposed to air during fabrication.

Die approbierte gedruckte Originalversion dieser Dissertation ist an der TU Wien Bibliothek verfügbar.
The approved original version of this doctoral thesis is available in print at TU Wien Bibliothek.
TU Bibliothek WIEN Your knowledge hub

4.4 Temperature-dependent cantilever characterization

The results of the electrical characterization led to the question of how the performance of the cantilevers changes under temperature in combination when fabricated under different atmospheres. The corresponding results are presented and discussed in the following.

$IrO_x/TiO_x/IrO_x$ cantilevers were measured with the MSA in resonance at different temperatures and atmospheres (in air or in moisturized nitrogen with varying relative humidity). During fabrication, both interfaces were in contact with air. Unfortunately, due to necessary lift-off steps, the fabrication of cantilevers where the bottom interface was exposed to air was impossible. *Figure 98 a* shows the tip deflection as a function of applied voltage at various temperature levels in air. In general, a decrease in tip deflection can be identified. For a more detailed measurement, an MSA surface raster scan of the cantilever, from which the curvature was determined, was performed and is shown in *Figure 98 b*. Again, a decrease in temperature at all applied voltages is observed. From the curvature/voltage, the flexoelectric coefficient at resonance was calculated using *equation 28*, and shown in *Figure 98 c*.

Die approbierte gedruckte Originalversion dieser Dissertation ist an der TU Wien Bibliothek verfügbar.
The approved original version of this doctoral thesis is available in print at TU Wien Bibliothek.
TU WIEN Bibliothek Your knowledge hub

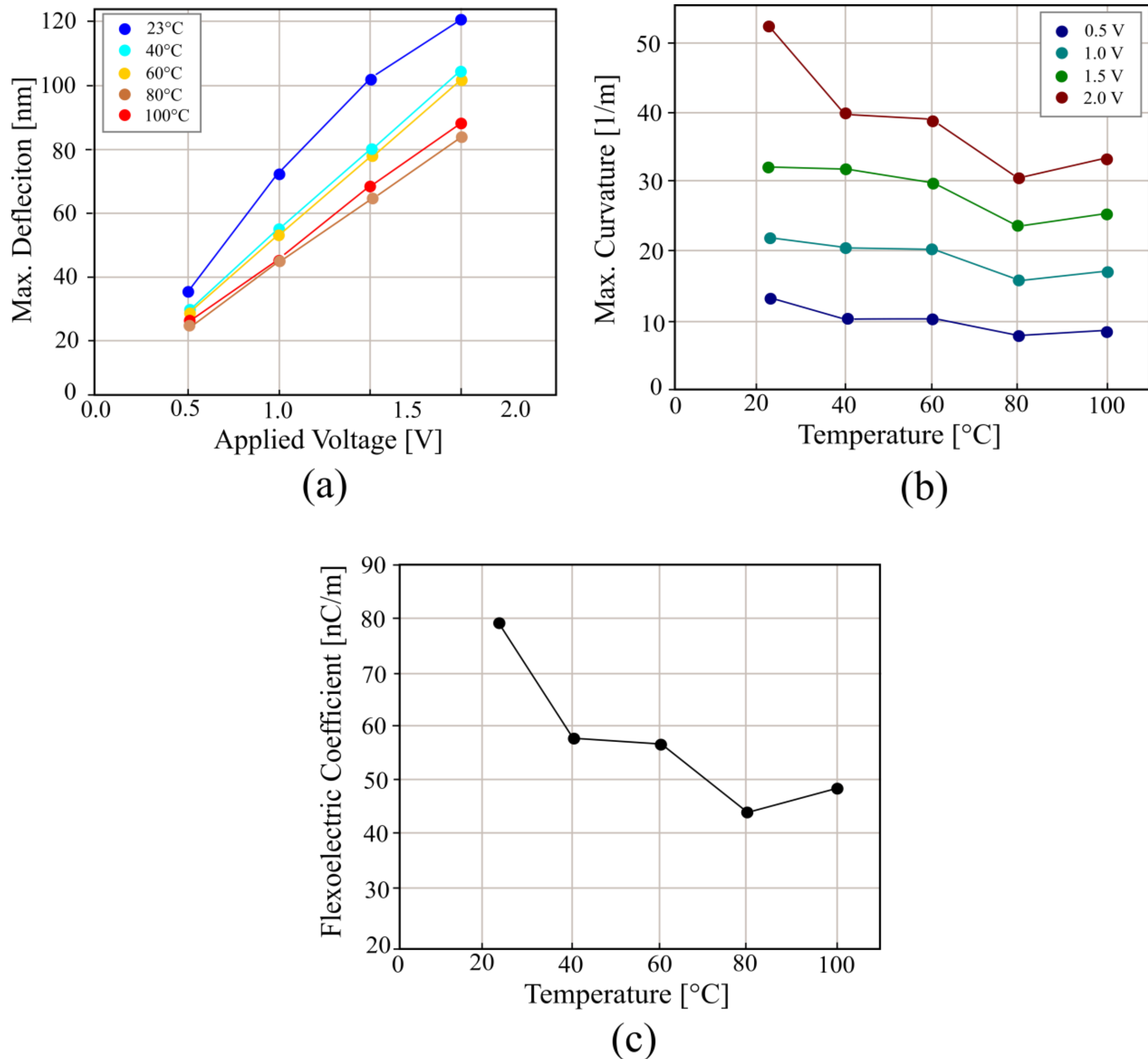

Figure 98 *MSA characterization of the IrOx/TiO$_x$/IrO$_x$ cantilevers from room temperature to 100°C. (a) Cantilever tip deflection as a function of the applied voltage. (b) Curvature resulting from MSA surface raster scans at different voltages. (c) The calculated flexoelectric coefficient at resonance over temperature.*

As can be seen, the actuation performance decreases over temperature. Several factors could be the cause:

- The permittivity decreases with temperature
- The stiffness increases over temperature
- An increased amount of losses, i.e. lower Q-factor
- Some specific impact on the flexoelectric effect causes the decrease.

Die approbierte gedruckte Originalversion dieser Dissertation ist an der TU Wien Bibliothek verfügbar.
The approved original version of this doctoral thesis is available in print at TU Wien Bibliothek.
TU Bibliothek WIEN Your knowledge hub

First, the permittivity decreases over temperature, as shown in section 4.3, although it decreases by ~10%, whereas the flexoelectric actuation decreases by almost 50%. This difference in decrease means that the drop in permittivity does not fully account for this effect.

With the thermo-mechanical spectrum of the cantilever at different temperatures shown in *Figure 99 a*, the second and third arguments can be disregarded. From room temperature to 100°C, there is no change in the full-width half-maximum of the resonance spectrum, which means that the *Q*-factor does not change significantly over temperature. Also, the resonance frequency does not vary significantly, as seen in *Figure 99 b*, which means that the Young's modulus can be regarded as constant.

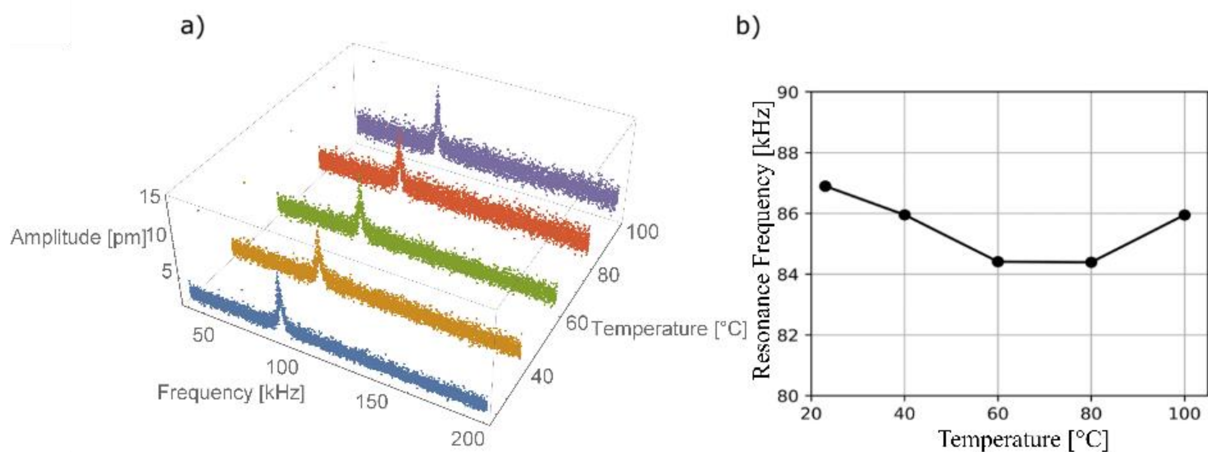

Figure 99 *(a) The cantilever amplitude-frequency spectrum due to thermal noise at temperatures ranging from room temperature to 100°C. (b) The cantilever resonance frequency over temperature.*

The only remaining possibility for the origin why the decrease in flexoelectric actuation over temperature occurs is a direct influence on the flexoelectric coefficient.

In section 4.3, it was shown that an electrically active TiO_y layer with a high amount of V_0 is present at the interface of IrO_x/TiO_x. As the interface plays a vital role in flexoelectric actuation, it is very likely, that there is a correlation between the presence of a reduced layer and the flexoelectric actuation. As the oxygen vacancies of the TiO_x act like an n-type dopant, meaning that there is an excess of electrons, it exhibits a higher electrical potential than stoichiometric TiO_2.[210] This leads to a larger field gradient at the interface. When temperature increases, the reduced interfacial layer is oxidized due to the OER of the IrO_x. This decreases the amount of charged oxygen vacancies and as such, weakens the field gradient. This could potentially explain the decrease in flexoelectric actuation.

Die approbierte gedruckte Originalversion dieser Dissertation ist an der TU Wien Bibliothek verfügbar.
The approved original version of this doctoral thesis is available in print at TU Wien Bibliothek.
TU Bibliothek WIEN Your knowledge hub

To further study the behaviour of the cantilever, a setup was designed where the cantilever can be exposed to a controlled atmosphere containing moisturized nitrogen while still being able to measure the cantilever with the MSA. It was shown that the oxygen from humid air can permeate through Pt electrodes via grain boundaries and potentially passivate the interfacial layer.[207] It is assumed that a similar effect is happening in the polycrystalline IrO_2 electrode. In accordance with the temperature-dependent leakage current measurements, this would result in a decrease in cantilever actuation.

For the atmosphere, moisturized nitrogen gas was used, where the relative humidity was changed from 5% to 75%. The resulting maximum cantilever deflection can be seen in *Figure 100*. Two different cantilevers were measured at varying humidity and voltages. The dots indicate measurements at an excitation voltage of 0.5 V, whereas the stars denote measurements at 2 V.

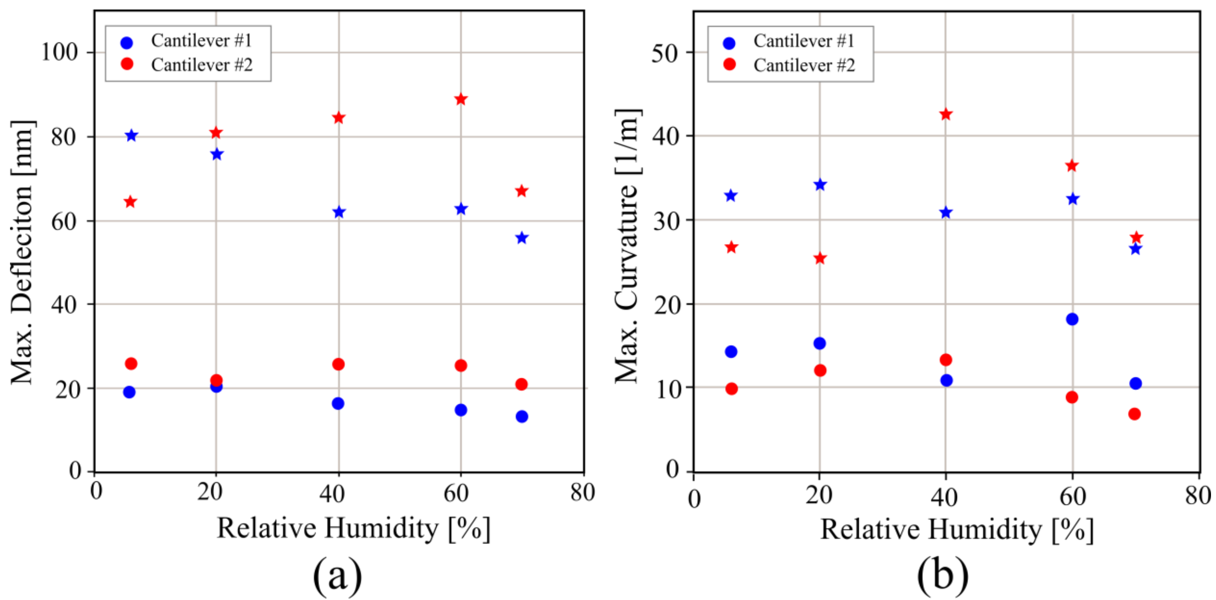

Figure 100 *(a) The maximum cantilever deflection of two cantilevers (red and blue) at varying relative humidity during operation. (b) The maximum curvature of the two cantilevers when changing the relative humidity. Dots denote measurements at a sinusoidal excitation of 0.5 V, while stars indicate a sinusoidal excitation profile of 2 V.*

Unfortunately, an explicit dependency of the cantilever behaviour concerning the relative humidity cannot be identified. This might be due to the thickness of the top electrode being too large, which inhibits the ability of the water molecules to permeate through the electrodes. As such, a decrease in electrode thickness might be beneficial. Also, the sample size must be increased, so that a measurement variance can be determined.

Die approbierte gedruckte Originalversion dieser Dissertation ist an der TU Wien Bibliothek verfügbar.
The approved original version of this doctoral thesis is available in print at TU Wien Bibliothek.
TU Bibliothek WIEN Your knowledge hub

5 Conclusio

This work investigated the flexoelectric effect of TiO_x and α-phase PVDF. Several MEMS cantilever designs were successfully fabricated with semiconductor-compatible process steps. Multiple techniques were used to analyse the Au/α-phase-PVDF/Au and $IrO_x/TiO_x/IrO_x$ cantilevers from an electrical and mechanical point of view.

For the fabrication of PVDF cantilevers, the atmospheric condition under which the PVDF is deposited on the wafer is very important. When processed at room temperature, the root mean squared roughness of the PVDF layer can reach values being in the range of the total PVDF film thickness, which makes it unusable for MEMS devices. To reduce the roughness, the PVDF film was deposited via a spin-on method on a pre-heated chuck, which resulted in smooth thin films with a low RMS roughness of ~18 nm. Atomic force microscopy confirmed a spherulitic grain structure with 1-4 µm large grains, typical for α-phase PVDF. Furthermore, the presence of mainly α-phase at deposition temperatures above 70°C was confirmed with Fourier transform infrared spectroscopy and X-ray diffraction analysis. A cantilever process was developed, and devices were fabricated successfully. The cantilevers were designed such that the device layer was omitted, typically needed in piezoelectric actuation schemes. This design theoretically eliminates electromechanical mechanisms other than the flexoelectric effect due to a centred neutral axis.

The mechanical deflection of the cantilevers, when excited by a sinusoidal electric field, was measured with a laser-Doppler vibrometer. The spectral response was measured, with excitation at half the measurement frequency, to identify the quadratic and second-order electromechanical effects. Only a small linear electromechanical coupling between stress and electric field could be determined from the resulting resonance spectra of these cantilevers. From the available data, it cannot be concluded that the flexoelectric effect is a significant part of the total electromechanical actuation. Also, it was not possible to distinguish the flexoelectric from the piezoelectric effect, as it was discovered that an asymmetry of the lateral size between

Die approbierte gedruckte Originalversion dieser Dissertation ist an der TU Wien Bibliothek verfügbar.
The approved original version of this doctoral thesis is available in print at TU Wien Bibliothek.
TU WIEN Bibliothek Your knowledge hub

the top electrode to the bottom electron leads to a shift of the neutral axis out of the centre of the cantilever. A centred neutral axis would be needed to distinguish the effects sufficiently. While these α-phase PVDF cantilevers do not show specific flexoelectric behaviour, it was demonstrated that the electrostrictive effect shows a significant actuation. This result extends the usability of PVDF in MEMS devices, as there is no need to convert the non-polar α-phase PVDF to the polar β-phase PVDF in a complex process. The electrostrictive actuation of the cantilevers shows a tip deflection of ~450 nm with a 60 µm long cantilever at 60 V. When compared to β-phase piezoelectric PVDF-TrFe, the electrostrictive cantilevers showed 30% of the tip deflection, which makes such devices useful for most MEMS resonator applications.

Additionally, the cantilever response at different temperatures was measured. Here the cantilever is exposed to the temperature while the thermally induced mechanical noise spectrum is observed. The temperature dependence of the quadratic electromechanical signal shows that a change in the deflection over temperature can be explained by a modification of the Young's modulus. Also, the devices are temperature stable up to 160°C; at higher temperatures, the PVDF film shows bubbles and degrades fast.

The analysis of TiO_x was another focus of this work. A fabrication process for flexoelectric TiO_x-based MEMS cantilevers is shown, where no backside etch is needed, and the number of steps in the process is limited to a minimum. Like the α-phase PVDF cantilevers, the device layer is omitted for the TiO_x cantilevers. A clear flexoelectric mechanism of the $IrO_x/TiO_x/IrO_x$ cantilevers was identified. An in-depth analysis of the various electromechanical mechanisms was performed, proving that the measured deflection originates from the flexoelectric effect. It was demonstrated that the flexoelectric TiO_x cantilevers are viable structures for low-voltage MEMS actuators, where the maximum tip deflection of a 100 µm long cantilever is ~231 nm at 2 V. The flexoelectric coefficient was determined to be 1.78 ± 0.16 nC m^{-1}. The flexoelectric coupling constant is calculated as 2.75 V, relatively close to the so-called Kogan's estimate of 3.14 V for TiO_2 in the *a/b* direction of the rutile unit cell. Cantilevers with a segmented top electrode were fabricated with the goal to artificially introduce a higher density of electric field gradients into the dielectric. An extensive analysis with finite-element simulations of the electric field in the dielectric was performed. Examples are presented that such an idea can be beneficial. However, the measurements do not show the increase in flexoelectric actuation that was theoretically predicted by the simulations. From these measurements it was concluded, that

TU Bibliothek WIEN Your knowledge hub
Die approbierte gedruckte Originalversion dieser Dissertation ist an der TU Wien Bibliothek verfügbar.
The approved original version of this doctoral thesis is available in print at TU Wien Bibliothek.

the electrode/dielectric interface is the main driving factor for flexoelectric behaviour in cantilevered MEMS devices.

$IrO_x/TiO_x/IrO_x$ plate capacitor structures were investigated to gain more knowledge about the impact of the interface on the electrical behaviour. The capacitors show a frequency- and temperature-dependent permittivity of ~ 78 to 60 between 50 and 300 kHz and 25 to 100°C. Various effects can be demonstrated with leakage current measurements, such as a generation of oxygen vacancies, a resulting memristive behaviour, and a significant contribution from capacitively induced leakage current, respectively. The IrO_x/TiO_x interface was chemically characterized with TEM EELS, where a ~5 nm thin, significantly reduced TiO_y layer (where $y < x$) was found close to the IrO_x electrode. Unfortunately, it was impossible to determine the chemical bond concentration of TiO^{3+} in the TiO_y layer, but as the EELS measurement suggests, the amount of TiO^{3+} is higher than in the bulk of the TiO_x layer.

A trap-assisted space-charge-limited current was identified as the dominating leakage current mechanism. The SCLC mechanism was confirmed by determing the slope of current-voltage curves obtained from cyclic-voltammetry measurements. These slopes were ~1 at voltages < 1 V (<100 kV/cm), about 17 between 1 and 2 V (100 - 200 kV/cm) and 2 for voltages above 2 V (<200 kV/cm), typical for SCLC with traps. The different slopes at the respective voltage ranges are explained as follows. In the low voltage regime, the traps are not active, and the dielectric relaxation time is substantially lower than the time electrons need to pass through the dielectrics. This leads to ohmic conduction. In the intermediate voltage regime, traps are activated along low resistance paths through the dielectric and contribute to conduction, likely due to trap-assisted tunnelling and hopping mechanisms. In the high-voltage regime, all traps are active, the dielectric relaxation time is larger than the electron's travel time, and a space-charge limited conduction is observed. Additionally, high electrical stress leads to the generation of additional oxygen vacancies.

Even in the initial configuration, the high amount of oxygen vacancies causes a capacitive leakage current behaviour. This capacitive behaviour happens when an electric field is applied, and the negatively charged oxygen ions move opposite the positively charged oxygen vacancies in the TiO_x. This charge movement introduces an internal electric field with a slow relaxation time (in seconds), leading to charges flowing even if the external applied electric field is zero.

TU Bibliothek WIEN Your knowledge hub
Die approbierte gedruckte Originalversion dieser Dissertation ist an der TU Wien Bibliothek verfügbar.
The approved original version of this doctoral thesis is available in print at TU Wien Bibliothek.

Other memristive effects are caused by two mechanisms. One is an interfacial effect, caused by dynamic trap activation and deactivation depending on stressing parameters. The other is a filament-forming behaviour, where electrically conductive filaments of oxygen vacancies form and dissociate. Filament forming can be reversible under certain conditions, thus causing hysteresis. The dominant effect depends on various stressing parameters, such as electric field amplitude, biasing hold time, temperature and dielectric layer thickness. Generally, the interfacial memristive behaviour is dominant at low electric fields (< 300 kV/cm), hold times (< 100 ms) and temperatures (< 70°C). Reversible filament-forming with switching capabilities was observed for samples with 50 nm dielectric layer thickness and temperatures above 70°C. Irreversible filament-forming happens at high electric field values, biasing hold times and temperatures and are considered to cause device failure.

An unintuitive behaviour is identified when performing the temperature-dependent evaluation of the leakage current characteristic. Counterintuitively, the leakage current decreases with an increase in temperature. It was shown that the temperature dependence changed depending on whether the IrO_x/TiO_x interface was exposed to the air during the fabrication process or kept under vacuum. When the interface was exposed to the latter condition, the leakage currents showed the expected increase with increasing temperature. If not, the leakage current decreased with increasing temperature. The catalytic activity of IrO_x with respect to water splitting provides a reasonable explanation for this behaviour. When IrO_x is exposed to a water or humidity containing atmosphere, oxygen-hydrogen (OH) bridges are bound to the surface. When an electric field is applied, these OH bridges deprotonate, and the oxygen that is now freely available can now passivate oxygen vacancies and therefore reduce the overall leakage currents.

The impact of this dependency on temperature and humidity was also investigated with TiO_x cantilevers. A setup was built where the cantilevers are exposed to temperature and to a nitrogen atmosphere with a varying amount of relative humidity while still being able to be measured under a laser Doppler vibrometer. The flexoelectric coefficient of the cantilevers was determined from room temperature to 100°C and at relative humidity values, ranging from 7 to 70%. Unfortunately, no clear dependence on the humidity could be observed, which could be caused by the selected thickness of the top electrode, preventing water from permeating down to the TiO_x interface. It is possible that a decrease in the top electrode thickness could allow the

Die approbierte gedruckte Originalversion dieser Dissertation ist an der TU Wien Bibliothek verfügbar.
The approved original version of this doctoral thesis is available in print at TU Wien Bibliothek.
TU Bibliothek WIEN Your knowledge hub

water to pass through. However, a temperature dependence is observed. The flexoelectric coefficient of the cantilever decreases with increasing temperature. We rule out possible sources for this decrease, such as higher mechanical or electrical losses, a reduction in permittivity or an increase in the Young's modulus. This, in turn, means that the decline in cantilever excitation amplitude originates from a decrease in the flexoelectric coefficient. As the flexoelectric effect in cantilevers originates from a field gradient at the interface to the electrodes, and we have shown that the interface has an increased amount of oxygen vacancies compared to the bulk of the TiO_x, these vacancies most likely impact the electric field gradient. When the temperature increases, the leakage current decreases due to a lower amount of oxygen vacancies.

Die approbierte gedruckte Originalversion dieser Dissertation ist an der TU Wien Bibliothek verfügbar.
The approved original version of this doctoral thesis is available in print at TU Wien Bibliothek.
TU WIEN Bibliothek Your knowledge hub

6 Outlook

Based on the results presented in this thesis many topics need to be studied in more detail. Most critical is to identify the role of oxygen vacancies with respect to the flexoelectric effect. While much effort went into this topic, the answer is still unclear. The previously discussed temperature-dependent laser-Doppler measurements of the TiOx cantilevers should be repeated as a first step. The oxygen vacancy density does likely have an impact on the flexoelectric behaviour. The next step is to improve the humidity measurements, mainly by finding a fabrication process, where the interface does not come in contact with air. The scientific questions that need to be answered are: What is the role of oxygen vacancies on the flexoelectric effect? Would an increase in vacancies increase the flexoelectric effect? In that case, the origin of the actuation in the TiO_x cantilevers is not purely of flexoelectric nature. If the vacancies decrease the flexoelectric actuation, the next step would be to reduce the defects as much as possible to maximize the flexoelectric effect at flexoelectric applications.

One of the prime applications for the flexoelectric effect is a flexoelectric microphone with ultra-thin membranes or an ultra-thin AFM cantilever. Using the flexoelectric effect for such application adds many possibilities regarding materials, as every dielectric exhibits a flexoelectric effect. However, for a commercially viable application, it is essential to find other electrode materials than the IrO_x electrodes, as they are expensive and complicated to integrate into a fabrication process.

Another interesting measurement is the thickness dependence of the flexoelectric effect in the TiO_x cantilevers. As it is proposed that the flexoelectric effect theoretically increases with decreasing film thickness, cantilevers at varying dielectric thicknesses must be investigated. The main question here is: Does the flexoelectric effect increase with decreasing thickness, and if yes, in what proportionality? The result will also allow a better interpretation of the electromechanical mechanism behind the TiO_x cantilevers.

It is also essential to look at other flexoelectric materials. Ta_2O_5 is especially interesting as a flexoelectric material, as it exhibits a high dielectric constant while showing low leakage

Die approbierte gedruckte Originalversion dieser Dissertation ist an der TU Wien Bibliothek verfügbar.
The approved original version of this doctoral thesis is available in print at TU Wien Bibliothek.
TU WIEN Bibliothek Your knowledge hub

currents. This is further supported as this material is extensively used in the production of capacitors. This material could be a potential candidate for flexoelectric applications.

TU Bibliothek WIEN Your knowledge hub
Die approbierte gedruckte Originalversion dieser Dissertation ist an der TU Wien Bibliothek verfügbar.
The approved original version of this doctoral thesis is available in print at TU Wien Bibliothek.

7 References

[1] S. Nagod, S. V Halse, Evolution of MEMS Technology, Int. Res. J. Eng. Technol. 12 (2017) 2395–56.

[2] F.T. Geyling, J.J. Forst, Semiconductor strain transducers, Bell Syst. Tech. J. 39 (1960) 705–731. https://doi.org/10.1002/j.1538-7305.1960.tb03939.x.

[3] K.E. Petersen, Silicon as a mechanical material, Micromechanics MEMS Class. Semin. Pap. to 1990. 70 (1997) 58–95. https://doi.org/10.1109/9780470545263.sect1.

[4] R.B. Hood, Automotive Semiconductor Pressure Sensors, SAE Trans. 85 (1976) 323–344.

[5] J. Zhang, C. Wang, C. Bowen, Piezoelectric effects and electromechanical theories at the nanoscale, Nanoscale. 6 (2014) 13314–13327. https://doi.org/10.1039/c4nr03756a.

[6] A.K. Tagantsev, Theory of flexoelectric effect in crystals, Sov.Phys. JETP. 61 (1985) 1246.

[7] J.M. Gregg, Stressing Ferroelectrics, 534 (2012).

[8] P. Zubko, G. Catalan, A.K. Tagantsev, Flexoelectric Effect in Solids, Annu. Rev. Mater. Res. 43 (2013) 387–421. https://doi.org/10.1146/annurev-matsci-071312-121634.

[9] K. Uchino, Advanced piezoelectric materials, Woodhead Publishing, 2010. https://doi.org/https://doi.org/10.1533/9781845699758.1.

[10] G. Han, J. Ryu, W.H. Yoon, J.J. Choi, B.D. Hahn, D.S. Park, Effect of film thickness on the piezoelectric properties of lead zirconate titanate thick films fabricated by aerosol deposition, J. Am. Ceram. Soc. 94 (2011) 1509–1513. https://doi.org/10.1111/j.1551-2916.2010.04276.x.

[11] K.P. Kelley, D.E. Yilmaz, L. Collins, Y. Sharma, H.N. Lee, D. Akbarian, A.C.T. Van Duin, P. Ganesh, R.K. Vasudevan, Thickness and strain dependence of piezoelectric coefficient in BaTiO3 thin films, Phys. Rev. Mater. 4 (2020) 24407.

Die approbierte gedruckte Originalversion dieser Dissertation ist an der TU Wien Bibliothek verfügbar.
The approved original version of this doctoral thesis is available in print at TU Wien Bibliothek.
TU WIEN Bibliothek Your knowledge hub

https://doi.org/10.1103/PhysRevMaterials.4.024407.

[12] M. Zhang, J. Yang, C. Si, G. Han, Y. Zhao, J. Ning, Research on the piezoelectric properties of AlN thin films for MEMS applications, Micromachines. 6 (2015) 1236–1248. https://doi.org/10.3390/mi6091236.

[13] A. Biancoli, C.M. Fancher, J.L. Jones, D. Damjanovic, Breaking of macroscopic centric symmetry in paraelectric phases of ferroelectric materials and implications for flexoelectricity, Nat. Mater. 14 (2015) 224–229. https://doi.org/10.1038/nmat4139.

[14] M.S. Majdoub, P. Sharma, T. Çağin, Dramatic enhancement in energy harvesting for a narrow range of dimensions in piezoelectric nanostructures, Phys. Rev. B - Condens. Matter Mater. Phys. 78 (2008) 2008–2009. https://doi.org/10.1103/PhysRevB.78.121407.

[15] E.V. Bursian, N.N. Trunov, Nonlocal piezoelectric effect, Fiz. Tverd. Tela. 16 (1974) 1187–1190.

[16] E.V. Bursian, O.I. Zaikovsk, Changes in curvature of a ferroelectric film due to polarization, Sov. Phys. Solid State. (1968).

[17] A. Abdollahi, F. Vásquez-Sancho, G. Catalan, Piezoelectric Mimicry of Flexoelectricity, Phys. Rev. Lett. 121 (2018) 205502. https://doi.org/10.1103/PhysRevLett.121.205502.

[18] W. Ma, L.E. Cross, Flexoelectric effect in ceramic lead zirconate titanate, Appl. Phys. Lett. 86 (2005) 1–3. https://doi.org/10.1063/1.1868078.

[19] T. Hu, Q. Deng, X. Liang, S. Shen, Measuring the flexoelectric coefficient of bulk barium titanate from a shock wave experiment, J. Appl. Phys. 122 (2017) 55106. https://doi.org/10.1063/1.4997475.

[20] U.K. Bhaskar, N. Banerjee, A. Abdollahi, Z. Wang, D.G. Schlom, G. Rijnders, G. Catalan, A flexoelectric microelectromechanical system on silicon, Nat. Nanotechnol. 11 (2016) 263–266. https://doi.org/10.1038/nnano.2015.260.

[21] J. Robertson, High dielectric constant oxides, Eur. Phys. J. Appl. Phys. 28 (2004) 265–291. https://doi.org/10.1051/epjap:2004206.

[22] J. Krupka, J. Breeze, A. Centeno, N. Alford, T. Claussen, L. Jensen, Measurements of Permittivity, Dielectric Loss Tangent, and Resistivity of Float-Zone Silicon at Microwave Frequencies, IEEE Trans. Microw. Theory Tech. 54 (2006) 3995–4001.

Die approbierte gedruckte Originalversion dieser Dissertation ist an der TU Wien Bibliothek verfügbar.
The approved original version of this doctoral thesis is available in print at TU Wien Bibliothek.
TU WIEN Bibliothek Your knowledge hub

https://doi.org/10.1109/TMTT.2006.883655.

[23] M. Schneider, A. Bittner, A. Klein, U. Schmid, Impact of film thickness and temperature on the dielectric breakdown behavior of sputtered aluminum nitride thin films, Microelectron. Eng. 140 (2015) 47–51. https://doi.org/10.1016/j.mee.2015.06.001.

[24] L. Shu, R. Liang, Z. Rao, L. Fei, S. Ke, Y. Wang, Flexoelectric materials and their related applications: A focused review, J. Adv. Ceram. 8 (2019) 153–173. https://doi.org/10.1007/s40145-018-0311-3.

[25] J. Lu, J. Lv, X. Liang, M. Xu, S. Shen, Improved approach to measure the direct flexoelectric coefficient of bulk polyvinylidene fluoride, J. Appl. Phys. 119 (2016). https://doi.org/10.1063/1.4943069.

[26] S. ryung Kwon, Structural analysis of truncated pyramids for flexoelectric sensing, J. Mech. Sci. Technol. 31 (2017) 5971–5975. https://doi.org/10.1007/s12206-017-1141-x.

[27] S. Baskaran, N. Ramachandran, X. He, S. Thiruvannamalai, H.J. Lee, H. Heo, Q. Chen, J.Y. Fu, Giant flexoelectricity in polyvinylidene fluoride films, Phys. Lett. A. 375 (2011) 2082–2084. https://doi.org/10.1016/j.physleta.2011.04.011.

[28] S. Baskaran, X. He, Y. Wang, J.Y. Fu, Strain gradient induced electric polarization in alpha-phase polyvinylidene fluoride films under bending conditions, (2011). https://doi.org/10.1063/1.3673817.

[29] S. Baskaran, X. He, Q. Chen, J.Y. Fu, Experimental studies on the direct flexoelectric effect in α -phase polyvinylidene fluoride films, Appl. Phys. Lett. 98 (2011) 1–4. https://doi.org/10.1063/1.3599520.

[30] T. Wongwirat, Z. Zhu, G. Rui, R. Li, P. Laoratanakul, H. He, H. Manuspiya, L. Zhu, Origins of Electrostriction in Poly(vinylidene fluoride)-Based Ferroelectric Polymers, Macromolecules. 53 (2020) 10942–10954. https://doi.org/10.1021/acs.macromol.0c02083.

[31] J. Liu, Y. Zhou, X. Hu, B. Chu, Flexoelectric effect in PVDF-based copolymers and terpolymers, Appl. Phys. Lett. 112 (2018). https://doi.org/10.1063/1.5028344.

[32] S. Stassi, I. Cooperstein, M. Tortello, C.F. Pirri, S. Magdassi, C. Ricciardi, Reaching silicon-based NEMS performances with 3D printed nanomechanical resonators, Nat. Commun. 12 (2021). https://doi.org/10.1038/s41467-021-26353-1.

Die approbierte gedruckte Originalversion dieser Dissertation ist an der TU Wien Bibliothek verfügbar.
The approved original version of this doctoral thesis is available in print at TU Wien Bibliothek.
TU Bibliothek WIEN Your knowledge hub

[33] P. V. Yudin, A.K. Tagantsev, Fundamentals of flexoelectricity in solids, Nanotechnology. 24 (2013). https://doi.org/10.1088/0957-4484/24/43/432001.

[34] C. Lee, P. Ghosez, X. Gonze, Lattice dynamics and dielectric properties of incipient ferroelectric TiO2 rutile, Phys. Rev. B. 50 (1994) 13379–13387. https://doi.org/10.1103/PhysRevB.50.13379.

[35] M. Mikami, S. Nakamura, O. Kitao, H. Arakawa, Lattice dynamics and dielectric properties of TiO2 anatase: A first-principles study, Phys. Rev. B - Condens. Matter Mater. Phys. 66 (2002) 1–6. https://doi.org/10.1103/PhysRevB.66.155213.

[36] J. Narvaez, F. Vasquez-Sancho, G. Catalan, Enhanced flexoelectric-like response in oxide semiconductors, Nature. 538 (2016) 219–221. https://doi.org/10.1038/nature19761.

[37] R.J. Kennedy, P.A. Stampe, The influence of lattice mismatch and film thickness on the growth of TiO2 on LaAlO3 and SrTiO3 substrates, J. Cryst. Growth. 252 (2003) 333–342. https://doi.org/https://doi.org/10.1016/S0022-0248(02)02514-9.

[38] A. Sawa, Resistive switching in transition metal oxides, Mater. Today. 11 (2008) 28–36. https://doi.org/10.1016/S1369-7021(08)70119-6.

[39] M. Saadi, P. Gonon, C. Vallée, C. Mannequin, H. Grampeix, E. Jalaguier, F. Jomni, A. Bsiesy, On the mechanisms of cation injection in conducting bridge memories: The case of HfO2 in contact with noble metal anodes (Au, Cu, Ag), J. Appl. Phys. 119 (2016). https://doi.org/10.1063/1.4943776.

[40] R. Waser, M. Aono, Nanoionics-based resistive switching memories., Nat. Mater. 6 (2007) 833–40. https://doi.org/10.1038/nmat2023.

[41] A. Wedig, M. Luebben, D.Y. Cho, M. Moors, K. Skaja, V. Rana, T. Hasegawa, K.K. Adepalli, B. Yildiz, R. Waser, I. Valov, Nanoscale cation motion in TaOx, HfOx and TiOx memristive systems, Nat. Nanotechnol. 11 (2016) 67–74. https://doi.org/10.1038/nnano.2015.221.

[42] B.J. Choi, D.S. Jeong, S.K. Kim, C. Rohde, S. Choi, J.H. Oh, H.J. Kim, C.S. Hwang, K. Szot, R. Waser, B. Reichenberg, S. Tiedke, Resistive switching mechanism of TiO 2 thin films grown by atomic-layer deposition, J. Appl. Phys. 98 (2005). https://doi.org/10.1063/1.2001146.

Die approbierte gedruckte Originalversion dieser Dissertation ist an der TU Wien Bibliothek verfügbar.
The approved original version of this doctoral thesis is available in print at TU Wien Bibliothek.
TU WIEN Bibliothek Your knowledge hub

[43] S.K. Kim, K.M. Kim, D.S. Jeong, W. Jeon, K.J. Yoon, C.S. Hwang, Titanium dioxide thin films for next-generation memory devices, J. Mater. Res. 28 (2013) 313–325. https://doi.org/10.1557/jmr.2012.231.

[44] D.B. Strukov, G.S. Snider, D.R. Stewart, R.S. Williams, The missing memristor found, Nature. (2008). https://doi.org/10.1038/nature06932.

[45] K.M. Kim, B.J. Choi, Y.C. Shin, S. Choi, C.S. Hwang, Anode-interface localized filamentary mechanism in resistive switching of Ti O2 thin films, Appl. Phys. Lett. 91 (2007) 6–9. https://doi.org/10.1063/1.2749846.

[46] C. Rohde, B.J. Choi, D.S. Jeong, S. Choi, J.S. Zhao, C.S. Hwang, Identification of a determining parameter for resistive switching of TiO2 thin films, Appl. Phys. Lett. 86 (2005) 1–3. https://doi.org/10.1063/1.1968416.

[47] Y. Sato, K. Kinoshita, M. Aoki, Y. Sugiyama, Consideration of switching mechanism of binary metal oxide resistive junctions using a thermal reaction model, Appl. Phys. Lett. 90 (2007). https://doi.org/10.1063/1.2431792.

[48] D. Cooper, C. Baeumer, N. Bernier, A. Marchewka, C. La Torre, R.E. Dunin-Borkowski, S. Menzel, R. Waser, R. Dittmann, Anomalous Resistance Hysteresis in Oxide ReRAM: Oxygen Evolution and Reincorporation Revealed by In Situ TEM, Adv. Mater. 29 (2017) 1–8. https://doi.org/10.1002/adma.201700212.

[49] L. Huang, K.E. Gubbins, L. Li, X. Lu, Water on titanium dioxide surface: A revisiting by reactive molecular dynamics simulations, Langmuir. 30 (2014) 14832–14840. https://doi.org/10.1021/la5037426.

[50] D.F. Abbott, D. Lebedev, K. Waltar, M. Povia, M. Nachtegaal, E. Fabbri, C. Copéret, T.J. Schmidt, Iridium oxide for the oxygen evolution reaction: Correlation between particle size, morphology, and the surface hydroxo layer from operando XAS, Chem. Mater. 28 (2016) 6591–6604. https://doi.org/10.1021/acs.chemmater.6b02625.

[51] D.R. Baker, M.B. Graziano, B.M. Hanrahan, Nanostructured Antireflective Iridium Oxide Coating for Water Oxidation, J. Phys. Chem. C. 122 (2018) 12207–12214. https://doi.org/10.1021/acs.jpcc.8b03874.

[52] D.J.D. Matienzo, D. Settipani, E. Instuli, T. Kallio, Active IrO2 and NiO thin films prepared by atomic layer deposition for oxygen evolution reaction, Catalysts. 10 (2020)

TU WIEN Bibliothek Your knowledge hub
Die approbierte gedruckte Originalversion dieser Dissertation ist an der TU Wien Bibliothek verfügbar.
The approved original version of this doctoral thesis is available in print at TU Wien Bibliothek.

1–13. https://doi.org/10.3390/catal10010092.

[53] S. Das, B. Wang, Y. Cao, M.R. Cho, Y.J. Shin, S.M. Yang, L. Wang, M. Kim, S. V Kalinin, L. Chen, T.W. Noh, Controlled manipulation of oxygen vacancies using nanoscale flexoelectricity, Nat. Commun. 2017 (n.d.) 1–8. https://doi.org/10.1038/s41467-017-00710-5.

[54] D. Lee, A. Yoon, S.Y. Jang, J. Yoon, J. Chung, M. Kim, J.F. Scott, T.W. Noh, Giant Flexoelectric Effect in Ferroelectric Epitaxial Thin Films, 057602 (2011) 1–4. https://doi.org/10.1103/PhysRevLett.107.057602.

[55] L.H.E.-M.S. Kandelousi, Dielectrics under Electric Field, in: IntechOpen, Rijeka, 2017: p. Ch. 4. https://doi.org/10.5772/intechopen.72231.

[56] G.D. Mahan, Ionic polarization, Ferroelectrics. 136 (1992) 57–64. https://doi.org/10.1080/00150199208016066.

[57] C.H. Chuang, W.C. Weng, W.J. Chang, D.H. Lee, Real-time monitoring via patch-type piezoelectric force sensors for Internet of Thing in logistics, 2016 IEEE 11th Annu. Int. Conf. Nano/Micro Eng. Mol. Syst. NEMS 2016. 17 (2016) 325–328. https://doi.org/10.1109/NEMS.2016.7758259.

[58] J. Robertson, R.M. Wallace, High-K materials and metal gates for CMOS applications, Mater. Sci. Eng. R Reports. 88 (2015) 1–41. https://doi.org/10.1016/j.mser.2014.11.001.

[59] Y. Sugiyama, S. Pidin, Y. Morisaki, Approaches to using Al2O3 and HfO2 as gate dielectrics for CMOSFETs, Fujitsu Sci. Tech. J. 39 (2003) 94–105.

[60] J.S. Kim, The effect of the gate oxide thickness on the speed of MOS integrated circuits, NBS Publ. 87–3668 (1987).

[61] R. Chau, S. Datta, M. Doczy, B. Doyle, J. Kavalieros, M. Metz, High-κ/metal-gate stack and its MOSFET characteristics, IEEE Electron Device Lett. 25 (2004) 408–410. https://doi.org/10.1109/LED.2004.828570.

[62] S.A. Mojarad, K.S.K. Kwa, J.P. Goss, Z. Zhou, N.K. Ponon, D.J.R. Appleby, R.A.S. Al-Hamadany, A. O'Neill, A comprehensive study on the leakage current mechanisms of Pt/SrTiO3/Pt capacitor, J. Appl. Phys. 111 (2012). https://doi.org/10.1063/1.3673574.

[63] M. Evstigneev, Introduction to Semiconductor Physics and Devices, Springer Cham, 2022. https://doi.org/https://doi.org/10.1007/978-3-031-08458-4.

Die approbierte gedruckte Originalversion dieser Dissertation ist an der TU Wien Bibliothek verfügbar.
The approved original version of this doctoral thesis is available in print at TU Wien Bibliothek.
TU Bibliothek WIEN Your knowledge hub

[64] J. Frenkel, On pre-breakdown phenomena in insulators and electronic semi-conductors [3], Phys. Rev. 54 (1938) 647–648. https://doi.org/10.1103/PhysRev.54.647.

[65] H. Schroeder, Poole-Frenkel-effect as dominating current mechanism in thin oxide films - An illusion?!, J. Appl. Phys. 117 (2015). https://doi.org/10.1063/1.4921949.

[66] S. Simeonov, I. Yourukov, E. Kafedjiiska, A. Szekeres, Inter-trap tunnelling in thin SiO2 films, Phys. Status Solidi Appl. Res. 201 (2004) 2966–2979. https://doi.org/10.1002/pssa.200406849.

[67] M.S. Kim, B. Kaczer, S. Starschich, M. Popovici, J. Swerts, O. Richard, K. Tomida, C. Vrancken, S. Van Elshocht, I. Debusschere, L. Altimime, J.A. Kittl, Understanding of trap-assisted tunneling current - Assisted by oxygen vacancies in RuO x/SrTiO 3/TiN MIM capacitor for the DRAM application, 2012 4th IEEE Int. Mem. Work. IMW 2012. (2012) 41–44. https://doi.org/10.1109/IMW.2012.6213661.

[68] K.P. McKenna, J. Blumberger, First principles modeling of electron tunneling between defects in m-HfO2, Microelectron. Eng. 147 (2015) 235–238. https://doi.org/10.1016/j.mee.2015.04.009.

[69] A. Rose, Space-charge-limited in Solids, Phys. Rev. 97 (1955). https://doi.org/10.1088/0022-3727/4/11/427.

[70] G.T. Wright, Mechanisms of space-charge-limited current in solids, Solid State Electron. 2 (1961) 165–189. https://doi.org/10.1016/0038-1101(61)90034-X.

[71] Y. Yu, C. Wang, C. Jiang, I. Abrahams, Z. Du, Q. Zhang, J. Sun, X. Huang, Resistive switching behavior in memristors with TiO2 nanorod arrays of different dimensions, Appl. Surf. Sci. 485 (2019) 222–229. https://doi.org/10.1016/j.apsusc.2019.04.119.

[72] J. Pospisil, O. Zmeskal, S. Nespurek, J. Krajcovic, M. Weiter, A. Kovalenko, Density of bulk trap states of hybrid lead halide perovskite single crystals: temperature modulated space-charge-limited-currents, Sci. Rep. 9 (2019) 1–8. https://doi.org/10.1038/s41598-019-40139-y.

[73] A.A. Petrov, N. V. Andreeva, A.S. Ivanov, Mechanism of electron transport and bipolar resistive switching in lead oxide thin films, AIP Adv. 8 (2018). https://doi.org/10.1063/1.5041839.

[74] D.S. Jeong, R. Thomas, R.S. Katiyar, J.F. Scott, H. Kohlstedt, A. Petraru, C.S. Hwang,

Die approbierte gedruckte Originalversion dieser Dissertation ist an der TU Wien Bibliothek verfügbar.
The approved original version of this doctoral thesis is available in print at TU Wien Bibliothek.
TU Bibliothek WIEN Your knowledge hub

Emerging memories: Resistive switching mechanisms and current status, Reports Prog. Phys. 75 (2012). https://doi.org/10.1088/0034-4885/75/7/076502.

[75] J.J. Yang, M.D. Pickett, X. Li, D.A.A. Ohlberg, D.R. Stewart, R.S. Williams, Memristive switching mechanism for metal/oxide/metal nanodevices, Nat. Nanotechnol. 3 (2008) 429–433. https://doi.org/10.1038/nnano.2008.160.

[76] B. Sun, Y. Chen, M. Xiao, G. Zhou, S. Ranjan, W. Hou, X. Zhu, Y. Zhao, S.A.T. Redfern, Y. Norman Zhou, A Unified Capacitive-Coupled Memristive Model for the Nonpinched Current-Voltage Hysteresis Loop, Nano Lett. 19 (2019) 6461–6465. https://doi.org/10.1021/acs.nanolett.9b02683.

[77] X.D. Liu, Q. Yang, L. Yuan, D. Qi, X. Wei, X. Zhou, S. Chen, L. Cao, Y. Zeng, J. Jia, C. Wang, Oxygen vacancy-rich WO3 heterophase structure: A trade-off between surface-limited pseudocapacitance and intercalation-limited behaviour, Chem. Eng. J. 425 (2021) 131431. https://doi.org/https://doi.org/10.1016/j.cej.2021.131431.

[78] Y. Noguchi, H. Matsuo, Y. Kitanaka, M. Miyayama, Ferroelectrics with a controlled oxygen-vacancy distribution by design, Sci. Rep. 9 (2019) 1–10. https://doi.org/10.1038/s41598-019-40717-0.

[79] H. Dong, X. Zhang, Y. Cheng, J. Wu, L. Zhang, Z. Zhang, Z. Yin, Transient Negative Capacitance Induced by Charged Oxygen Vacancy Drift in HfO2-Based Films, Phys. Status Solidi – Rapid Res. Lett. n/a (2023) 2300137. https://doi.org/https://doi.org/10.1002/pssr.202300137.

[80] Y. Gogotsi, R.M. Penner, Energy Storage in Nanomaterials - Capacitive, Pseudocapacitive, or Battery-like?, ACS Nano. 12 (2018) 2081–2083. https://doi.org/10.1021/acsnano.8b01914.

[81] S.J. Song, J.Y. Seok, J.H. Yoon, K.M. Kim, G.H. Kim, M.H. Lee, C.S. Hwang, Real-time identification of the evolution of conducting nano-filaments in TiO2 thin film ReRAM, Sci. Rep. 3 (2013) 1–6. https://doi.org/10.1038/srep03443.

[82] M. Born, K. Huang, M. Lax, Dynamical Theory of Crystal Lattices, Am. J. Phys. (1955). https://doi.org/10.1119/1.1934059.

[83] S.M. Kogan, Piezoelectric effect during inhomogeneous deformation and acoustic scattering of carriers in crystals, Sov. Phys. Solid State. 5 (1964) 2069–2070.

Die approbierte gedruckte Originalversion dieser Dissertation ist an der TU Wien Bibliothek verfügbar.
The approved original version of this doctoral thesis is available in print at TU Wien Bibliothek.
TU WIEN Bibliothek Your knowledge hub

[84] R.D. Mindlin, Polarization gradient in elastic dielectrics, Int. J. Solids Struct. 4 (1968) 637–642. https://doi.org/10.1016/0020-7683(68)90079-6.

[85] P. V. Yudin, R. Ahluwalia, A.K. Tagantsev, Upper bounds for flexoelectric coefficients in ferroelectrics, Appl. Phys. Lett. 104 (2014). https://doi.org/10.1063/1.4865208.

[86] W. Huang, K. Kim, S. Zhang, F.G. Yuan, X. Jiang, Scaling effect of flexoelectric (Ba,Sr)TiO3 microcantilevers, Phys. Status Solidi - Rapid Res. Lett. 5 (2011) 350–352. https://doi.org/10.1002/pssr.201105326.

[87] E. Meirzadeh, D. V. Christensen, E. Makagon, H. Cohen, I. Rosenhek-Goldian, E.H. Morales, A. Bhowmik, J.M.G. Lastra, A.M. Rappe, D. Ehre, M. Lahav, N. Pryds, I. Lubomirsky, Surface Pyroelectricity in Cubic SrTiO3, Adv. Mater. 31 (2019) 1–5. https://doi.org/10.1002/adma.201904733.

[88] A.K. Tagantsev, A.S. Yurkov, Flexoelectric effect in finite samples, J. Appl. Phys. 112 (2012) 1–14. https://doi.org/10.1063/1.4745037.

[89] A.K. Tagantsev, Piezoelectricity and flexoelectricity in crystalline dielectrics, Phys. Rev. B. 34 (1986) 5883–5889. https://doi.org/10.1103/PhysRevB.34.5883.

[90] R. Resta, Towards a bulk theory of flexoelectricity, Phys. Rev. Lett. 105 (2010) 1–5. https://doi.org/10.1103/PhysRevLett.105.127601.

[91] E.M. LIFSHITZ, A.M. KOSEVICH, L.P. PITAEVSKII, CHAPTER II - THE EQUILIBRIUM OF RODS AND PLATES, in: E.M. LIFSHITZ, A.M. KOSEVICH, L.P.B.T.-T. of E. (Third E. PITAEVSKII (Eds.), Butterworth-Heinemann, Oxford, 1986: pp. 38–86. https://doi.org/https://doi.org/10.1016/B978-0-08-057069-3.50009-7.

[92] E.M. LIFSHITZ, A.M. KOSEVICH, L.P. PITAEVSKII, CHAPTER I - FUNDAMENTAL EQUATIONS, in: E.M. LIFSHITZ, A.M. KOSEVICH, L.P.B.T.-T. of E. (Third E. PITAEVSKII (Eds.), Butterworth-Heinemann, Oxford, 1986: pp. 1–37. https://doi.org/https://doi.org/10.1016/B978-0-08-057069-3.50008-5.

[93] K. Uchino, Electrostrictive Materials, Encycl. Vib. (2001) 475–490. https://doi.org/10.1006/rwvb.2001.0078.

[94] B. Qiao, X. Wang, S. Tan, W. Zhu, Z. Zhang, Synergistic Effects of Maxwell Stress and Electrostriction in Electromechanical Properties of Poly(vinylidene fluoride)-Based Ferroelectric Polymers, Macromolecules. 52 (2019) 9000–9011.

TU Bibliothek, WIEN Your knowledge hub
Die approbierte gedruckte Originalversion dieser Dissertation ist an der TU Wien Bibliothek verfügbar.
The approved original version of this doctoral thesis is available in print at TU Wien Bibliothek.

https://doi.org/10.1021/acs.macromol.9b01580.

[95] S. Holz, S. Kiricenko, L. Rissing, Integration of PVDF (Polyvinylidene Fluoride) in MEMS Production, Meet. Abstr. . MA2014-02 (2014) 685. https://doi.org/10.1149/06401.0189ecst.

[96] O.A. Bauchau, J.I. Craig, Euler-Bernoulli beam theory BT - Structural Analysis, in: O.A. Bauchau, J.I. Craig (Eds.), Springer Netherlands, Dordrecht, 2009: pp. 173–221. https://doi.org/10.1007/978-90-481-2516-6_5.

[97] S. Schmid, Fundamentals of Nanomechanical Resonators, Springer Nature, 2016.

[98] F. Di Paolo, Networks and Devices Using Planar Transmissions Lines, 1st ed., CRC Press, 2000. https://doi.org/10.1201/9781315220369.

[99] P.J. Kelly, R.D. Arnell, Magnetron sputtering: A review of recent developments and applications, Vacuum. 56 (2000) 159–172. https://doi.org/10.1016/S0042-207X(99)00189-X.

[100] F. Abraham, Homogeneous Nucleation Theory, 1st ed., Academic Press, New York, 1974.

[101] D.B. Hall, P. Underhill, J.M. Torkelson, Spin coating of thin and ultrathin polymer films, Polym. Eng. Sci. 38 (1998) 2039–2045. https://doi.org/10.1002/pen.10373.

[102] F. Karouta, A practical approach to reactive ion etching, J. Phys. D. Appl. Phys. 47 (2014). https://doi.org/10.1088/0022-3727/47/23/233501.

[103] L. Filipovic, R.L. De Orio, S. Selberherr, Process and reliability of SF6/O2 plasma etched copper TSVs, 2014 15th Int. Conf. Therm. Mech. Multi-Physics Simul. Exp. Microelectron. Microsystems, EuroSimE 2014. (2014) 2–5. https://doi.org/10.1109/EuroSimE.2014.6813768.

[104] F.I. Chang, R. Yeh, G. Lin, P.B. Chu, E.G. Hoffman, E.J. Kruglick, K.S.J. Pister, M.H. Hecht, Gas-phase silicon micromachining with xenon difluoride, Microelectron. Struct. Microelectromechanical Devices Opt. Process. Multimed. Appl. 2641 (1995) 117. https://doi.org/10.1117/12.220933.

[105] S. Timoshenko, S. Woinowsky-Krieger, Theory of Plates and Shells, McGraw-Hill, New York, 1959.

Die approbierte gedruckte Originalversion dieser Dissertation ist an der TU Wien Bibliothek verfügbar.
The approved original version of this doctoral thesis is available in print at TU Wien Bibliothek.
TU WIEN Bibliothek Your knowledge hub

[106] D. Mardare, G.I. Rusu, Structural and electrical properties of TiO2 RF sputtered thin films, Mater. Sci. Eng. B Solid-State Mater. Adv. Technol. 75 (2000) 68–71. https://doi.org/10.1016/S0921-5107(00)00387-1.

[107] J.A. Puértolas, J.F. García-García, F.J. Pascual, J.M. González-Domínguez, M.T. Martínez, A. Ansón-Casaos, Dielectric behavior and electrical conductivity of PVDF filled with functionalized single-walled carbon nanotubes, Compos. Sci. Technol. 152 (2017) 263–274. https://doi.org/10.1016/j.compscitech.2017.09.016.

[108] S.J. Rothberg, M.S. Allen, P. Castellini, D. Di Maio, J.J.J. Dirckx, D.J. Ewins, B.J. Halkon, P. Muyshondt, N. Paone, T. Ryan, H. Steger, E.P. Tomasini, S. Vanlanduit, J.F. Vignola, An international review of laser Doppler vibrometry: Making light work of vibration, Opt. Lasers Eng. 99 (2017) 11–22. https://doi.org/10.1016/j.optlaseng.2016.10.023.

[109] R. Kowarsch, C. Rembe, Lateral resolution limit of laser Doppler vibrometer microscopes for the measurement of surface acoustic waves, Sci. Rep. 11 (2021) 1–9. https://doi.org/10.1038/s41598-021-96684-y.

[110] A.G. Mychkovsky, N.A. Chang, S.L. Ceccio, Bragg cell laser intensity modulation: Effect on laser doppler velocimetry measurements, Appl. Opt. 48 (2009) 3468–3474. https://doi.org/10.1364/AO.48.003468.

[111] C. Rembe, S. Boedecker, A. Dräbenstedt, F. Pudewills, G. Siegmund, Heterodyne laser-Doppler vibrometer with a slow-shear-mode Bragg cell for vibration measurements up to 1.2 GHz, Eighth Int. Conf. Vib. Meas. by Laser Tech. Adv. Appl. 7098 (2008) 70980A. https://doi.org/10.1117/12.802930.

[112] M. V. Salapaka, H.S. Bergh, J. Lai, A. Majumdar, E. McFarland, Multi-mode noise analysis of cantilevers for scanning probe microscopy, J. Appl. Phys. 81 (1997) 2480–2487. https://doi.org/10.1063/1.363955.

[113] G.A. Matei, J.A. Thoreson, J.R. Pratt, D.B. Newell, N.A. Burnham, Precision and accuracy of thermal calibration of atomic force microscopy cantilevers, Rev. Sci. Instrum. 77 (2006) 083703. https://doi.org/10.1063/1.2336115.

[114] M.A. Poggi, A.W. Mcfarland, J.S. Colton, L.A. Bottomley, A Method for Calculating the Spring Constant of Atomic Force Microscopy Cantilevers with a Nonrectangular Cross Section, Anal. Chem. 77 (2005) 1192–1195. https://doi.org/10.1021/ac048828h.

TU Bibliothek Your knowledge hub WIEN
Die approbierte gedruckte Originalversion dieser Dissertation ist an der TU Wien Bibliothek verfügbar.
The approved original version of this doctoral thesis is available in print at TU Wien Bibliothek.

[115] E.S. Ameh, A review of basic crystallography and x-ray diffraction applications, Int. J. Adv. Manuf. Technol. 105 (2019) 3289–3302. https://doi.org/10.1007/s00170-019-04508-1.

[116] N. Jalili, K. Laxminarayana, A review of atomic force microscopy imaging systems: Application to molecular metrology and biological sciences, Mechatronics. 14 (2004) 907–945. https://doi.org/10.1016/j.mechatronics.2004.04.005.

[117] S.N. Magonov, V. Elings, M.-H. Whangbo, Phase imaging and stiffness in tapping-mode atomic force microscopy, Surf. Sci. 375 (1997) L385–L391. https://doi.org/https://doi.org/10.1016/S0039-6028(96)01591-9.

[118] C. Berthomieu, R. Hienerwadel, Fourier transform infrared (FTIR) spectroscopy, Photosynth. Res. 101 (2009) 157–170. https://doi.org/10.1007/s11120-009-9439-x.

[119] K.D. Vernon-Parry, Scanning Electron Microscopy : An introduction, III-Vs Rev. 13 (2000) 40–44.

[120] R. Gauvin, Review of transmission electron microscopy for the characterization of materials, Proc. SPIE. 10291 (n.d.) 102910C. https://doi.org/https://doi.org/10.1117/12.279840.

[121] G. Greczynski, L. Hultman, X-ray photoelectron spectroscopy: Towards reliable binding energy referencing, Prog. Mater. Sci. 107 (2020) 100591. https://doi.org/10.1016/j.pmatsci.2019.100591.

[122] F.A. Stevie, C.L. Donley, Introduction to x-ray photoelectron spectroscopy, J. Vac. Sci. Technol. A. 38 (2020) 063204. https://doi.org/10.1116/6.0000412.

[123] M.R. Ardigo, M. Ahmed, A. Besnard, Stoney formula: Investigation of curvature measurements by optical profilometer, Adv. Mater. Res. 996 (2014) 361–366. https://doi.org/10.4028/www.scientific.net/AMR.996.361.

[124] A. Bally, Electronic properties of nano-crystalline titanium dioxide thin films, 2094 (1999) 140.

[125] N. Rahimi, R.A. Pax, E.M.A. Gray, Review of functional titanium oxides. I: TiO2 and its modifications, Prog. Solid State Chem. 44 (2016) 86–105. https://doi.org/10.1016/j.progsolidstchem.2016.07.002.

[126] D.A.H. Hanaor, C.C. Sorrell, Review of the anatase to rutile phase transformation, J.

Die approbierte gedruckte Originalversion dieser Dissertation ist an der TU Wien Bibliothek verfügbar.
The approved original version of this doctoral thesis is available in print at TU Wien Bibliothek.
TU Wien Bibliothek Your knowledge hub

Mater. Sci. 46 (2011) 855–874. https://doi.org/10.1007/s10853-010-5113-0.

[127] A. Wypych, I. Bobowska, M. Tracz, A. Opasinska, S. Kadlubowski, A. Krzywania-Kaliszewska, J. Grobelny, P. Wojciechowski, Dielectric properties and characterisation of titanium dioxide obtained by different chemistry methods, J. Nanomater. 2014 (2014). https://doi.org/10.1155/2014/124814.

[128] E.S. Sabisky, H.J. Gerritsen, Measurements of Dielectric Constant of Rutile (TiO2) at Microwave Frequencies between 4.2° and 300°K, J. Appl. Phys. 33 (1962) 1450. https://doi.org/10.1063/1.1728753.

[129] P. Soundarrajan, K. Sankarasubramanian, K. Sethuraman, K. Ramamurthi, Controlled (110) and (101) crystallographic plane growth of single crystalline rutile TiO2 nanorods by facile low cost chemical methods, CrystEngComm. 16 (2014) 8756–8768. https://doi.org/10.1039/c4ce00820k.

[130] F.J. Maier, M. Schneider, J. Schrattenholzer, U. Schmid, Electrical and Microstructural Characterization of TiO2Thin Films for Flexoelectric Devices, J. Phys. Conf. Ser. 1837 (2021) 4–11. https://doi.org/10.1088/1742-6596/1837/1/012009.

[131] Y. Liu, H. Masumoto, T. Goto, Electrical and Optical Properties of IrO2 Thin Films Prepared by Laser-ablation, Mater. Trans. 45 (2004) 3023–3027. https://doi.org/10.3131/jvsj.39.331.

[132] F. Nattino, N. Marzari, Operando XANES from first-principles and its application to iridium oxide, Phys. Chem. Chem. Phys. 22 (2020) 10807–10818. https://doi.org/10.1039/c9cp06726d.

[133] M. Li, I. Katsouras, C. Piliego, G. Glasser, I. Lieberwirth, P.W.M. Blom, D.M. De Leeuw, Controlling the microstructure of poly(vinylidene-fluoride) (PVDF) thin films for microelectronics, J. Mater. Chem. C. 1 (2013) 7695–7702. https://doi.org/10.1039/c3tc31774a.

[134] J. Harry, W.M. Paul, D. Leeuw, M. Dago, Revisiting the delta-phase of poly(vinylidene fluoride) for solution-processed ferroelectric thin films, Nat. Mater. 12 (2013) 433–438. https://doi.org/10.1038/nmat3577.

[135] M. Li, H.J. Wondergem, M.J. Spijkman, K. Asadi, I. Katsouras, P.W.M. Blom, D.M. De Leeuw, Revisiting the δ-phase of poly(vinylidene fluoride) for solution-processed

Die approbierte gedruckte Originalversion dieser Dissertation ist an der TU Wien Bibliothek verfügbar.
The approved original version of this doctoral thesis is available in print at TU Wien Bibliothek.
TU WIEN Bibliothek Your knowledge hub

ferroelectric thin films, Nat. Mater. 12 (2013) 433–438. https://doi.org/10.1038/nmat3577.

[136] I. Katsouras, K. Asadi, M. Li, T.B. Van Driel, K.S. Kjær, D. Zhao, T. Lenz, Y. Gu, P.W.M. Blom, D. Damjanovic, M.M. Nielsen, D.M. De Leeuw, The negative piezoelectric effect of the ferroelectric polymer poly(vinylidene fluoride), Nat. Mater. 15 (2016) 78–84. https://doi.org/10.1038/nmat4423.

[137] Y. Liu, H. Aziguli, B. Zhang, W. Xu, W. Lu, J. Bernholc, Q. Wang, Ferroelectric polymers exhibiting behaviour reminiscent of a morphotropic phase boundary, Nature. 562 (2018) 96–100. https://doi.org/10.1038/s41586-018-0550-z.

[138] E. Fukada, T. Furukawa, Piezoelectricity and ferroelectricity in polyvinylidene fluoride, Ultrasonics. 19 (1981) 31–39. https://doi.org/10.1016/0041-624X(81)90030-5.

[139] K.S. Ramadan, D. Sameoto, S. Evoy, A review of piezoelectric polymers as functional materials for electromechanical transducers, Smart Mater. Struct. 23 (2014) 033001. https://doi.org/10.1088/0964-1726/23/3/033001.

[140] K.R. Rashmi, A.S. Rao, A. Jayarama, R. Pinto, Piezoelectric P(VDF-TrFE) micro cantilevers and beams for low frequency vibration sensors and energy harvesters, Sensors Actuators A. 295 (2019) 574–585. https://doi.org/10.1016/j.sna.2019.06.021.

[141] J. Hafner, M. Teuschel, J. Schrattenholzer, M. Schneider, U. Schmid, Optimized Batch Process for Organic MEMS Devices, Proceedings. 2 (2018) 904. https://doi.org/10.3390/proceedings2130904.

[142] C. Ribeiro, C.M. Costa, D.M. Correia, J. Nunes-Pereira, J. Oliveira, P. Martins, R. Gonçalves, V.F. Cardoso, S. Lanceros-Méndez, Electroactive poly(vinylidene fluoride)-based structures for advanced applications, Nat. Protoc. 13 (2018) 681–704. https://doi.org/10.1038/nprot.2017.157.

[143] Y. Xin, H. Sun, H. Tian, C. Guo, X. Li, S. Wang, C. Wang, The use of polyvinylidene fluoride (PVDF) films as sensors for vibration measurement : A brief review, Ferroelectrics. 502 (2021) 28–42. https://doi.org/10.1080/00150193.2016.1232582.

[144] X. Wang, F. Sun, G. Yin, Y. Wang, B. Liu, M. Dong, Tactile-Sensing Based on Flexible PVDF Nanofibers via Electrospinning : A Review, Sensors. 18(2) (2018) 330. https://doi.org/10.3390/s18020330.

TU Bibliothek WIEN Your knowledge hub
Die approbierte gedruckte Originalversion dieser Dissertation ist an der TU Wien Bibliothek verfügbar.
The approved original version of this doctoral thesis is available in print at TU Wien Bibliothek.

[145] D. Li, J. Xiong, Y. Guo, G. Li, Ferroelectric phase transition effect of doping trifluoroethylene monomer in poly (vinylidene fluoride), J. Appl. Phys. 115 (2014) 204106. https://doi.org/10.1063/1.4880296.

[146] D.E. Septiyani Arifin, J.J. Ruan, Study on the curie transition of P(VDF-TrFE) copolymer, IOP Conf. Ser. Mater. Sci. Eng. 299 (2018). https://doi.org/10.1088/1757-899X/299/1/012056.

[147] F. Li, L. Jin, Z. Xu, S. Zhang, Electrostrictive effect in ferroelectrics: An alternative approach to improve piezoelectricity, Appl. Phys. Rev. 1 (2014) 011103. https://doi.org/10.1063/1.4861260.

[148] R.E. Newnham, V. Sundar, R. Yimnirun, J. Su, Q.M. Zhang, Electrostriction: Nonlinear electromechanical coupling in solid dielectrics, J. Phys. Chem. B. 101 (1997) 10141–10150. https://doi.org/10.1021/jp971522c.

[149] T. Furukawa, N. Seo, Electrostriction as the origin of piezoelectricity in ferroelectric polymers, Jpn. J. Appl. Phys. 29 (1990) 675–680. https://doi.org/10.1143/JJAP.29.675.

[150] J. Hafner, M. Teuschel, D. Disnan, M. Schneider, U. Schmid, Large bias-induced piezoelectric response in the ferroelectric polymer P(VDF-TrFE) for MEMS resonators, Mater. Res. Lett. 9 (2021) 195–203. https://doi.org/10.1080/21663831.2020.1868593.

[151] K. Uchino, Electrostrictive Actuators: Materials and Applications., Am. Ceram. Soc. Bull. 65 (1986) 647–652.

[152] M. Hikita, M. Nagao, G. Sawa, M. Ieda, Dielectric breakdown and electrical conduction of poly(vinylidene-fluoride) in high temperature region, J. Phys. D. Appl. Phys. 13 (1980) 661–666. https://doi.org/10.1088/0022-3727/13/4/019.

[153] J. Ryu, S. Eom, P. Li, C.H. Liow, S. Hong, Ferroelectric Polymer PVDF-Based Nanogenerator, in: S.J. Kim, A. Chandrasekhar, N.R. Alluri (Eds.), Nanogenerators, IntechOpen, Rijeka, 2019. https://doi.org/10.5772/intechopen.90368.

[154] M.C. Salvadori, A.R. Vaz, L.L. Melo, M. Cattani, Nanostructured Gold Thin Films: Young Modulus Measurement, Surf. Rev. Lett. 10 (n.d.) 571–575.

[155] C.-H. Cho, Characterization of Young's modulus of silicon versus temperature using a "beam deflection" method with a four-point bending fixture, Curr. Appl. Phys. 9 (2009) 538–545.

TU Bibliothek WIEN Your knowledge hub
Die approbierte gedruckte Originalversion dieser Dissertation ist an der TU Wien Bibliothek verfügbar.
The approved original version of this doctoral thesis is available in print at TU Wien Bibliothek.

[156] J.K.H. Hörber, M.J. Miles, Scanning Probe Evolution in Biology, Science (80-.). 302 (2003) 1002–1006. https://doi.org/10.1126/science.1067410.

[157] T. Ando, T. Uchihashi, N. Kodera, D. Yamamoto, A. Miyagi, M. Taniguchi, H. Yamashita, High-speed AFM and nano-visualization of biomolecular processes, Pflugers Arch. Eur. J. Physiol. 456 (2008) 211–225. https://doi.org/10.1007/s00424-007-0406-0.

[158] V. Sencadas, S. Lanceros-Méndez, R. Sabater I Serra, A. Andrio Balado, J.L. Gómez Ribelles, Relaxation dynamics of poly(vinylidene fluoride) studied by dynamical mechanical measurements and dielectric spectroscopy, Eur. Phys. J. E. 35 (2012) 41. https://doi.org/10.1140/epje/i2012-12041-x.

[159] S. Lee, Y.Y. Kim, Y. Cho, A comparative study on the elastic characteristics of an aluminum thin-film using laser optical measurement techniques, Coatings. 7 (2017) 143. https://doi.org/10.3390/coatings7090143.

[160] X. Cai, T. Lei, D. Sun, L. Lin, A critical analysis of the α, β and γ phases in poly(vinylidene fluoride) using FTIR, RSC Adv. 7 (2017) 15382–15389. https://doi.org/10.1039/c7ra01267e.

[161] S. Wolff, F. Jirasek, S. Beuermann, M. Türk, Crystal phase transformation of α into β phase poly(vinylidene fluoride) via particle formation caused by rapid expansion of supercritical solutions, RSC Adv. 5 (2015) 66644–66649. https://doi.org/10.1039/c5ra12142f.

[162] G.T. Davis, J.E. McKinney, M.G. Broadhurst, S.C. Roth, Electric-field-induced phase changes in poly (vinylidene fluoride), J. Appl. Phys. 49 (1978) 4998.

[163] N. Della Schiava, K. Thetpraphi, M.Q. Le, P. Lermusiaux, A. Millon, J.F. Capsal, P.J. Cottinet, Enhanced figures of merit for a high-performing actuator in electrostrictive materials, Polymers (Basel). 10 (2018) 1–15. https://doi.org/10.3390/polym10030263.

[164] H. Nesser, H. Debéda, J. Yuan, A. Colin, P. Poulin, I. Dufour, C. Ayela, All-organic microelectromechanical systems integrating electrostrictive nanocomposite for mechanical energy harvesting, Nano Energy. 44 (2018) 1–6. https://doi.org/10.1016/j.nanoen.2017.11.036.

[165] A. Pimpin, Y. Suzuki, N. Kasagi, Microelectrostrictive actuator with large out-of-plane

Die approbierte gedruckte Originalversion dieser Dissertation ist an der TU Wien Bibliothek verfügbar.
The approved original version of this doctoral thesis is available in print at TU Wien Bibliothek.
TU WIEN Bibliothek Your knowledge hub

deformation for flow-control application, J. Microelectromechanical Syst. 16 (2007) 753–764. https://doi.org/10.1109/JMEMS.2007.895222.

[166] T. Khudiyev, J. Clayton, E. Levy, N. Chocat, A. Gumennik, A.M. Stolyarov, J. Joannopoulos, Y. Fink, Electrostrictive microelectromechanical fibres and textiles, Nat. Commun. 8 (2017) 1–7. https://doi.org/10.1038/s41467-017-01558-5.

[167] R.E. Pelrine, R.D. Kornbluh, J.P. Joseph, Electrostriction of polymer dielectrics with compliant electrodes as a means of actuation, Sensors Actuators, A Phys. 64 (1998) 77–85. https://doi.org/10.1016/S0924-4247(97)01657-9.

[168] P. Taylor, P. Güthner, T. Ritter, K. Dransfeld, Temperature dependence of the piezoelectric constant of thin PVDF and P (VDF-TrFE) films, Ferroelectrics. 127 (1992) 7–11. https://doi.org/10.1080/00150199208223338.

[169] J. Lu, X. Liang, W. Yu, S. Hu, S. Shen, Temperature dependence of flexoelectric coefficient for bulk polymer polyvinylidene fluoride, J. Phys. D. Appl. Phys. 52 (2019). https://doi.org/10.1088/1361-6463/aaf543.

[170] C. Birleanu, M. Pustan, V. Merie, R. Müller, R. Voicu, A. Baracu, S. Craciun, Temperature effect on the mechanical properties of gold nano films with different thickness, IOP Conf. Ser. Mater. Sci. Eng. 147 (2016) 012021. https://doi.org/10.1088/1757-899X/147/1/012021.

[171] A.M. Vinogradov, V.H. Schmidt, G.F. Tuthill, G.W. Bohannan, Damping and electromechanical energy losses in the piezoelectric polymer PVDF, Mech. Mater. 36 (2004) 1007–1016. https://doi.org/10.1016/j.mechmat.2003.04.002.

[172] M.A. Jithin, L.G. Kolla, N. Bhat, S. Mohan, Y. Morozumi, S. Kaushal, Pulsed DC Magnetron Sputtered Rutile TiO2 films for next generation DRAM capacitors, MRS Online Proc. Libr. 1561 (2013) 3. https://doi.org/10.1557/opl.2013.823.

[173] J. Racko, M. Mikolášek, L. Harmatha, J. Breza, B. Hudec, K. Fröhlich, J. Aarik, A. Tarre, R. Granzner, F. Schwierz, Analysis of leakage current mechanisms in RuO2–TiO2–RuO2 MIM structures, J. Vac. Sci. Technol. B, Nanotechnol. Microelectron. Mater. Process. Meas. Phenom. 29 (2011) 01AC08. https://doi.org/10.1116/1.3534022.

[174] K. Fröhlich, J. Aarik, M. Ťapajna, A. Rosová, A. Aidla, E. Dobročka, K. Hušková, Epitaxial growth of high-κ TiO[sub 2] rutile films on RuO[sub 2] electrodes, J. Vac. Sci.

Die approbierte gedruckte Originalversion dieser Dissertation ist an der TU Wien Bibliothek verfügbar.
The approved original version of this doctoral thesis is available in print at TU Wien Bibliothek.
TU Bibliothek Your knowledge hub WIEN

Technol. B Microelectron. Nanom. Struct. 27 (2009) 266. https://doi.org/10.1116/1.3021030.

[175] D. Rafieian, W. Ogieglo, T. Savenije, R.G.H. Lammertink, Controlled formation of anatase and rutile TiO_2 thin films by reactive magnetron sputtering, AIP Adv. 5 (2015) 097168. https://doi.org/10.1063/1.4931925.

[176] D.B. Rogers, S.R. Butler, R.D. Shannon, A. Wold, R. Kershaw, Single Crystals of Transition-Metal Dioxides, Inorg. Synth. (1972) 135–145. https://doi.org/https://doi.org/10.1002/9780470132449.ch27.

[177] U. Diebold, The surface science of titanium dioxide, Surf. Sci. Rep. 48 (2003) 53–229. https://doi.org/10.1016/S0167-5729(02)00100-0.

[178] M. Drabik, A. Choukourov, A. Artemenko, J. Matousek, O. Polonskyi, P. Solar, J. Pesicka, J. Lorincik, D. Slavinska, H. Biederman, Aging of nanocluster Ti/TiOx films prepared by means of gas aggregation cluster source, Surf. Coatings Technol. 205 (2011) 48–52. https://doi.org/10.1016/j.surfcoat.2011.02.013.

[179] J. V. Rojas, M. Toro-Gonzalez, M.C. Molina-Higgins, C.E. Castano, Facile radiolytic synthesis of ruthenium nanoparticles on graphene oxide and carbon nanotubes, Mater. Sci. Eng. B Solid-State Mater. Adv. Technol. 205 (2016) 28–35. https://doi.org/10.1016/j.mseb.2015.12.005.

[180] N. Cui, L. Gu, Y. Lei, J. Liu, Y. Qin, X. Ma, Y. Hao, Z.L. Wang, Dynamic Behavior of the Triboelectric Charges and Structural Optimization of the Friction Layer for a Triboelectric Nanogenerator, ACS Nano. 10 (2016) 6131–6138. https://doi.org/10.1021/acsnano.6b02076.

[181] M. Drabik, A. Choukourov, A. Artemenko, O. Polonskyi, O. Kylian, J. Kousal, L. Nichtova, V. Cimrova, D. Slavinska, H. Biederman, Structure and composition of titanium nanocluster films prepared by a gas aggregation cluster source, J. Phys. Chem. C. 115 (2011) 20937–20944. https://doi.org/10.1021/jp2059485.

[182] A.W. Leissa, The free vibration of rectangular plates, J. Sound Vib. 31 (1973) 257–293. https://doi.org/https://doi.org/10.1016/S0022-460X(73)80371-2.

[183] I. Gheewala, R. Smith, S.D. Kenny, Nanoindentation and nanoscratching of rutile and anatase {TiO}2studied using molecular dynamics simulations, J. Phys. Condens. Matter.

Die approbierte gedruckte Originalversion dieser Dissertation ist an der TU Wien Bibliothek verfügbar.
The approved original version of this doctoral thesis is available in print at TU Wien Bibliothek.
TU Bibliothek WIEN Your knowledge hub

20 (2008) 354010. https://doi.org/10.1088/0953-8984/20/35/354010.

[184] D.M. Potrepka, M. Rivas, H. Yu, R.G. Polcawich, M. Aindow, G.R. Fox, Characterization of IrOxsputtering for IrO2and IrO2/Pt bottom-electrode piezoelectric micro-electro-mechanical systems applications, Thin Solid Films. 638 (2017) 127–137. https://doi.org/10.1016/j.tsf.2017.07.024.

[185] X.Y. Liu, Y.M. Liu, S. Takekawa, K. Kitamura, F.S. Ohuchi, J.Y. Li, Nanopolar structures and local ferroelectricity of Sr0.61Ba 0.39Nb2O6 relaxor crystal across Curie temperature by piezoresponse force microscopy, J. Appl. Phys. 106 (2009). https://doi.org/10.1063/1.3273481.

[186] J. Sladek, V. Sladek, S.M. Hosseini, Analysis of a curved Timoshenko nano-beam with flexoelectricity, Acta Mech. 232 (2021) 1563–1581. https://doi.org/10.1007/s00707-020-02901-6.

[187] L. Qi, S. Huang, G. Fu, S. Zhou, X. Jiang, On the mechanics of curved flexoelectric microbeams, Int. J. Eng. Sci. 124 (2018) 1–15. https://doi.org/https://doi.org/10.1016/j.ijengsci.2017.11.022.

[188] A. Abdollahi, C. Peco, D. Millán, M. Arroyo, I. Arias, Computational evaluation of the flexoelectric effect in dielectric solids, J. Appl. Phys. 116 (2014). https://doi.org/10.1063/1.4893974.

[189] S.J. Freakley, J. Ruiz-Esquius, D.J. Morgan, The X-ray photoelectron spectra of Ir, IrO2 and IrCl3 revisited, Surf. Interface Anal. 49 (2017) 794–799. https://doi.org/10.1002/sia.6225.

[190] H. Idriss, On the wrong assignment of the XPS O1s signal at 531–532 eV attributed to oxygen vacancies in photo- and electro-catalysts for water splitting and other materials applications, Surf. Sci. 712 (2021) 2–7. https://doi.org/10.1016/j.susc.2021.121894.

[191] S.J. Kerber, J.J. Bruckner, K. Wozniak, S. Seal, S. Hardcastle, T.L. Barr, The nature of hydrogen in x-ray photoelectron spectroscopy: General patterns from hydroxides to hydrogen bonding, J. Vac. Sci. Technol. A Vacuum, Surfaces, Film. 14 (1996) 1314–1320. https://doi.org/10.1116/1.579947.

[192] M.D. Stamate, Dielectric properties of TiO 2 thin films deposited by a DC magnetron sputtering system, Thin Solid Films. 372 (2000) 246–249.

TU WIEN Bibliothek Your knowledge hub
Die approbierte gedruckte Originalversion dieser Dissertation ist an der TU Wien Bibliothek verfügbar.
The approved original version of this doctoral thesis is available in print at TU Wien Bibliothek.

[193] S. Kashiwaya, J. Morasch, V. Streibel, T. Toupance, W. Jaegermann, A. Klein, The Work Function of TiO2, Surfaces. 1 (2018) 73–89. https://doi.org/10.3390/surfaces1010007.

[194] B.R. Chalamala, Y. Wei, R.H. Reuss, S. Aggarwal, B.E. Gnade, R. Ramesh, J.M. Bernhard, E.D. Sosa, D.E. Golden, Effect of growth conditions on surface morphology and photoelectric work function characteristics of iridium oxide thin films, Appl. Phys. Lett. 74 (1999) 1394–1396. https://doi.org/10.1063/1.123561.

[195] B. Sun, M. Xiao, G. Zhou, Z. Ren, Y.N. Zhou, Y.A. Wu, Non–zero-crossing current-voltage hysteresis behavior in memristive system, Mater. Today Adv. 6 (2020). https://doi.org/10.1016/j.mtadv.2020.100056.

[196] F. Messerschmitt, M. Kubicek, J.L.M. Rupp, How Does Moisture Affect the Physical Property of Memristance for Anionic-Electronic Resistive Switching Memories?, Adv. Funct. Mater. 25 (2015) 5117–5125. https://doi.org/10.1002/adfm.201501517.

[197] B.D. Hoskins, D.B. Strukov, Maximizing stoichiometry control in reactive sputter deposition of TiO 2 , J. Vac. Sci. Technol. A Vacuum, Surfaces, Film. 35 (2017) 020606. https://doi.org/10.1116/1.4974140.

[198] M. Xiao, K.P. Musselman, W.W. Duley, N.Y. Zhou, Resistive switching memory of TiO2 nanowire networks grown on ti foil by a single hydrothermal method, Nano-Micro Lett. 9 (2017) 1–9. https://doi.org/10.1007/s40820-016-0116-2.

[199] S. Kim, Y.K. Choi, A Comprehensive Study of the Resistive Switching Mechanism in Al/TiOx/TiO2/Al-Structured RRAM, IEEE Trans. Electron Devices. 56 (2009) 3049–3054.

[200] L.E. Yu, S. Kim, M.K. Ryu, S.Y. Choi, Y.K. Choi, Structure effects on resistive switching of Al/TiOχ/Al devices for RRAM applications, IEEE Electron Device Lett. 29 (2008) 331–333. https://doi.org/10.1109/LED.2008.918253.

[201] S. Abdelouahed, K.P. McKenna, Relevance of non-equilibrium defect generation processes to resistive switching in TiO2, J. Appl. Phys. 118 (2015). https://doi.org/10.1063/1.4932225.

[202] C. Mannequin, P. Gonon, C. Vallée, L. Latu-Romain, A. Bsiesy, H. Grampeix, A. Salaün, V. Jousseaume, Stress-induced leakage current and trap generation in HfO 2 thin

Die approbierte gedruckte Originalversion dieser Dissertation ist an der TU Wien Bibliothek verfügbar.
The approved original version of this doctoral thesis is available in print at TU Wien Bibliothek.
TU Bibliothek Your knowledge hub WIEN

films, J. Appl. Phys. 112 (2012). https://doi.org/10.1063/1.4756993.

[203] F. Chiu, A Review on Conduction Mechanisms in Dielectric Films, Adv. Mater. Sci. Eng. 2014 (2014). https://doi.org/http://dx.doi.org/10.1155/2014/578168.

[204] H. Hirakawa, M. Hashimoto, Y. Shiraishi, T. Hirai, Photocatalytic Conversion of Nitrogen to Ammonia with Water on Surface Oxygen Vacancies of Titanium Dioxide, J. Am. Chem. Soc. 139 (2017) 10929–10936. https://doi.org/10.1021/jacs.7b06634.

[205] R. Martin, M. Kim, C.J. Lee, M.S. Shariff, F. Feng, R.J. Meyer, A. Asthagiri, J.F. Weaver, Molecular chemisorption of N2 on IrO2(110), J. Chem. Phys. 152 (2020). https://doi.org/10.1063/1.5142210.

[206] D.S. Jeong, H. Schroeder, U. Breuer, R. Waser, Characteristic electroforming behavior in Pt/ TiO2 /Pt resistive switching cells depending on atmosphere, J. Appl. Phys. 104 (2008). https://doi.org/10.1063/1.3043879.

[207] T. Heisig, C. Baeumer, U.N. Gries, M.P. Mueller, C. La Torre, M. Luebben, N. Raab, H. Du, S. Menzel, D.N. Mueller, C.L. Jia, J. Mayer, R. Waser, I. Valov, R.A. De Souza, R. Dittmann, Oxygen Exchange Processes between Oxide Memristive Devices and Water Molecules, Adv. Mater. 30 (2018) 1–7. https://doi.org/10.1002/adma.201800957.

[208] G. Zhang, H. Wang, J. Yang, Q. Zhao, L. Yang, H. Tang, C. Liu, H. Chen, Y. Lin, F. Pan, Temperature Effect on Co-Based Catalysts in Oxygen Evolution Reaction, Inorg. Chem. 57 (2018) 2766–2772. https://doi.org/10.1021/acs.inorgchem.7b03168.

[209] S. Czioska, K. Ehelebe, J. Geppert, D. Escalera-López, A. Boubnov, E. Saraçi, B. Mayerhöfer, U. Krewer, S. Cherevko, J.D. Grunwaldt, Heating up the OER: Investigation of IrO2 OER Catalysts as Function of Potential and Temperature**, ChemElectroChem. 202200514 (2022) 1–9. https://doi.org/10.1002/celc.202200514.

[210] S. Selçuk, A. Selloni, Influence of external electric fields on oxygen vacancies at the anatase (101) surface, J. Chem. Phys. 141 (2014). https://doi.org/10.1063/1.4893559.

Die approbierte gedruckte Originalversion dieser Dissertation ist an der TU Wien Bibliothek verfügbar.
The approved original version of this doctoral thesis is available in print at TU Wien Bibliothek.
TU Bibliothek WIEN Your knowledge hub